UNIVERSITY OF NATAL

TURBULENT MIXING AND DISPERSION IN ENVIRONMENTAL FLOWS

by

Subhas Karan Venayagamoorthy

BScEng (Summa Cum Laude), GMSAICE

Submitted in fulfillment of the academic requirements for the degree of

Master of Science in Engineering,

In the

Civil Engineering Programme

University of Natal

2002

Durban

March 2002

ABSTRACT

Stably stratified flows are common in the environment such as in the atmospheric boundary layer, the oceans, lakes and estuaries. Understanding mixing and dispersion in these flows is of fundamental importance in applications such as the prediction of pollution dispersion and for weather and climate prediction/models.

Mixing efficiency in stratified flows is a measure of the proportion of the turbulent kinetic energy that goes into increasing the potential energy of the fluid by irreversible mixing. This can be important for parameterizing the effects of mixing in stratified flows. In this research, fully resolved direct numerical simulations (DNS) of the Navier-Stokes equations are used to study transient turbulent mixing events. The breaking of internal waves in the atmosphere could be a source of such episodic events in the environment. The simulations have been used to investigate the mixing efficiency (integrated over the duration of the event) as a function of the initial turbulence Richardson number $Ri = N^2L^2/u^2$, where N is the buoyancy frequency, L is the turbulence length scale, and u is the turbulence velocity scale. Molecular effects on the mixing efficiency have been investigated by varying the Prandtl number $Pr = \nu/\kappa$, where ν is the viscosity and κ is the scalar diffusivity. Comparison of the DNS results with grid turbulence experiments has been carried out. There is broad qualitative agreement between the experimental and DNS results. However the experiments suggest a maximum mixing efficiency of 6% while our DNS gives values about five times higher. Reasons for this discrepancy are investigated. The mixing efficiency has also been determined using linear theory. It is found that the results obtained for the very stable cases converge on those obtained from DNS suggesting that strongly stratified flows exhibit linear behaviour.

Lagrangian analysis of mixing is fundamental in understanding turbulent diffusion and mixing. Dispersion models such as that of Pearson, Puttock & Hunt (1983) are based on a Lagrangian approach. A particle-tracking algorithm (using a cubic spline interpolation scheme following Yeung & Pope, 1988) was developed and incorporated into the DNS code to enable an investigation into the fundamental aspects of mixing and diffusion from a Lagrangian perspective following fluid elements. From the simulations, the ensemble averaged rate of mixing as a function of time indicates clearly that nearly all the mixing in these flows occurs within times of order 3 L/u. The mean square vertical displacement statistics show how the stable stratification severely inhibits the vertical displacement of fluid elements but has no effect on displacements

in the transverse direction. This is consistent with the Pearson, Puttock & Hunt model. The important link that asymptotic value of the mean square vertical displacement is a measure of the total irreversible mixing that has occurred in the flow is made. However the results show that the change in density of the fluid elements is only weakly correlated to the density fluctuations during the time when most of the mixing occurs, which contradicts a key modeling assumption of the PPH theory. Improvements to the parameterization of this mixing are investigated.

Flow structures in stably stratified turbulence were examined using flow visualization software. The turbulence structure for strong stratification resembles randomly scattered pancakes that are flattened in the horizontal plane. It appears that overturning motions are the main mechanism by which mixing occurs in these flows.

In memory of my father

The late Mr S N Venayagamoorthy

who taught me the value of education

PREFACE

I, Subhas Karan Venayagamoorthy hereby declare that the whole of this dissertation is my own work and has not been submitted in part, or in whole to any other University. Where use has been made of the work of others, it has been duly acknowledged in the text. This research work was carried out in the Centre for Research in Environmental, Coastal and Hydrological Engineering, School of Civil Engineering, Surveying and Construction, University of Natal, Durban, under the supervision of Professor D D Stretch.

5/03/2002 ..... V.S. Karan .....

Date Signature

As the candidate's supervisor I have approved this dissertation for submission

Signed: ..... Name: D. D. STRETCH Date: 5/03/2002

ACKNOWLEDGEMENTS

I wish to express sincere thanks to my supervisor, Professor Derek D Stretch for his encouragement, guidance, useful suggestions, imparted knowledge, cooperation and constant support throughout my studies. Thank you very much Professor Stretch.

I also wish to thank:

- The academic staff of the Civil Engineering Programme for their commitment, availability and excellence. I also extend my thanks to the technical and administrative staff of the Civil Engineering Programme for all the support provided during my studies. I wish to specially thank Mrs Tina Warby for her pleasant attitude, and for all the encouragement and assistance she offered to me during my studies.

- My family for their support, encouragement and prayers during the course of my studies

- The friends from Kingdom Life Church, Glenmore for their love, prayers, and encouragement.

- Finally to Jesus Christ, my Maker, Saviour and Lord for his presence, love, help and support throughout my MScEng studies.

TABLE OF CONTENTS

LIST OF FIGURES

LIST OF TABLES

LIST OF SYMBOLS

b	buoyancy flux
B	integral buoyancy flux
C_d	drag coefficient
e	average energy per unit volume
E_0	Initial total energy
E_s	Energy in the fundamental "sloshing" modes
F_T	Froude number
g	acceleration due to gravity
k	wavenumber
k_{max}	highest resolvable wavenumber
k_0	minimum wavenumber
KE_0	Initial kinetic energy
L_0	initial length scale of most energetic eddies
M	number of particles
N	number of grid points
N	Brunt-Vaisala frequency
N^{-1}	buoyancy time scale
Nt	non-dimensional buoyancy time
p	pressure
Pe	Peclet number
PE_0	Initial potential energy
Pr	Prandtl number
q_0	mean turbulent velocity magnitude
R^2	coefficient of determination
Re	Reynolds number
Ri	gradient Richardson number
R_f	flux Richardson number
$R_w(\tau)$	Lagrangian velocity autocorrelation
Sc	Schmidt number
t	non-dimensional time (units of L_0/ u_0)
T_{BV}	Brunt- Väisälä period
T_L	Lagrangian integral time scale
U	tow speed
u	horizontal velocity component

$\left\|\overline{u^2}\right\|$	mean square horizontal velocity
$\underline{u}$	velocity vector
u_0	initial velocity scale
v	horizontal velocity component
w	vertical velocity component
$\left\|\overline{w^2}\right\|$	mean square vertical velocity
w_0	initial vertical velocity
W	total work done
$\overline{Z^2}$	mean square vertical displacement
ε_{KE}	kinetic energy dissipation
ε_{PE}	potential energy dissipation
κ	molecular diffusivity
η	vertical displacement
η	mixing efficiency
η	Kolmogorov scale
ρ	density
ρ'	density fluctuation
ρ_0	reference density
$\overline{\rho}$	mean density
$\overline{\rho^2}$	mean square density
$\sigma_{\overline{\rho}}$	standard deviation of density
μ	molecular viscosity
$\left\|\overline{v^2}\right\|$	mean square horizontal velocity
ν	kinematic viscosity
$\overline{\omega^2}$	enstrophy = mean square of vorticity
$\left\|\overline{\omega^2}\right\|$	normalized mean square vorticity
$\left\|\overline{\omega}_H\right\|$	magnitude of horizontal vorticity
ω_z	vertical vorticity
$\overline{\omega_z^2}$	mean square vertical vorticity
γ	mixing factor

LIST OF ABBREVIATIONS

CGBF	counter gradient buoyancy flux
DNS	direct numerical simulations
LES	large eddy simulations
KE	kinetic energy
KH	Kimura & Herring (1996)
Mb	megabytes
MHz	megahertz
PE	potential energy
PPH	Pearson, Puttock & Hunt (1983)
RAM	random access memory
RDT	rapid distortion theory
TKE	turbulent kinetic energy

CHAPTER 1

INTRODUCTION

1.1 Introduction

Stably stratified flows are common in the environment such as in the atmospheric boundary layer, the oceans, lakes and estuaries. The presence of the stable stratification has substantial effect on many physical processes involved such as the mixing efficiency and rates of mixing. The importance of mixing can be obvious to the layman by simply visiting a huge industrial or urban complex when there is an atmospheric inversion. It will be apparent that the stable stratification inhibits the vertical mixing of the pollutants thereby increasing their concentration near the ground, resulting in unpleasant conditions. Understanding mixing and dispersion in these flows is of fundamental importance in applications such as the prediction of pollution dispersion and for weather and climate prediction.

A great deal of effort has gone into research and development of simple and effective theories and models in stably stratified turbulence. Publications in this field are broad encompassing fundamental aspects to the more specific applications in engineering and geophysics. This dissertation investigates the aspects of mixing in stably stratified turbulence using direct numerical simulations (DNS). DNS involves the complete solution of the three-dimensional Navier-Stokes equations to obtain a full description of a turbulent flow i.e. where the flow variables such as the velocity and pressure are known as a function of space and time

1.2 Project Background and Objectives

The mixing efficiency is important in the parameterization of mixing processes that occur in stably stratified flows. It is the proportion of turbulent kinetic energy that goes into increasing the potential energy of the fluid by irreversible mixing. The mixing efficiency has been calculated mostly by way of laboratory experiments and more recently using direct numerical simulations (DNS). However there has been a lack of coherence in the different approaches employed thus far.

The rate of mixing is dependent on small scale mixing processes. This is particularly relevant to stably stratified flows as noted by Pearson, Puttock & Hunt (1983), hereafter referred to as PPH. PPH made use of a Lagrangian approach to study mixing and dispersion in stably stratified turbulence. The theory of PPH modelled the density exchange between fluid elements, which highlighted the particular importance of small scale mixing in the flows. However, there have been no definitive evaluations done on such theories to validate the small scale mixing formulations used in them, mainly due to the difficulty in gathering Lagrangian statistics in the laboratory.

The main objectives of this study are:

- To perform DNS of stably stratified flows (albeit at low to moderate Reynolds numbers due to computing limitations) and calculate the mixing efficiency for different strengths of stratifications from these simulations.

- Compare the DNS mixing efficiency results with those obtained from laboratory experiments and suggest possible reasons for the discrepancies noted.

- To use a Lagrangian approach to explicitly address the issue of small scale mixing in stably stratified turbulence by extracting the density exchanges following fluid elements. This would provide an understanding on how the density of the fluid particles change with time (and/or space) and hence a basis to evaluate the adequacy of the PPH theory on small scale mixing and gain fundamental understanding into the physics governing such processes.

- To study the flow structures in stably stratified turbulence by means of flow visualizations and relate the structural features to mixing.

1.3 Dissertation Layout

The technical content of this dissertation has been arranged into five further chapters and two appendices. The next five chapters generally present information and results on the context of this dissertation. Other relevant information and program code listings are included in the appendices.

Chapter Two presents a literature review on mixing in stably stratified flows. Definitions of some of the basic parameters used in the context of this research are provided

together with the equations of motions governing such flows. Review of work done on mixing efficiency and energetics in stratified flows by various authors is carried out and observations drawn.

In Chapter Three, a study of transient (decaying) mixing events in stably stratified turbulence using DNS is reported. The formulation of DNS is provided briefly together with the underlying assumptions. The results on the mixing efficiency of various stably stratified flows are presented. Discrepancies between DNS and experimental results are discussed. The energetics governing these flows are addressed by means of the energy, buoyancy flux and various spectra plots. Rapid Distortion Theory is used to investigate whether strongly stratified turbulence is dominated by internal (linear) waves.

Chapter Four presents the innovative part of this dissertation in that it presents the Lagrangian approach used to gain fundamental understanding on the physics of small scale mixing in stably stratified flows. The particle-tracking algorithm used for this study is presented first. The Lagrangian statistics on displacements and rate of mixing are shown. The correlation of the rate of mixing to the density fluctuations and other parameters are presented. Adequacy of the Pearson, Puttock & Hunt theory is tested.

The structures in stably stratified flows are investigated by means of flow visualizations in Chapter Five. Three-dimensional plots of flow visualizations of enstrophy, horizontal vorticity, vertical vorticity, density, vertical density gradients are presented. Qualitative inferences on the structures and their relationship to mixing are presented. Flow structures for very strong stable stratifications from DNS and RDT simulations are studied to identify any similarities.

Chapter Six concludes this dissertation summarizing what has been done and the main findings thereof in this study. Directions on further work from the author's point of view waiting in this exciting and important field in fluid dynamics are indicated.

Appendix A provides tables and program listing referred to in Chapter Three and Appendix B gives the particle tracking program listing discussed in Chapter Four.

1.4 New Contributions

While the work of this thesis is primarily an extension of the work of others (e.g. Riley, Metcalfe & Weissman 1981, Kimura & Herring 1996), it nevertheless makes the following meaningful and original contribution to research in stably stratified flows:

- The extraction of the change in density due to mixing following fluid elements provides an original and efficient method to gain fundamental understanding into the small scale mixing processes in stably stratified turbulence. This has allowed a preliminary investigation into the adequacy of the mixing theory used in current dispersion models.

1.5 Research Publications

Two international conference papers (Stretch et al, 2001 and Venayagamoorthy et al, 2002) have been presented on some aspects and findings of the work of this dissertation.

1.6 Summary

This dissertation investigates primarily the mixing in stably stratified flows under decaying turbulence. The investigation is carried out by means of direct numerical simulations (DNS) using both Eulerian and Lagrangian approaches.

The main body of the dissertation starts in the next chapter which provides a brief literature review on stratified turbulence.

CHAPTER 2

LITERATURE REVIEW OF MIXING IN STABLY STRATIFIED FLOWS

2.1 Introduction

Stably stratified flows are common in the environment such as the atmospheric boundary layer, the oceans, lakes and estuaries. In stably stratified flows, the mean potential density increases with depth, in most of the regions and for most of the time. Hence when in equilibrium, the lighter fluid lies above the heavier fluid. The tilting of any density surface will consequently produce a restoring force resulting in motion that can overshoot the equilibrium position. This gives rise to oscillatory motions about the equilibrium position resulting in internal waves. The converse, which when the lighter fluid lies below the heavier, results in instability leading to overturning forces and convective motions (Turner, 1973), (see figure 2.1).

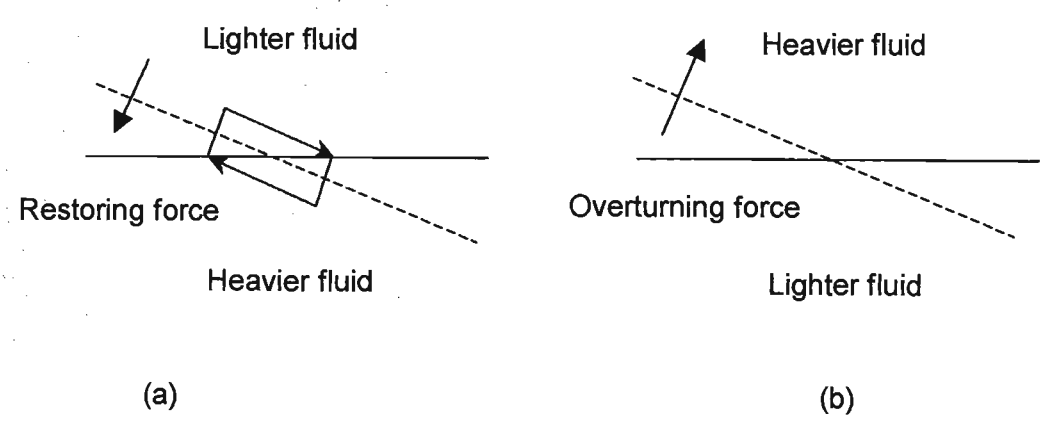

Figure 2.1: Displacements from hydrostatic equilibrium, (a) stable and (b) unstable density distributions.

In this chapter, a brief review of stably stratified turbulence is presented highlighting key background information that was fundamental to this research. Published work on mixing efficiency and dispersion in stratified turbulence using experiments, DNS and theoretical approaches are discussed to address key issues of importance in this field.

2.2 The equations of motion and the Boussinesq Approximation

The momentum (Navier-Stokes) equations with the force of gravity included can be written as:

$$\rho\frac{D\underline{u}}{Dt}=\rho\left(\frac{\partial\underline{u}}{\partial t}+(\underline{u}\cdot\nabla\underline{u})\right)=-\nabla p+\rho\underline{g}+\mu\nabla^2\underline{u} \tag{2.1}$$

Here $\underline{g}$ = (0,0, -g), the x and y axes being in the horizontal plane and z is vertically upwards. The first term on the right hand side of equation (2.3) takes into account the pressure forces and the second term allows for buoyancy forces in the fluid. The last term describes the shear stresses due to the molecular viscosity, μ.

Equation (2.1) can be further simplified to yield the so-called Boussinesq approximation based on the assumptions that (Turner, 1973) variations of density are neglected in so far as their effect on inertia are concerned, but are retained in the buoyancy terms (the validity of this assumption has been based on dimensional arguments). The assumption formally requires that the density variations are small (i.e. $\rho'/\rho_0 << 1$). This enables the momentum equation to be written in the Boussinesq approximation as:

$$\frac{D\underline{u}}{Dt}=-\frac{1}{\rho_0}\nabla p+\frac{\rho'}{\rho_0}\underline{g}+\nu\nabla^2\underline{u} \tag{2.2}$$

where ρ' is the density fluctuation from the background mean density and ρ_0 is a constant reference density and p is the kinematic pressure, which allows for the hydrostatic contribution from $\rho_0+\overline{\rho}(z)$. This is coupled with mass conservation to yield (in the Boussinesq approximation):

$$\nabla\cdot\underline{u}=0 \tag{2.3}$$

and

$$\frac{D\rho}{Dt}=\kappa\nabla^2\rho \tag{2.4}$$

where κ is the molecular diffusivity.

The DNS code used for this research has been based on this simplified form of the momentum equation in its non-dimensional form together with equations for mass conservation.

2.3 Basic Parameters Common to Stratified Turbulence

Several parameters are fundamental in the subject of stratified turbulence. These parameters will be frequently used throughout this dissertation and hence will be defined here. The detailed relevance of these parameters will be dealt with where appropriate in the subsequent chapters.

2.3.1 Buoyancy frequency and period

In a uniformly stably stratified flow, the density increases linearly downwards as shown in figure 2.2

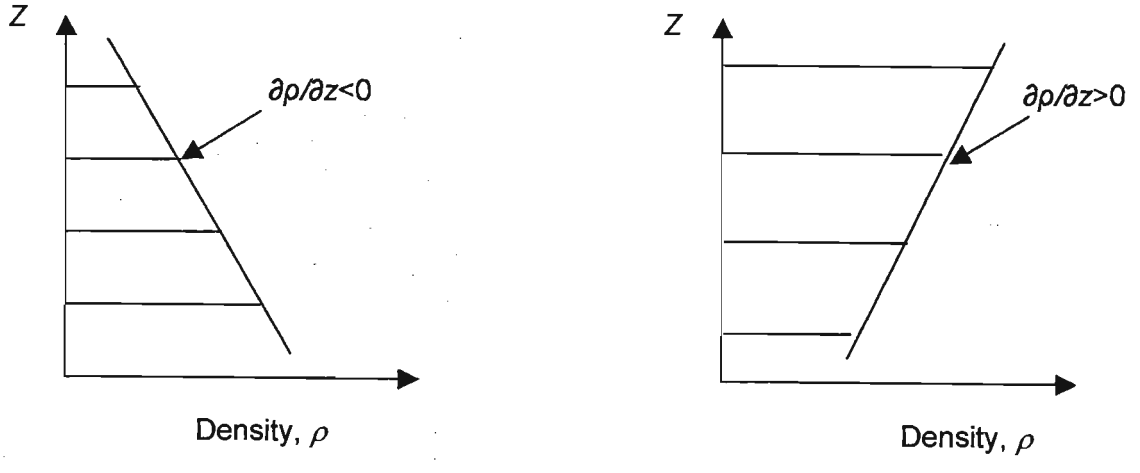

Figure 2.2: The variation of density with depth z, (a) stable case, and (b) unstable case

Consider a fluid particle displaced by a small distance η vertically from its equilibrium position in a stable environment (see figure 2.2(a)). The net force acting on the fluid particle is the weight of the fluid displaced by the particle by

$$F = (m - m_p)g \tag{2.5}$$

where m is the mass of the ambient fluid and m_p is the particle mass. The Lagrangian form of Newton's second law of motion gives the particle acceleration as:

$$m_p \frac{d^2 z}{dt^2} = m_p a_z = (m - m_p) g \tag{2.6}$$

Rearranging and simplifying gives

$$a_z = \left(\frac{\rho - \rho_0}{\rho_0} \right) g = \frac{\Delta \rho}{\rho_0} g \tag{2.7}$$

Using Taylor series expansion of density and height (ρ, z) relative to the particle's initial conditions, together with equation (2.7), the vertical displacement η of the particle can be described by

$$\frac{d^2 \eta}{dt^2} = \left(\frac{g}{\rho} \frac{\partial \rho}{\partial z} \right) \eta \tag{2.8}$$

Equation (2.8) describes the motion of the displaced fluid particle and is clearly a simple harmonic motion. The term $(-g/\rho \, \partial\rho/\partial z)^{\frac{1}{2}}$ is known as the Brunt-Väisälä frequency or the buoyancy frequency, N, with dimensions of t^{-1}. It is the frequency of vertically propagating gravity waves in a stable atmosphere. In the case considered, the density gradient, $\partial\rho/\partial z < 0$, hence the solution to equation (2.8) will be given by

$$\eta = \frac{w_0}{N} SinNt \tag{2.9}$$

This indicates that in the absence of friction, a displaced fluid particle in a stable density field will try and migrate to fluid of its own density but in doing so will overshoot that position as described earlier in section 2.1 and in figure 2.3. The overshoot will be eventually be restricted as the buoyancy force overcomes the acceleration and attempts to return to its equilibrium position. A dampening in the overshoot will eventually occur due to friction (e.g. Streeter, Wylie & Bedford, 1998).

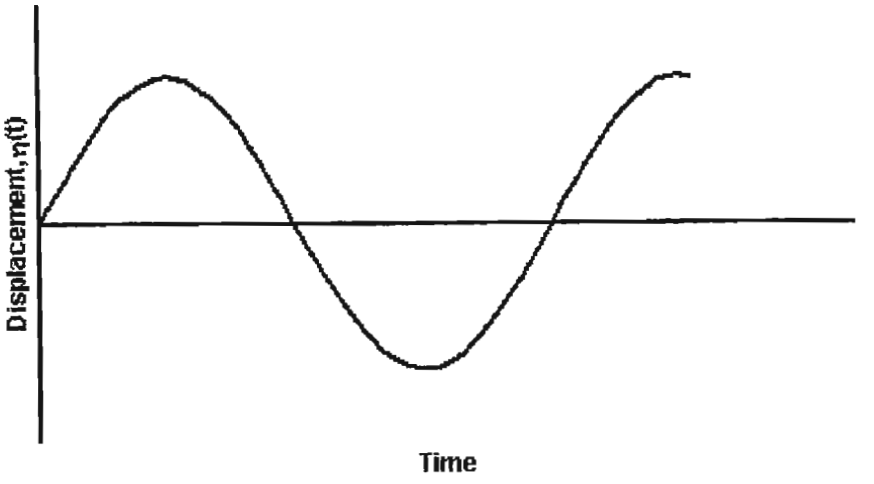

Figure 2.3: Particle displacement versus time in a stably stratified flow (undamped motion)

The buoyancy period (T_{BV}) associated with the buoyancy frequency is $2\pi/N$ and is typically a few minutes in the atmosphere and the oceanic thermocline and up to a few hours in the deep ocean (Turner, 1973).

2.3.2 Richardson number and Froude number

The Richardson number *Ri,* is a non-dimensional parameter that is used as a measure of the strength of the stratification and is an indication of the relative importance of buoyancy to inertial forces in the fluid. It may be expressed as:

$$Ri = \left(\frac{NL_0}{u_0} \right)^2 \tag{2.10}$$

where L_0, u_0 are the length and velocity scales of the most energetic eddies in the turbulent motion.

The Froude number is another non-dimensional parameter describing the ratio of inertial to buoyancy forces and maybe defined as

$$F_T = u_0 / NL_0 = Ri^{-1/2} \tag{2.11}$$

2.3.3 The Reynolds number

The Reynolds number *Re* is a ratio of the inertial forces to the viscous forces in the flow. It is given by

$$Re = u_0 L_0 / \nu \tag{2.12}$$

where ν is the kinematic viscosity. Flow at velocity u_0 and length scale L_0 can be considered inviscid at large enough *Re* numbers, however, when the fluid is strongly stratified, the density gradient can suppress vertical motions, introducing much smaller length scales into the problem. This means that *Re* in this scenario will not necessarily be large and hence viscous as well as molecular diffusion effects could become relevant in the physics of the flow (Turner, 1973).

2.3.4 The Peclet and Prandtl (or the Schmidt) number

The Prandtl number *Pr* (or equivalently the Schmidt number *Sc*) characterizes molecular diffusion effects in the flow and is given by the ratio, $Pr = \nu/\kappa$, where ν is the kinematic viscosity and κ is the molecular diffusivity of the fluid. The Peclet number $Pe = u_0 L_0 / \kappa = Pr.Re$ determines the importance of molecular effects at scales u_0, L_0, for the flow.

2.3.5 The Flux Richardson number

An Integral flux Richardson number R_f may be defined as the ratio of the time integral of the buoyancy flux to the change in the turbulent kinetic energy over the same period of time. The turbulent kinetic energy (TKE) per unit mass is equal to ½ (u^2 + v^2 + w^2) where *u*, *v* & *w* are the velocity components respectively. Whence

$$R_f = B / \Delta KE = \int b dt / \Delta KE \tag{2.13}$$

where $b = \frac{-g}{\rho_0} \overline{\rho w}$ and ΔKE = change in TKE

2.4 Energetics of Stratified Turbulent Flows

The energetics involved in stratified flows are crucial in understanding and evaluating the mixing characteristics in stably stratified flows. Winters et al (1995) provide a thorough discussion on the energetics of density-stratified flows (in the Boussinesq approximation). In stratified flows, buoyancy restoring forces are created when fluid displacements occur and this provides a pathway for conversion between kinetic and potential energy in the flow. They carried out their analysis based on the notion that for a closed fluid system, only reversible diabatic processes can change the probability density function of the density. This scenario is appropriate to the DNS used in this research, as the background potential energy of the fluid cannot change due to boundary fluxes (see section 3.3.2). The evolution of energy of a stratified fluid has been recently re-examined by Rottman, Seshadri, Nomura & Stretch, (2001) who derived exact equations for the energetics in a stratified fluid.

The energetics of homogenous stably stratified turbulent flows are described by

$$\frac{d}{dt}(KE) = -b - \varepsilon_{KE} \tag{2.14}$$

$$\frac{d}{dt}(PE) = +b - \varepsilon_{PE} \tag{2.15}$$

where the buoyancy flux $b = (-g/\rho_0)\overline{\rho w}$, the kinetic energy KE= ½ $(\overline{u}^2 + \overline{v}^2 + \overline{w}^2)$, the potential energy PE = ½ $g/\rho_0(-\partial\overline{\rho}/\partial z)^{-1}\overline{\rho}^2$ and ε_{KE} and ε_{PE} are the kinetic energy and potential energy dissipation rates respectively.

Figure 2.4 shows the energy diagram for a density stratified flow (Winters et al, 1995).

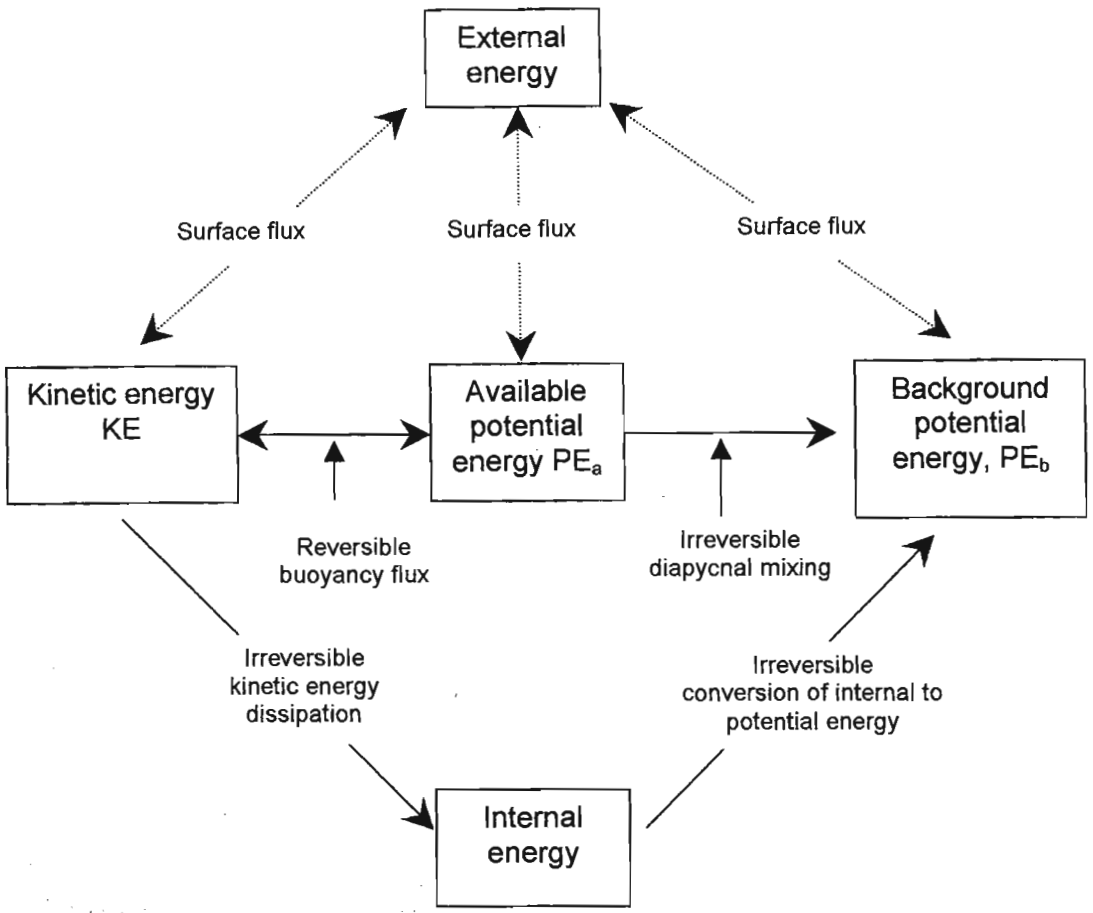

Figure 2.4: Flow chart showing the energetics of density stratified flow (Winters, et al, 1995).

The energy in a stratified flow can be stored as kinetic, available potential, background potential, or internal energy. The transfer of energy can occur through buoyancy flux, diabatic mixing or viscous dissipation. The initial available potential energy of the flow is set equal to zero for all the simulations conducted for this research. The simulations were initialized with a specified initial kinetic energy, which is given by the energy spectrum.

2.5 Mixing Efficiency

The term mixing efficiency has been defined in several ways, all of which have the same basic physical interpretation. The mixing efficiency in stratified flows can be defined as the proportion of turbulent kinetic energy that goes into increasing the

potential energy (background) of the fluid by irreversible mixing (Stretch et al, 2001). This mixing efficiency is therefore synonymous with the flux Richardson number R_f, defined by equation (2.13) in section 2.3.5, which is the fraction of the available kinetic energy that is used to do the mixing (Linden, 1980).

Decaying turbulence in stratified flows has been extensively studied by laboratory experiments (Linden 1979, Linden 1980, Dickey & Mellor 1980, Britter, Hunt, Marsh & Snyder 1983, Rohr, Itsweire & Van Atta 1984 and recently by Rehmann & Koseff 2000 and Barry, Ivey, Winters & Imberger 2001). Theoretical models have been developed (e.g. Weinstock 1978, Pearson, Puttock & Hunt 1983) to describe mixing and dispersion in stably stratified flows. Direct numerical simulations (Riley, Metcalfe & Weissman 1981, Metais & Herring 1989, Kimura & Herring 1996) are being increasingly used to gain better understanding of stratified turbulence. The focus of most of these researches has been primarily in understanding and evaluating the relationship between the buoyancy and overturning scales and their evolution (Fernando, 1991). Mixing efficiency results using DNS have been published by Oduyemi (1993), Stretch et al (2000), Stretch et al (2001) and Venayagamoorthy et al (2002).

2.5.1 Laboratory Experiments on Mixing Efficiency

Most of the laboratory experiments on mixing efficiency have been done by towing a biplanar grid through stratified water using salt, heat, or salt and heat. A discussion of the experiments by Rottman & Britter (1986) and Rehmann & Koseff (2000) is presented and will be used later for comparison with the DNS results obtained from this research. The experimental facilities consisted of a large stratified tank, typical sizes were 4 m long, 0.8 m wide and 1.2 m deep (Rehmann & Koseff, 2000) and 25 m long, 2.47 m wide and 1.2 m deep (Rottman & Britter, 1986), (see figure 2.5 for schematic layout).

The density profiles used were linear with the buoyancy frequency between 0.17 and 1.60 s^{-1}. A biplanar grid was suspended from a towing tank carriage that travels on rails at speeds in the range 2.0 cm/s to 50 cm/s. The drag force on the grid was measured by towing the grid through the tank in the lengthways direction at constant speed. The fluid was allowed to settle between tows until there was no visible motion before the next tow was begun. The horizontal component of the force on the grid was measured

with a calibrated load cell. Form drag was predominant in these experiments with a drag coefficient C_d = 1.4 reported by Rottman & Britter (1986).

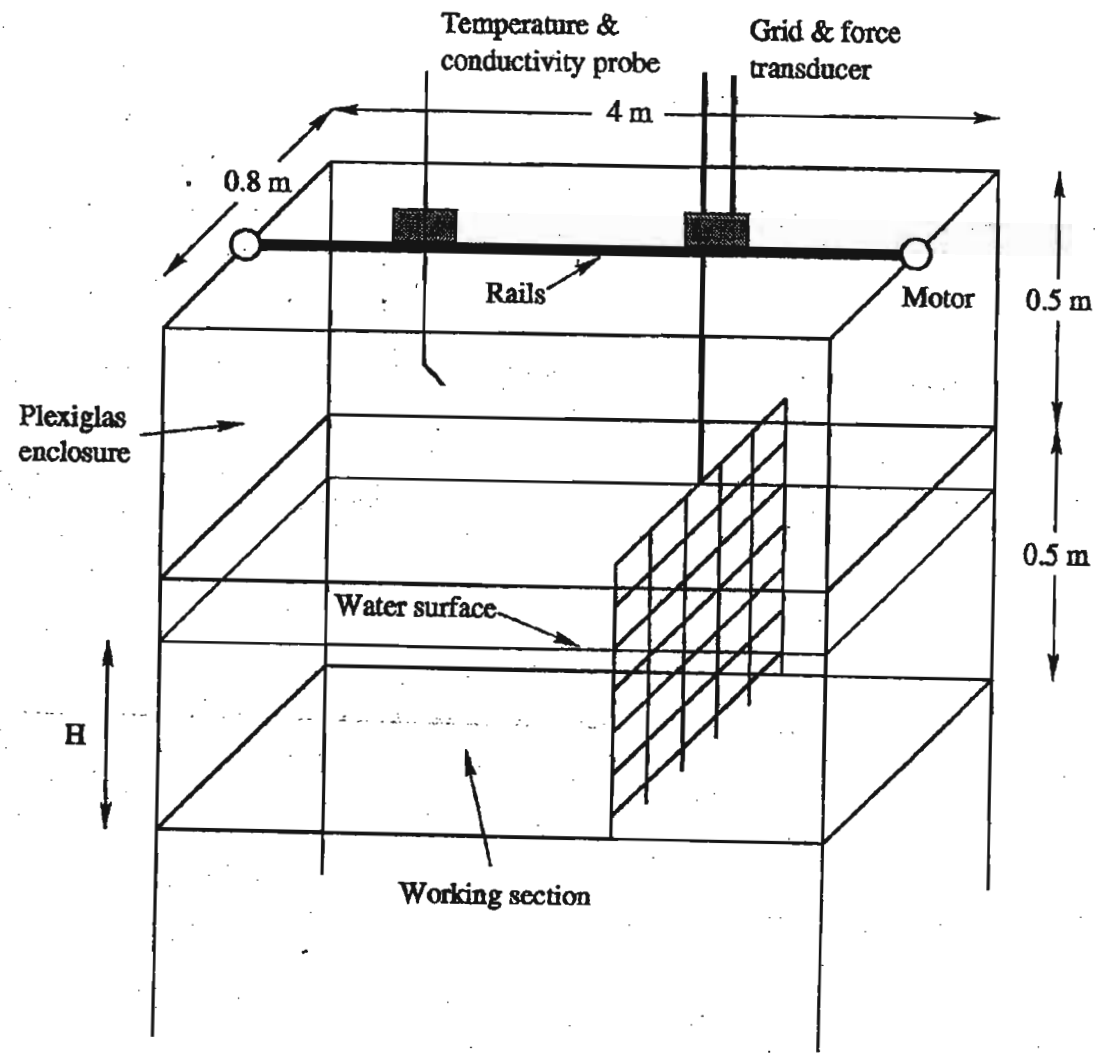

Figure 2.5: Schematic diagram of the experimental facility. The water depth H was 35 cm (Rehmann & Koseff, 2000).

The mixing efficiency of the turbulence produced by the grid was measured by towing the grid at constant speeds over the length of the tank. Asymmetry was eliminated by conducting the experiments in even number of tows for a given tow speed. The number of tows ranged from 4 to 100 for the experiments conducted by Rehmann & Koseff (2000) and 10 to 40 for those done by Rottman & Britter (1986). Each set of tows was continued until the density profile had eroded to a degree where it was no longer linear. Note the density profiles were obtained by measuring the salinity (or temperature) of the water at various depths.

Rottman and Britter (1986) indicate that the density profile changed initially by developing well mixed layers at the top and bottom of the tank while the central portion remained nearly linear with initial N value. They drew the analogy that grid-generated turbulence may be visualized as raising the centre of mass of the water in the tank by diffusing heavier fluid up the uniform density gradient or vice versa. An example of the evolution of the mean vertical density profile in the experiments is shown in figure 2.6.

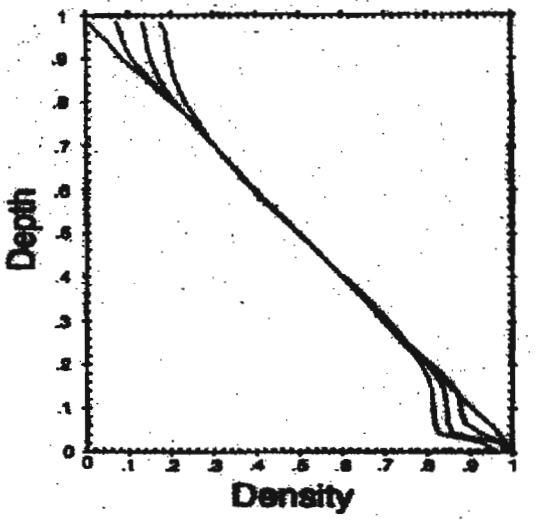

Figure 2.6: The evolution of the vertical distribution of density after n=0, 10, 28 and 40 grid tows, for the case with Ri = 0.41, from Rottman & Britter (1986). The vertical coordinate is scaled by the depth of the water in the tank and the density is scaled such that initially it is zero at the top of the tank and unity at the bottom.

The main interest in these experiments was to determine the mixing efficiency, which is the change in potential energy of the fluid as a fraction of the total energy input (i.e. the work done to tow the grid up and down the tank). The mixing efficiency in these experiments is measured as a function of the Richardson number $Ri = (NM/U)^2$, in which N is the initial buoyancy frequency of the fluid, M is the grid mesh length, and U is the towing speed. It was assumed that all of the work done by towing the grid was transferred into turbulent kinetic energy; an assumption that remains open to question, (see section 3.6.2). The integral form of the flux Richardson number R_f gives this fraction. Figure 2.7 gives the plot of R_f versus Ri for the experiments conducted by Rehmann & Koseff (2000), Rottman & Britter (1986) and Britter (1985), (see Table A.1 in appendix A for the experimental results).

Rehmann & Koseff (2000) developed a scaling analysis that yields three distinct regimes of behaviour of R_f classified by the initial strength of stratification characterized by Ri as shown in figure 2.7. These scalings can be deduced using simple energy arguments (noting that these arguments are not necessarily unique). In section 3.6.1 in chapter 3, these simple energy arguments are presented to deduce these scalings.

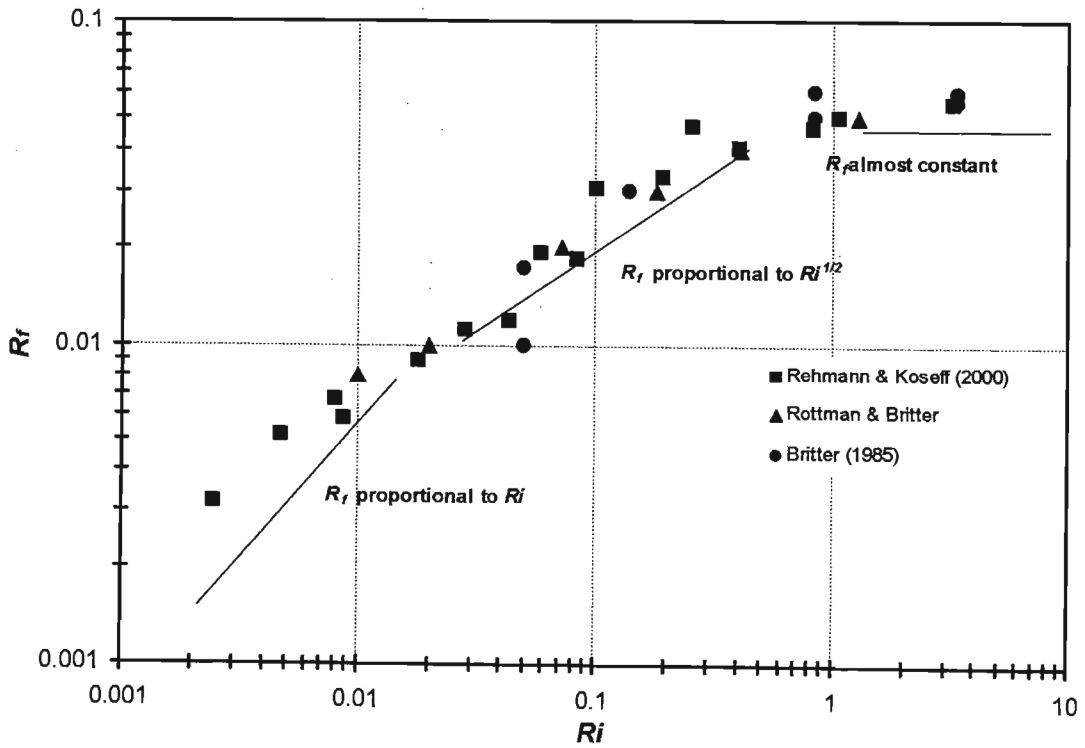

Figure 2.7: Mixing efficiency results from towed grid experiments

The results of these experiments are fairly consistent:

(a) There appears to be no strong dependence on the molecular diffusivity (although there are some uncertainties about this conclusion)
(b) For $Ri < 0.1$, the mixing efficiency increases approximately linearly with Ri.
(c) For $0.1 < Ri < 1$, the mixing efficiency increases approximately like $Ri^{1/2}$.
(d) For $Ri > 1$, the mixing efficiency appears to approach a constant value of about 6%.

There are two main issues worth noting from these results, viz:

Firstly, since none of these laboratory experiments could achieve values of Ri greater than about 10, there remains some uncertainty about the strongly stable limit. Some different experiments e.g. those done by Linden (1980) where a horizontal grid was dropped through a sharp density interface, have suggested that R_f should decrease for sufficiently large Ri. Linden (1979) indicates that R_f increases with stratification at small Ri until it reaches a maximum and then decreases again at high Ri. His speculation was that at high Ri a significant fraction of the turbulent kinetic energy is used to generate internal waves and provided these waves do not break, they do not contribute to mixing, but are eventually dissipated by viscosity. However the mechanism for the decrease in R_f remains uncertain. Agreement with Linden's results on the shape of the R_f versus Ri curve was obtained in experiments conducted by Rohr et al (1984). However it is worth noting that R_f in their case was calculated in an essentially steady state flow while Linden used an average for R_f over the total duration of unsteady mixing events.

The second issue is that the maximum mixing efficiency value of 6% for these experiments is lower than those that has been measured in other types of mixing experiments where values of 10%-20 % have been noted, see e.g. Linden (1979) and Park, Whitehead & Gnanadeskian (1994).

In chapter 3 of this dissertation, DNS of decaying, homogenous, stably stratified turbulence is used to address these two issues.

Recently, Barry et al (2001) have measured diapycnal diffusivities in stratified fluids using linearly stratified salt solutions. Turbulence was generated by horizontal oscillations of a rigid vertical grid. Their purpose was to measure and obtain the relationship between the turbulent diffusivity for mass K_ρ as a function of other turbulent

parameters given in equation 1.16 of their paper. They compared their results with existing turbulent mixing models (e.g. Osborn, 1980). They suggest a mechanism of turbulent mixing where K_ρ changes through modification of the r.m.s. turbulent velocity scale U_t and not via an adjustment of the turbulent length scale L_t. The uncertainty in the generalization of their findings to stratified flows (which are rarely stationary in nature) lies in the fact that their analysis ignores the previous history of the flow and is based on local parameters at an instant in the flow.

2.5.2 DNS Research on Mixing Efficiency in Stratified Flows

Pioneering work on homogenous turbulence in density stratified fluids using DNS was carried out by Riley et al (1981). They reported results on the effects of stratification by performing simulations for a range of different initial Froude numbers (related to *Ri*, see equation (2.14)). They made use of pseudo-spectral methods in their DNS code meaning that the spatial derivatives in the Navier-Stokes equations are evaluated in Fourier (wave-number) space while the non-linear terms are computed in physical space. This approach of computing the non-linear terms in physical space is computationally less costly than in a purely spectral method. Transformations between wave-number space and physical space and vice versa are effected efficiently using a finite Fourier transform algorithm such as the Fast Fourier Transform. Periodic boundary conditions are naturally imposed in all three spatial directions for such simulations which forces mass continuity.

The objectives of their investigation were mainly to develop a better understanding of the effects of stratification on turbulence and develop models for the decay of turbulence with density stratification. They did not however calculate the mixing efficiency of the different flows simulated. They provide discussions on the energetics of the flow such as energy decay with time, the evolution of the buoyancy flux with time etc. They found a power law relationship for the decay of energy of the form given by equation (2.16) with n = 1.5. This agrees with most laboratory data found for homogenous turbulence decay where n is about 1.2.

$$\frac{e(t)}{e_0} = A(t - t_0)^{-n} \tag{2.16}$$

where $e(t)$ is the total energy, e_0 is the initial value of $e(t)$, A is constant approximately equal to 1.13, and t_0 is a virtual origin.

They indicate that the growth of horizontal scales was enhanced with increasing stratification, whereas the vertical scales were inhibited. What remains unclear is whether this means a reverse cascade of energy transfer from the small scales to the large scales. If this is the case, then it would suggest that strongly stably stratified flow is approximately two-dimensional! Further their results show that the horizontal component of vorticity becomes larger than the vertical component as the stratification increases. They present a "Low Froude Number Theory" to model the numerical results theoretically. An important observation worth noting is the presence of wave-like features in the flow fields at the lower Froude numbers and an inhibiting effect on the dissipation rates by the stratification. However Riley et al (1981) observed that the flow fields did not become internal wave fields (at least in the time periods computed) and thus cannot be described by linear or weakly non-linear theory. In this research this point is addressed by conducting simulations with even smaller Froude numbers than they used and comparing the results obtained for mixing efficiency with those obtained using linear theory (i.e. Rapid Distortion Theory (RDT)).

Mixing efficiency using DNS at 32^3 uniformly spaced points have been calculated using the code of Riley et al (1981) by Oduyemi (1993). The results indicate qualitatively similar trends to the experimental results but significant quantitative differences were observed. The reasons for the discrepancies were attributed to differences in Prandtl and Reynolds numbers between the simulations and laboratory. Stretch et al (2000) indicate similar trends in their results. Their speculations are that the initial conditions could be the controlling feature of the mixing efficiency in this class of flow. However since the numerical simulations cannot span a large enough range of *Pr*, they do not rule out definitively any significant *Pr* effects. In the work described in chapter 3 of this dissertation, the issue of *Pr* effects is addressed by running a series of simulations at varying *Ri, Pr* and *Re* numbers.

2.6 Lagrangian Statistics and Diffusion in Stratified Turbulence

Taylor (1921) was the first to recognise the importance of Lagrangian statistics in the problem of turbulent dispersion when he formulated his classical theory for a fluid particle's mean square displacement in homogenous stationary turbulence. He derived a relationship between the Lagrangian autocorrelation function of the fluid particle velocity and its mean square displacement. Firstly, it is imperative to explain the concept of a fluid particle (or element):

A fluid particle is a mathematical point moving with the local velocity of the fluid continuum or alternatively a fluid particle is a point which moves with the velocity of the fluid at that point. This means that the Lagrangian velocity (velocity of the fluid particle) $V\langle t\rangle$ is equal to the Eulerian velocity u at the particle's position, i.e.

$$V\langle t\rangle = u\big(X\langle t\rangle, t\big) \tag{2.17}$$

where $\langle t\rangle$ denotes coordinates following a fluid particle.

Equation (2.17) implies that

$$\frac{d}{dt}X\langle t\rangle = V\langle t\rangle \tag{2.18}$$

Equation (2.18) can be integrated to give (Squires & Eaton, 1991)

$$X\langle t\rangle = X_0 + \int_{t_0}^{t} V\langle \tau\rangle d\tau \tag{2.19}$$

Multiplying (2.19) by (2.18) and averaging yields (for stationary flows)

$$\frac{d}{dt}\overline{X^2}\langle t\rangle = 2\overline{V^2}\int_{t_0}^{t} R_L\langle \tau\rangle d\tau \tag{2.20}$$

where an overbar(s), denote ensemble averages and

$$R_L(t,\tau) = \frac{\overline{V\langle t\rangle V\langle t+\tau\rangle}}{\overline{V^2}} \tag{2.21}$$

is the Lagrangian velocity autocorrelation function.

Equation (2.20) can be integrated to get the short and long term behaviour of the dispersion predicted by Taylor and given in equations (2.22) and (2.23) (Riley & Patterson, 1974):

$$\overline{X^2}\langle t\rangle \approx \overline{V^2}t^2 \quad \text{for } t << T_L, \text{ assuming } R_L(\tau) \approx 1 \tag{2.22}$$

and

$$\overline{X^2}\langle t\rangle \approx \overline{V^2}T_L t \quad \text{for } t >> T_L \tag{2.23}$$

where $T_L = \int_0^\infty R_L(\tau)\,d\tau$ is the Lagrangian integral time scale.

These equations show that at short dispersion times, where the fluid particles have moved only a short distance from their initial positions, the mean square displacement varies quadratically with time. On the other hand, for long times (where the fluid particle's velocity is no longer correlated with its original value), the dispersion increases linearly with time (Truesdall, 1993).

This important framework by Taylor paved the way for research employing analytical, experimental and numerical studies to understand and predict dispersion in turbulent flows. The collection of Lagrangian statistics from laboratory experiments has proved to be few due to the difficulty of tracking fluid particles in time. Snyder & Lumley (1971) were the first to obtain Lagrangian statistics from grid-generated turbulent flows. Recently, Sato & Yamamoto (1987) have also obtained relevant results. The only notable experiment to address specifically turbulent diffusion in the presence of stable stratification is that of Britter et al (1983). The discussion here will be limited to the key fundamental theoretical developments by Csanady (1964), which has been improved on by PPH. Lagrangian results using DNS were first presented by Riley & Patterson (1974) in their decaying isotropic turbulence simulations. They were the first to exploit the instantaneous Eulerian velocity fields available from DNS to track fluid particles (albeit using a linear interpolation scheme). Yeung & Pope (1988) developed numerically efficient and accurate interpolation schemes for particle tracking (e.g. cubic spline interpolation that was used in this research and is discussed extensively in chapter 4 of this dissertation). They gathered Lagrangian statistics in isotropic turbulence. The only recent DNS work specifically on diffusion in stably stratified decaying turbulence was by Kimura & Herring (1996). It must be noted however that Kaneda & Ishida (2000) have used DNS to gather Lagrangian statistics to validate their linearized theory on strongly stratified turbulence.

2.6.1 Pearson, Puttock and Hunt Model

The theoretical model put forward by PPH is an extension of the work by Csanady (1964) and uses a Langevin or 'random-force' type equation to model vertical turbulent diffusion in a statistically stationary, homogenously stratified flow. The outcome of their model was to derive the mean square vertical displacement $\overline{Z^2}(t)$ and the Lagrangian velocity autocorrelation $R_w(\tau)$ of small particles in terms of some random forces acting on them.

PPH show that when there is no change of the fluid elements' density (the mixing factor described by dimensionless parameter $\gamma = 0$) the mean square displacement $\overline{Z^2}$ of the tagged particles will cease to grow beyond time $t \geq N^{-1}$ and its asymptotic value will approach $\overline{w^2}/N^2$ (see section 3.2 for the derivation of this result). This is based on the argument that the fluid elements only have kinetic energy of order ½ $\rho(\overline{w})^2$. Over a timescale long compared with the turbulence decay time, the fluid elements can change their density (i.e. $\gamma << 1$) allowing for a slow linear growth given by

$$\overline{Z}^2 = \overline{w}^2 / N^2 (\zeta_z^2 + 2N^2 t \tau_m) \tag{2.24}$$

where ζ_z is a dimensionless parameter that is dependent on the shape of the turbulent pressure gradient spectrum. Hunt (1982, 1985) shows that ζ_z has a value in the range $0.5 < \zeta_z < 1.5$ for most kinds of spectra. The value of τ_m is dependent on the mixing process and is given by $\tau_m = \gamma^2/N$. PPH define γ as a mixing factor that relates the rate of mixing with the density fluctuations by

$$\kappa \nabla^2 \rho' = -\gamma N \rho' \tag{2.25}$$

where κ is the molecular diffusivity and ρ' is density fluctuation from the mean. It must be emphasized that γ is difficult to estimate *a priori* (typically γ lies in the range 0.1-0.4 in the stable atmospheric boundary layer).

The equation for the density perturbation following a fluid element can be written as (Csanady, 1964, PPH, 1983):

$$\frac{d\rho\langle t\rangle}{dt} = \frac{d\rho'}{dt}\langle t\rangle + w\langle t\rangle\frac{\partial\overline{\rho}}{\partial z} = \kappa\nabla^2\rho'\langle t\rangle \tag{2.26}$$

where $\rho = \rho_0 + \overline{\rho}(z) + \rho'$ and $\frac{d}{dt}$ denotes total derivatives.

The expression for $\rho'(t)$ obtained by integrating equation (2.26) yields equation (4.3) in the PPH paper, i.e.

$$\rho'\langle t\rangle - \rho'\langle 0\rangle = \int_0^t \left(-\frac{\partial\overline{\rho}}{\partial z} w\langle t'\rangle + \kappa\nabla^2\rho'\langle t'\rangle \right) dt' \tag{2.27}$$

This equation describes how the density perturbations are initiated by the vertical advection of the fluid elements within a background density gradient (i.e. a reversible segregation) given by the integral of the first term on the right hand side of the equation and by the actual change in the density of fluid elements produced by mixing with neighbouring elements given by the integral of the second term on the right hand side. This formulation is used in calculating the instantaneous rate of mixing of fluid particles by calculating the change in density due to mixing following fluid particles (see section 4.2).

The PPH theory has been compared with laboratory results obtained from diffusion experiments by Britter et al, 1983. The outcome of the comparisons is not clear due to the fact that the grid turbulence decays and hence is not stationary which contradicts a key requirement of the PPH model. With some modifications introduced to account for the decay, some general agreement between the PPH model and experiments has been noted by Britter et al (1983).

Recent work by Kimura & Herring (1996) on diffusion in stably stratified decaying turbulence using DNS has focused on comparing their dispersion results with the PPH model. They extended the PPH theory for decaying turbulence in order to compare their simulation results with the theoretical results. They found qualitatively different behaviour in the time evolution of the vertical plume width predicted by PPH. In order to get agreement in the qualitative behaviour, Kimura & Herring excluded molecular mixing from the PPH theory. They found that both single-particle dispersion and particle pair separation were strongly inhibited in the vertical direction by stable

stratification while being relatively unaffected in the transverse directions, which is consistent with experimental results and the PPH model. In their investigation, visualizations of the enstrophy (mean square vorticity) fields for different strengths of stratification were made. They observed scattered pancake-shaped vortex patches lying almost in the horizontal plane especially for very strongly stable cases. They suggested that the scattered pancakes seem to be a good surrogate for the final structures in decaying stratified turbulence.

The PPH theory is widely used in industrial air quality modelling since it is incorporated in many current dispersion models such as ADMS developed by the Cambridge Environmental Research Associates (Carruthers, Holroyd, Hunt, Weng, Robin, Apsley, Smith, Thomson & Hudson, 1991). These models use modifications to the PPH theory in an adhoc way to simulate dispersion in non-stationary, non-homogenous shear stratified flows, which is more representative of the stable atmospheric boundary layer. To the author's knowledge there has been no clear validation done of the PPH theory for diffusion in stably stratified flows. It is therefore imperative that comprehensive studies be carried out to validate and/or improve the PPH model for diffusion in stably stratified flows.

Chapter 4 of this dissertation describes preliminary Lagrangian results obtained using particle tracking in DNS of decaying homogenous stratified turbulence and lays the groundwork for further research to comprehensively address this very important problem in environmental engineering.

2.7 Summary

This chapter has introduced the fundamental parameters and equations governing stratified flows. A brief review of experiments and DNS focusing on the mixing efficiency of turbulence and diffusion in stably stratified flows has been given. The next chapter describes the numerical experiments conducted during this research in the context of mixing efficiency in transient turbulent events.

CHAPTER 3

TRANSIENT MIXING EVENTS IN STABLY STRATIFIED TURBULENCE

3.1 Introduction

In this chapter, a description and discussion of the direct numerical simulations (DNS) of transient (i.e. decaying), homogenous, stably stratified turbulence is given within an Eulerian framework. The early sections of this chapter provide the theoretical aspect of the simulations (i.e. problem formulation, DNS formulation etc.). These simulations are used to determine the mixing efficiency as a function of the stratification. The DNS results are compared with results obtained from the grid turbulence experiments discussed in section 2.5.1. Discrepancies between DNS and experimental results are discussed. Molecular effects on the mixing efficiency are investigated. Results on the energetics of these transient turbulent flows are presented. Comparison of DNS results with rapid distortion theory (RDT) is presented to show how well linear theory can predict mixing efficiency in stably stratified turbulence.

3.2 Problem Statement

The main interest in this aspect of the research is in the energetics and mixing characteristics integrated over the full duration of these transient turbulent flows. In particular an attempt was made to answer the following question:

"Integrated over the duration of the turbulence decay, how much of the initial kinetic energy goes into increasing the background potential energy of the fluid as compared to the fraction that is dissipated into heat"?

3.3 Formulation of DNS

DNS involves the complete solution of the three-dimensional Navier-Stokes equations to obtain a full description of a turbulent flow i.e. where the flow variables such as the velocity and pressure are known as a function of space and time. The numerical experiments described in this dissertation were carried out with the DNS code used by Riley, Meltcalfe & Weissman (1981). The code makes use of pseudo-spectral methods,

which provides an efficient numerical basis for evaluating the spatial derivatives while computing the non-linear terms of the Navier-Stokes equations in physical space. The code is written in the Fortran 77 programming language.

The simulations are based on the non-dimensionalized Navier-Stokes equations within the Boussinesq approximation, i.e.

$$\frac{\partial}{\partial t}\underline{u} + \underline{u}\cdot\nabla\underline{u} = -\frac{1}{\rho_0}\nabla p + \underline{g}\frac{\rho'}{\rho_0} + \nu\nabla^2\underline{u} \tag{3.1}$$

$$\nabla\cdot\underline{u} = 0 \tag{3.2}$$

$$\frac{\partial\rho'}{\partial t} + \underline{u}\cdot\nabla\rho' + w\frac{d\overline{\rho}}{dz} = \kappa\nabla^2\rho' \tag{3.3}$$

Here $\underline{x}$ = (x,y,z) is a right-handed Cartesian coordinate system with z directed in the vertical. $\underline{u}$ = (u,v,w) is the corresponding velocity, ρ_0 is a constant reference density, ρ' is the density fluctuation from the ambient $\rho_0 + \overline{\rho}(z)$, p is the kinematic pressure (Batchelor, 1967) which allows for the hydrostatic contribution from $\rho_0 + \overline{\rho}(z)$, $\underline{g}$ = (0,0, $-g$) is the gravity vector, ν is the kinematic viscosity and κ is the molecular diffusivity (Riley et al, 1981).

The solutions are computed in a 2π-periodic (in all three spatial directions) box of 32^3, 64^3 or 128^3 grid points. The mean vertical density gradient is assumed constant in space, which implies horizontal statistical homogeneity. The 2π length for the computational box is chosen conveniently so that the wave number components are all integers. A modified leap-frog time differencing scheme is used to advance the time steps except for every 25th step where an Euler scheme is used for smoothing. Further details of the code are given in Riley et al (1981).

3.3.1 Initialization of the Flow

The numerical simulations were initialised in the usual way with a solenoidal, Gaussian, isotropic velocity field using random Fourier modes with a specified energy spectrum.

The three-dimensional energy spectrum of the initial turbulence is given by (see e.g. Townsend, 1976):

$$E(k) = Cu_0^2 L_0^5 k^4 \exp[-\frac{1}{2}k^2 L^2] \tag{3.4}$$

where C is a constant scaling factor and k is the wave number.
The initial total energy was exclusively kinetic in form i.e., the initial density fluctuations (and hence the initial turbulent potential energy $PE_0 = -\frac{1}{2}\frac{g}{\rho_0}(\frac{\partial\overline{\rho}}{\partial z})^{-1}\overline{\rho^2}$) were set to zero. As indicated in the problem statement in section 3.2, one of the main objectives is to compare the DNS results with experimental data and as such appropriate representation of the initial conditions is crucial. Experimental measurements downstream of grid-generated turbulence in stratified fluids indicate that the potential energy close to the grid (say at x/M = 10, where M is the grid mesh length in this context) is typically only a small fraction (<1%) of the kinetic energy (Keller & Van Atta, 2000). The above initialisation scheme is thus a reasonable model for the initial state of stratified grid generated turbulence.

The stable stratification for each numerical experiment was specified by the initial Richardson number, which was varied in the range $0 < Ri < 1000$, noting that the Richardson number for these simulations is defined in terms of the initial turbulence velocity and length scales as per equation (2.10). The numerical code consists of an initialization file that allows input of values for Re, Ri and Pr (see appendix A for printouts of the program files).

3.3.2 Comparing DNS with Experiments

For the numerical simulations carried out here, the turbulence remains homogenous (but not isotropic) for all times. This includes the buoyancy fluxes and dissipation rates. This means that in this idealized scenario the mean fields are decoupled from the turbulence and so there will be no change in the mean density field and hence no change in the background potential energy. The fact that there will be no change in the mean density field can be argued as follows (Tennekes & Lumley, 1973):

If the instantaneous density ρ is decomposed into the mean density $\overline{\rho}$ and its density fluctuation ρ', the conservation equation for $\overline{\rho}$ becomes (in the absence of mean flow)

$$\frac{\partial \overline{\rho}}{\partial t} = -\nabla F + \kappa \nabla^2 \overline{\rho} \tag{3.5}$$

where $F = \overline{\rho \underline{u}}$ is the mass flux.

For a homogenous flow with a uniform mean density gradient, $\nabla F = 0$ and $\kappa \nabla^2 \overline{\rho} \approx 0$. Hence $\frac{\partial}{\partial t}\overline{\rho} = 0$ which implies that the mean density field remains constant.

For the experiments, the turbulence is homogenous in the interior of the tank, but not near the boundaries. Thus the turbulent density flux will be homogenous in the interior of the tank but near the boundaries the gradients of the turbulent density flux produce changes to the background mean density profile. As mentioned in section 2.5.1 and shown in figure 2.6, these changes in the mean density profile result in an increase in height of the centre of mass of the fluid column and hence an increase in the background potential energy.

In figure 3.1, the buoyancy flux across the horizontal (upper and lower) boundaries of the flow is zero. The vertical mass flux across the box is non-zero. Due to the buoyancy effects, fluid mass will be transferred up or down through the layer via the buoyancy flux. The flux near the boundaries therefore becomes non-uniform and hence to conform to the zero boundary conditions, the mean density profile gets altered at the boundaries. The total mass transfer that occurs will be equal to the integrated flux through the box and will therefore determine the amount of kinetic energy that is converted into potential energy by irreversible mixing. Hence the central homogenous region of the flow, which is modelled by the DNS, can be viewed as a turbulent "pump" (an idea due to Dr Stretch) that transfers mass virtually through the system, which ultimately changes the potential energy by raising the centre of mass of the fluid column. Therefore the key to comparing the simulations with the experiments is to use the time-integrated buoyancy flux from the homogenous simulations to represent the change in the background potential energy in the physical experiment

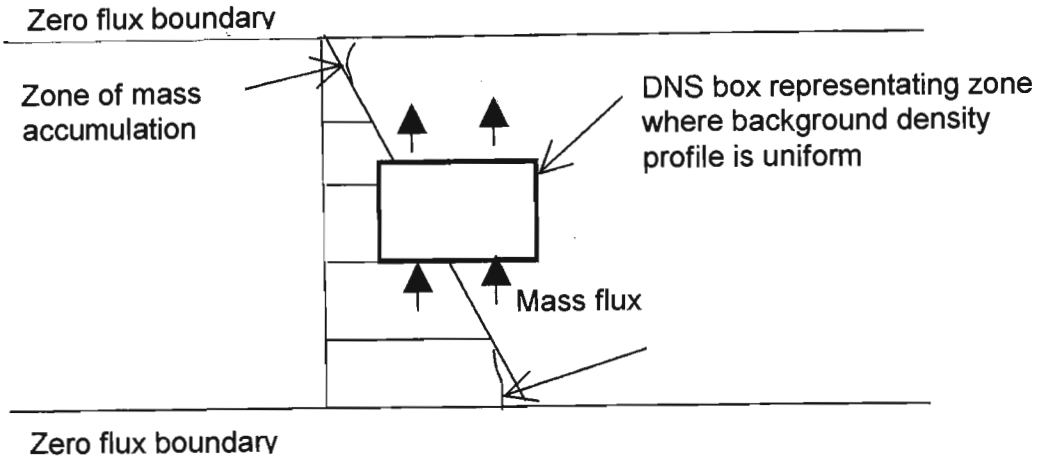

Figure 3.1: Schematic sketch to illustrate mass transfer via buoyancy flux in DNS studies to match the behaviour of the bounded experiment.

3.3.3 Resolution Issues in DNS

The numerical accuracy of the simulations depends on both the spatial and temporal resolutions. In DNS, the number of spatial grid points is determined by two constraints namely:

1. The size of the computational domain must be large enough to encompass the largest turbulence scale
2. The Eulerian grid used must be finely spaced to resolve the smallest scales of motion, which are of order of the Kolmogorov scale $\eta = (\nu/\varepsilon)^{1/4}$.

The ratio of these two scales (cubed) provides an estimate for the total number, *N*, of mesh points required. It can be shown that the number of grid points required for a well-resolved simulation will scale as $Re^{9/4}$. So for example, doubling the *Re* would mean an almost fivefold increase in the number of grid points required (Moin & Kim, 1997). This is the current major limitation of DNS in modelling these turbulent flows and limits the simulations to low or modest *Re* numbers at best.

The spatial resolution of the simulations can be determined using the non-dimensional parameter $k_{max}\eta$, where k_{max} is the highest resolvable wave number and is the largest integer multiple of k_0, the minimum wave number (set = 1 in the simulations). The k_{max} should not exceed $\sqrt{2}/3\,Nk_0$ where *N* is the number of grid points. It is 30 k_0 for a 64^3 grids (Yeung & Pope 1988, Eswaran & Pope 1998a). These authors indicate that a

value of $k_{max}\eta = 1$ is adequate for most statistics. The simulations at 64^3 grid points used in this study satisfy this criterion quite adequately. Also the dissipation spectra (both energy and scalar) of a simulation (which are computed in the statistics in the DNS code) provide a visual diagnostic on the adequacy of the spatial resolution (as it dictates the smallest wave number that needs to be resolved). A properly resolved simulation should have a well-defined peak with a smooth decay at the higher wave numbers. It can be seen from the samples in figures 3.2 and 3.3 (for energy and scalar dissipation spectra respectively) that this criterion was adequately met in the present study.

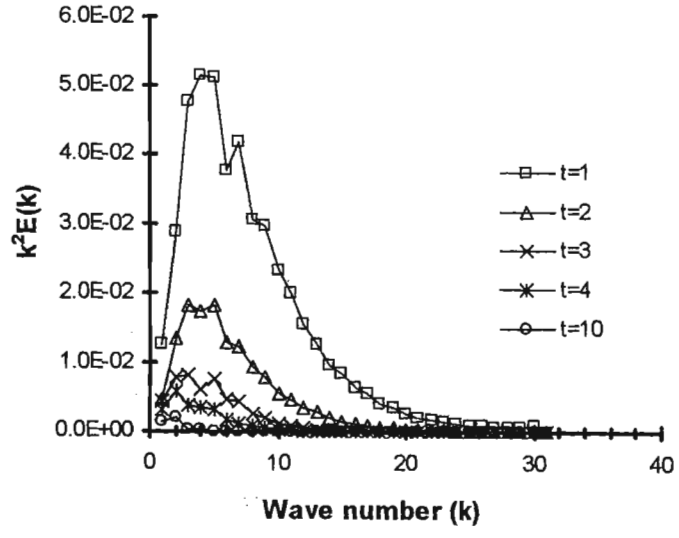

Figure 3.2: Sample plots of the energy dissipation spectra for Ri = 10 at 64^3 grids with a time step of Δt = 0.005 and Re = 200.

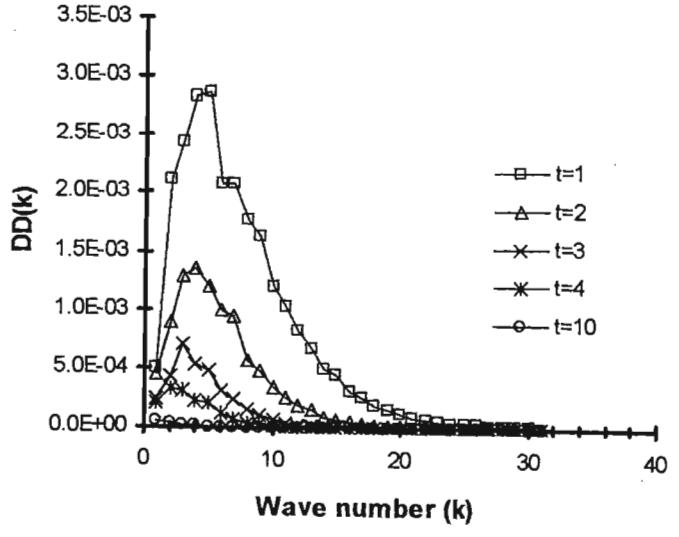

Figure 3.3: Sample plots of the density dissipation spectra for Ri = 10 at 64^3 grids with a time step of Δt = 0.005 and Re = 200.

The accuracy of the temporal resolution is determined by the time step Δt, which must be small to ensure numerical stability in the time integration as well as provide a sufficient number of points to compute the integrals of relevant quantities (e.g. the buoyancy flux) from the simulation. The turbulence was allowed to decay until approximately 99 percent of the initial turbulent energy had dissipated. The simulation must span a long enough time to achieve this and it was found that about ten times the initial time scale L_0/u_0 was typically required (see figure 3.4).

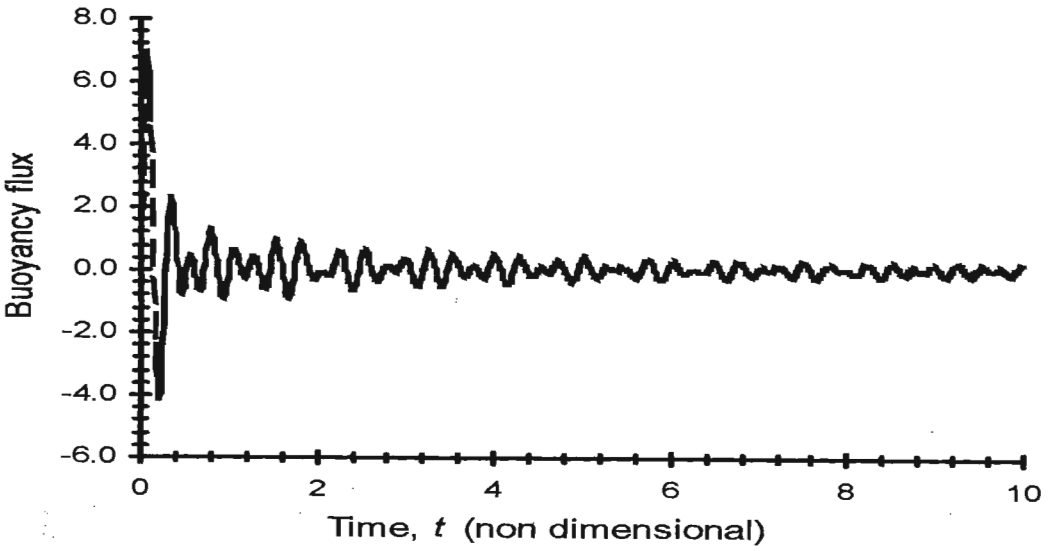

Figure 3.4: Sample plot of buoyancy flux with time computed by DNS for the case with Ri =158. The integrated buoyancy flux is found using the trapezoidal rule, the accuracy of which depends on the size of the time step Δt.

3.4 Length, Time and Velocity Scales in Stratified Flows

Turbulent motion occurs with a wide range of scales, from large (overturning) scales down to the smallest (dissipation) scales. The length and time scales associated with turbulent flows may be quite difficult to define due to differences in the orders of magnitude involved in the rates of the different processes such as non-linear transfer, decay, mixing and molecular diffusion. The length, time and velocity scales relevant in the context of this research are discussed here in non-dimensional units (for ease of comparison between laboratory and DNS results).

3.4.1 Time Scales

Two important time scales for transient stably stratified turbulent flows are:

1. The initial time scale (also called the Lagrangian time scale) $T_L=L_0/u_0$, which characterizes the initial turnover time of the most energetic eddies in the turbulent flow. Time non-dimensionalized with this time scale will be used to describe the non-linear energy transfer and decay of turbulence.

2. The buoyancy time scale N^{-1} in characterizing the effects of the buoyancy forces. Time non-dimensionalized with this buoyancy time scale will be used to characterize the importance of buoyancy forces in the evolution of the flow e.g. of the buoyancy flux.

Note that the Richardson number *Ri* is the ratio of the Lagrangian time scale T_L to the buoyancy time scale N^{-1}.

3.4.2 Length and Velocity Scales

The existence of several length scales is a fundamental characteristic of turbulence at high *Re* numbers. The dimensions of the flow field limit the largest length scales while the smallest scales are constrained by the diffusive action of molecular viscosity (Tennekes & Lumley, 1973).

For the transient turbulent mixing events reported in this dissertation, the initial length and velocity scales, L_0 and u_0 respectively, are determined by the specified initial energy spectrum. The computational box used is of length 2π, implying that it can accommodate about six overturning scales. Buoyancy effects will restrict the maximum vertical displacement of a fluid element to w_0/N, a result which can be derived as follows:

Consider a fluid element moving a distance Δz upward from its equilibrium position in a stably stratified fluid, where its vertical kinetic energy per unit mass (VKE) was $\frac{1}{2} w_0^2$.

Noting that $\Delta\rho = \frac{\partial \overline{\rho}}{\partial z} \cdot \Delta z$, then $-g\frac{\Delta\rho}{\rho_0} = -\frac{g}{\rho_0} \cdot \frac{\partial \overline{\rho}}{\partial z} \cdot \Delta z = N^2 \Delta z$

therefore the change in potential energy is $\Delta PE = \int N^2 \Delta z \, dz = N^2 \Delta z^2 / 2$

equating this change in potential energy with the initial kinetic energy, we get:

$$N^2 \Delta z^2 / 2 = w_0^2 / 2$$

simplifying gives

$$\Delta z = \frac{w_0}{N} \tag{3.6}$$

This indicates as mentioned in section 2.6.1, that the vertical displacement of a fluid element cannot exceed w_0/N and is a length scale of importance in stably stratified flows. The fluid element displacement can only exceed this limiting value by changing its density (PPH, 1983, Hunt, 1985).

3.5 Actual Numerical Experiments

The core of the results obtained for this research are from 64^3 grid simulations. Earlier results from 32^3 DNS by the author (Venayagamoorthy, 2000) are included to provide a comparison with 64^3 results. Simulations results at 128^3 grid resolution are also presented to show trends in the results due to the resolution (and *Re* numbers) of the simulations. The Richardson number *Ri* for the simulations ranged from $0 < Ri < 1000$. The case where $Ri = 0$ denotes a flow where buoyancy effects are absent and the scalar is passive. Table 3.1 provides a list of the main simulations done for this research.

The main set of simulations was carried out at a Prandtl number *Pr* of 0.5 and Reynolds number *Re* of 200. The simulations at 32^3 were at *Re* of 100 and those at 128^3 were at *Re* of 400. Only the Richardson number *Ri* was varied to simulate the different stratification conditions. The initial energy for all the simulation conducted for this research was exclusively kinetic in form. The simulations were carried out on an 866 MHz Pentium III processor with 256 MB of RAM. An average time of 8 seconds was required per time step for the 64^3 resolutions without particle tracking.

The main diagnostics describing the energetics for each of the flow simulations were archived for post processing. These included the mean square velocity, vorticity, density, buoyancy flux, kinetic, potential and total energy etc, which were saved at selected time intervals (in most cases at every 5^{th} time step). The energy, energy dissipation, energy transfer, density, density dissipation, density transfer and buoyancy spectra were also archived at the same times. Time integrated contributions for the buoyancy flux, kinetic and potential energy dissipation rates were post processed from the archived results using a Fortran program to enable the computations of the mixing efficiency of the flows (see appendix A for program listing).

A few simulations were done with the density fields initialised only at t = 1.0 i.e. from t = 0 to 1, the Richardson number Ri was set equal to zero. This allowed the velocity derivative skewness (which characterizes the non-linear transfer) to get to its maximum value before the stratification was introduced. This was done to assess the effects on the mixing efficiency calculated from the main simulations where the density fields were initialized at t = 0.

The simulations for Ri of 0, 0.39, 1.58, 10, 39,5, 158 and 1000 were repeated for Prandtl numbers Pr of 0.1, 1.0 and 2.0 to investigate molecular effects on the mixing efficiency in these flows. Resolution issues as discussed in section 3.3.3 precluded simulations at larger Pr. The laboratory experiments described in section 2.5.1 were conducted at much higher Prandtl and Peclet numbers (Pe = $Re.Pr$). Although the attainable Peclet numbers in DNS were small, it was nevertheless felt that a limited investigation of the molecular effects would be useful.

Table 3.1: List of numerical simulations at 64^3 grid resolution

Simulation No.	Froude No. Fr	Richardson No. Ri	Time step size Δt	Total No. of Time steps
1	∞	0	0.005	2000
2	10.00	0.39	0.005	2000
3	5.00	1.58	0.005	2000
4	1.99	10.00	0.005	2000
5	1.00	39.50	0.005	2000
6	0.50	157.91	0.002	5000
7	0.20	1000.00	0.002	5000

3.6 Results and Discussion on Mixing Efficiency

The DNS results on mixing efficiency are presented and discussed in this section.

3.6.1 Mixing Efficiency Results

The archived results of the simulations shown in Table 3.1 were post processed to get the time-integrated buoyancy flux and the integrals of the kinetic and potential energy dissipations as well as the initial and final kinetic energies. These results together with those of simulations at 32^3 and 128^3 grid resolutions are presented in Table A.2 in appendix A. The mixing efficiency is synonymous with the integral flux Richardson number R_f, defined in equation (2.16). As a check, this value should also be equal to the ratio of the change in potential energy to the change in kinetic energy over the duration of the event. In this investigation since the initial potential energy was zero for all the simulations this is also equal to the integral of the potential energy dissipation divided by the change in kinetic energy.

Figure 3.5 is a plot of mixing efficiency (η) versus Richardson number Ri for the DNS. The results from several sets of numerical simulations at different resolution are shown in the plot (i.e. 32^3, 64^3 and 128^3 grids). The DNS results are all for $Pr = 0.5$.

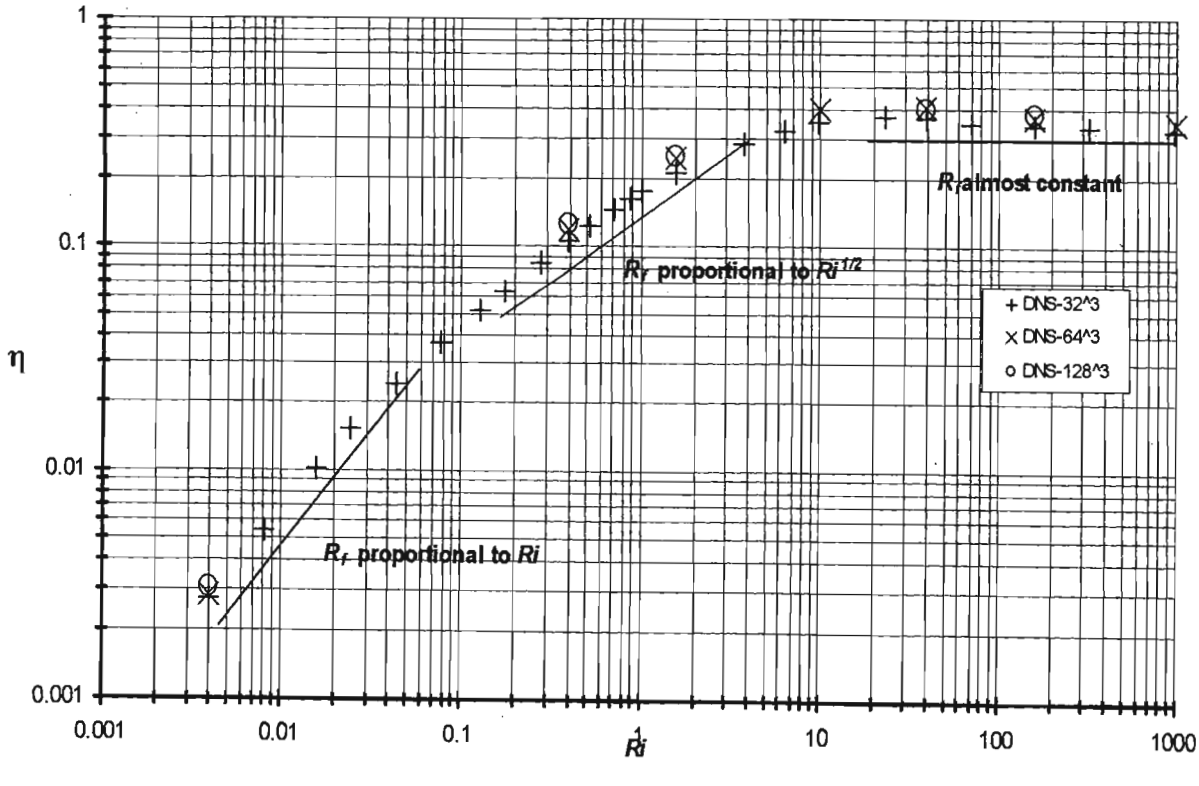

Figure 3.5: The mixing efficiency η plotted versus Ri for DNS.

The mixing efficiency at low Richardson numbers *Ri* is small, e.g. 0.3% for *Ri* = 0.004. This can be attributed to the turbulence vigorously mixing fluid of nearly constant density so that only small changes in potential energy are produced (as only low amounts of buoyancy flux are produced) and most of the kinetic energy is dissipated directly into heat. Under more strongly stratified conditions (higher *Ri*), the mixing efficiency seems to approach a constant value of approximately 30%. The range of Richardson numbers for the DNS is large enough to be conclusive regarding this limit. The small decrease in mixing efficiency as the strength of stratification increases seems to be associated with oscillations in the buoyancy flux (see figure 3.4). These oscillations are due to buoyancy restoring forces that drive fluid elements back towards their equilibrium positions in the density gradient with an associated counter-gradient (or negative) buoyancy flux (CGBF). These negative values contribute to reducing the time integrated buoyancy flux and hence the mixing efficiency (Venayagamoorthy et al, 2002). This indicates that vertical mixing is inhibited, as the strength of the stratification increases because most turbulent eddies are unable to stir the fluid.

Differences in the mixing efficiency results for DNS at different grid resolutions were small with a maximum divergence of 18% noted between the 32^3 and 128^3 grid results. It is worth noting that there is a steady shift in the mixing efficiency values between 32^3 and 64^3 grid simulations and negligible shift from 64^3 to 128^3 grid simulation indicating convergence in the results. The results for the mixing efficiency with density fields initialized at time t =1 agree closely with those of the simulations initialized at time t = 0 (see table A.3 in appendix A)

3.6.2 Scaling of Mixing Efficiency using Energy Arguments

The three distinct regimes suggested by Rehmann & Koseff (2000) are evident in the DNS results for the mixing efficiency as shown in figure 3.5. These scalings can be deduced using simple energy arguments (Stretch, 2001, personal communication):

First it is assumed that most of the energy dissipation and mixing occurs within a time $t/T_L = u_o t/L_0 \leq 3$. This will be referred to as the active mixing period. The assumption will be justified later.

Case (i): Weak stratification *Ri* < 0.1

Since $Ri < 0.1$, in this case, it follows that during the active mixing period, $u_0 t/L_0 \leq 3$, hence $Nt \leq 1$. It can therefore be assumed that mixing is relatively unaffected by buoyancy. Then the displacement of fluid elements will be of order wT_L so that the density fluctuations are $\rho' \sim wT_L \left| \frac{\partial \overline{\rho}}{\partial z} \right|$ and $\frac{g}{\rho_0} \overline{\rho w} \sim w^2 T_L \left| \frac{\partial \overline{\rho}}{\partial z} \right| \cdot \frac{g}{\rho_0} = w^2 N^2 T_L$. It follows that $R_f = \frac{B}{KE_0} \sim \frac{w^2 N^2 T_L^2}{w^2} = Ri$. Therefore it can be expected that $R_f \sim Ri$ for $Ri < 0.1$

Case (ii): Intermediate stratification $0.1 < Ri < 10$

For time t within one Brunt- Väisälä period ($T_{BV} = 2\pi/N$), it follows that during the active mixing period, $Nt \leq 2\pi/3 \approx 2$. It can be assumed here that the buoyancy forces would have taken effect and therefore play an important role in the flow. Hence the displacement of the fluid elements will tend to be of order w/N. Hence the density fluctuations will be $\rho' \sim \frac{w'}{N} \cdot \left| \frac{\partial \overline{\rho}}{\partial z} \right|$, then $\frac{g}{\rho_0} \overline{\rho w} \sim \frac{g}{\rho_0} \frac{w^2}{N} \left| \frac{\partial \overline{\rho}}{\partial z} \right| = w^2 N$. It follows that $R_f = \frac{B}{KE_0} \sim \frac{w^2 N T_L}{w^2} = N T_L = Ri^{1/2}$. Therefore it can be expected that $R_f \sim Ri^{1/2}$ for $0.1 < Ri < 10$.

Case (iii): Strong stratification $Ri > 10$

For $Nt > 2\pi$ or substantially greater than 2π for strong stratifications, the existence of interval waves in these flows is assumed, noting however that dissipation continues to be strong in decaying turbulence whereas internal waves alone are generally non-dissipative.

Using the length scale of w/N for vertical displacement, the density fluctuation is $\rho' \sim \frac{w}{N} \cdot \left| \frac{\partial \overline{\rho}}{\partial z} \right|$, hence $\frac{g}{\rho_0} \overline{\rho w} = w^2 N$. Since most of the buoyancy flux occurs within one Brunt- Väisälä period, the integrated buoyancy flux will scale on the buoyancy time scale of N^{-1}. It follows that $R_f = \frac{B}{KE_0} =$ constant. Hence it can be expected that R_f will be almost a constant for $Ri > 10$

3.6.3 Comparison with Laboratory Results

Figure 3.6 shows the experimental results (discussed in 2.5.1) of mixing efficiency by Britter (1985), Rottman & Britter (1986) and Rehmann & Koseff (2000) superimposed with the DNS results of this investigation. There is some arbitrariness in relating the definitions used for *Ri* between the laboratory experiments ($(Ri = NM/U)^2$) and DNS ($(Ri = NL_0/u_0)^2$). We assume for the purposes of this investigation that the two are equal. Thus, it can be argued that the two data sets could be shifted relative to each other along the *X* - axis to allow for this.

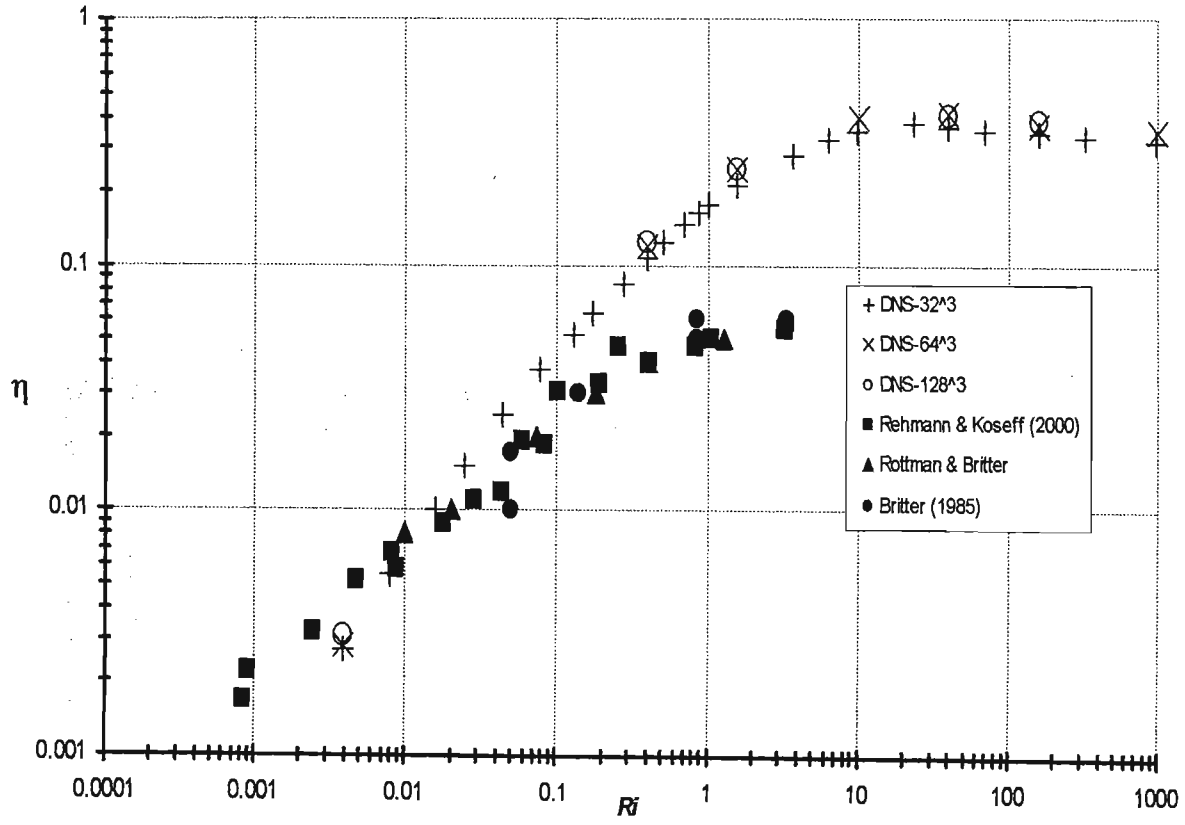

Figure 3.6: The mixing efficiency η plotted versus Ri for both experiments and DNS.

The general trend in the mixing efficiency with increasing stratification is qualitatively similar for the experiments and the DNS. There are however significant quantitative differences: in particular the maximum mixing efficiency measured in the grid experiments was 6%, compared to values of 30% or more for the DNS results. The maximum predicted by theoretical models using linear theory (such as the RDT presented in section 3.8) is 25% for the very strongly stratified cases at a Pr =1. This seems to suggest that the experiments are underestimating the mixing efficiency. Possible explanations for the disparity in the results are discussed in the subsections below to try and reconcile the discrepancy in the magnitudes of the mixing efficiencies between the experiments and the simulations.

3.6.3.1 Prandtl Number effects

The significance of molecular diffusivity effects is not clearly understood, as the simulations do not span a large enough range of Prandtl numbers. The grid turbulence experiments of Rottman & Britter (1986) and Rehmann & Koseff (2000) cover a range of Prandtl (or Schmidt) numbers $7 < Pr < 700$ using heat or salt stratification. Their measurements of the mixing efficiency for different values of the Prandtl number agreed to within experimental uncertainty. The numerical simulations, for $0.1 < Pr < 2.0$, indicated very little variations in the mixing efficiency in the regime $Ri < 10$. However, significant increases in Prandtl number effects were noted for simulations of the strongly stable cases, $Ri > 10$ (see figure 3.7). In particular the mixing efficiency decreases with increasing Pr in this regime. This result suggests that molecular effects dominate the flow at stronger stratifications. It is not clear whether these molecular effects are associated with the low Reynolds numbers of the simulations. Since the experiments were all in the regime $Ri < 10$, it is tentatively concluded that molecular effects cannot account for the observed discrepancy in mixing efficiency between the experiments and the numerical simulations. The numerical results are tabulated in Table A.4 in appendix A.

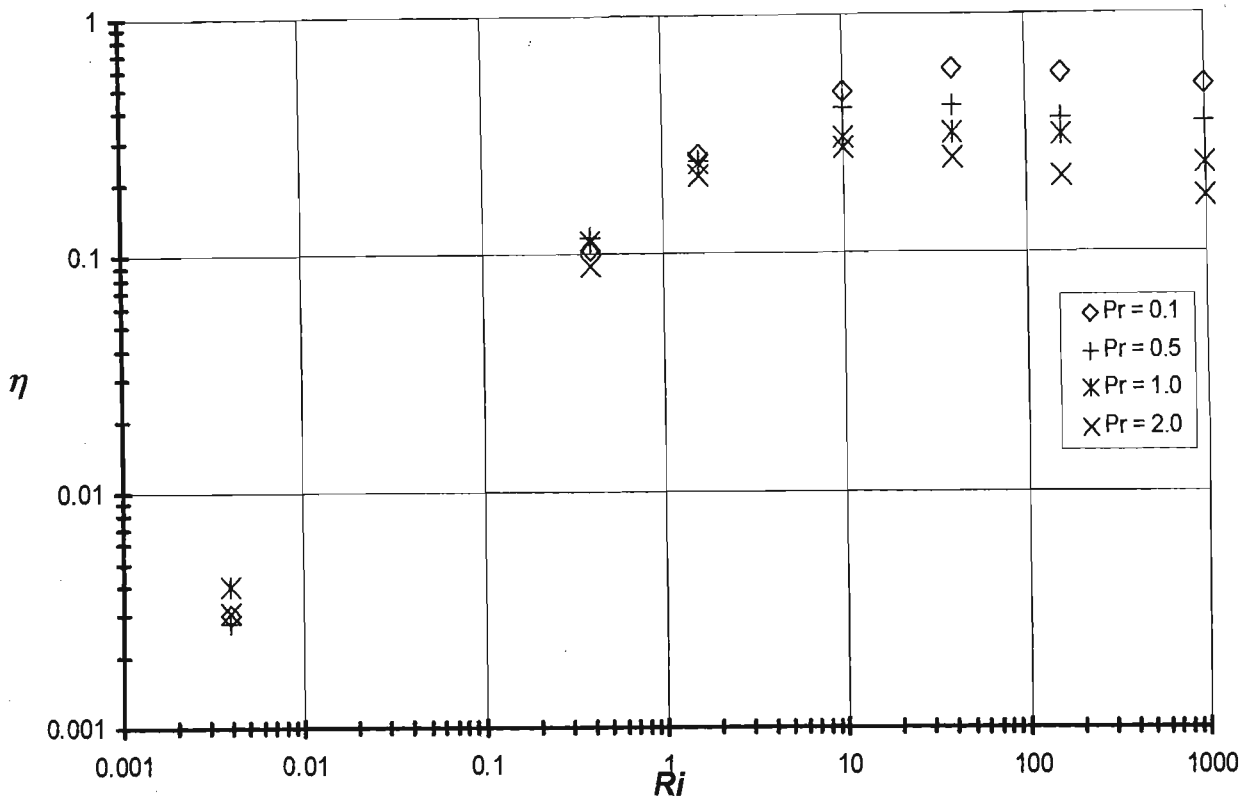

Figure 3.7: Mixing efficiency results from DNS at Re = 200 (64^3 resolution) and for varying Prandtl numbers

3.6.3.2 Initial Conditions

An alternative explanation for the low mixing efficiencies obtained in the experiments concerns the validity of the assumption that all the work done in towing the grid goes into turbulent kinetic energy which is then available for mixing of the fluid. The possibility that some of this work goes into internal or surface wave energy is ignored despite observations reported by Rottman & Britter (1986) of significant sloshing motions.

The average energy per unit volume, e, input into the water by towing the grid through it is (Stretch et al, 2001):

$$e = C_D \frac{1}{2} \bar{\rho} U^2 \tag{3.7}$$

in which C_D is the drag coefficient of the grid, $\bar{\rho}$ is the mean density of the water in the tank and U is the tow speed. The ratio of the energy input in towing the grid to the turbulent kinetic energy may therefore be expressed as

$$e \Big/ \frac{1}{2}\bar{\rho} q_0^2 = C_D U^2 \Big/ q_0^2 \tag{3.8}$$

where $q_0 = (\overline{u}^2 + \overline{v}^2 + \overline{w}^2)^{\frac{1}{2}}$ is the mean turbulent velocity magnitude with subscript *0* indicating that the location is just downstream of the grid. In the experiments it was assumed that this ratio is unity i.e. that all the work done in towing the grid goes into the turbulence. Drag coefficients were reported as $C_D \sim 1$. Direct turbulence measurements were not made in these experiments but other grid turbulence measurements typically yield $q_0/U \approx 0.1$ near the grid (Keller & Van Atta, 2000). These estimates suggest that only a small proportion of the towing work actually emerges in the form of turbulent kinetic energy downstream of the grid. If this is the case, it explains the apparently low values of mixing efficiencies reported for the experiments. Note that values of $q_0/U \approx 0.5$ would increase the experimentally determined mixing efficiencies by a factor of five, which would agree with the simulation results. Stretch et al (2001) speculate that small amplitude free-surface standing waves, or "sloshing" modes, are initiated by the grid tows and that the energy in these waves can account for the remaining energy from the work done in towing the grids. They use linear theory to get an estimate of the Energy E_s in the fundamental "sloshing" mode (which has a wavelength equal to twice the length of the tank) as:

$$E_s = (1/4)\bar{\rho} g a^2 L d \tag{3.9}$$

where g is the acceleration due to gravity, a is the amplitude, L is the length of the tank, and d is the width of the tank. As a proportion of the work done in towing the grid the energy in the sloshing mode may be expressed as

$$E_s / W = \frac{1}{2}\frac{1}{C_D}\left(\frac{gh}{U^2}\right)(a/h)^2 \tag{3.10}$$

where $W = edhL$ is the total work done in towing the grid over one length of the tank and h is the depth of the water in the tank. For typical values of gh/U^2 (e.g. 40 to 5500, Rehmann & Koseff, 2000) sloshing amplitudes between 2 – 20 % of the water depth could account for all of the towing work

3.7 Energetics

In this section, the energetics of stably stratified turbulence calculated using DNS is discussed.

3.7.1 Energy Plots

Energy plots showing the total, kinetic and potential energies were plotted for six different stratifications i.e. for Ri = 0, 0.39, 1.58, 10, 158 & 1000 with Brunt- Väisälä periods (T_{BV}) of ∞, 10, 5, 2, 0.5, & 0.2 in non-dimensional time units of L_0/ u_0 .The plots are shown in figure 3.8. The energies were calculated as a function of time from the start of the simulation.

In all cases the potential energy is initially zero. For the strong stratifications, i.e. Ri = 10, 158 & 1000, the potential energy grows rapidly and peaks at approximately $T_{BV}/3$. The potential energy then decays while oscillating with period of order half T_{BV}. These observations tie in very well with those indicated by Riley et al (1981). For the unstratified case (Ri =0), there is no growth in the potential energy since there will be no production of any buoyancy fluxes. A very similar result is evident for the weakly stratified case (Ri = 0.39) where a small change in the potential energy is observed.

The kinetic energy initially decays (or more correctly transfers into potential energy) quite rapidly for the cases with high Ri compared to cases with low Ri due to a faster conversion of kinetic energy to potential energy. However the decay is halted in the very strongly stratified cases (i.e. Ri = 158, 1000) soon after the peak in potential energy occurs (see figure 3.8). In fact the kinetic energy increases after the peak in the potential energy indicating a feedback of energy from potential to kinetic via a counter-gradient buoyancy flux (CGBF). For the lower Ri cases, the kinetic energy levels off soon after the peak in potential energy and then continues to decay to almost zero at times of the order of 10 L_0/u_0.

Plots of the energy with time on a log-log scale are shown in figure 3.9. It can be deduced from these plots that a power law relationship exists for the decay of total energy with time of the form:

$$E(t) \sim t^{-\alpha} \qquad \text{with } \alpha > 1 \tag{3.11}$$

This is consistent with observations made by Riley et al (1981) and most laboratory data for homogenous turbulence decay. The relationship is comparable to the result $E(t) \sim t^{10/7}$ proposed by Kolmogorov (1942).

Figure 3.10 presents plots of the contributions to the total dissipation due to the of potential and kinetic energies for the six cases with Ri = 0, 0.39, 1,58, 10, 158, & 1000. It is clear that the potential energy dissipation forms a considerable part of the total dissipation especially for the strongly stable cases (i.e. with Ri of 10 and upwards). The patterns in the plots are similar to those observed for the energy shown in figure 3.8.

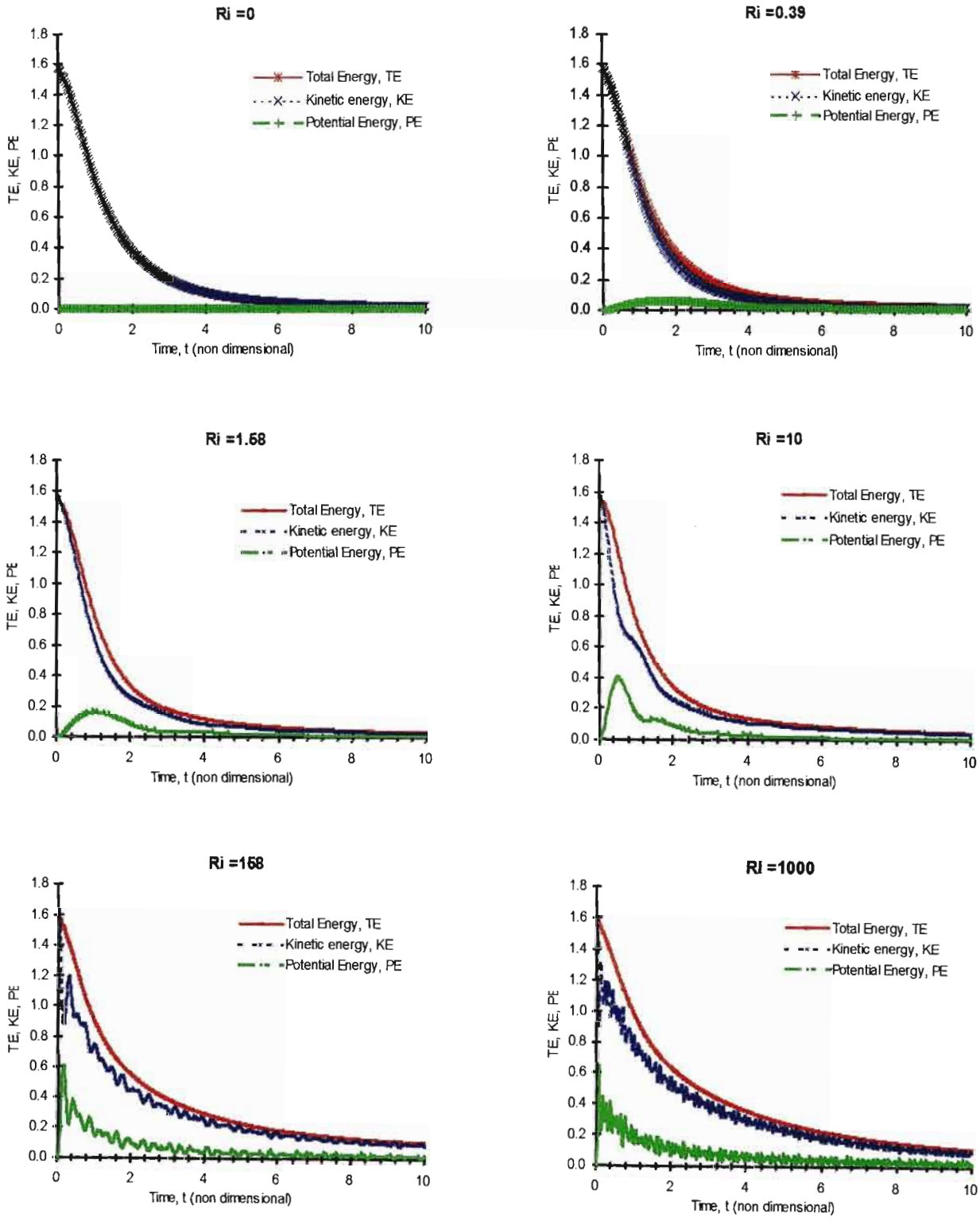

Figure 3.8: Plots of total, kinetic and potential energies with time for Ri = 0, 0.39, 1.58, 10, 158 & 1000

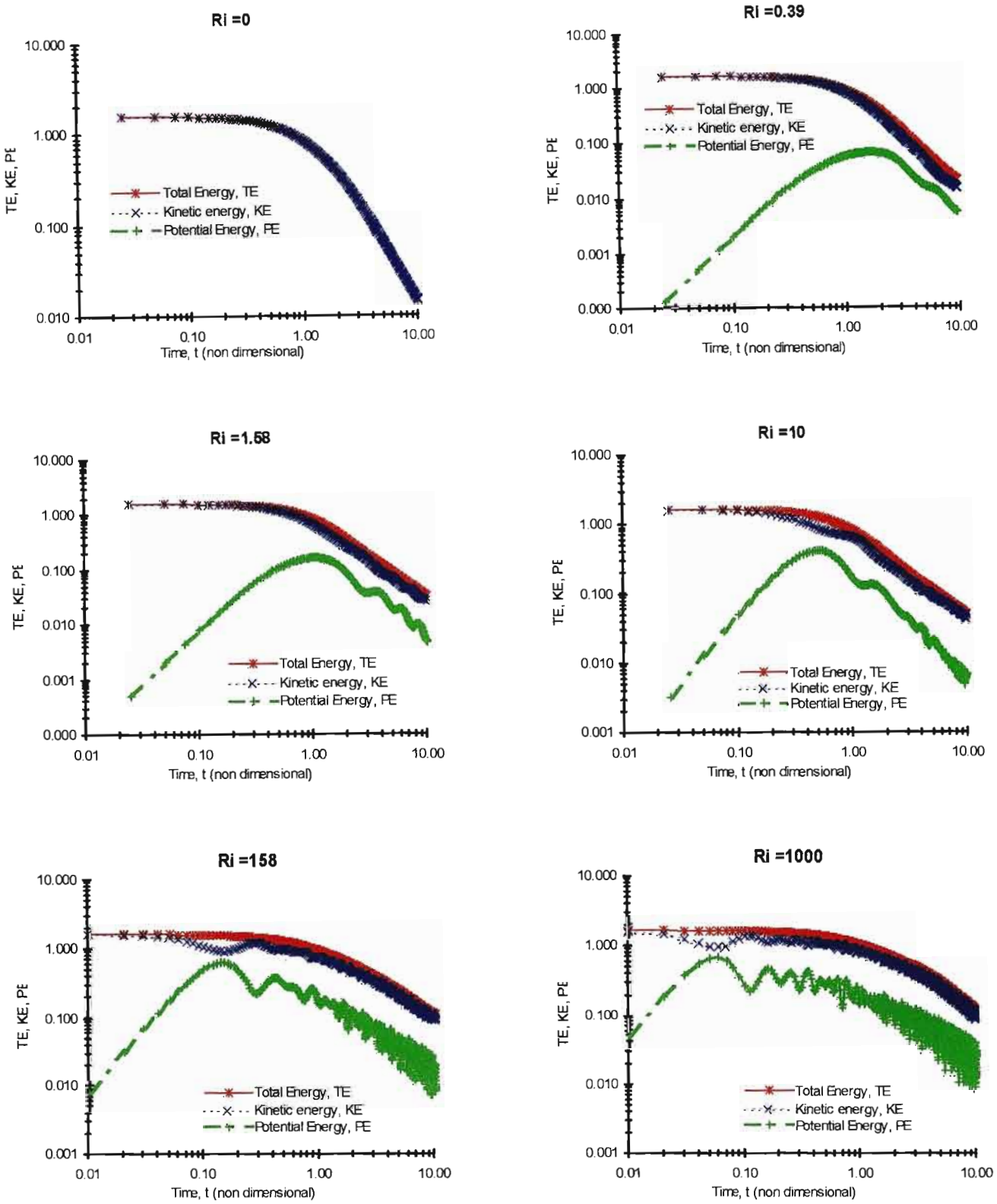

Figure 3.9: Plots of total, kinetic and potential energies with time (on log-log scale) for Ri = 0, 0.39, 1.58, 10, 158 & 1000

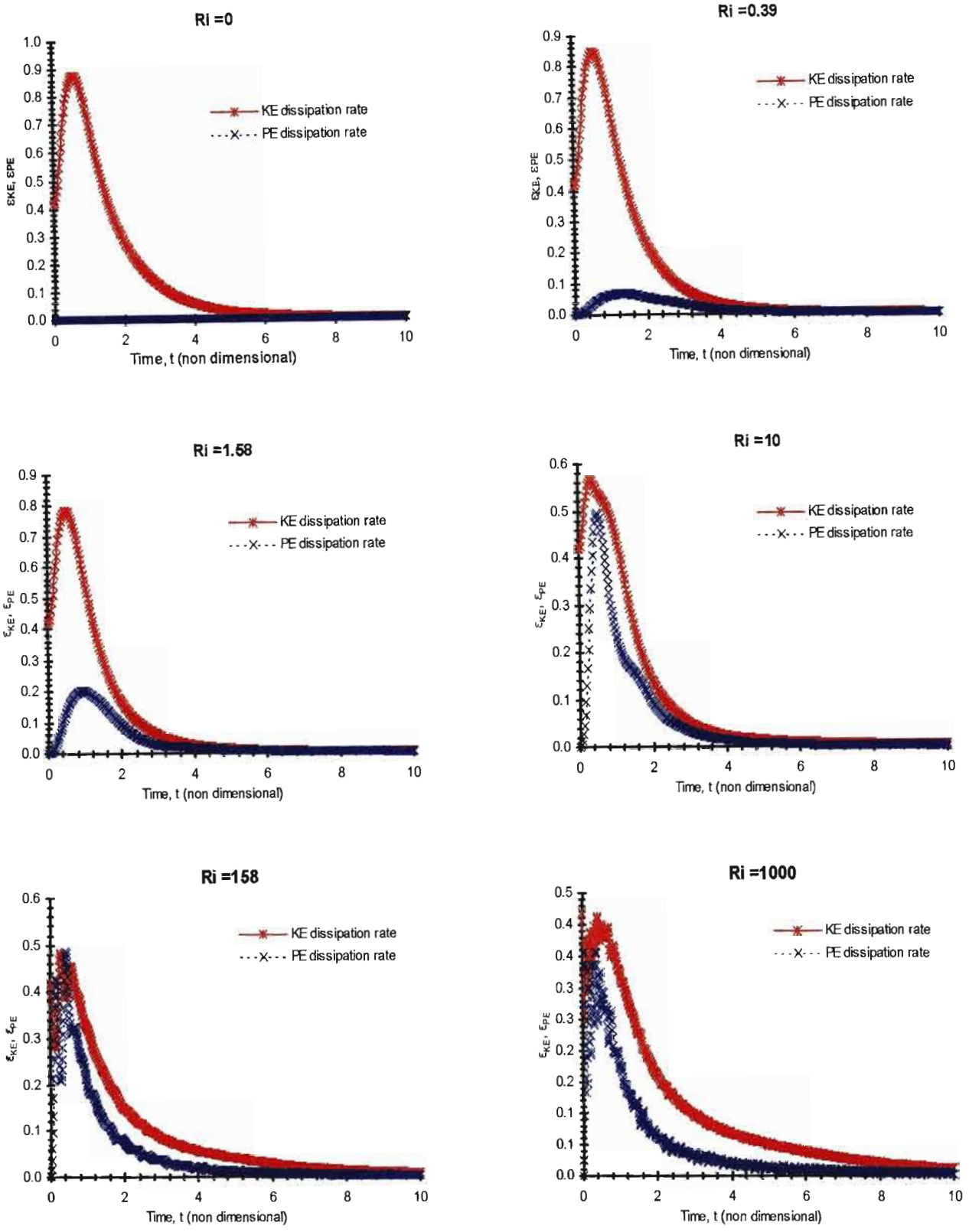

Figure 3.10: Plots of dissipation of kinetic energy and potential energy for Ri = 0, 0.39, 1.58, 10, 158, & 1000

3.7.2 Buoyancy Flux

Figure 3.11 shows the plots of the buoyancy flux with time for six *Ri* cases. The buoyancy flux has been defined in equation (2.16) in section 2.3.5. It is given as:

$$b = \left(\frac{-g}{\rho_0}\right)\overline{\rho w} \tag{3.15}$$

For all cases the buoyancy flux is initially zero since there are no density fluctuations. For the strongly stratified cases (*Ri* = 10,158, & 1000), the buoyancy flux grows very rapidly providing a flux of density in the direction of decreasing mean density implying a gradient flux. The flux peaks at about the same time that the potential energy peaks and then becomes negative. This indicates the onset of the counter-gradient flux mentioned in section 3.7.1. This process is physically established when the fluid elements have converted all their vertical kinetic energy to potential energy, and start to migrate back towards their equilibrium levels, which represents the conversion of potential energy back into kinetic energy. Riley et al (1981) indicate that a simple eddy-diffusion model for the buoyancy flux will not adequately treat this effect, posing another complexity in the development of turbulence models for this class of flows.

Figure 3.12 shows plots of the buoyancy flux with time non-dimensionalized with *N*, for all six *Ri* cases. The peak in the flux occurs at $Nt \approx 1$ for all the *Ri* cases (except for *Ri* = 0 for obvious reasons), and seems to be independent of *Ri* and *Re* and consistent with the predictions by Hunt, Stretch & Britter (1988). This could indicate a characteristic time to the onset of significant effects of the stratification as also suggested by Holt, Koseff & Ferzigher (1992). The first zero crossings of the buoyancy flux occurs at $Nt \approx 2$ for *Ri* = 10, 158 & 1000 and $Nt \approx 3.0$ & 2.4 for *Ri* = 0.39 and 1.58 respectively. These values are consistent with those suggested by Hunt et al (1988) using inviscid rapid distortion theory, Riley et al (1981) and Itsweire, Helland & Van Atta (1986) in their unsheared stratified flow studies. The flux then oscillates about zero with decaying amplitude and a period of approximately half the buoyancy period T_{BV}.

The integral of the buoyancy flux for the six *Ri* cases are shown in figure 3.13. The integrated flux attains its maximum value at $t \approx 3$ (which scales to $Nt \approx 2$ for all cases), before decreasing and asymptoting to a constant positive value after approximately one buoyancy period. The ratio of this value to the initial kinetic energy gives the mixing efficiency as discussed in section 3.6.1. It is clear that the buoyancy flux production is

complete in about three turnover times. Therefore the assumption that most of the energy is dissipated within three turnover times in deducing the scalings in section 3.6.2 seems reasonable. Also superimposed on figure 3.3 is the integrated potential energy dissipation. The integrals of the buoyancy flux and the potential energy dissipation converge at times of order $3L_0/u_0$ in all the cases.

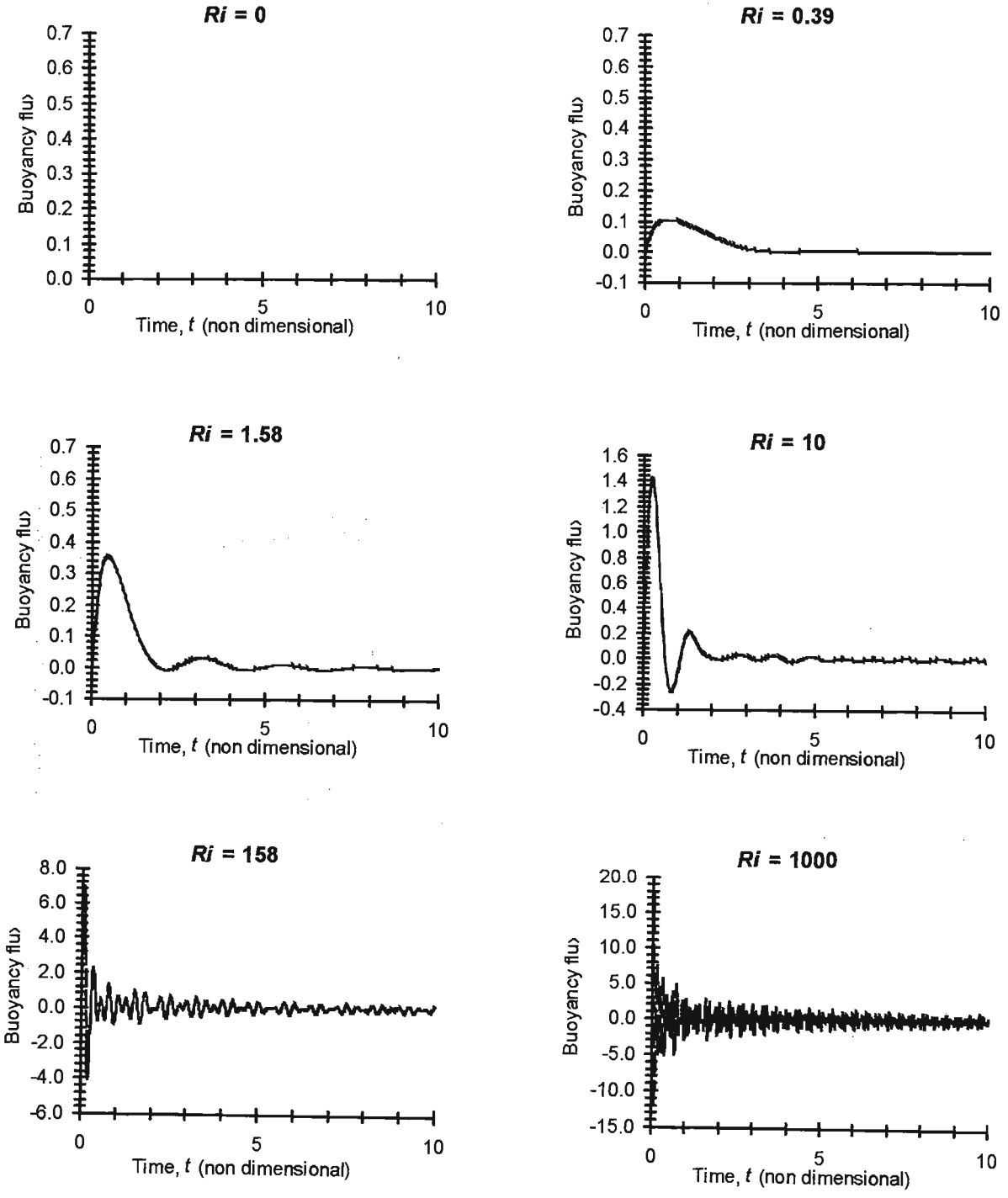

Figure 3.11: Plots of buoyancy flux with time for Ri = 0, 0.39, 1.58, 10, 158, & 1000

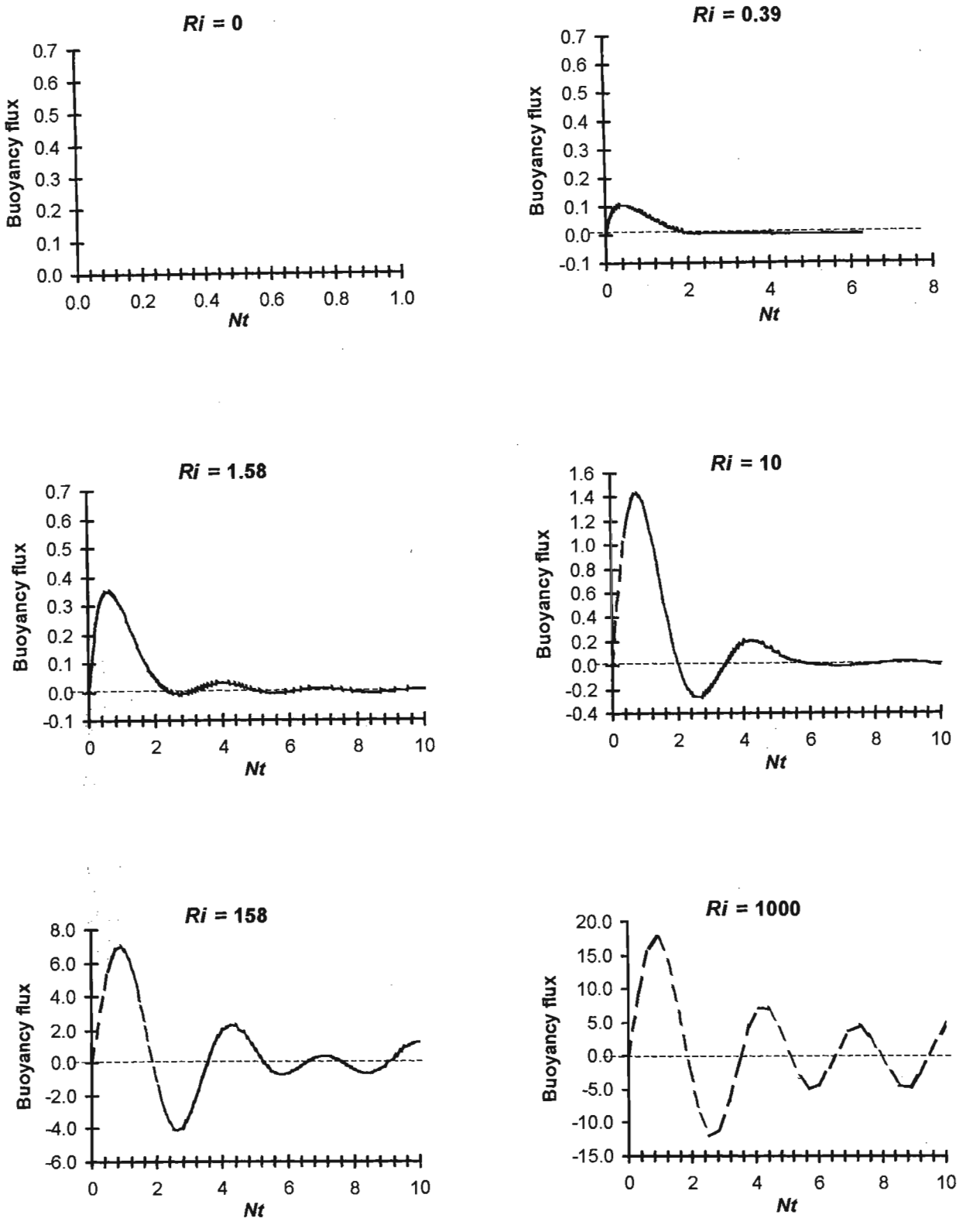

Figure 3.12: Plots of buoyancy flux with time in Nt units for Ri = 0, 0.39, 1.58, 10, 158, & 1000

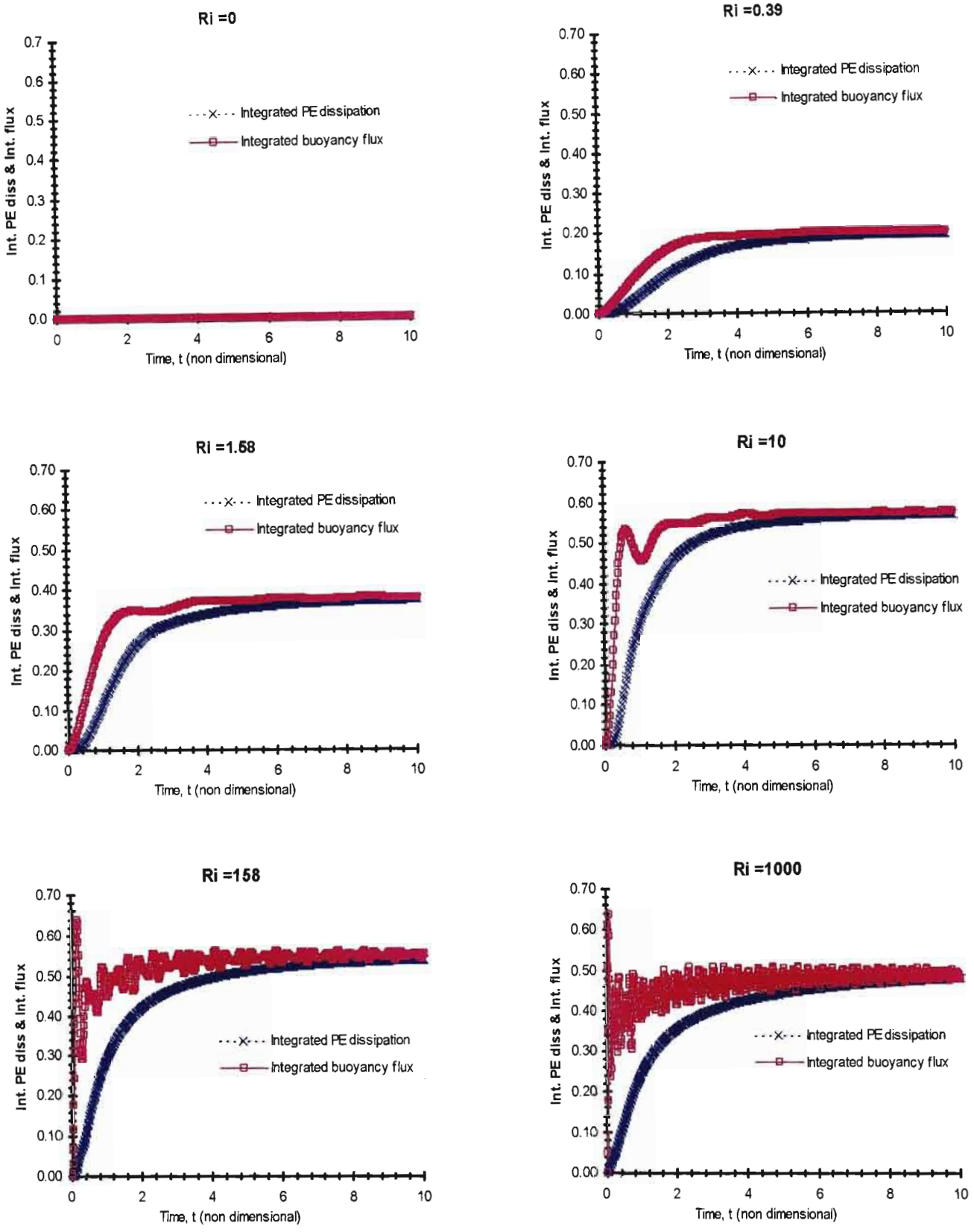

Figure 3.13: Plots of integrals of the buoyancy flux and potential energy for Ri = 0, 0.39, 1.58, 10, 158 & 1000

3.7.3 Energy, Energy Dissipation and Energy Transfer Spectra

Figures 3.14, 3.15 and 3.16 give the energy, energy dissipation and the energy transfer spectra plots for Richardson numbers Ri = 0, 0.39, 1.58, 10, 158, and 1000 at various times.

The energy spectra as shown in figure 3.14 are plotted on a log-log scale. These plots reveal that the high wave number energy is gradually eroded for all cases. However, Riley et al (1981) note that the reduction of energy with wave number is faster than laboratory results due to the low Reynolds numbers in the simulations. Changes in the slope of the energy spectrum with increasing Ri (or N) are evident from the plots. Kimura and Herring (1996) also indicate steeper slopes in their simulation results suggesting the inhibition of the energy cascade for strong stratifications. The trends observed in the shape of the energy spectra plots in this research agree with their plots and those of Riley et al (1981).

Figure 3.15 shows the energy dissipation spectra at different times for the six cases. These plots clearly indicate peaks in energy dissipation and subsequent decay at high wave numbers. The velocity scales are therefore properly resolved giving confidence in the numerical accuracy of the simulations as discussed in section 3.3.3. The plots for the different Ri cases all exhibit the same trend with depletion of small scale energy as the stratification increases.

Figure 3.16 shows the energy transfer spectra for all the six different Ri flows. The transfer spectrum at each time integrates (with respect to the wave number k) to zero. The cascade of energy is clear in that large scales transfer energy to small scales i.e. low wave numbers lose energy at the expense of high wave numbers. The zero crossing wave number decreases with time and the transfer diminishes with time as the flow decays. The spectral energy transfer gives a measure of the non-linearity in a flow. It can be seen from the plots that there is reduction in the energy transfer with increasing Ri, implying that non-linear effects are reduced. RDT results (see section 3.8) reveal that dynamics of the vertical velocity field is linearizes for high Ri. It appears that the non-linear effects are still dominating the horizontal structure of the flow (e.g. there is still significant non-linear transfer at Ri = 1000) and hence the bulk of the energy transfer reflected in figure 3.16 at the high Ri values is in the horizontal motions.

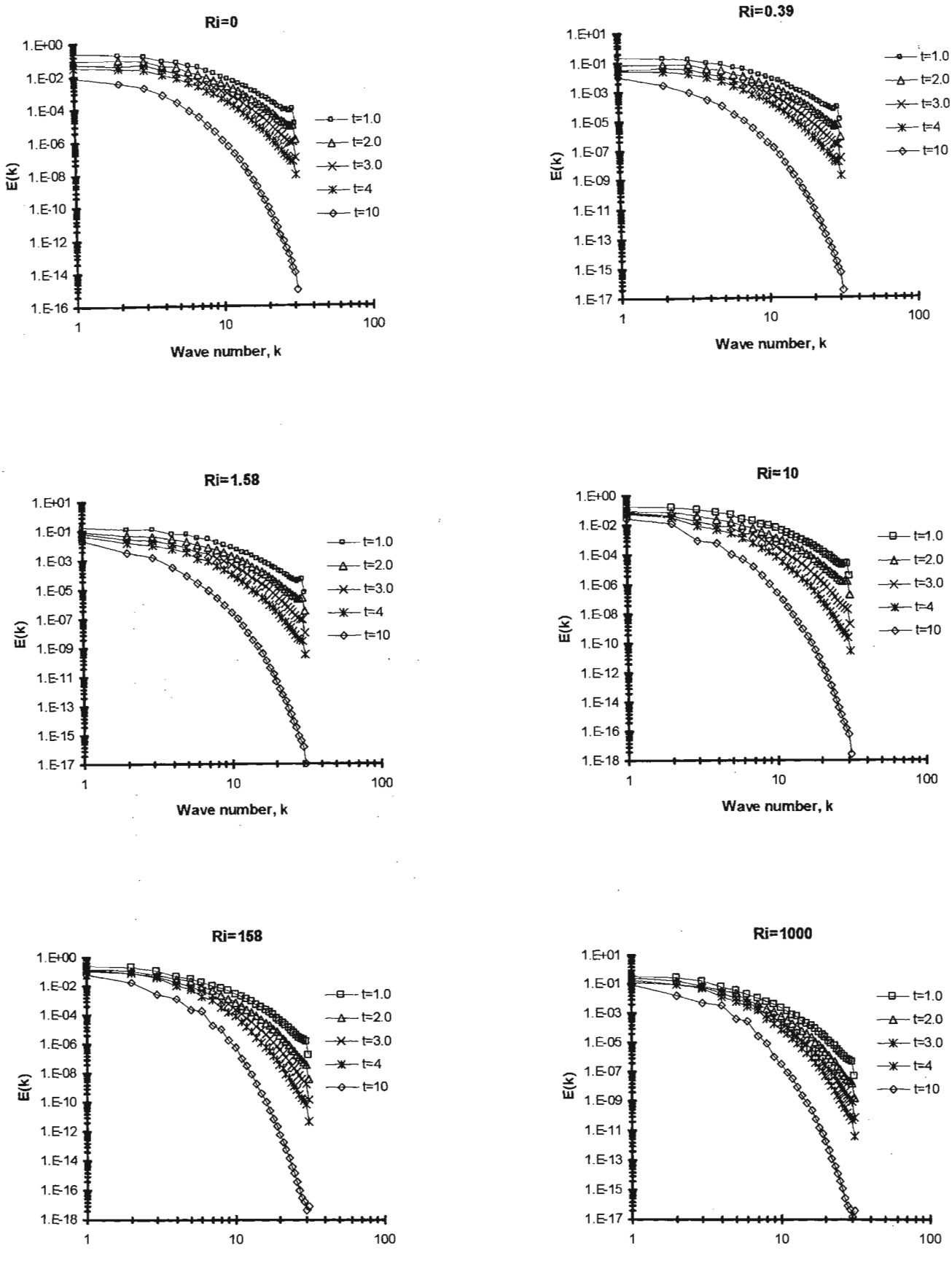

Figure 3.14: Plots of energy spectra for Ri = 0, 0.39, 1.58, 10, 158, & 1000

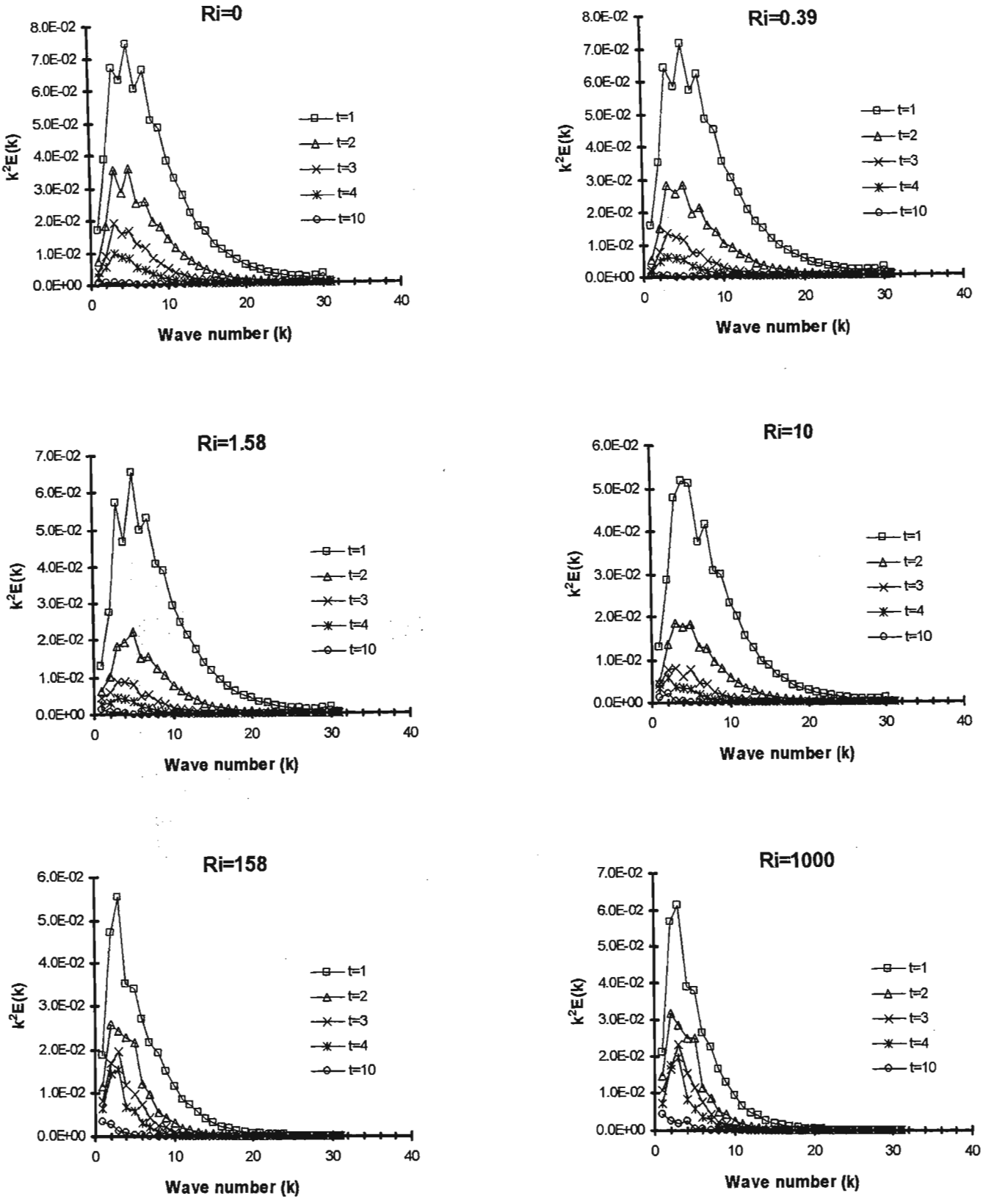

Figure 3.15: Plots of energy dissipation spectra for Ri = 0, 0.39, 1.58, 10, 158, & 1000

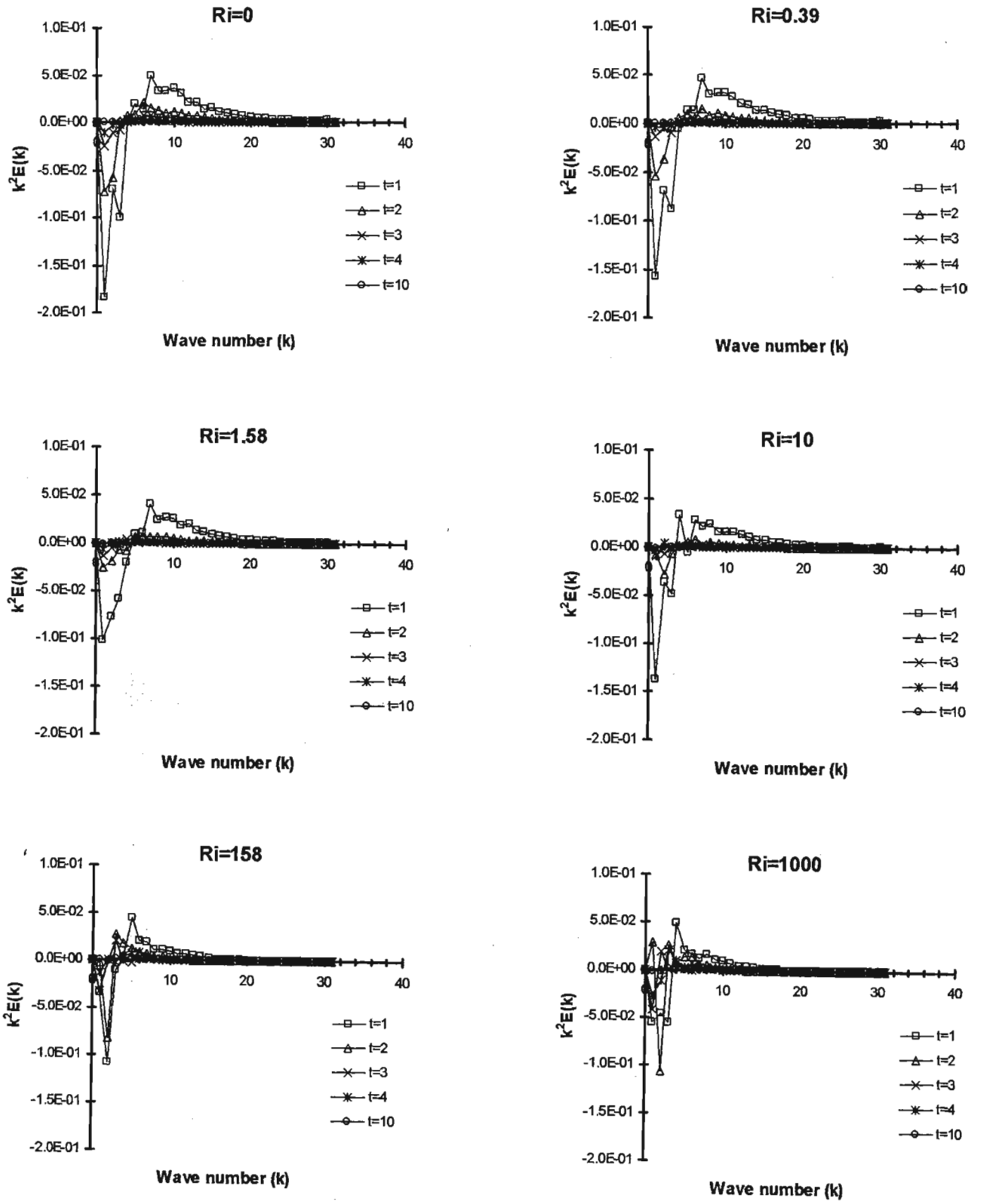

Figure 3.16: Plots of energy transfer spectra for Ri = 0, 0.39, 1.58, 10, 158, & 1000

3.7.4 Velocity Derivative Skewness

The velocity derivative skewness is a convenient measure of the rate of energy transfer. Figure 3.17 shows the plot of the horizontal and vertical components of the velocity derivative skewness for all the six *Ri* cases. The velocity derivative skewness in all three spatial directions remains large negative throughout the simulation for the unstratified case (*Ri* = 0), indicating strong non-linear transfer is occurring. This trend persists for the weakly stratified cases too (*Ri* = 0.39 & 1.58). However, a significant change in velocity derivative skewness of the vertical velocity is noted from between *Ri* = 1.58 to *Ri* = 10. The skewness drops rapidly to almost zero and oscillates around this value throughout the simulation period. On the other hand, the velocity derivative skewness of the horizontal velocity components stays large negative and gradually decays in time.

Riley et al (1981) have also shown in their results using 32^3 grid simulations that the velocity derivative skewness of the vertical velocity is small. The results of this strongly support their finding that stratification greatly diminishes the spectral energy transfer in the vertical motions. The effect of the low Reynolds number on this conclusion remains uncertain. The plots of the velocity derivative skewness with time at both 32^3 and 128^3 resolution are shown in figures 3.18 and 3.19. The initial Reynolds's numbers were 100 and 400 respectively. It can be observed that the trends in velocity derivative skewness at higher *Re* are similar to those in figure 3.17 indicating that non-linear effects are still been suppressed in the vertical motions. It is speculated from this observation that linear dynamics may dominate the vertical motion of strongly stratified turbulence even at high *Re* numbers.

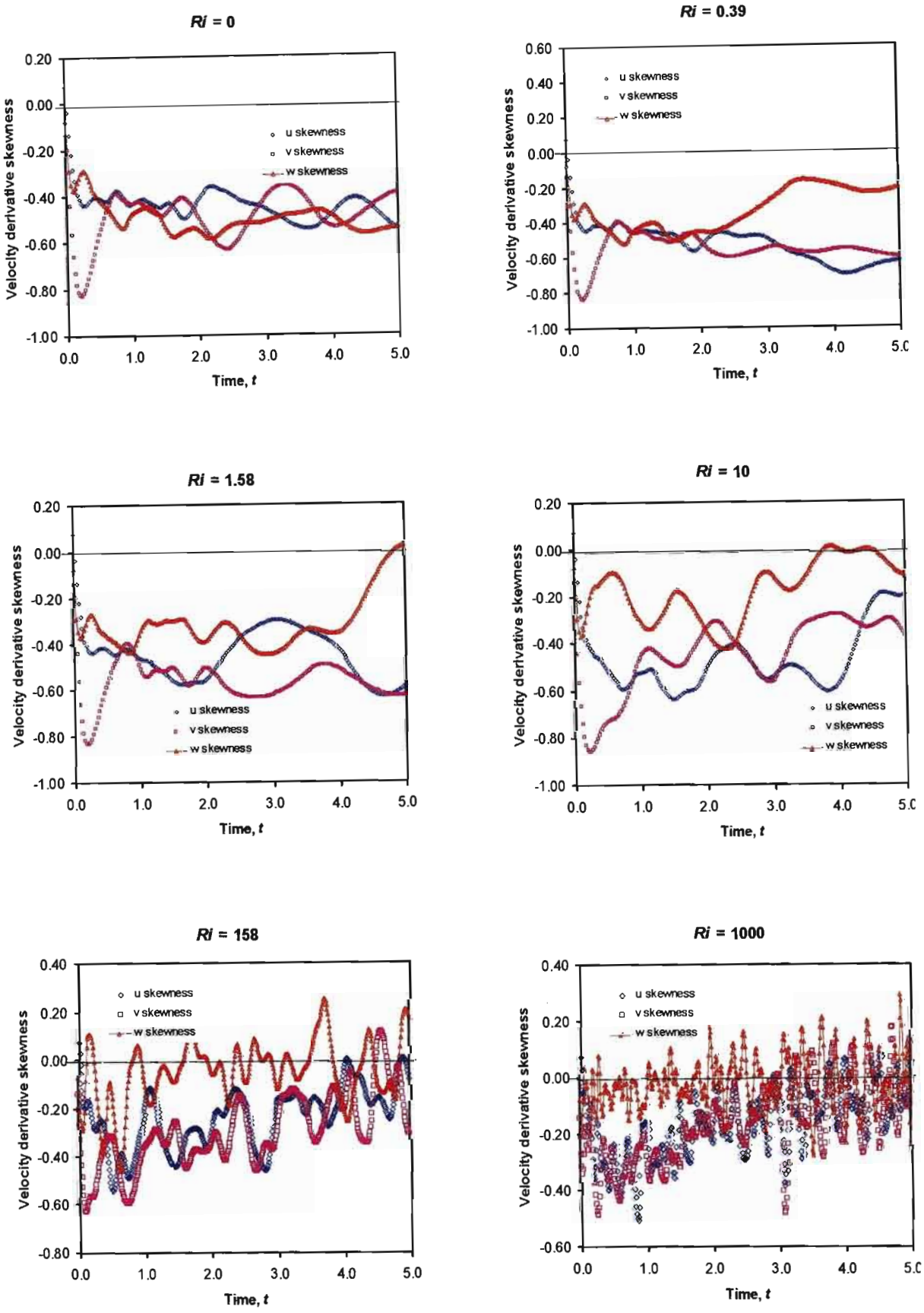

Figure 3.17: The velocity derivative skewness versus time at Re = 200 (64^3 grid) for Ri = 0, 0.39, 1.58, 10, 158 & 1000.

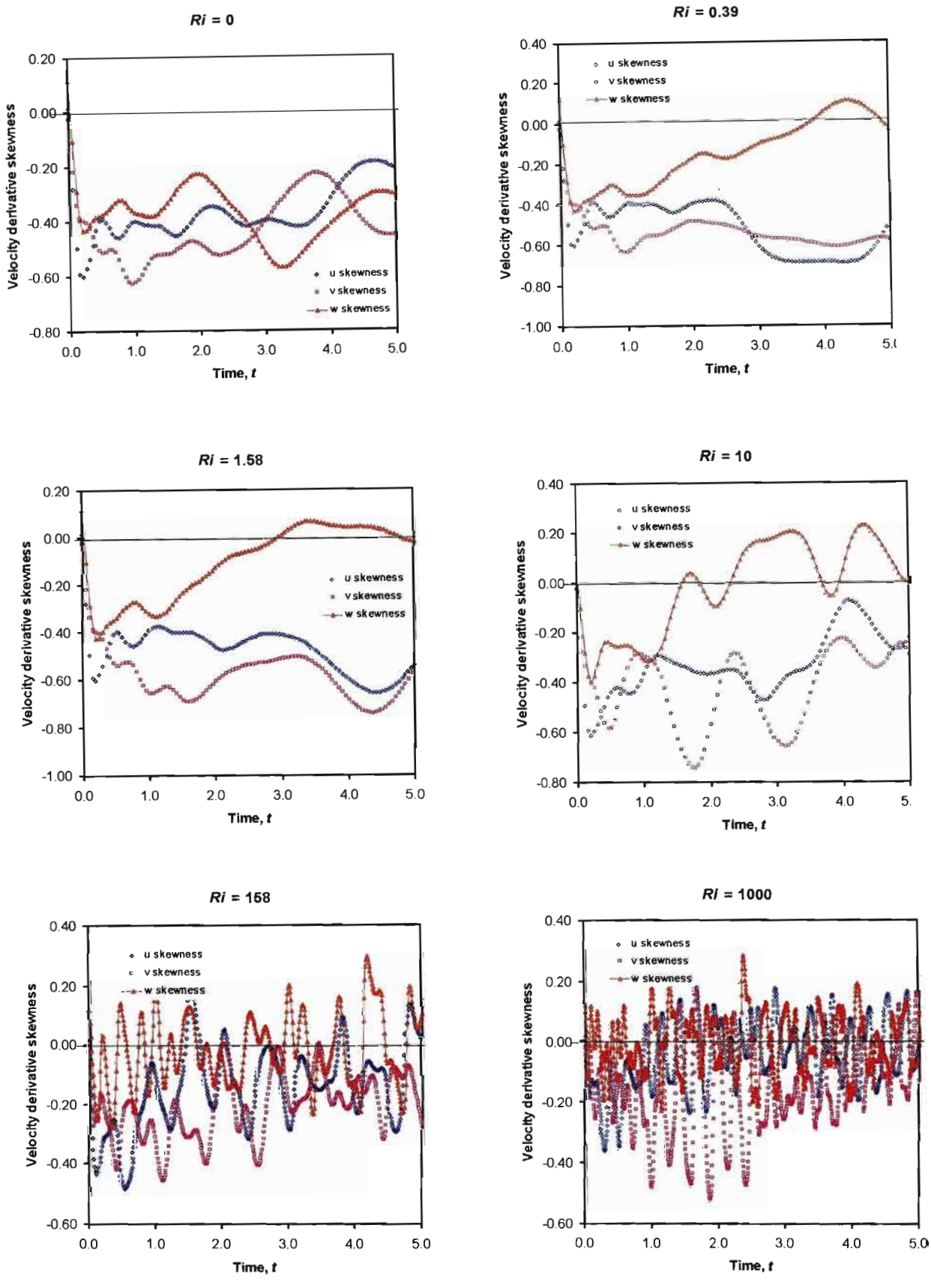

Figure 3.18: The velocity derivative skewness versus time at Re = 100 (32^3 grid) for Ri = 0, 0.39, 1.58, 10, 158 & 1000.

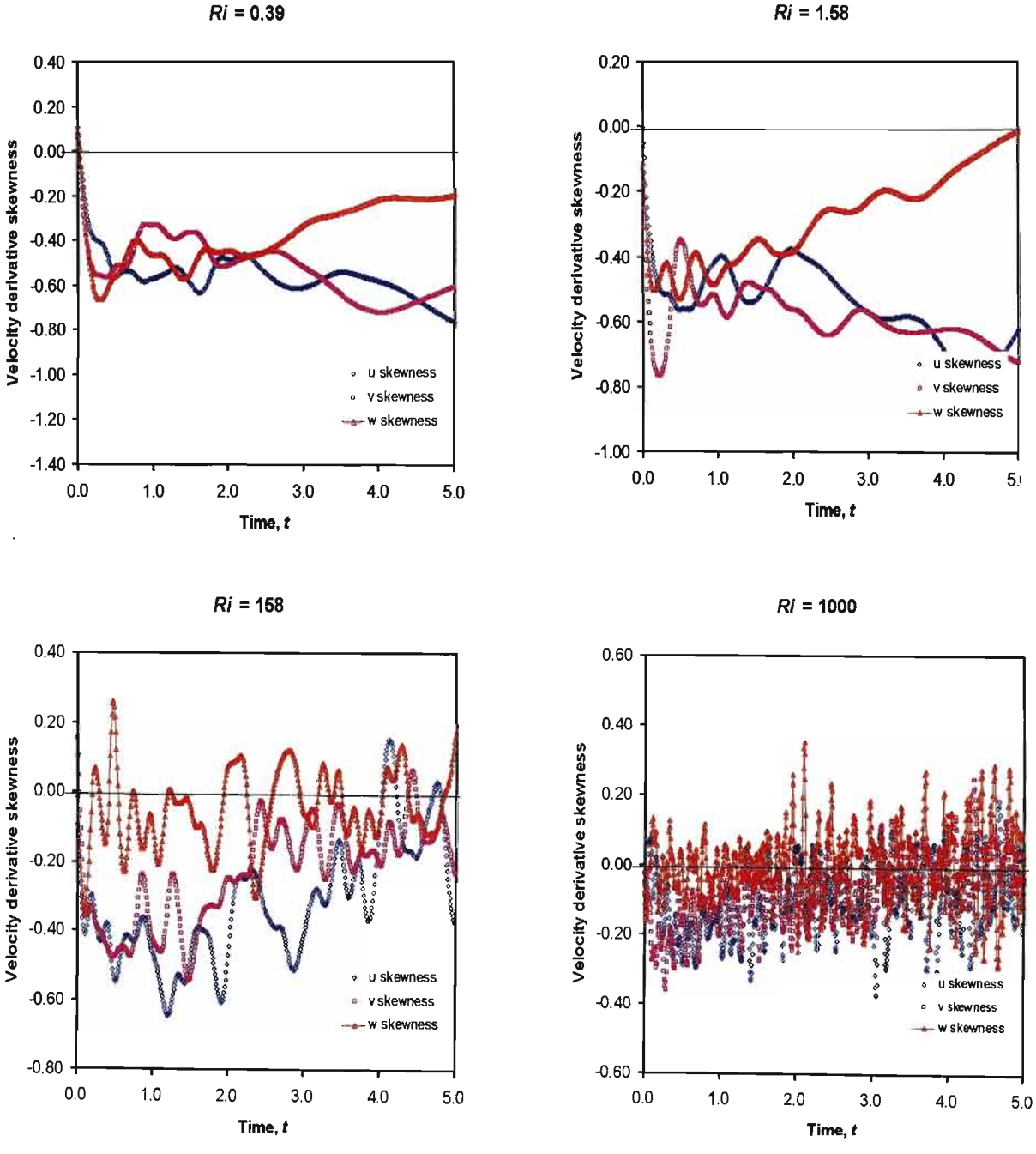

Figure 3.19: The velocity derivative skewness versus time at Re = 400 (128^3 grid) for Ri = 0.39, 1.58, 158 & 1000.

3.7.5 Density, Density Dissipation, Density Transfer and Buoyancy Spectra

Figures 3.20, 3.21, 3.22 and 3.23 show plots of the density, density dissipation, density transfer and buoyancy spectra for Richardson numbers Ri = 0, 0.39, 1.58, 10, 158, and 1000 at various times.

In Figure 3.20, the plots of the density spectra for all six Ri cases have similar tendency to the energy spectra plots. Decay is apparent and rapid at the large wave numbers with no obvious changes in the form of the spectra with increasing Ri.

Figure 3.21 shows the plots of the density dissipation spectra at different times for the six Ri cases. These plots clearly indicate peaks in density dissipation and decay. It is evident once gain from these plots that the numerical simulations are adequately resolved. The magnitudes of the density dissipation at the low wavenumbers decrease with increasing Ri.

Figure 3.22 shows the plots of the density transfer spectra at different times for the six Ri cases. It can be seen that there is negligible transfer of density fluctuation energy from the large scales to small scales for the high Ri cases (i.e. Ri = 10, 158 & 1000) indicating the inhibiting effects imposed by the stable stratification on the flow. Also as the density fluctuations strongly depend on the vertical velocity field of the flow, it is reasonable to suggest that this provides further evidence that the vertical dynamics of the flow is linearizing in these high Ri cases.

Figure 3.23 gives the plots (on logarithmic scales) of the buoyancy spectra for all six Ri cases. It is clear that the buoyancy flux is confined to the large scales. The fluxes are positive for the low Ri cases (Ri = 0 & 0.39), indicating down gradient transfer consistent with the energy versus time plots shown in figure 3.8. In the high Ri cases, the flux changes from positive to negative in magnitude at the low wavenumbers with time. This indicates the presence of counter gradient fluxes (see section 3.7.2 also).

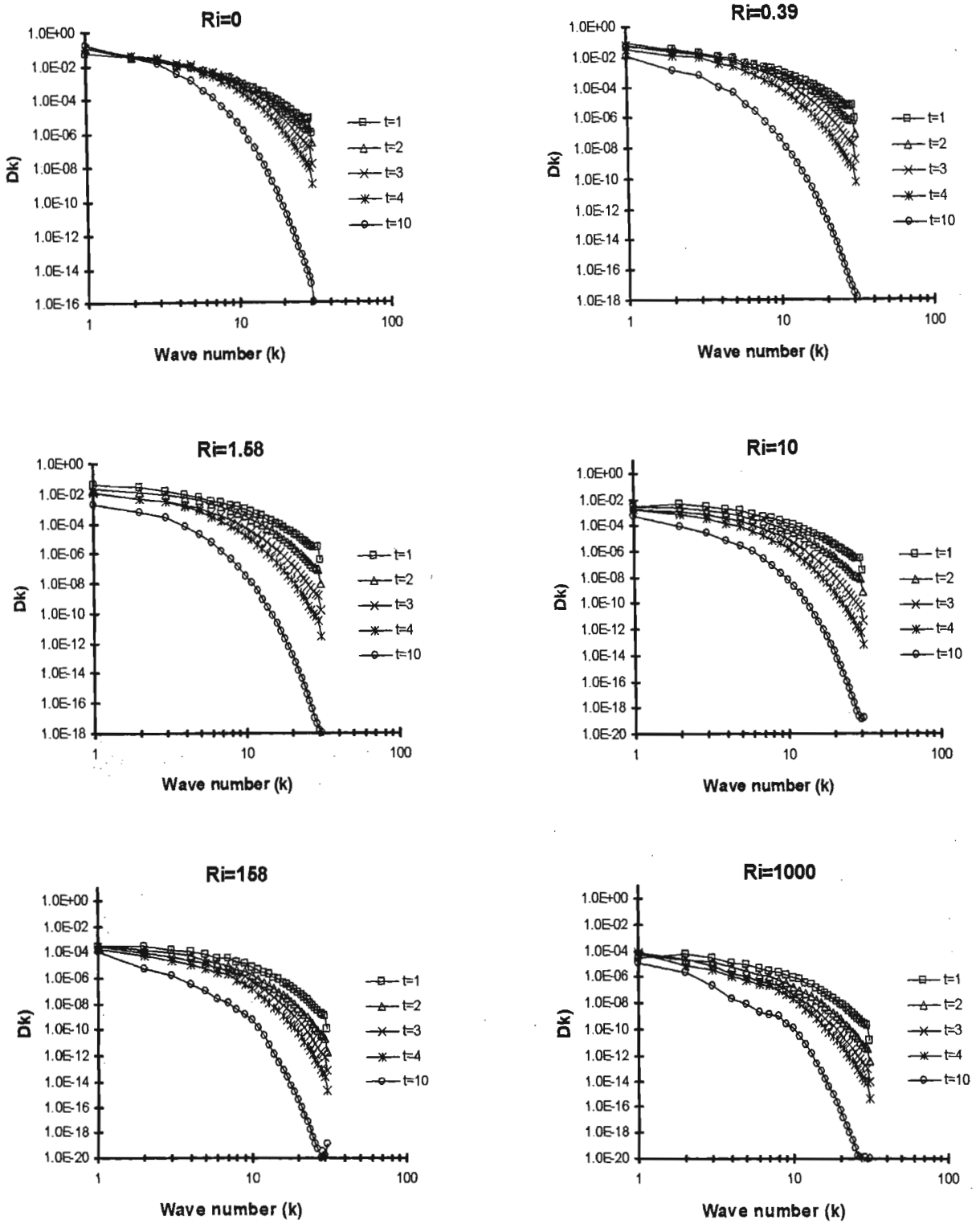

Figure 3.20: Plots of density spectra for Ri = 0, 0.39, 1.58, 10, 158, & 1000

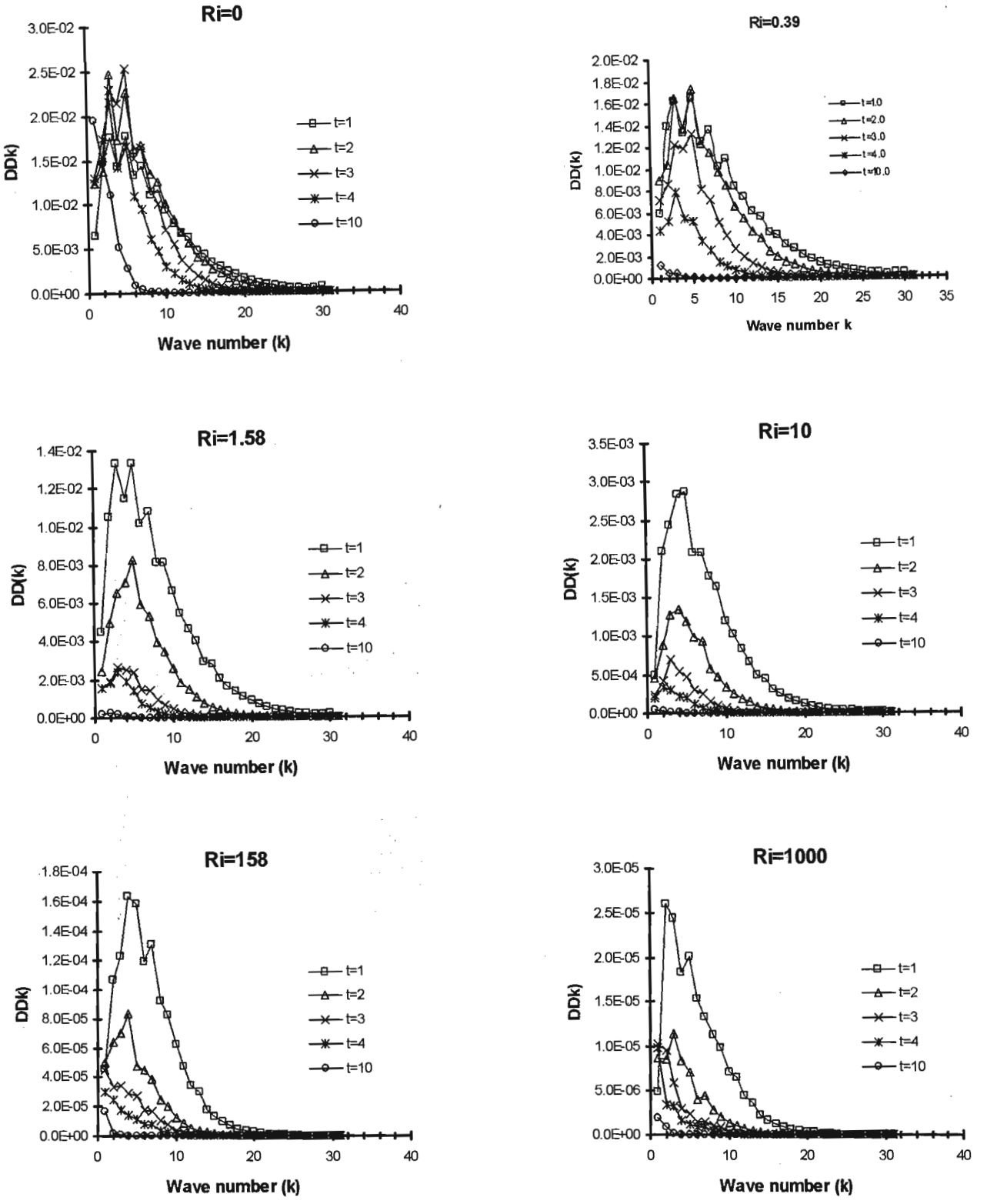

Figure 3.21: Plots of density dissipation spectra for Ri = 0, 0.39, 1.58, 10, 158, & 1000

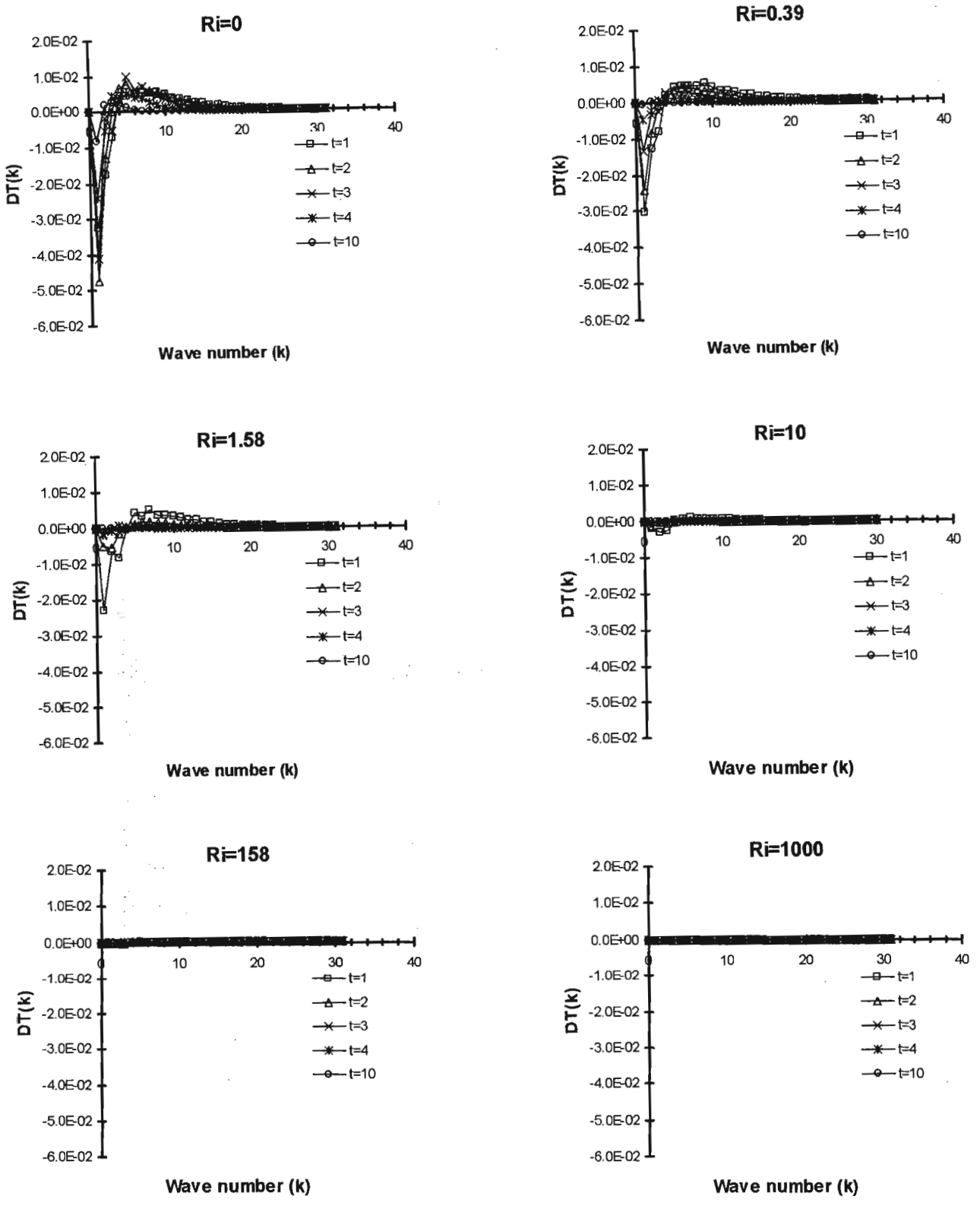

Figure 3.22: Plots of density transfer spectra for Ri = 0, 0.39, 1.58, 10, 158, & 1000

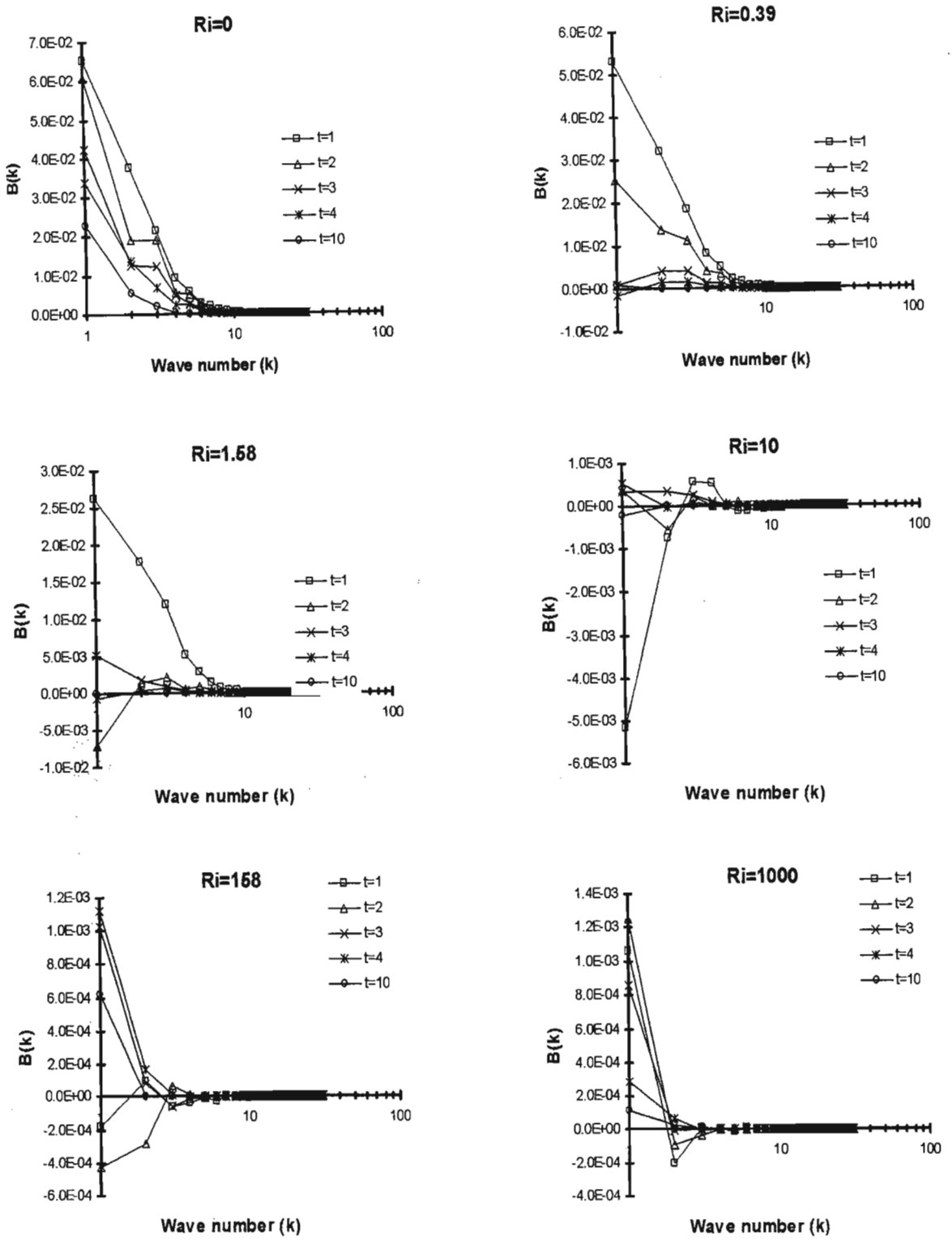

Figure 3.23: Plots of buoyancy spectra for Ri = 0, 0.39, 1.58, 10, 158, & 1000

3.8 Rapid Distortion Theory

The rapid distortion theory (RDT) is a linearized approximation of the Navier-Stokes equations. This linearized approximation can be solved analytically without difficulty. A review of RDT is given by Hunt & Carruthers (1990). The validity of RDT in stably stratified flow is based on the condition that the non-linear term $(\underline{u}\cdot\nabla)\underline{u}$ in the Navier-Stokes equations is small compared to the buoyancy term $g\rho/\rho_0$ (Derbyshire & Hunt, 1985).

Hunt, Stretch & Britter (1988), have used RDT to study the structure of stably stratified turbulent flows. Hanazaki & Hunt (1996) extended that work to determine the asymptotic (large time) partition of energy between the potential energy associated with density fluctuation and the kinetic energy associated with each of the velocity components during the subsequent development of turbulence based on initial kinetic energy and potential energy. Recently, Kaneda & Ishida (2000) also made use of RDT for studying vertical diffusion in strongly stratified flows.

In this study, a series of RDT simulations were carried out by simply turning the non-linear terms off in the DNS code. This approach has the distinct advantage in that it allows the comparison of results in detail and directly with DNS results for exactly the same initialisations. Further, using the code automatically filters out scales that are larger than the computational domain. There were three main questions to address, viz:

1. Does RDT predict the mixing efficiency for large *Ri*?
2. What are the effects of the *Pr* on the mixing efficiency?
3. What are the effects of *Re* and *Pe* for large *Ri* flows?

3.8.1 Mixing Efficiency using RDT

A series of RDT simulations at resolutions ranging from 32^3 to 128^3 and for *Ri* in the range 0.004 to 1000 were done. The results of the mixing efficiency calculated from these simulations were plotted against those obtained from the full turbulence simulations (DNS) as shown in figure 3.24. The *Pr* was varied in the range 0.1 - 2.0, to enable direct comparison with DNS results. The numerical results are presented in table A.5 in appendix A.

The mixing efficiency values are closely predicted by the RDT simulations, improving as Ri increases. At Ri = 1.58, they are within 10-20%, at Ri = 158 within 10%, at Ri = 1000 within 2-5% etc. In chapter 4, we present sample plots of particle tracks at these very stable flows and find that the particles move essentially in a horizontal plane with small vertical oscillations at the buoyancy period (see figures 4.11(e) & 4.11(f)). This can be interpreted as essentially a superposition of internal waves with some residual horizontal motion.

Figure 3.25 shows the buoyancy flux versus time (non-dimensionalized by N) for both RDT and DNS at Ri = 1000. The results plot on top of each other with only small differences which can be attributed to the slightly lower dissipation of the linearized case for times $1 < t < 2$, which results in a higher energy level at later times. Figure 3.26 shows the integral of the buoyancy flux as well as the potential energy dissipation for both RDT and DNS at Ri = 1000. Figure 3.27 shows the energy decay in time for the RDT simulation is slower than that for the DNS.

It is clear that the vertical dynamics of the flows are weakly non-linear and then only for a limited duration during the decay period (i.e. at times $1 < t < 2$, where t is non-dimensionalized by L_0/u_0). It is reasonable to suggest that RDT can be used to describe the vertical dynamics in strongly stable stratified flows.

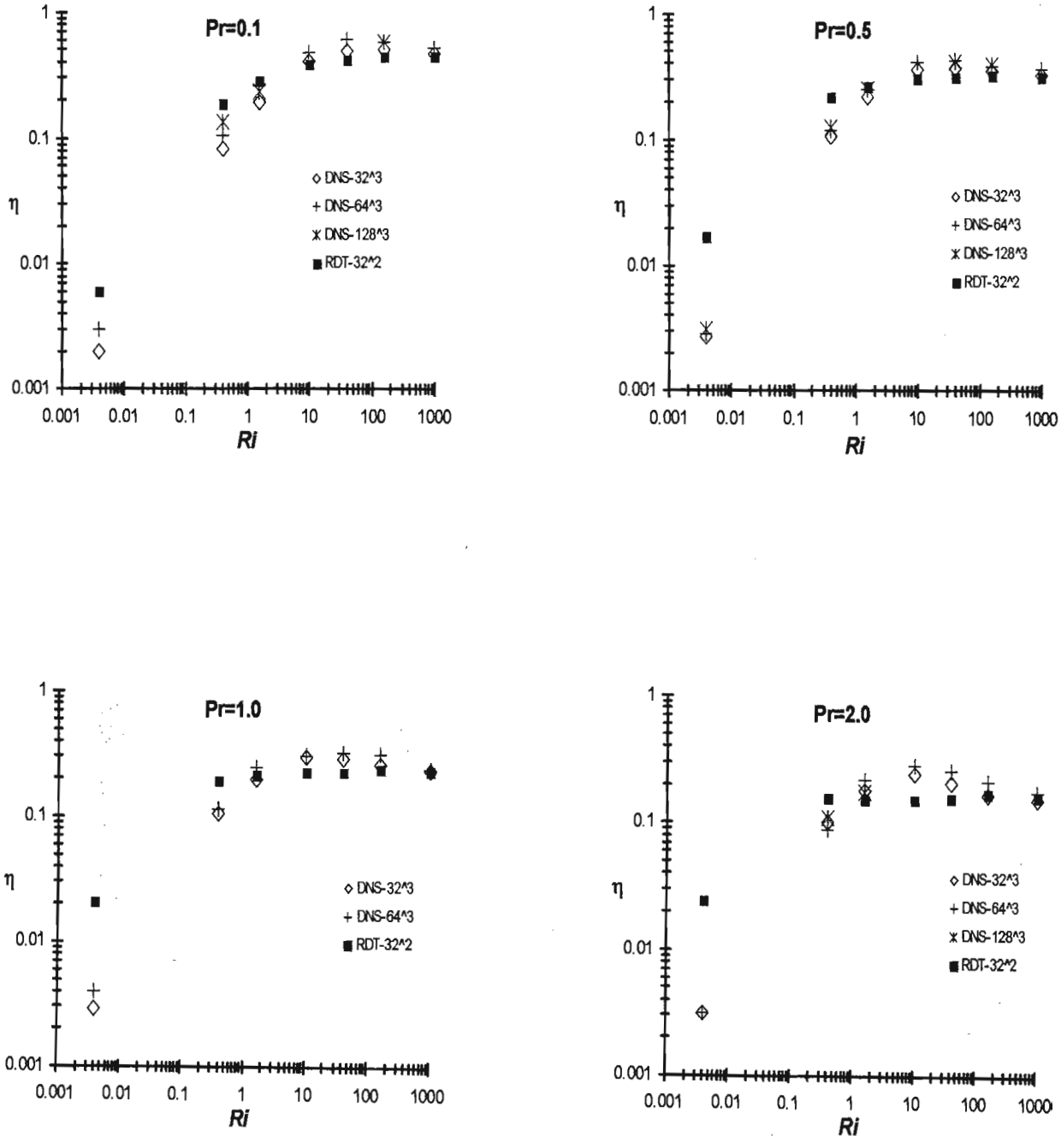

Figure 3.24: Mixing efficiency versus Ri for Pr = 0.1, 0.5, 1.0, 2.0, from RDT and DNS results

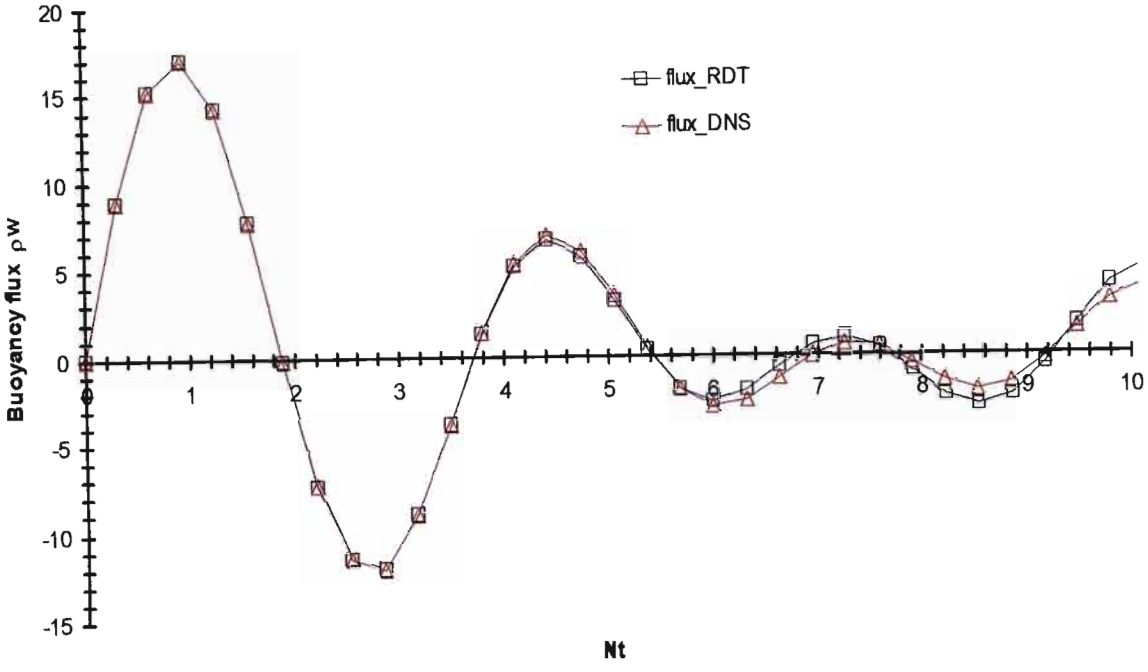

Figure 3.25: Plot of buoyancy flux versus Nt for Ri = 1000 from both RDT and DNS, Note the small divergence due to lower dissipation in the RDT simulation.

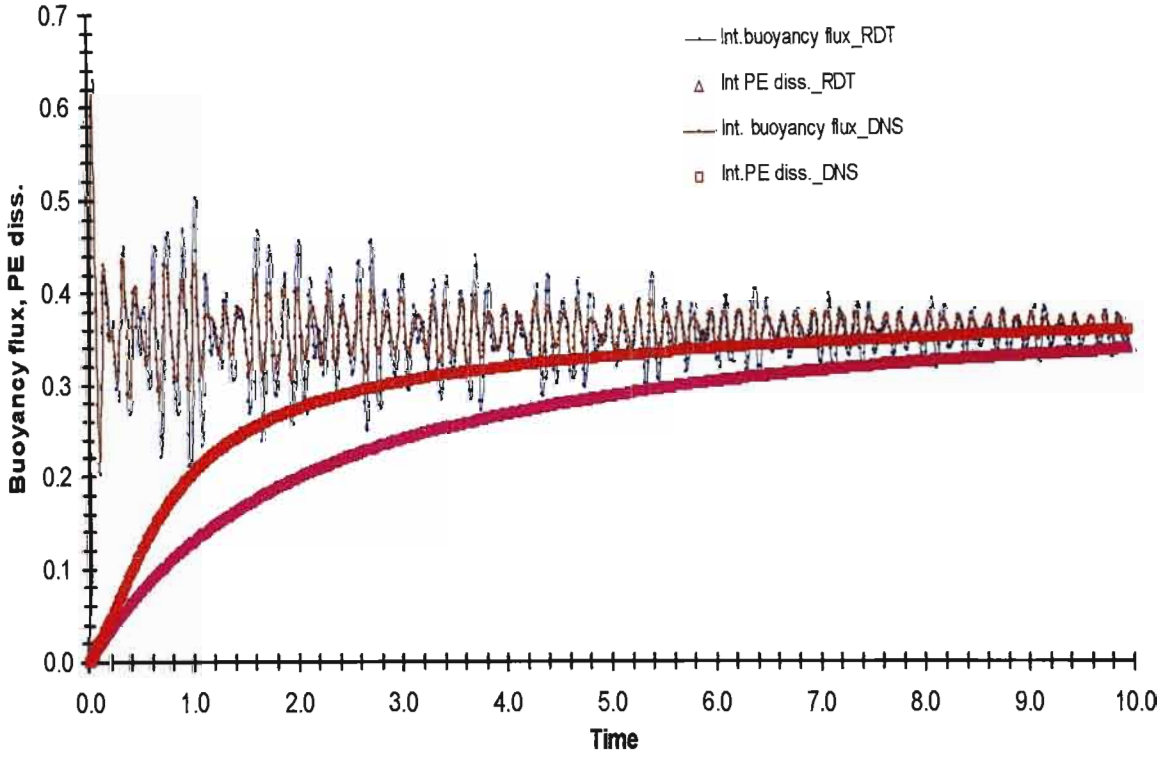

Figure 3.26: Plot of integrated buoyancy flux and potential energy dissipation with time for Ri = 1000 from both RDT and DNS

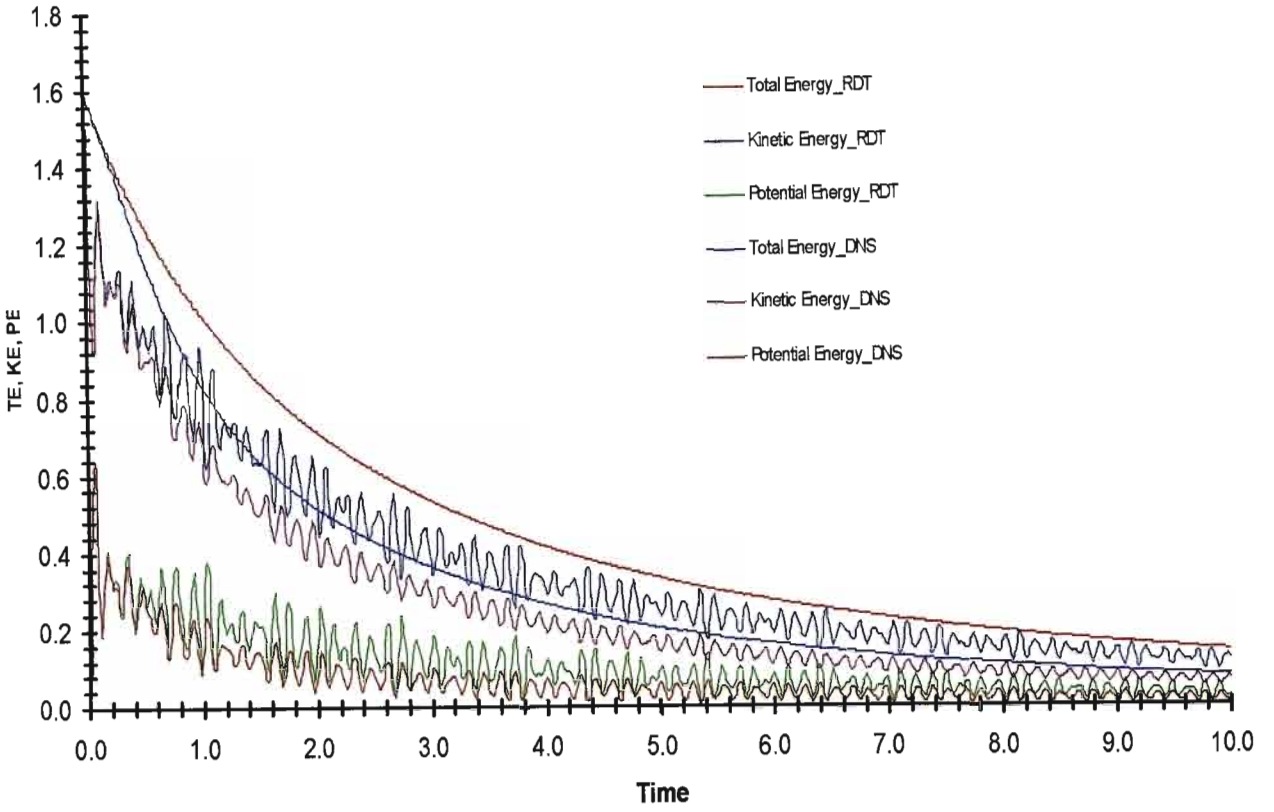

Figure 3.27: Plots of total, kinetic and potential energies with time Ri = 1000 from both RDT and DNS

3.8.2 Prandtl and Reynolds Number Effects

It was noted in section 3.6.3.1 that *Pr* effects increase as *Ri* increases (especially for *Ri* > 1). These effects are well reproduced by the RDT simulations for these high *Ri* values. RDT simulations here have been used to expand the range of *Pr* to 1000. It is found that the mixing efficiency tends to zero as *Pr* increases (at least for these *Re* numbers) as shown in figure 3.28. An approximate power law $\eta \sim Pr^{-1/2}$ is suggested by the data. The results obtained contradict the experimental data (e.g. Rottman & Britter, 1986), however it must be noted that the experiments are at much lower *Ri*. Further the simulations were at much lower *Re* and hence it remains uncertain whether these flows become more non-linear at high *Ri* when the *Re* numbers are higher. The trends in the DNS results for mixing efficiency from *Re* = 100 to *Re* = 400 (see figure 3.5), suggest that this might be the case but the *Re* number range is too small to be conclusive on this issue.

As noted in figures 3.26 & 3.27, the RDT simulations have somewhat smaller dissipation than the full turbulence simulations. This can be compensated for by using an "eddy" viscosity/diffusivity, i.e. by reducing the effective *Re* numbers of the RDT simulations. The *Re* was reduced from 100 to 40 and then to 30 for the all the RDT simulations at *Pr* of 1.0. The results are shown in figure 3.29. It is apparent that the mixing efficiency results for low *Ri* cases (the strongly non-linear cases) can also be reproduced using this approach. The asymptotic value of the mixing efficiency at high *Ri* is unaffected by changes in *Re*.

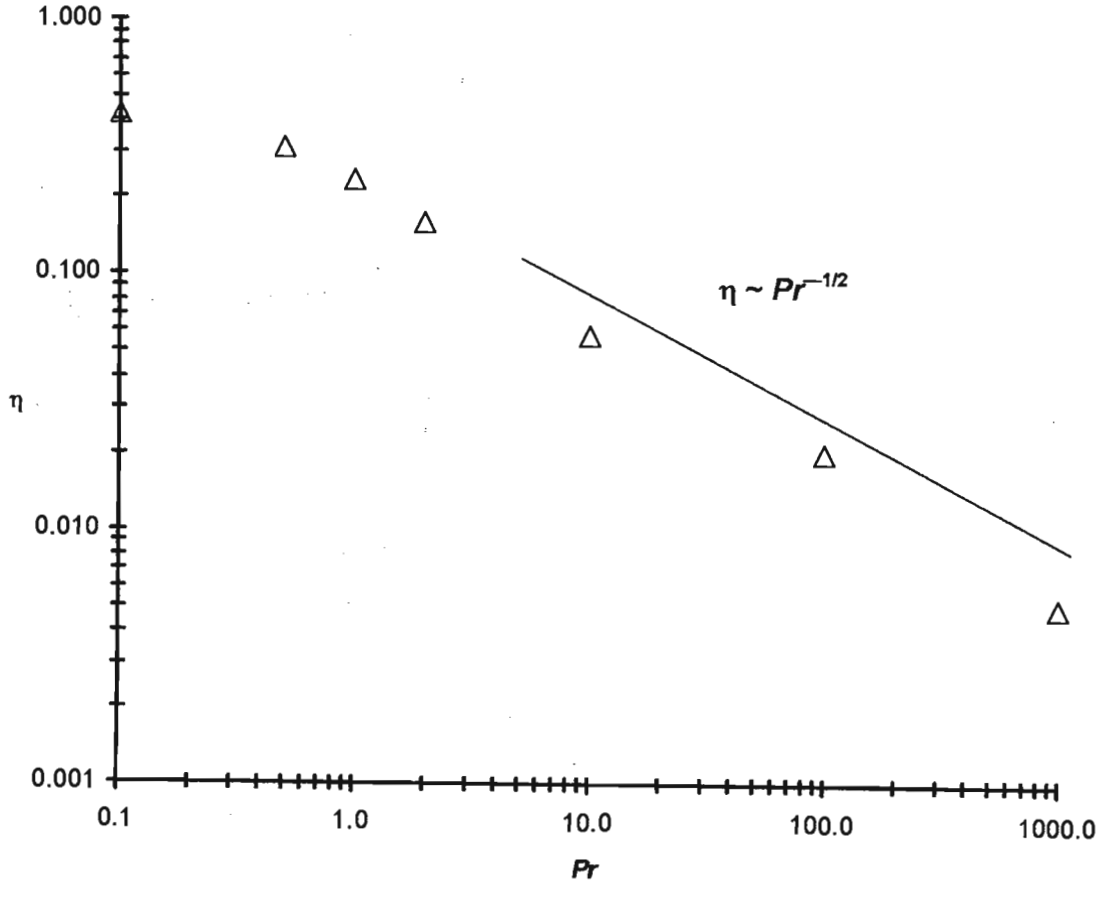

Figure 3.28: Mixing efficiency versus Pr number (on log scales) for Ri = 1000 using RDT simulations.

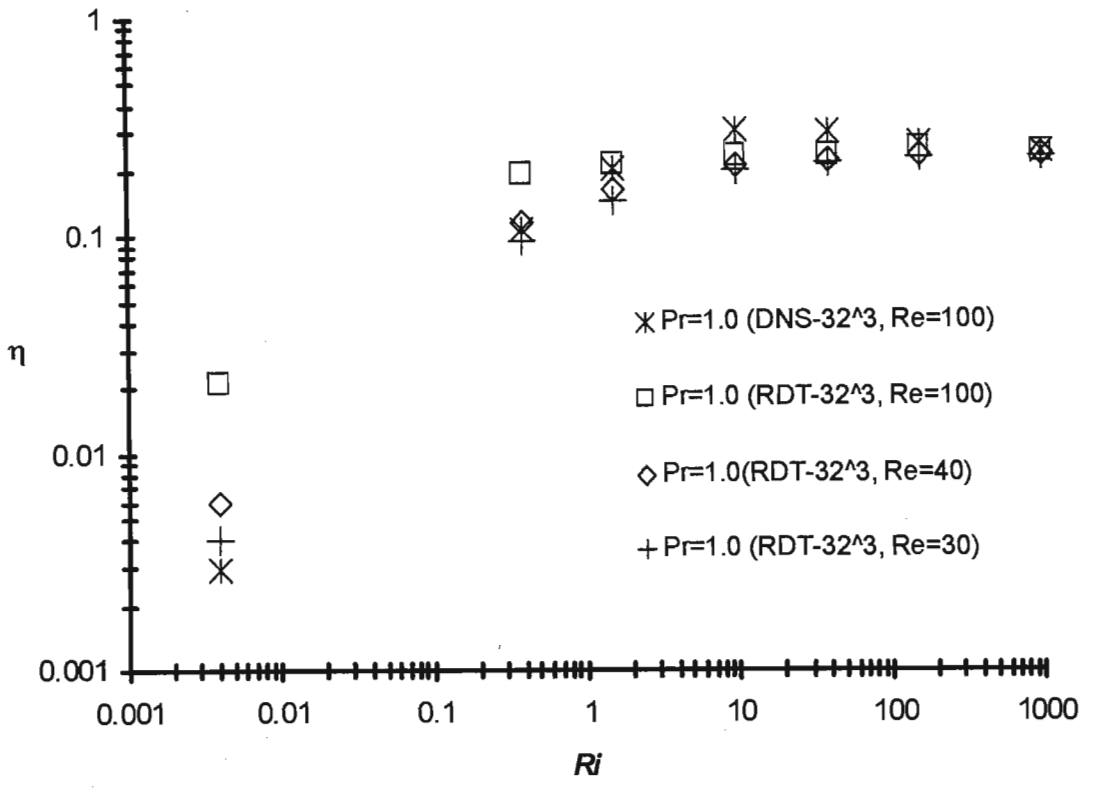

Figure 3.29: Mixing efficiency versus Ri for varying Re numbers using RDT simulations

In summary, the results suggest that RDT provides a very good approximation of the vertical dynamics of very strongly stably stratified flows which are thus essentially linear comprising mainly internal waves superimposed on quasi-horizontal motions.

3.9 Summary

This chapter has presented the results and discussion on the mixing efficiency using DNS of transient turbulent events within an Eulerian framework. RDT simulations were presented to draw comparison with DNS and infer the dynamics involved in the strongly stable cases. Results have been presented to support the notion that the vertical dynamics associated with strongly stably stratified flows is highly linear. Chapter 4 describes the research carried out using a Lagrangian approach where a particle-tracking algorithm was developed in the hope of leading towards a deeper understanding of mixing in stratified turbulence.

CHAPTER 4

LAGRANGIAN ANALYSIS OF STABLY STRATIFIED TURBULENCE

4.1 Introduction

Fluid motion is usually described in an Eulerian framework where the flow is defined at fixed positions in space. On the other hand, a Lagrangian description of the flow follows the motion of particular fluid particles beginning from their initial positions and a corresponding set of initial times (Sawford, 2001). The Lagrangian approach enables an investigation where direct questions can be asked about the motion of the material fluid elements (Yeung & Pope, 1989). In this chapter, we present the research work done using the Lagrangian approach to gain a deeper understanding of mixing and dispersion in stably stratified turbulence. A discussion on the particle-tracking algorithm that was developed and incorporated into the DNS code is presented first. Particle tracks and displacement statistics are presented and consistency with similar published work is verified. A fundamental aspect of this research involved calculating the instantaneous rate of mixing of fluid elements with their surrounding fluid. The analyses of these mixing events are discussed to draw insights into small scale mixing processes in this class of flows.

4.2 Problem Statement

A clear problem statement is obviously quite difficult to make in a study of this nature. However, the main question in this part of the investigation revolved around the mixing characteristics in stratified flow, specifically an attempt was made to address the following fundamental question:

" How do the density of the fluid particles change with time (and/or space) in stably stratified turbulence"?

Answering this question requires deeper probing into firstly where the mixing occurs and whether it is intermittent in time and space and secondly what are the mechanisms that cause mixing. A thorough understanding of the mixing processes cannot be obtained from just DNS. Nevertheless, DNS probably provides the only viable option at

this stage to gain some understanding into these processes. In this research we use the particle mixing and displacement statistics to test the PPH theory. However, it is important to recognize that the PPH theory is valid for stationary flow and caution must be exercised in generalizing the results obtained here for decaying turbulence.

4.3 Particle Tracking Algorithm

In order to gather Lagrangian statistics, it was necessary to develop and incorporate a particle-tracking algorithm into the DNS code of Riley et al (1981). Given an evolving 3-D periodic turbulent velocity field at discrete collocation (grid) points (which is readily available from the Eulerian DNS), an interpolation scheme was required to determine the velocity at any arbitrary position within the field. Using this interpolation scheme, the advection tracks of fluid particles can be computed from some set of initial starting positions by numerical integration.

Denoting $\underline{x}\langle \underline{x}_0, t\rangle$ and $\underline{u}\langle \underline{x}_0, t\rangle$ as the position and velocity at time t of a fluid particle with initial position $\underline{x}_0$ at time $t = 0$, the equation of motion of the particle is (e.g.Yeung & Pope, 1988):

$$\frac{\partial \underline{x}\langle \underline{x}_0, t\rangle}{\partial t} = \underline{u}(\underline{x}_0, t) \tag{4.1}$$

The Lagrangian velocity $\underline{u}\langle \underline{x}_0, t\rangle$ is related to the Eulerian velocity $\underline{u}(\underline{x}, t)$ by

$$\underline{u}\langle \underline{x}_0, t\rangle = \underline{u}\big(\underline{x}\langle \underline{x}_0, t\rangle, t \big) \tag{4.2}$$

The particle position is obtained by integrating equation (4.1) in time. Equation (4.2) essentially implies that the particle's velocity equals that of the fluid velocity at the instantaneous particle position as discussed earlier in section 2.6. The Eulerian velocity $\underline{u}$ is computed on a 3-D grid network at every time step. Hence the particle velocity can be obtained by interpolating the fluid velocity at the particle position.

There are a lot of errors that arise in the computation of particle displacements. Yeung & Pope (1988) indicate that numerical inaccuracies in the Eulerian velocity field will affect the particle trajectories. This should not cause a problem in the accuracy of the

results in this study as it was verified that the simulations were of adequate accuracy in section 3.3.3. The other sources of errors are due to the temporal resolution, i.e. the time step and the interpolation error in obtaining particle velocities. Statistical sampling error has also to be taken into account when ensemble averages over a sample of *M* particles are used as approximations to the true Lagrangian statistics.

4.3.1 Time Integration of Particle Motion

After the release of particles, equation (4.1) is integrated for the first time advancement using the Euler scheme and thereafter by a second-order accurate Adams-Bashforth scheme in each coordinate direction given by equation 4.3.

$$x_{istep+1,\,kk} = x_{istep,\,kk} + \frac{\Delta t}{2}\left[3u_{istep,\,kk} - u_{istep-1,\,kk}\right] \tag{4.3}$$

where *istep*-1 is the time at the previous time step and Δt = *istep* – (*istep* – 1), (see the main program listing given in appendix B). The Adams-Bashforth scheme is computationally less expensive than similar second-order accurate schemes like the predictor-corrector method. The time step size Δt is kept constant throughout the simulation and chosen in accordance with the criteria discussed in section 3.3.3. It is obvious that the particle track will not coincide with the grid points (where the fluid velocity is known), hence the fluid velocity, u_i, has to be interpolated to the particle position so that the particle can be advanced to its next time position using equation (4.3) (Truesdell, 1993).

4.3.2 Fluid Velocity Interpolation

Different interpolation schemes can be used to obtain the particle velocities (Yeung & Pope 1988, Balachander & Maxey 1989, Truesdell 1993). However, it is imperative that a scheme be chosen that is both numerically accurate and computationally efficient. Two interpolation schemes were explored in this study namely:

- Ordinary linear interpolation scheme
- Cubic Spline interpolation scheme

The linear interpolation scheme was considered initially because of its simplicity. It only requires the nodal values at the 8 vertices surrounding the interpolation cell. The

dependent variable is approximated as a linear function in each direction. There are only 8 unknown coefficients, and hence enforcing the collocation condition suffices to determine the interpolation weights uniquely (Yeung & Pope, 1988). The linear scheme is second-order accurate and discontinuous. The basic algorithm and formulation is well described by Truesdell (1993). Due to highly non-linear variations in the turbulent velocity fields, the linear scheme proved to be inadequate and was abandoned. However, it proved useful to have started with a linear scheme before proceeding to the complicated cubic spline interpolation scheme.

The cubic spline scheme developed for this study essentially follows the formulation given by Yeung & Pope (1988). It has the distinct advantage over the linear scheme in that it is formally fourth-order accurate and provides twice-continuously differentiable approximations.

There are essentially two main steps involved in cubic spline interpolation schemes: (1) evaluating the cubic spline coefficients; and (2) performing the interpolation. For the one-dimensional case, the spline approximation is given by:

$$g(x) = \sum_{i=0}^{N_b-1} b_i(x) e_i \tag{4.4}$$

where $b_i(x)$ is the i th basis function, e_i is the corresponding coefficient, and the sum is taken over N_b basis functions. At any given location, only four basis functions are non-zero (Yeung & Pope , 1988). The 1-D expressions for the basis functions are given in equations B.1 in appendix B.

The velocity fields obtained from the Eulerian DNS are periodic in 2π and hence it is logical to continue the basis functions and their coefficients periodically outside the interval considered. The DNS computes statistics at N equispaced nodes in each direction and hence it is found that we require $N_b = N + 3$ basis functions located at the nodes and their periodic extensions (i.e. one extended basis function to the left of the first node and two basis functions to the right of the *Nth* node). The periodic velocity function $\underline{u}$ can be extended to have $N + 3$ collocation points, hence the basis function coefficients can be determined from the N_b collocation conditions. The solution for the coefficients is obtained from an N_b^2 symmetric periodic tridiagonal system of equations:

$$\sum_{j=i}^{N} T_{ij}\, e_j = u_i \qquad (i = 0,\ldots..,\ N_b), \tag{4.5}$$

where

$$T_{ij} = \begin{cases} \frac{2}{3} & i = j \\ \frac{1}{6} & |i-j| = 1 \\ \frac{1}{6} & (i,j) = (1,N)\ or\ (N,1) \\ 0 & otherwise \end{cases} \tag{4.6}$$

The IMSL numerical libraries subroutine for matrix inversion is used to solve the system given in equation (4.5) in our particle tracking code (see subroutine "spline_init." in appendix B). Since the matrix inversion is required only once at the start of each simulation to compute the spline coefficients, other more efficient methods for solving sparse matrices were not explored (e.g. Ahlberg, Wilson & Walsh, 1967).

The key thing to recognize is that the 3-D spline can be represented as the tensor product of three 1-D splines as follows (de Boor, 1978):

$$u(x,y,z) = \sum_{k=0}^{N_b-1} \sum_{j=0}^{N_b-1} \sum_{i=0}^{N_b-1} b_i(x) c_j(y) d_k(z) e_{ijk}, \tag{4.7}$$

where $\{ b_i \}$, $\{ c_j \}$, and $\{ d_k \}$ are the 1-D basis functions in the x, y and z coordinate directions respectively and e_{ijk} are the cubic spline coefficients. Equation (4.7) can be written in an orderly decomposed format at the collocation points denoted by x_I, y_J, z_K (I, J, K = 0,...., N_b – 1), as:

$$u(x_I, y_J, z_K) = \sum_{i=0}^{N_b-1} b_i(x_I) E_{iJK} \tag{4.8}$$

where

$$E_{iJK} = \sum_{j=0}^{N_b-1} c_j(y_J) F_{ijK} \tag{4.9}$$

and

$$F_{IjK} = \sum_{k=0}^{N_b-1} d_k(z_K) e_{ijk} \tag{4.10}$$

Solving equations (4.8), (4.9) & (4.10), sequentially yields N_b^3 cubic spline coefficients. A subroutine was written to perform this evaluation (see subroutine "spline" in appendix B). Basically, the inverse of the coefficient matrix $\{T_{ij}\}$ obtained from the "spline_init." subroutine, together with the relevant velocity field are passed into the "spline" subroutine and it outputs the 3-D spline coefficient matrix $\{e_{ijk}\}$ to the main program. The 3-D velocity fields were extracted from the evolving simulations via the Image subroutine (see appendix B). Once the fields are in the spline subroutine, they are periodically extended from N to $N + 3$ collocation points to obtain the u_i matrix. Using the extended field, the matrix $\{E_{iJK}\}$ is generated using equation (4.5). With the $\{E_{iJK}\}$ matrix used instead of $\{u_i\}$ in equation (4.5), the solution for the F_{ijK} matrix is obtained and make use of equation (4.5) once again with $\{F_{ijK}\}$ replacing $\{u_i\}$ to solve for the spline coefficients e_{ijk}. The time spent for this computation is proportional to N^3.

The next step following the evaluation of the spline coefficients is to generate the basis functions at the particle position using equations B.1 in appendix B, and then to interpolate the particle velocity using the tensor product notation given in equation (4.7). The subroutine "interpolate" in appendix B gives the Fortran code for the interpolation. It was necessary to wrap-around particles that did not fall in the range 1 to N back into the computational domain in order to generate the basis functions and exploit the spatial periodicity of the calculation.

4.3.3 Particle Initializations and Sample Size

Fluid particles having different initial positions have behaviours, which are statistically identical in homogenous turbulence. This allows for ensemble averages to be taken over all (M) particles used in the simulations. The initial positions of the particles are chosen to be coincident with a subset of $M = 512$ (i.e. 8^3) Eulerian grid points, which form an equispaced cubic sublattice. This initialization technique has been used previously by Riley & Patterson (1974) and Yeung & Pope (1989) in their homogenous isotropic turbulence simulations. The obvious advantage of this choice lies in the fact that it ensures maximum statistical independence between the particles and minimizes the sampling errors.

In the sections that follow, results of particle displacements, rates of mixing etc, will be presented. Invariably, almost all the statistics include an ensemble average of the

statistic. It is obvious from the central limit theorem that the relative error of an ensemble average varies as $M^{-1/2}$. Truesdell (1993) carried out a test by monotonically increasing the number of particles included in the calculation for various dispersion statistics. He showed that 22^3 particles are sufficient for an ensemble average of the random dispersion process. However, due to computational and time constraints in this study, only 8^3 particles were used. The ensemble average statistics obtained for the particle displacements (see section 4.5) are in close agreement to those obtained by Kimura & Herring (1996) using 24^3 pairs of particles and Kaneda & Ishida (2000) using 512 particles.

4.4 Particle Tracking Simulations

The particle-tracking algorithm developed for this study is coded in a general form and can be used with the DNS code of Riley et al (1981) for any grid resolution. In this study, 64^3 DNS particle tracking is used to obtain the Lagrangian statistics. The code takes about 65 CPU seconds per time step for a 64^3 simulation on an Intel Pentium III 866 MHz processor. The time spent is linearly dependent on the number of the particles M, tracked. A 32^3 simulation takes about 8 CPU seconds. Kimura and Herring (1996) have used fast Fourier transforms for solving the tridiagonal matrix equation for the spline function. It is possible to cut down on the computational time using such an approach.

The simulations done incorporating particle tracking at 64^3grid resolution were at a Re of 200 and Pr of 0.5. The Richardson number was in the range $0 < Ri < 1000$ and is identical to the list given in Table 3.1. The values of the Re, Ri, number of grid points and tracer particles ($M = 512$) are identical to those used by Kaneda & Ishida (2000) in their DNS with only the Pr different (they used a Pr of 1) The relevant statistics such as the particle coordinates, velocities and density fluctuations were archived at every 5^{th} time step (due to memory restrictions). Since the time steps used in this study were small (see table 3.1), it was noted that storing the important statistics every 5^{th} time step provides an acceptable level of accuracy for the purposes of the study.

Sample plots of 3-D particle trajectories obtained from a preliminary simulation at 32^3 resolution at Ri of 158 are shown in figure 4.1. The plots support the notion that vertical displacements are suppressed by the stable stratifications as indicated by Kimura & Herring (1996, hereafter referred as KH).

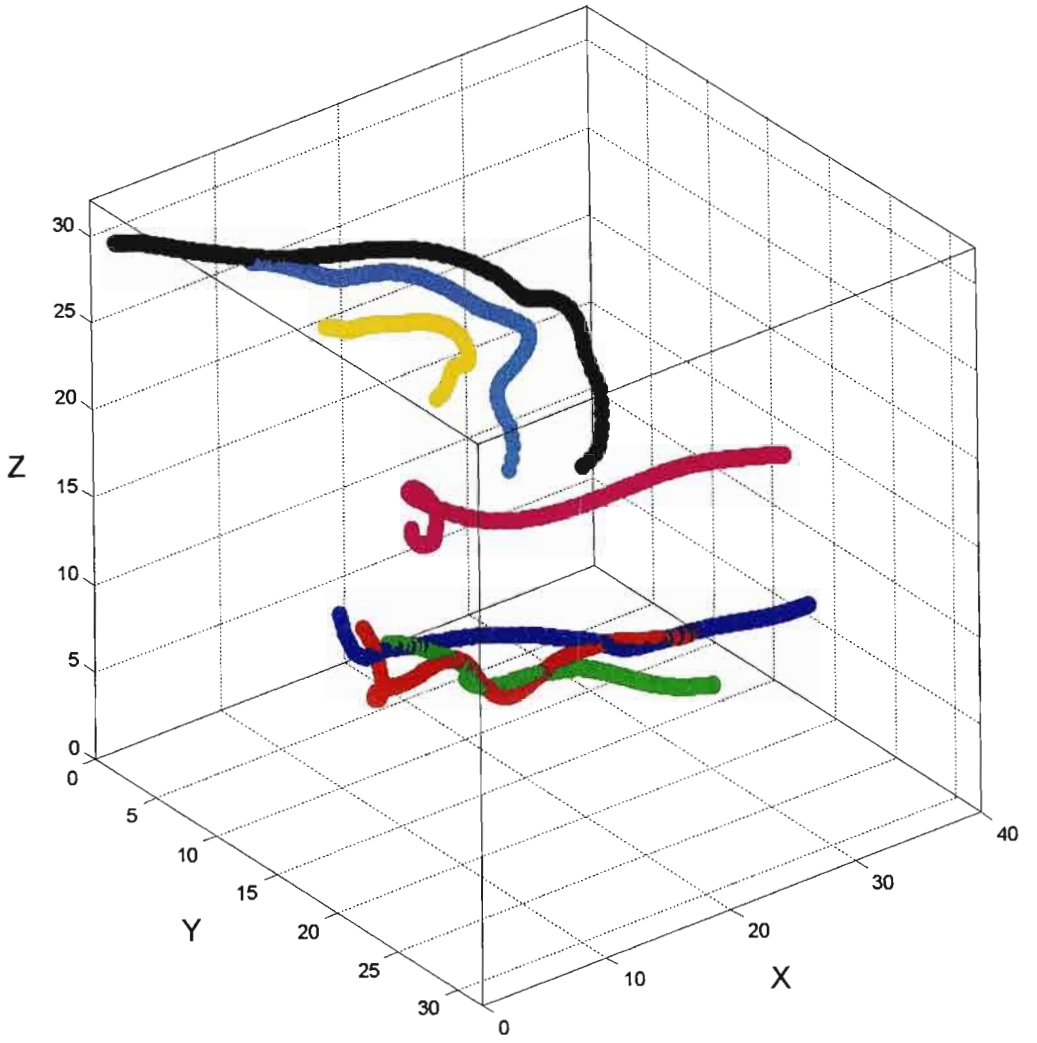

Figure 4.1: Sample plots of particle tracks at Ri = 158 at 32^3 resolution. Note how the vertical displacements of the particles are suppressed compared to their horizontal displacements.

4.5 Particle Displacement Statistics

The archived results of the simulations were post processed to obtain the mean square displacements, $\overline{\Delta z^2}\langle t\rangle, \overline{\Delta x^2}\langle t\rangle and\ \overline{\Delta y^2}\langle t\rangle$, of the particles from their initial positions for Ri = 0, 0.39, 1.58, 10, 39.5, 158, and 1000. Figure 4.2 shows the mean square vertical displacement with time for the different Ri cases. A sharp decrease in the particle displacement is evident as the Ri number increases. At high Ri the asymptotic value is proportional to Ri^{-1}. Figure 4.3 shows the mean square displacement scaled by Ri versus time on the Nt scale for Ri = 0.39, 1.58, 10, 39.5, 158, and 1000. It is important to note that the leveling off in the displacements occurs at $Nt \approx 2$ and that there is collapse of the displacements to within an order of unity. This result agrees very closely with the observations made by KH, Kaneda & Ishida (2000, hereafter referred as KI) and PPH. Nicolleau & Vassilicos (2000) have also shown that the vertical displacement for the high Ri cases is bounded in time. The mean square value at Ri = 1000 shows a slight decrease with time. Such a decrease is also seen in the DNS of KH and KI. Comparisons of the RDT model developed by KI with their DNS shows how RDT predicts almost exactly the mean square displacement at high Ri values.

The leveling out of $\overline{\Delta z^2}\langle t\rangle$ can be explained by looking at the mixing characteristics of the flows. Plots of the root mean square rate of mixing (see figure 4.9 in section 4.7) show clearly that most of the mixing between the fluid elements has occurred at times of the order $3L_o/u_o$. This implies that the effect of the density exchange between fluid elements at times beyond 3 L_o/u_o is negligibly small which limits any further growth in the particle displacements as suggested by PPH (1983).

At late times it is noticed that there is no further growth in the vertical displacement of the fluid elements, which must imply that the fluid elements have attained a new equilibrium position in the background density gradient and hence a new potential energy. Therefore the asymptotic value of the mean square vertical displacement gives a measure of the irreversible mixing that has occurred between fluid elements and can be related to the mixing efficiency (see section 4.7.2). This interpretation for the asymptotic limit has not been offered previously in literature (e.g. Kimura & Herring, 1996, PPH, 1983).

Essentially repeating the work done by KH, the probability distribution functions for the vertical displacement, Δz, were plotted as shown in figure 4.4. These plots confirm KH's observation of particles ceasing to migrate vertically even at modest stratifications (Ri = 1.58). The vertical suppression is consistent with the PPH theory and is attributed to energy constraints imposed by buoyancy forces.

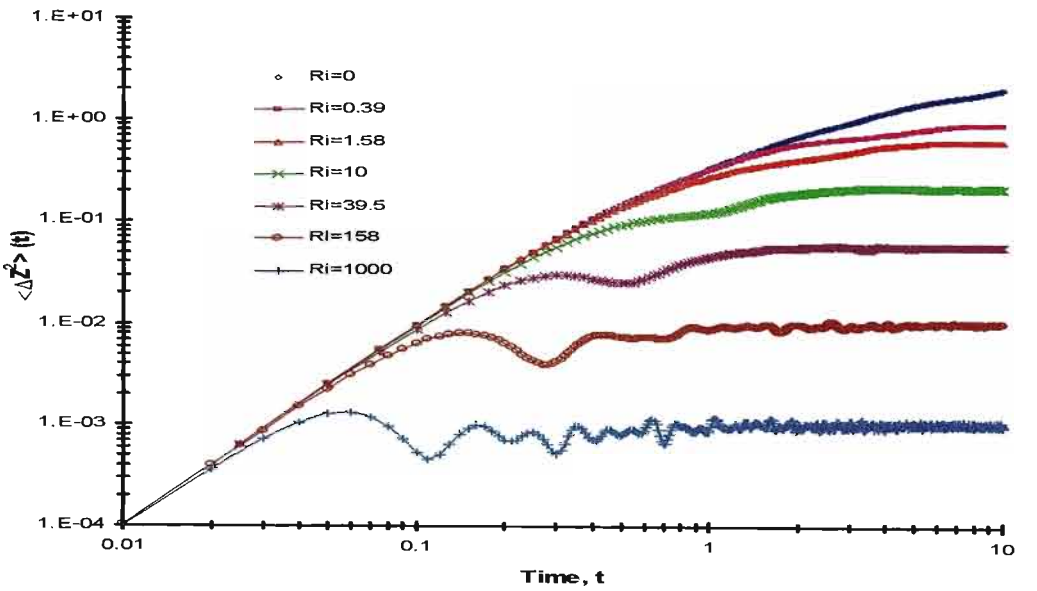

Figure 4.2: The mean square of the vertical displacement $\overline{\Delta z^2}\langle t \rangle$ *for Ri = 0, 0.39, 1.58, 10, 39.5, 158 & 1000.*

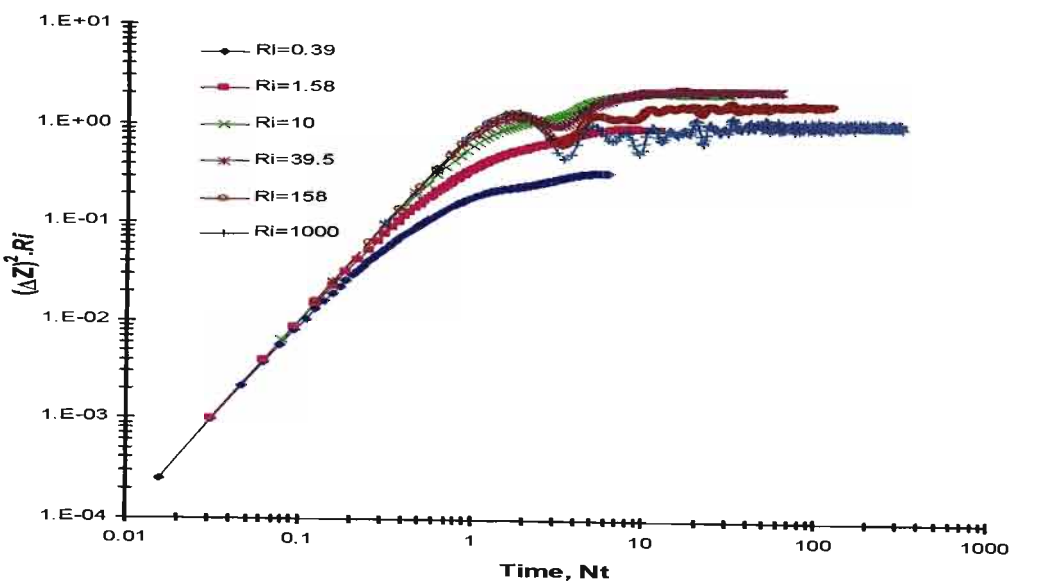

Figure 4.3:The scaled mean square of the vertical displacement $Ri \cdot \overline{\Delta z^2}$ *versus Nt for Ri= 0.39, 1.58, 10, 39.5, 158 & 1000.*

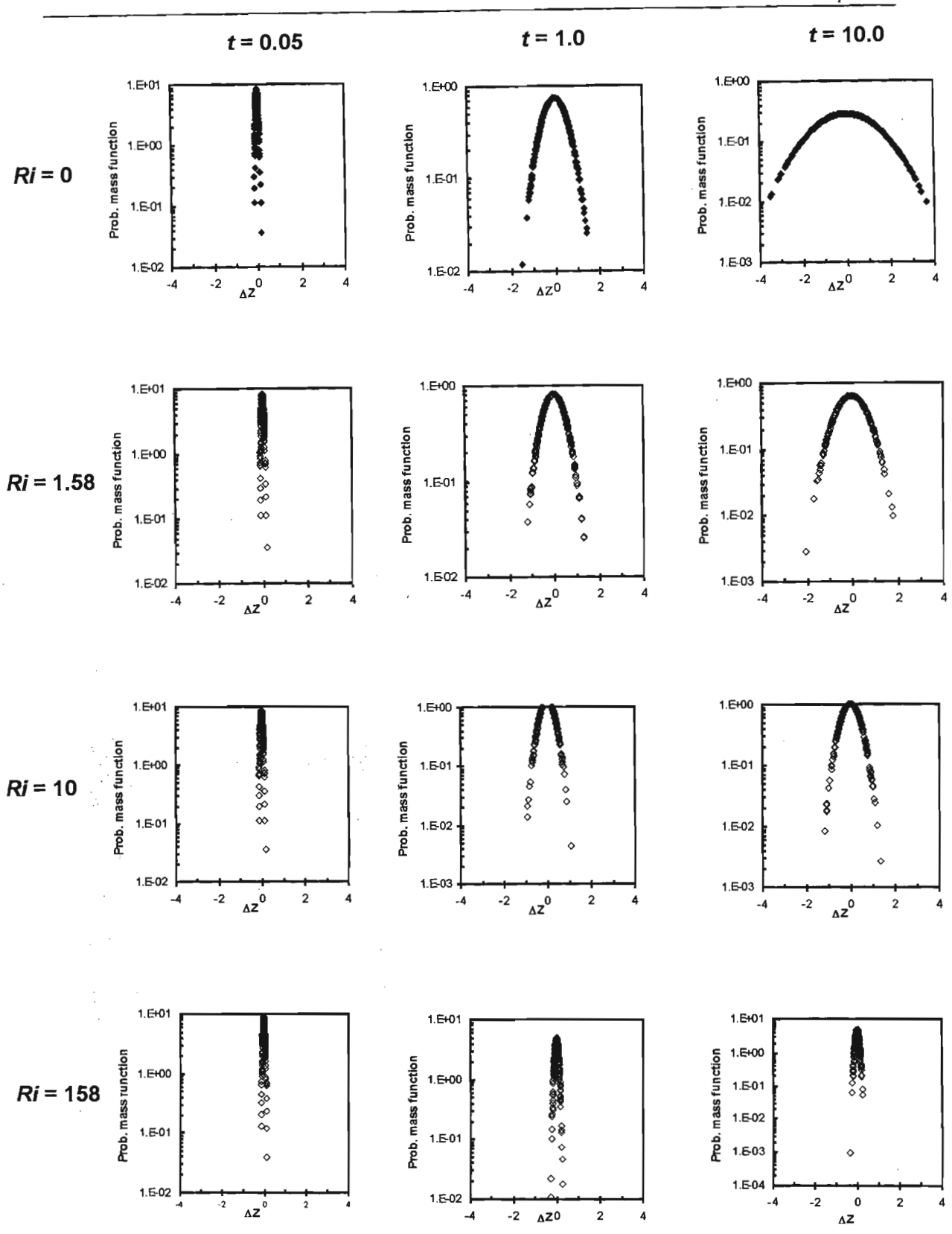

Figure 4.4: Probability distribution of the vertical displacement Δz for Ri = 0, 1.58, 10, and 158 at t = 0.05, 1.0, 10.0.

The root mean square (standard deviation) vertical displacement of the particles is shown in figure 4.5. It is clear for small times, the growth is consistent with the initial Taylor range, $\Delta z' \sim t^1$ for all the *Ri* cases. For the unstratified case (*Ri* = 0), the growth is like $t^{1/2}$ at long times again consistent with Taylor's theory. There is no obvious $t^{1/2}$ growth observed for the cases with *Ri* > 0. PPH suggested that such growth could occur at late times due to mixing between fluid elements (see section 4.7 for a discussion on the mixing of fluid particles). The vertical displacement limit of w_0/N imposed by buoyancy effects was calculated for each of the high *Ri* flows and compared with the asymptotic root mean square values shown in figure 4.5 (see table 4.1). It is found that this limit predicts reasonably well the long time behaviour of particle displacements suggesting that density exchanges are not occurring in any significant amounts to alter this limit at late times, especially in the high *Ri* flows studied here. This observation is consistent with the PPH model with $\gamma = 0$.

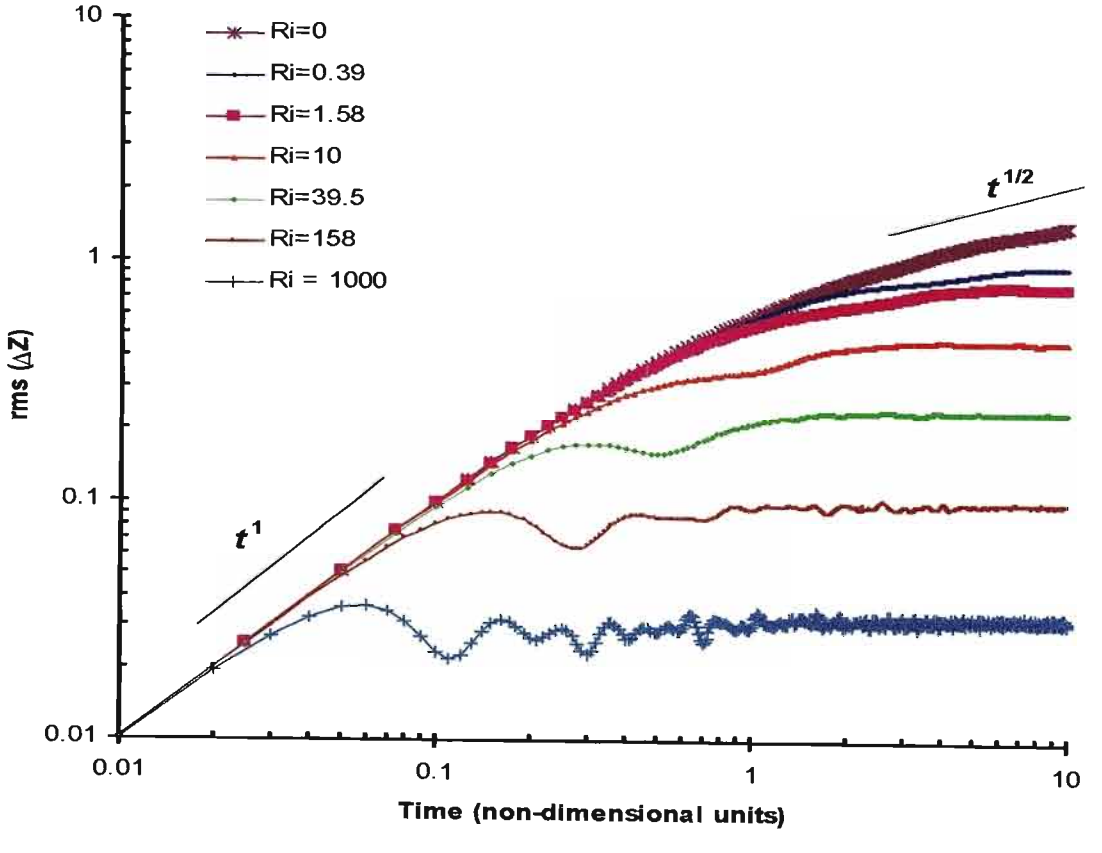

Figure 4.5: Root mean square vertical displacements as a function of time for Ri = 0, 0.39, 1.58, 10, 39.5, 158 and 1000 from DNS particle tracking at 64^3 grid resolution.

Table 4.1: Comparison of theoretical upper bound limit of vertical displacement (PPH) with root mean square vertical displacements from DNS particle tracking. Note the vertical velocity used is the root mean square of the initial velocity at the start of every simulation, as this would dictate the energy available to disperse the particles.

Ri	***w_0/N*** **(calculated)**	**r.m.s. vertical displacement (DNS) at $L_0/u_0 = 10$**
1.58	0.804	0.753
10	0.319	0.449
39.5	0.160	0.235
158	0.081	0.099
1000	0.031	0.031

The mean square horizontal displacements, $\overline{\Delta x^2}\langle t\rangle and\ \overline{\Delta y^2}\langle t\rangle$, shown in figures 4.6 and 4.7, indicate that stable stratification has small effects on the particle displacements in the horizontal plane. It can also be seen that the horizontal displacements are slightly enhanced with increasing stratification. This would seem to suggest that there are non-linear residual horizontal motions present in these flows at late decay times. They evidently increase in scale at late times i.e. energy is being transferred from smaller to larger scales. This is consistent with the notion that the flow at these late times comprises of quasi-two dimensional turbulence (Riley et al, 1981). Flow visualizations of the enstrophy (mean squared vorticity) fields of these strongly stable cases show that the bulk of the contribution to the enstrophy is from the horizontal vorticity (see section 5.2.1). The probability distribution functions of the horizontal displacements for all the flows are quite similar to those of unstratified turbulence and are in agreement with the results of KH.

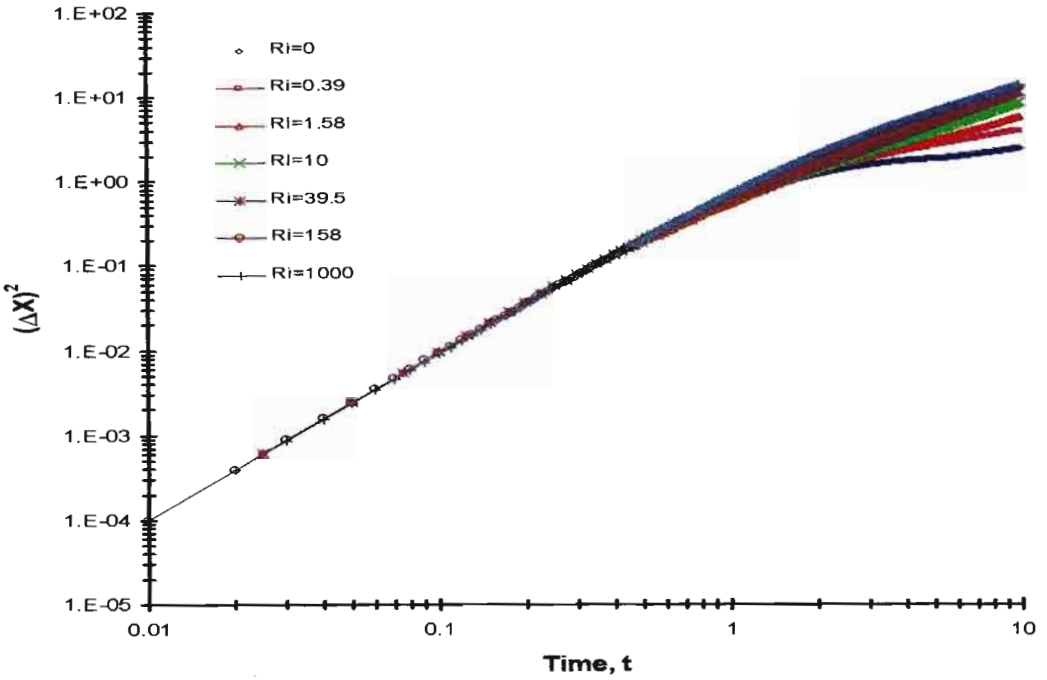

Figure 4.6: The mean square of the horizontal displacement $\overline{\Delta x^2}\langle t \rangle$ *for Ri = 0, 0.39, 1.58, 10, 39.5, 158 & 1000.*

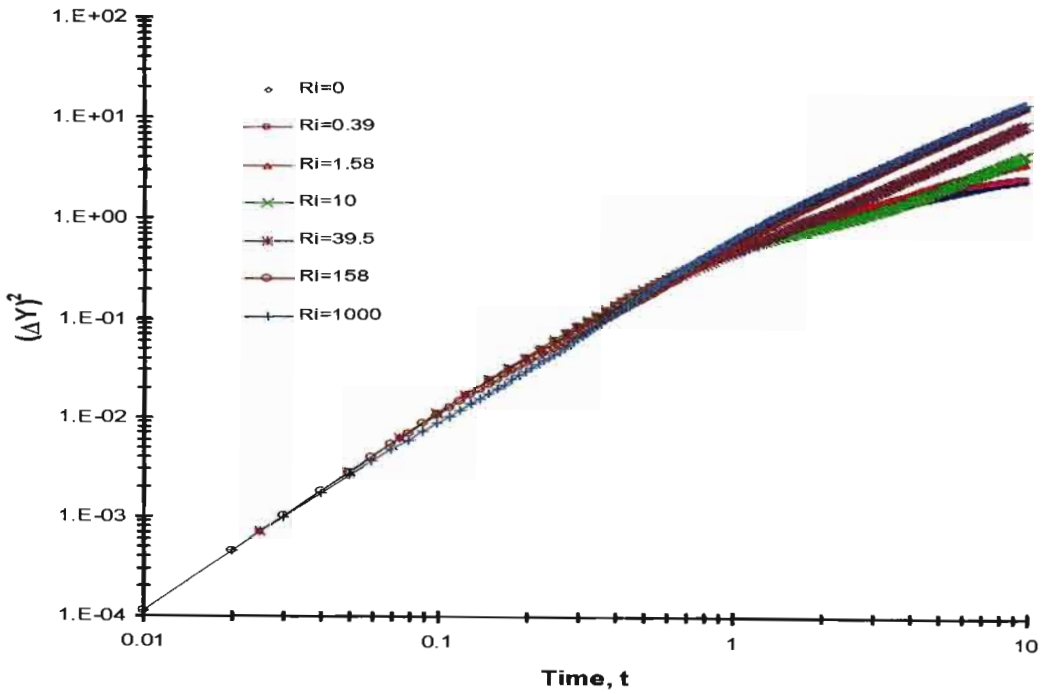

Figure 4.7: The mean square of the horizontal displacement $\overline{\Delta y^2}\langle t \rangle$ *for Ri = 0, 0.39, 1.58, 10, 39.5, 158 & 1000.*

4.6 Comparison of Eulerian and Lagrangian Statistics

In homogenous turbulence, Eulerian 'single-point' statistics from averages taken over all the grid points are formally equivalent to Lagrangian 'single particle' statistics from averages taken over an ensemble of individual fluid particles, at a given time (Monin & Yaglom, 1971, Tennekes & Lumley, 1973). As the number of particles, *M*, increases, the ensemble average will converge on the Eulerian 'one-point' averages (ergodicity).

Volume averaged Eulerian buoyancy flux, $\overline{\rho w}(t)$, was plotted against the ensemble averaged Lagrangian flux, $\overline{\rho w}\langle t \rangle$ to test the adequacy of the sample size used and also emphasize the important links between the two frames of reference used in this study. Figure 4.8 shows plots of the Eulerian and Lagrangian fluxes superimposed on each other for *Ri* = 1000. It can be noted that there is a close agreement in the results giving confidence to the numerical approach used to get the Lagrangian statistics in this study. Other parameters such as the root mean square rate of mixing, mean squares of velocities etc. can be similarly related.

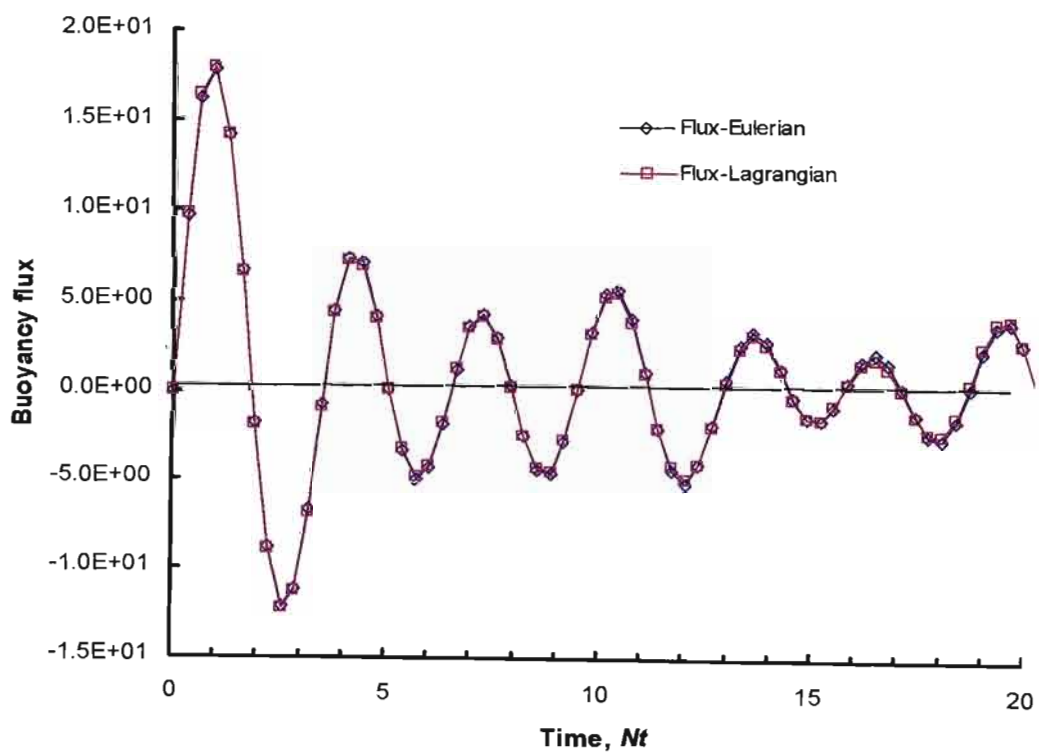

Figure 4.8: Eulerian buoyancy flux, $\overline{\rho w}(t)$ and Lagrangian buoyancy flux, $\overline{\rho w}\langle t \rangle$, versus Nt for Ri = 1000.

4.7 Particle Mixing Statistics

The mechanisms responsible for mixing internally in a stably stratified fluid are not well understood as the there are likely to be several processes that occur simultaneously (Turner, 1973). The rate of mixing obtained by following fluid elements will be of fundamental interest in understanding and modeling diffusion in stably stratified turbulence. Equation (4.3) in the PPH theory (see equation (2.26)) provides a formulation for calculating the instantaneous rate of mixing of fluid elements as follows:

From equation (2.26) in section 2.6.1 (following Csanady, 1964), the material derivative of the density fluctuations following a fluid element can be expressed as:

$$\frac{D}{Dt}\rho'\langle t\rangle = -w\langle t\rangle\overline{\frac{\partial\rho}{\partial z}} + \kappa\nabla^2\rho'\langle t\rangle \tag{4.11}$$

where the first term on the right hand side represents the advective term or the reversible segregation of the fluid particle and the second term gives the rate of molecular mixing of the fluid particle. Note that fluid particles can both gain or lose density to their surroundings.

Rearranging equation (4.11), we get the instantaneous rate of mixing of the fluid particle at any given time as:

$$\kappa\nabla^2\rho'\langle t\rangle = \frac{D}{Dt}\rho'\langle t\rangle + w\langle t\rangle\overline{\frac{\partial\rho}{\partial z}} \tag{4.12}$$

Using particle tracking, the density fluctuation, ρ', was extracted at each time for each particle using the Eulerian field for determining the density fluctuation at that time. Hence the rate of mixing of the particles can be calculated explicitly from equation (4.12).

4.7.1 Root Mean Square Rates of Mixing

The ensemble averaged rate of mixing as function of time was calculated for the different *Ri* flows and plotted as shown in figure 4.9a. It can be noted that nearly all the mixing in these flows occur within times of about 3 L_o/u_o. This provides an explanation

for the leveling out of the mean square displacements noted in figure 4.2. It was also noted in section 3.7.2 how the buoyancy flux production is complete in times of about 3 L_0/u_0. The reason for this can again be attributed to the mixing being complete at about the same time. The rate of mixing of fluid elements for the unstratified case is the highest as would be expected. The magnitude of the rate of mixing reduces with increasing stratification. Figure 4.9b shows the root mean square rate of mixing versus time non dimensionalized by N for Ri = 0.39, 1.58, 10, 39.5, 158 and 1000. The peaks occur at approximately Nt of 1 for the weakly stratified flows (Ri = 0.39, 1.58) and shifts to Nt of about 2 for the strongly stable cases. Mixing decreases rapidly for $Nt \geq 2\pi$ (i.e. after one buoyancy period).

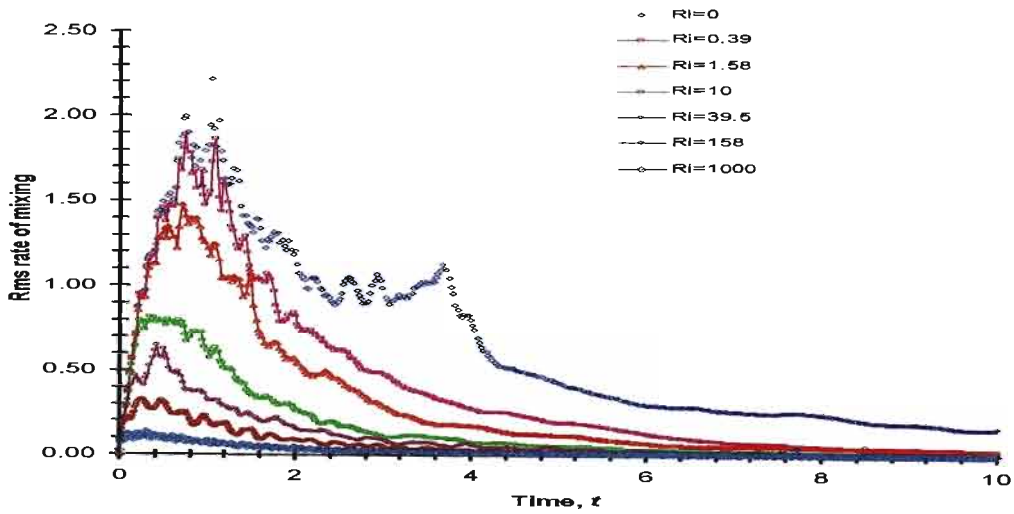

Figure 4.9a: The root mean square rate of mixing as function of time for Ri = 0, 0.39, 1.58, 10, 39.5, 158 & 1000, as computed from DNS particle tracking at 64^3 resolution.

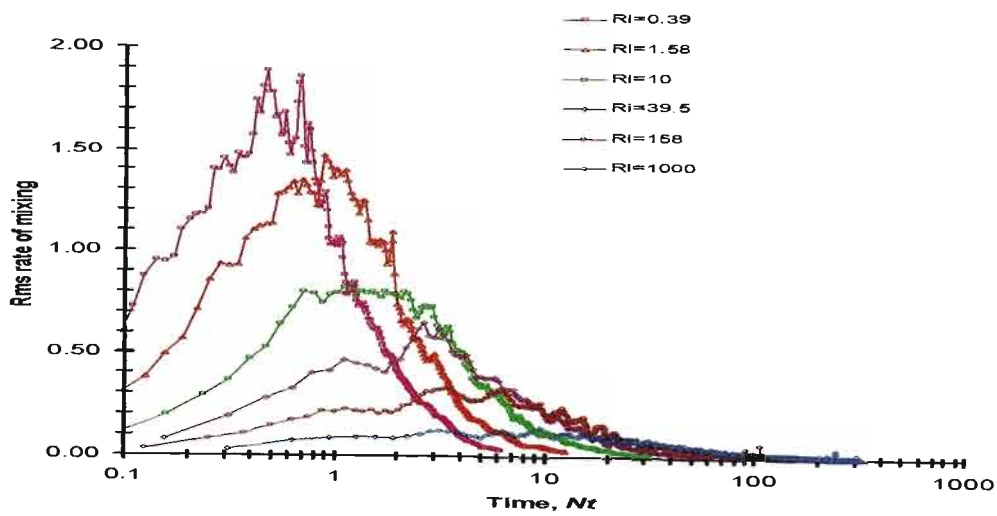

Figure 4.9b: The root mean square rate of mixing as function of time (Nt) for Ri = 0.39, 1.58, 10, 39.5, 158 & 1000, as computed from DNS particle tracking at 64^3 resolution.

4.7.2 Mixing Efficiency using Lagrangian Statistics

It was indicated in section 4.5, that the asymptotic value of the mean square vertical displacement is a measure of the irreversible mixing that has occurred in the flow. The mixing efficiency can thus be calculated directly from the mean square displacement if the initial kinetic energy is known as follows:

The change in potential energy per unit mass for the ensemble of fluid particles at late times is given by (see section 3.4.2 for the derivation),

$$\Delta PE = N^2 \overline{\Delta z}^2 / 2 \tag{4.13}$$

hence the mixing efficiency, $$\eta = \frac{\Delta PE}{\Delta KE} = \frac{N^2 \overline{\Delta z}^2 / 2}{\Delta KE} = \frac{Ri \cdot \overline{\Delta z}^2}{2 \Delta KE} \tag{4.14}$$

Table 4.2 shows the mixing efficiency results calculated using equation (4.14) for the different *Ri* cases together with the results calculated from equation (2.13) using the Eulerian statistics. The results compare well especially for the very strongly stable flow of *Ri* = 1000. The results agree in all cases to within a factor of less than two and agreement can be expected to improve with increasing sample size.

Table 4.2: Mixing efficiency results from both mean square particle displacements and buoyancy flux for Ri = 0.39, 1.58, 10, 39.5, 158, & 1000.

Ri	**Mean square vertical displacement** $\overline{\Delta z}^2$	**Change in potential energy** $\Delta PE = Ri\overline{\Delta z}^2$	**Change in kinetic energy** ΔKE	**Integrated Buoyancy flux, *B***	**Mixing efficiency** $\eta_L = \Delta PE/\Delta KE$	**Mixing efficiency** $\eta_E = B/\Delta KE$
0.39	0.851	0.166	1.567	0.198	0.106	0.126
1.58	0.567	0.448	1.554	0.378	0.288	0.243
10	0.202	1.010	1.540	0.572	0.656	0.371
39.5	0.055	1.087	1.505	0.588	0.722	0.391
158	0.010	0.782	1.492	0.553	0.524	0.371
1000	0.001	0.475	1.479	0.479	0.321	0.324

4.7.3 Distribution Functions of Mixing Events

The probability distribution functions for the rate of mixing calculated from the statistics at various times were analysed for the different *Ri* flows. The kurtosis excess for the distributions was calculated. All the cases showed positive kurtosis excess indicating that the distributions are relatively peaked compared to a normal distribution. The skewness of most of the distributions was small. The highest positive rate of mixing (particle loosing density to surrounding fluid) and lowest negative rate of mixing (particle gaining density from surrounding fluid) were identified for each of the *Ri* cases and the corresponding distribution of the mixing rates were plotted (see figures 4.10*a* to 4.10*c*). The kurtosis excess of the distributions at the times when these high mixing events occur is very high. It appears from the probability distribution functions that these high mixing events are very intermittent temporally as well as spatially.

4.7.3.1 Particle Tracks of High Mixing Events

Selected 3-D tracks of the particles exhibiting the highest mixing magnitudes were plotted for the different *Ri* flows (see figures 4.11a to 4.11f). Colour was used as an indicator of the rate of mixing of the particle. This approach gives a qualitative insight into issues such as where the mixing is occurring and more importantly what is happening to the particle when these high mixing events occur. Questions that arise out these plots include:

- How do the particle tracks differ with increasing stratifications?
- How are the important parameters such as the density fluctuation, vertical velocity, etc. correlated with the rate of mixing?
- Is there evidence of vortex motions or overturning near these mixing events?

All of the above questions cannot be answered definitively. The tracks for the low *Ri* flows show how the particles wander with freedom in all three spatial directions. On the other hand, in the strongly stable cases (*Ri* = 158 & 1000) the particles are more or less restricted to a horizontal plane with small vertical oscillations with period of order T_{BV}. This again corroborates the speculation that the vertical motions of these strongly stable flows are characterized by linear internal waves (see figures 4.11e & 4.11f). It can be seen from the tracks that these high mixing events are isolated (i.e. temporally intermittent) confirming the observation made in section 4.7.3.

The correlation of the rate of mixing with density fluctuations, vertical velocity, and acceleration, are discussed in sections 4.7.4 and 4.7.5. The flow structures associated with these flows are discussed in chapter 5.

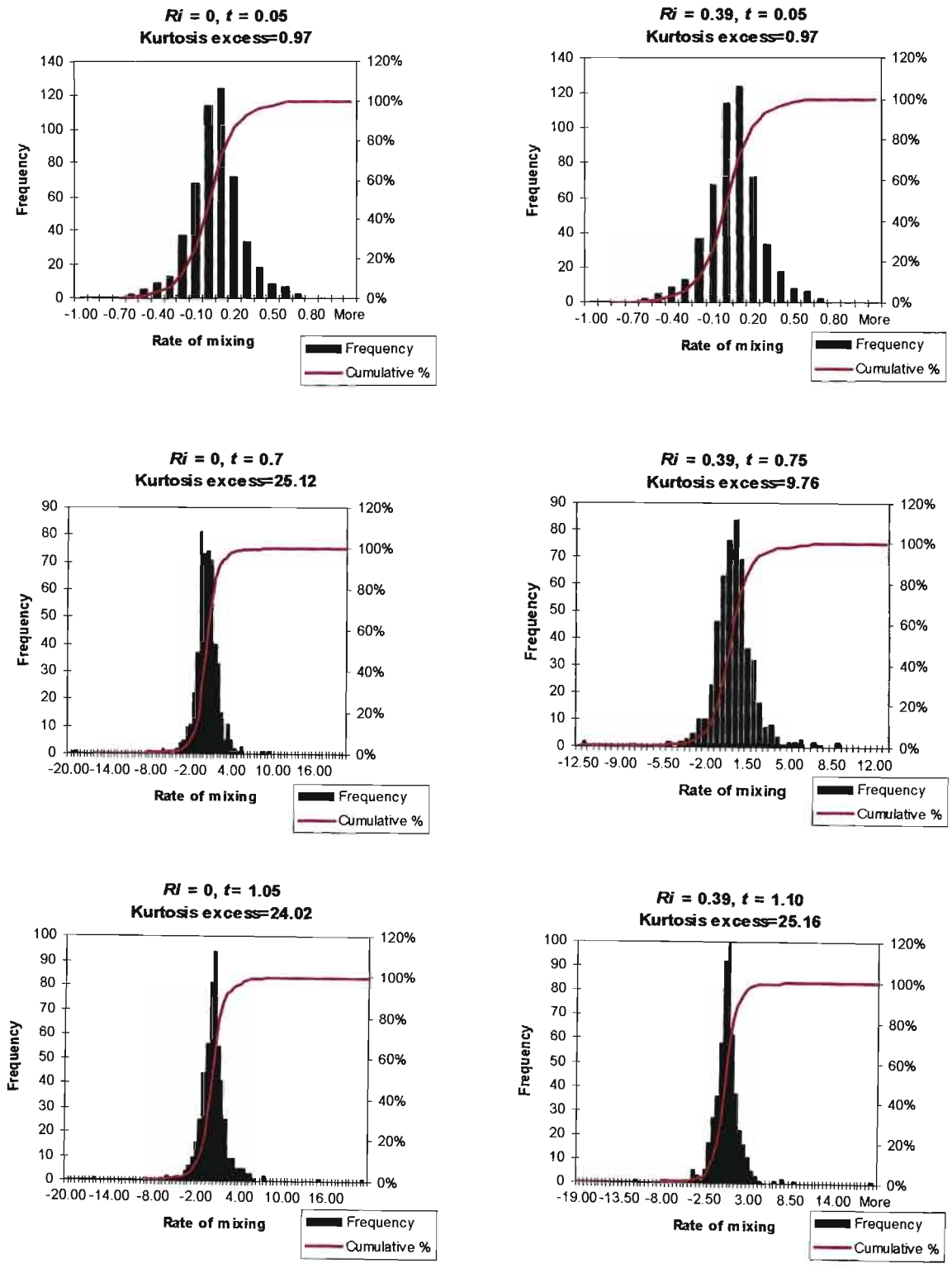

Figure 4.10a: Probability distribution of the rate of mixing $\kappa\nabla^2\rho'(t)$ for Ri = 0 & 0.39

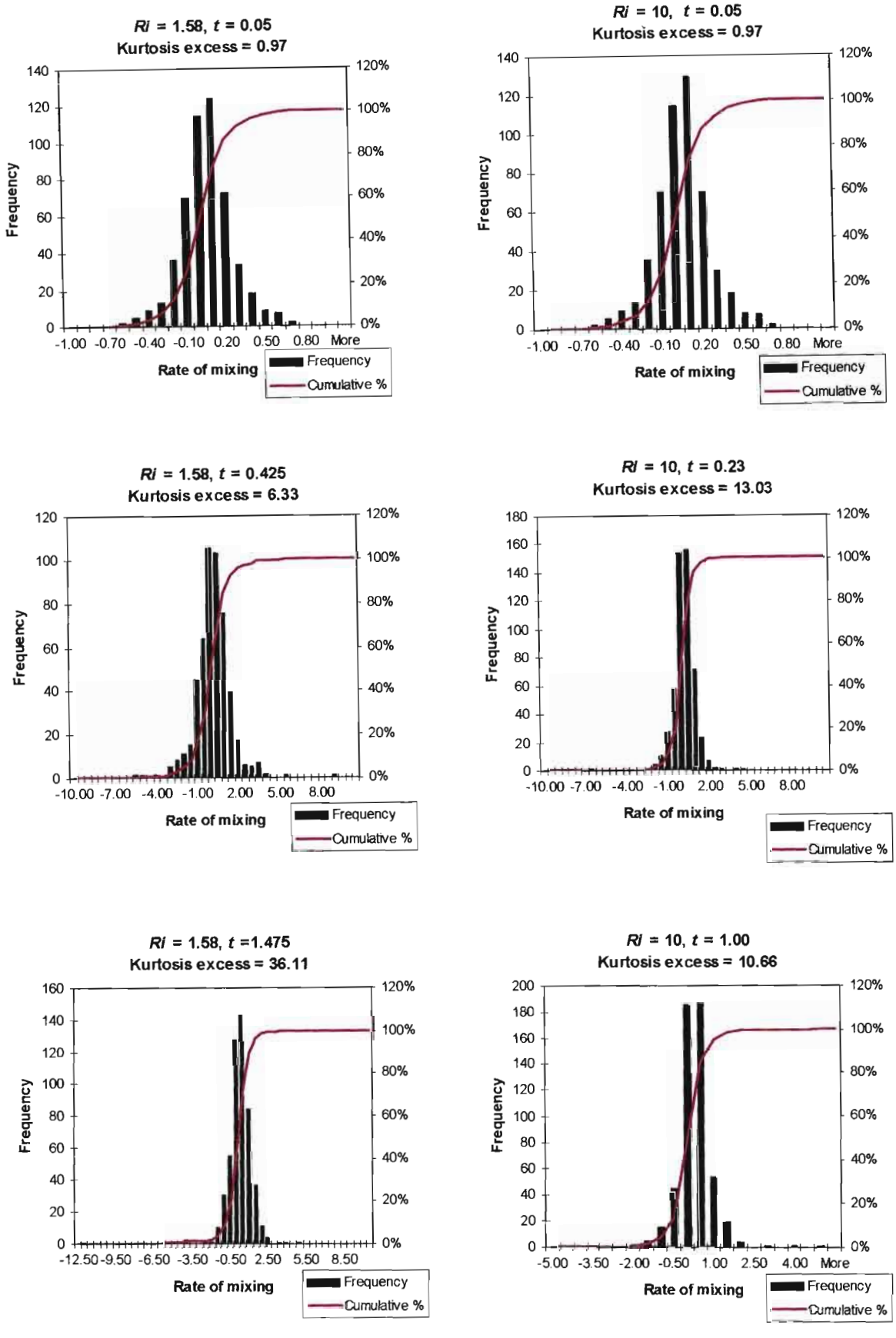

Figure 4.10b: Probability distribution of the rate of mixing $\kappa\nabla^2\rho'(t)$ for Ri = 1.58 & 10.

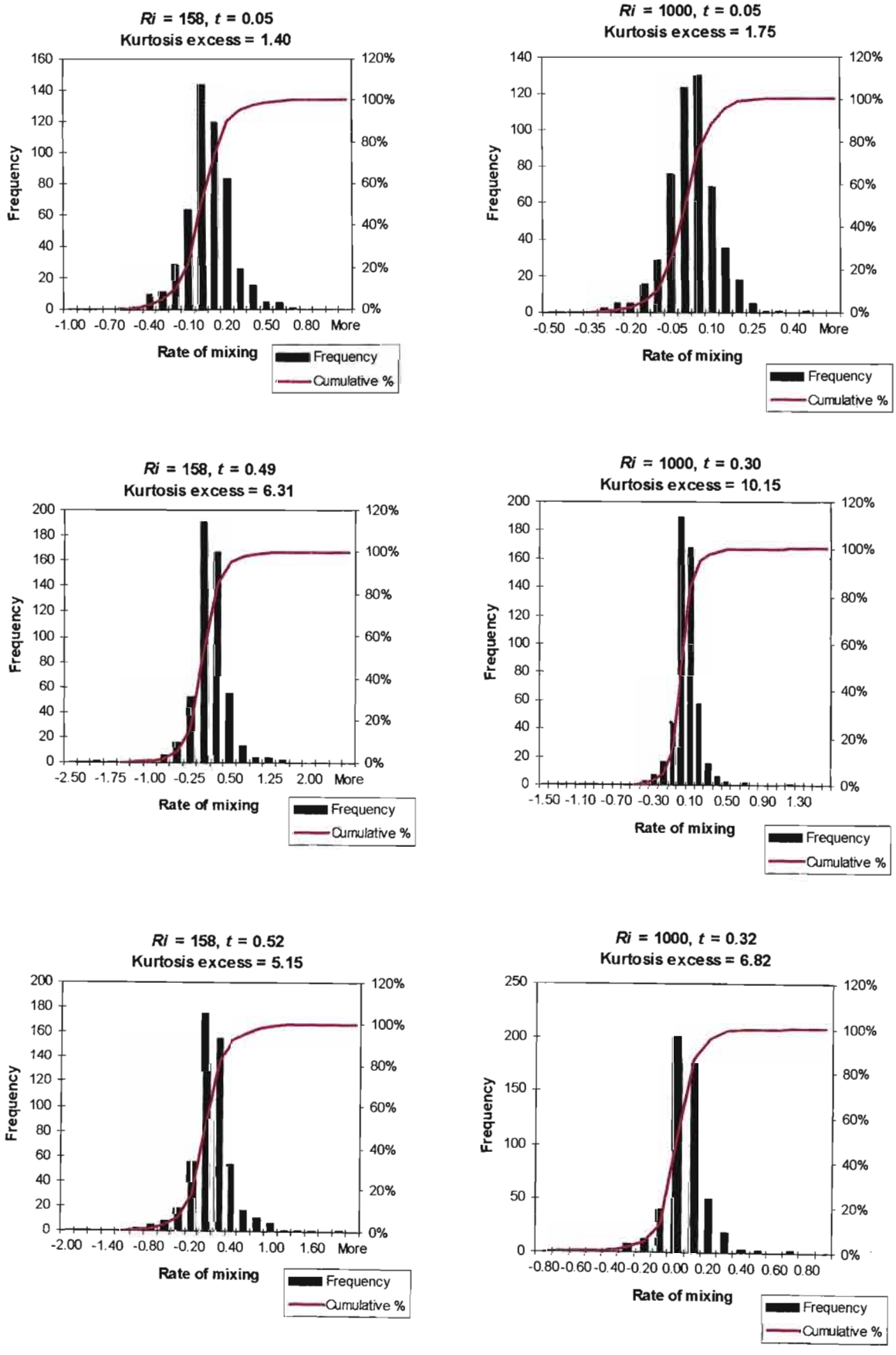

Figure 4.10c: Probability distribution of the rate of mixing $\kappa\nabla^2\rho'(t)$ for Ri = 158 & 1000.

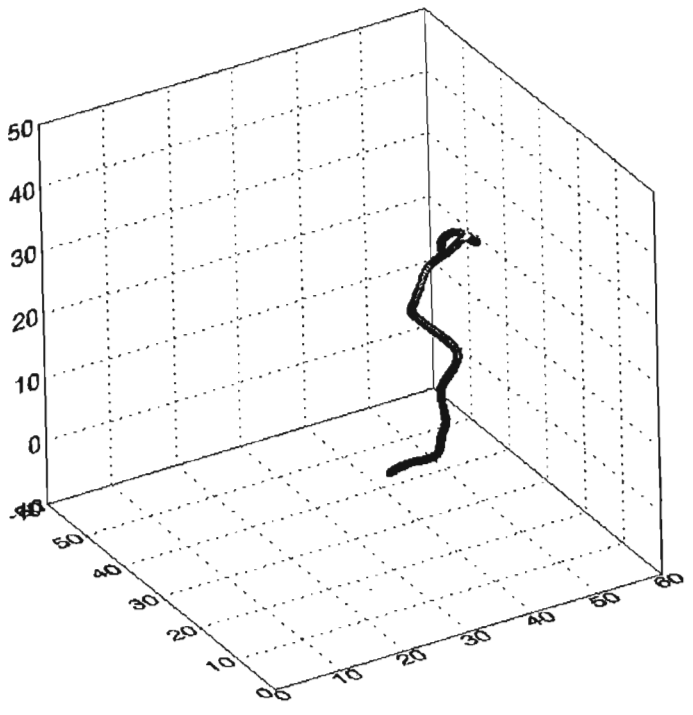

(a) Particle released at (42, 26, 34), Ri = 0, $\max . \kappa \nabla^2 \rho'(t) = -19.5$ *at t = 0.70*

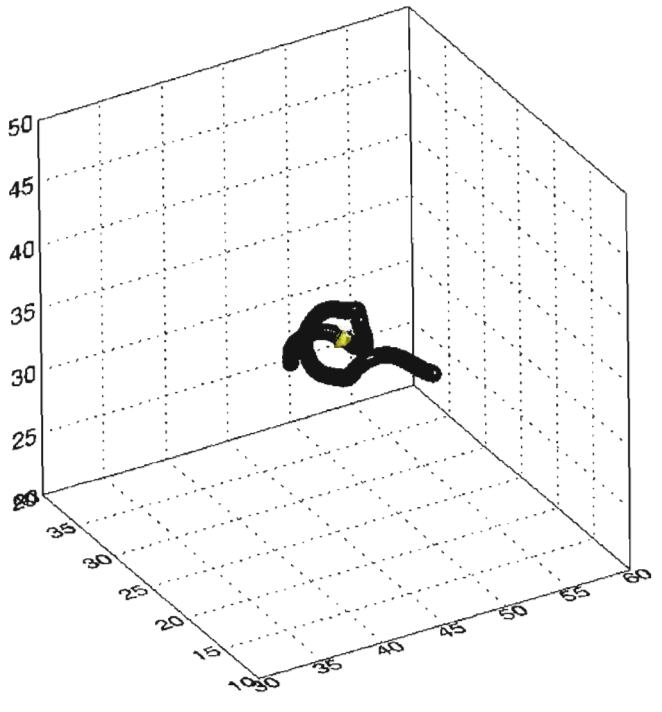

(b) Particle released at (42, 26, 34), Ri = 0.39, $\max . \kappa \nabla^2 \rho'(t) = -16.7$ *at t = 0.725*

Figures 4.11: Mixing rate of fluid particles using particle tracking in DNS for unstratified flow and low stratification. The regions marked in yellow indicate high mixing rates, (a) Ri = 0, (b) Ri = 0.39

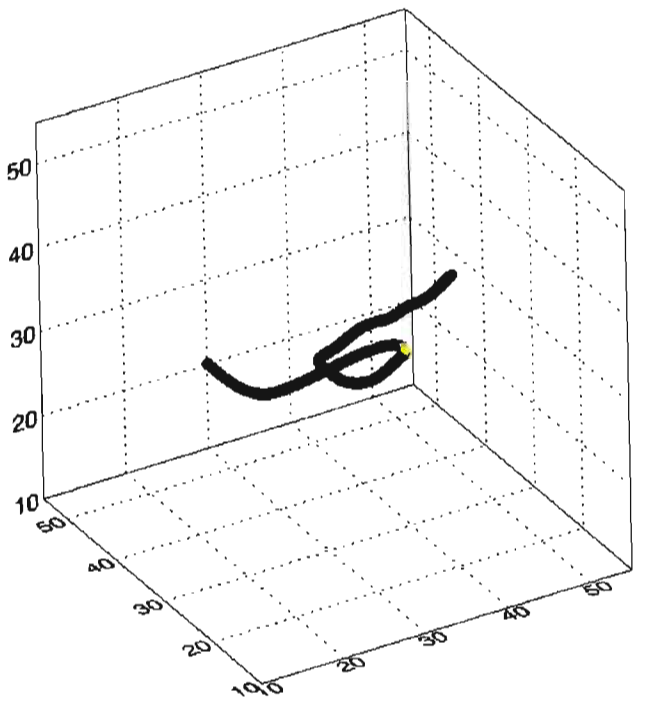

(c) Particle released at (18, 34, 34), Ri = 1.58, $\max.\kappa\nabla^2\rho'(t) = -12.32$ *at t = 1.475*

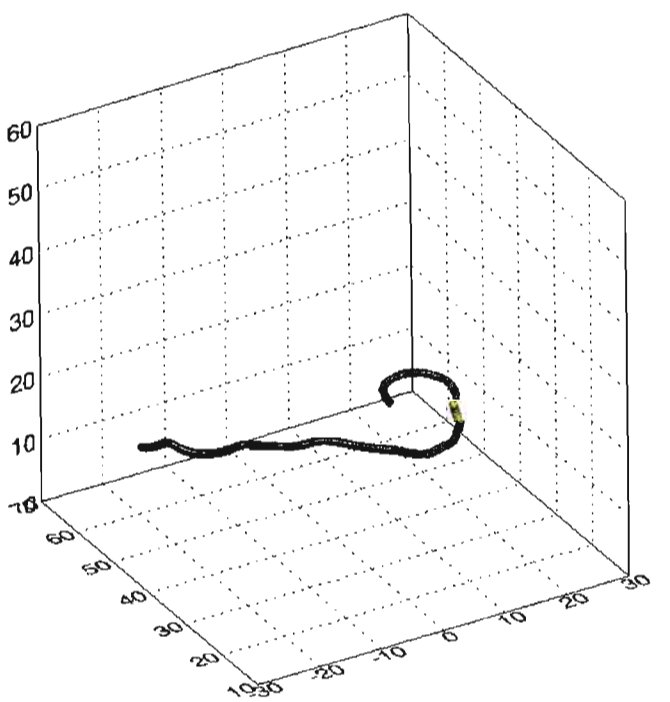

(d) Particle released at (10, 42, 18), Ri = 10, $\max.\kappa\nabla^2\rho'(t) = +4.83$ *at t = 1.0*

Figures 4.11: Mixing rate of fluid particles using particle tracking in DNS at intermediate to large Ri. The regions marked in yellow indicate high mixing rates, (c) Ri = 1.58, (d) Ri = 10

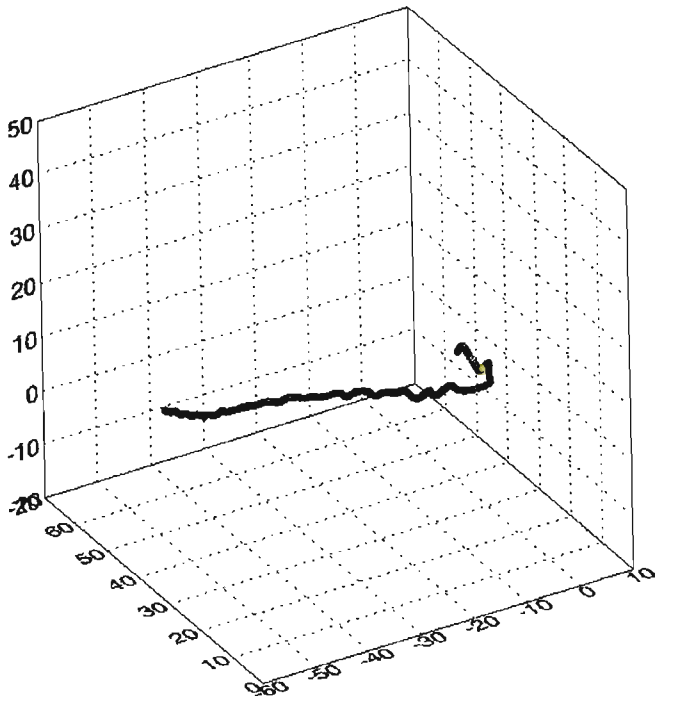

(e) Particle released at (2, 42, 2), Ri = 158, $\max . \kappa \nabla^2 \rho'(t) = +1.89$ *at t = 0.52*

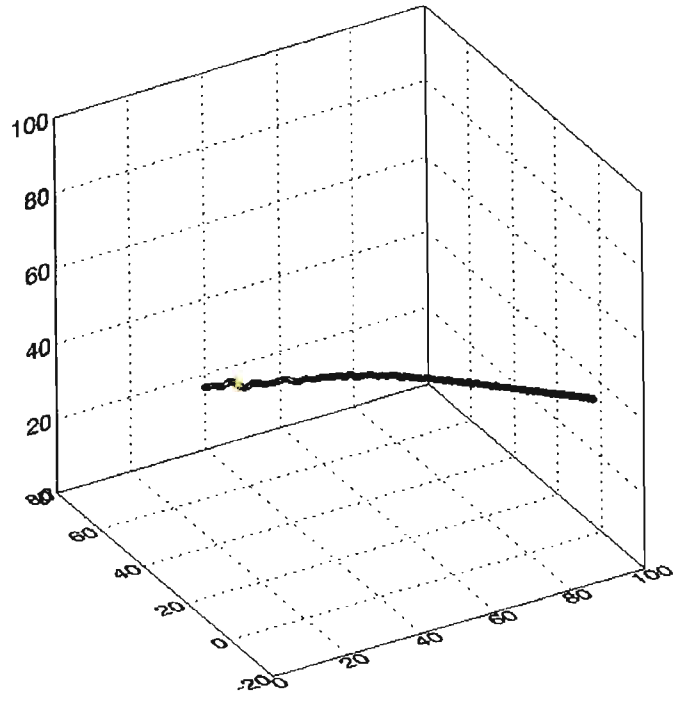

(f) Particle released at (18, 42, 42), Ri = 1000, $\max . \kappa \nabla^2 \rho'(t) = +1.12$ *at t =0.3*

Figures 4.11: Mixing rate of fluid particles using particle tracking in DNS at high Ri. The regions marked in yellow indicate high mixing rates. Note how the motion is restricted to a horizontal plane with small vertical oscillations, (e) Ri = 158, (f) Ri = 1000.

4.7.4 Correlations of Rate of Mixing with Density Perturbations

The PPH theory takes into account the small scale mixing in predicting the long time behaviour of the mean square vertical displacements. The mixing factor γ as indicated in section 2.6.1, is related to the rate of mixing $\kappa\nabla^2\rho'$ by equation (2.25) and given again in equation (4.15). Their model suggests that the mixing rate should be correlated with the density perturbations, ρ'.

$$\kappa\nabla^2\rho' = -\gamma N\rho' \tag{4.15}$$

The correlation coefficient between the mixing rate and ρ' was calculated for the ensemble of 512 particles at different times for all the *Ri* cases. The plots of the correlation coefficient with time for the different *Ri* flows are presented in figure 4.12. It is clear from this data that the rate of mixing and the density fluctuation are not strongly related, with correlation coefficients mostly in the range of 0.1 – 0.3. It can be noticed that the value of the correlation coefficient has an oscillatory behaviour with time for the most stable cases (see figure 4.15). This seems to be related to the wave-like character of the vertical dynamics in these strongly stable cases. Note however that the rates of mixing at these later times are negligibly small.

Scatter plots of mixing rate versus density fluctuations (normalized by their root mean square values) are shown at selected times (including times with highest mixing events) in figures 4.13a to 4.13 e for *Ri* = 0.39, 1.58, 10, 158 and 1000. Theoretically (based on the PPH model) the gradient of the straight line through this set of data points should be equal to the mixing factor γ multiplied by *N*. Best-fit lines were calculated for the data sets using the least squares method of linear regression. The mixing factor γ was calculated from the best-fit lines. The coefficient of determination R^2 is an indicator of how well the equation resulting from the regression analysis explains the relationship between the variables. The R^2 for the best-fit lines were calculated and shown in the scatter plots. It is clear that the regression equations obtained are not helpful in predicting the rate of mixing using ρ'.

There are no definitive patterns that can be identified from these plots to suggest a dependence of the rate of mixing on the density fluctuations as described by (4.15). It appears therefore that the PPH model is inadequate to describe the instantaneous small scale mixing in stably stratified turbulence.

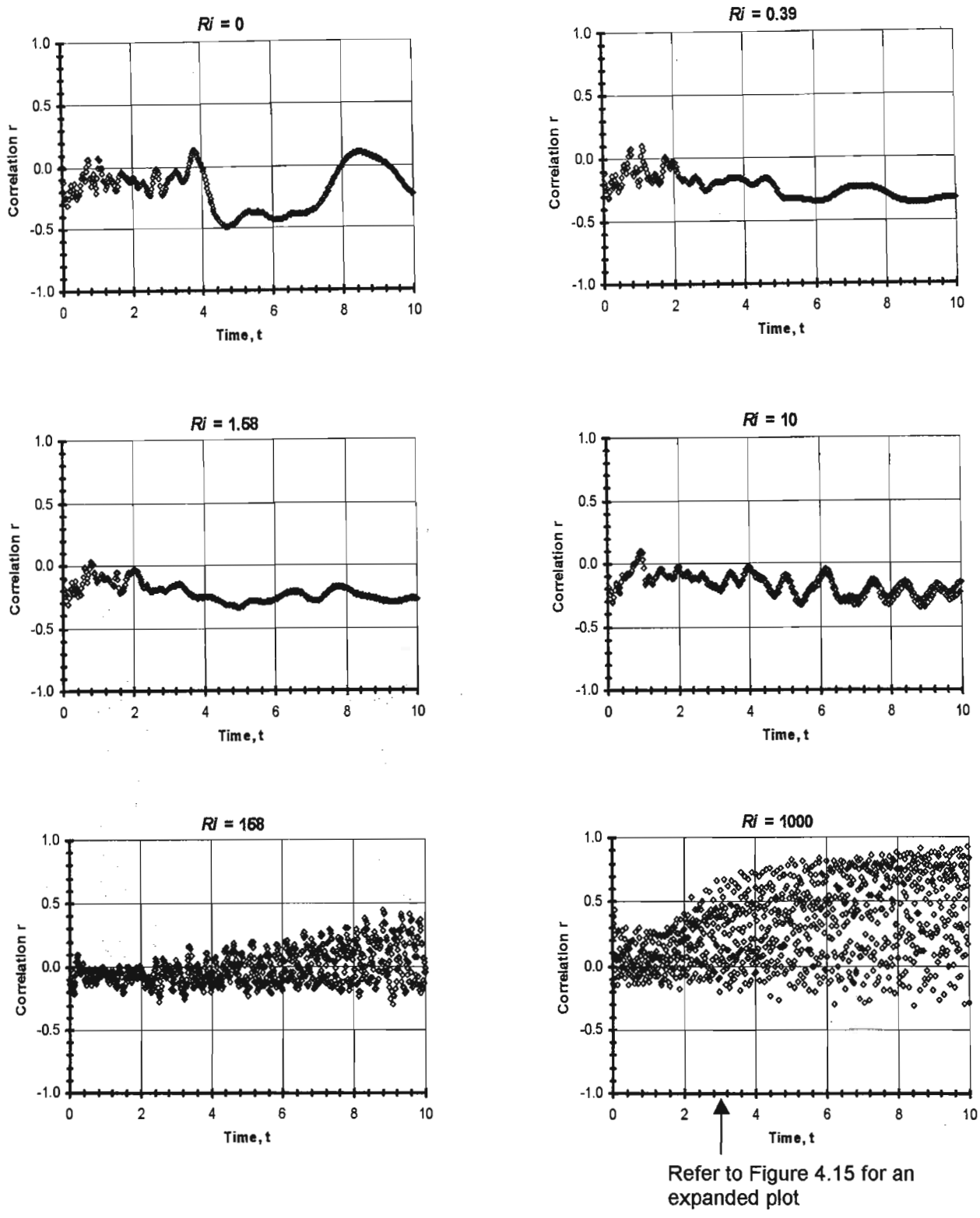

Figure 4.12: The correlation coefficient between the rate of mixing $\kappa\nabla^2\rho'(t)$ and $\rho'(t)$ versus time for Ri = 0, 0.39, 1.58, 10, 158 & 1000.

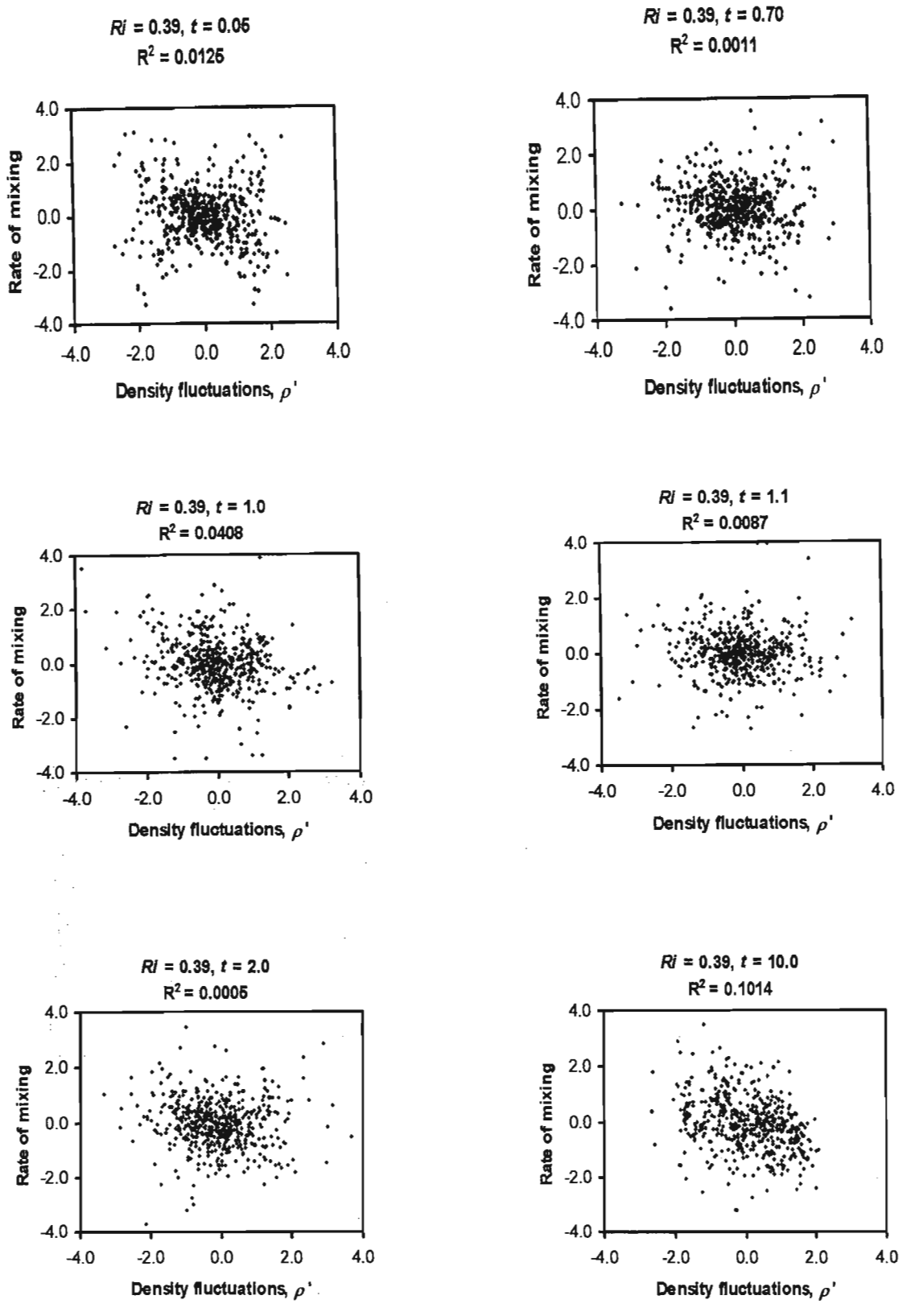

Figure 4.13a: Normalized scatter plots of the rate of mixing versus density fluctuations ρ' at t = 0.05, 0.7, 1.0, 1.1, 2.0 & 10.0 for Ri = 0.39. The coefficient of determination R^2 is indicated at the top of each plot. Fluctuations are normalized by their root mean square values.

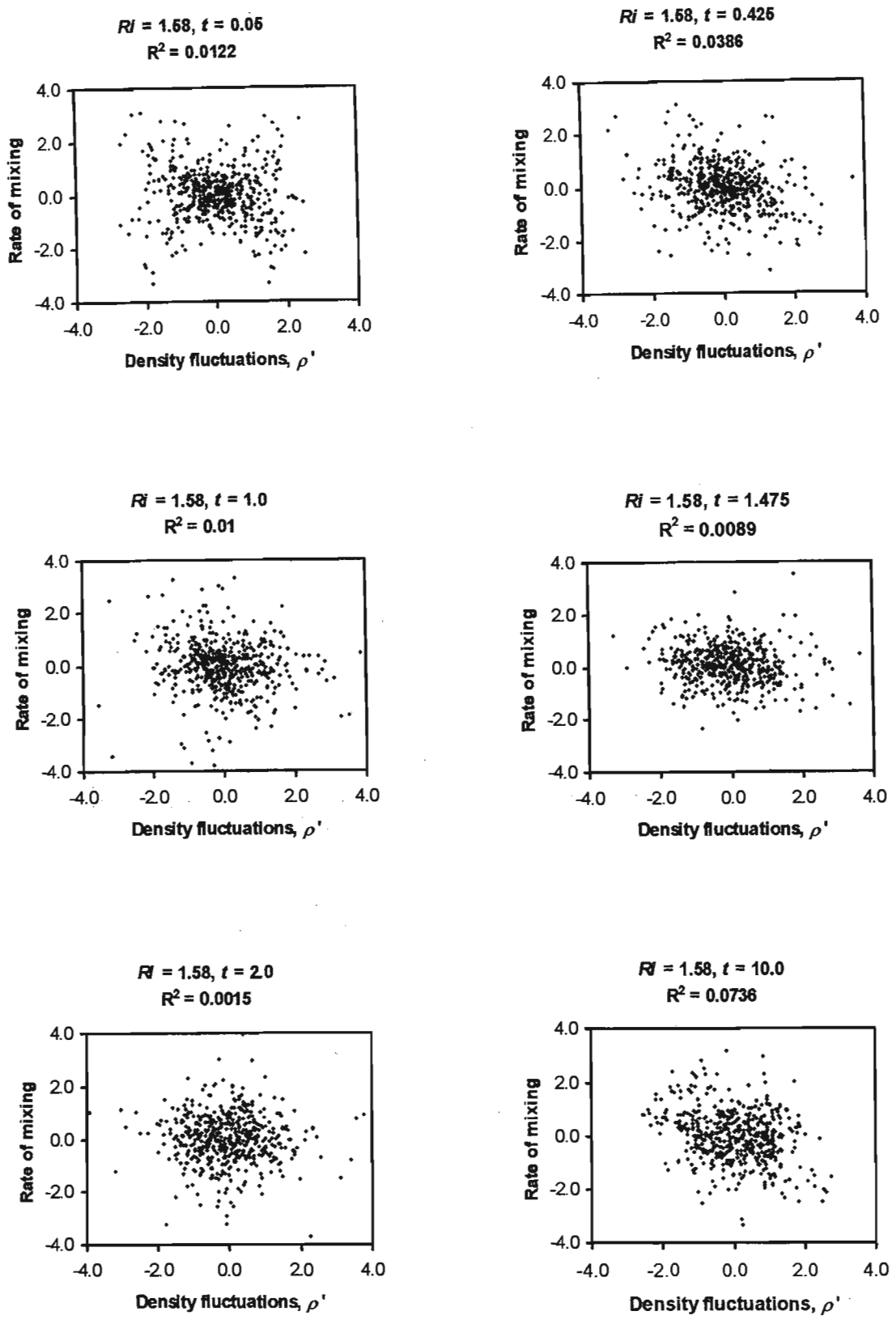

Figure 4.13b: Normalized scatter plots of the rate of mixing versus density fluctuations ρ' at t = 0.05, 0.42, 1.0, 1.475, 2.0 & 10.0 for Ri = 1.58. The coefficient of determination R^2 is indicated at the top of each plot. Fluctuations are normalized by their root mean square values.

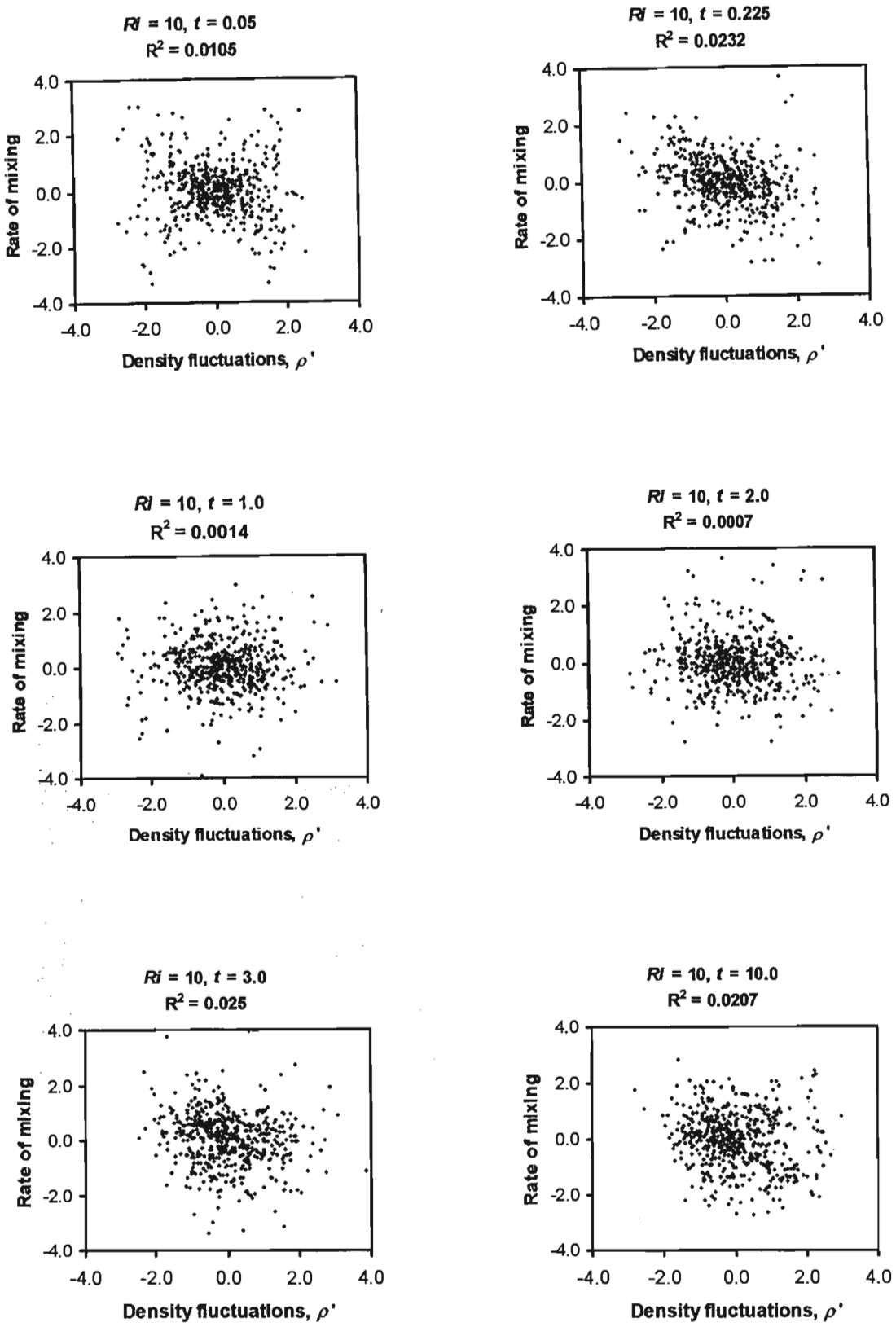

Figure 4.13c: Normalized scatter plots of the rate of mixing versus density fluctuations ρ' at t = 0.05, 0.225, 1.0, 2.0, 3.0 & 10.0 for Ri = 10. The coefficient of determination R^2 is indicated at the top of each plot. Fluctuations are normalized by their root mean square values.

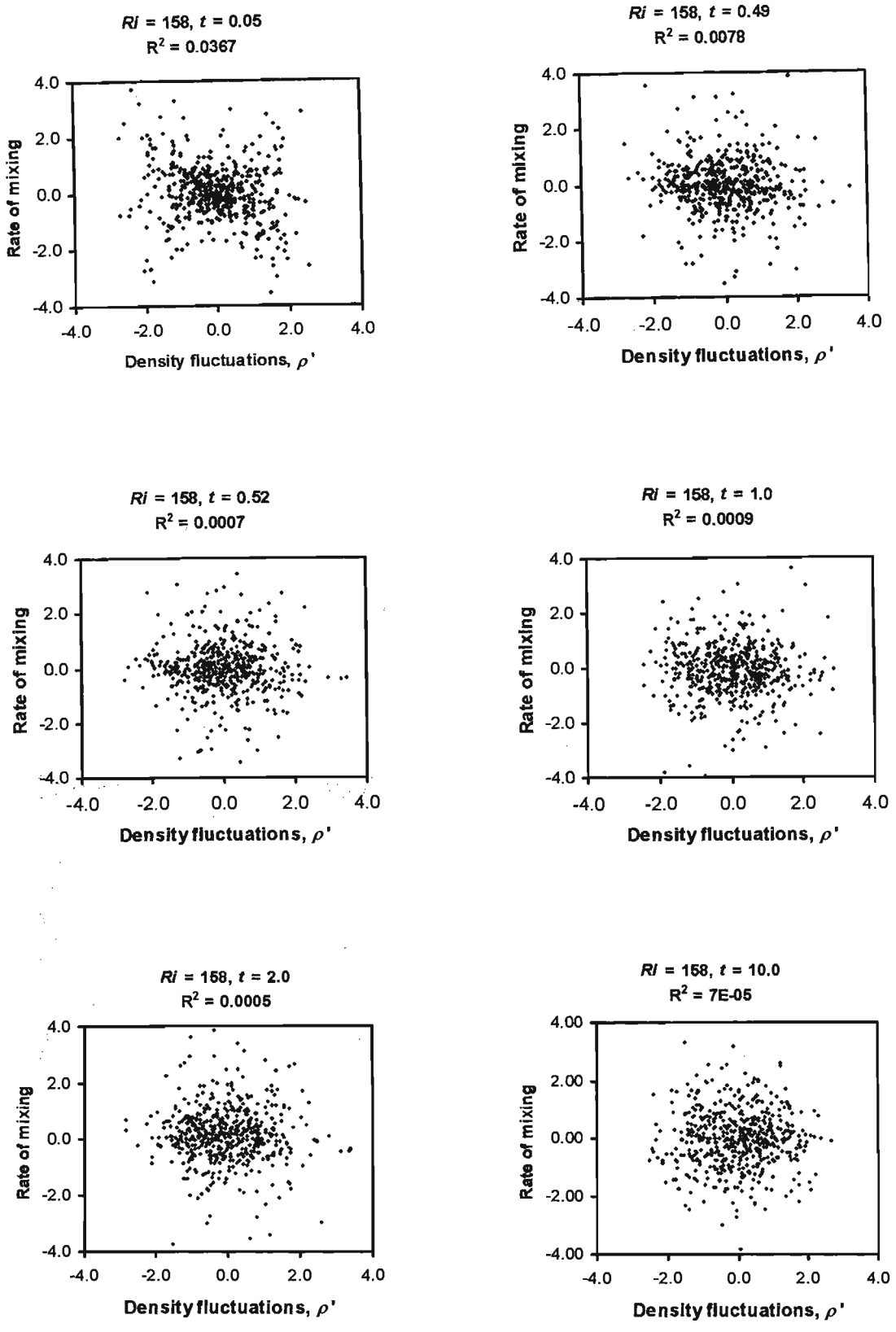

Figure 4.13d: Normalized scatter plots of the rate of mixing versus density fluctuations ρ' at t = 0.05, 0.49, 0.52, 1.0, 2.0 & 10.0 for Ri = 158. The coefficient of determination R^2 is indicated at the top of each plot. Fluctuations are normalized by their root mean square values.

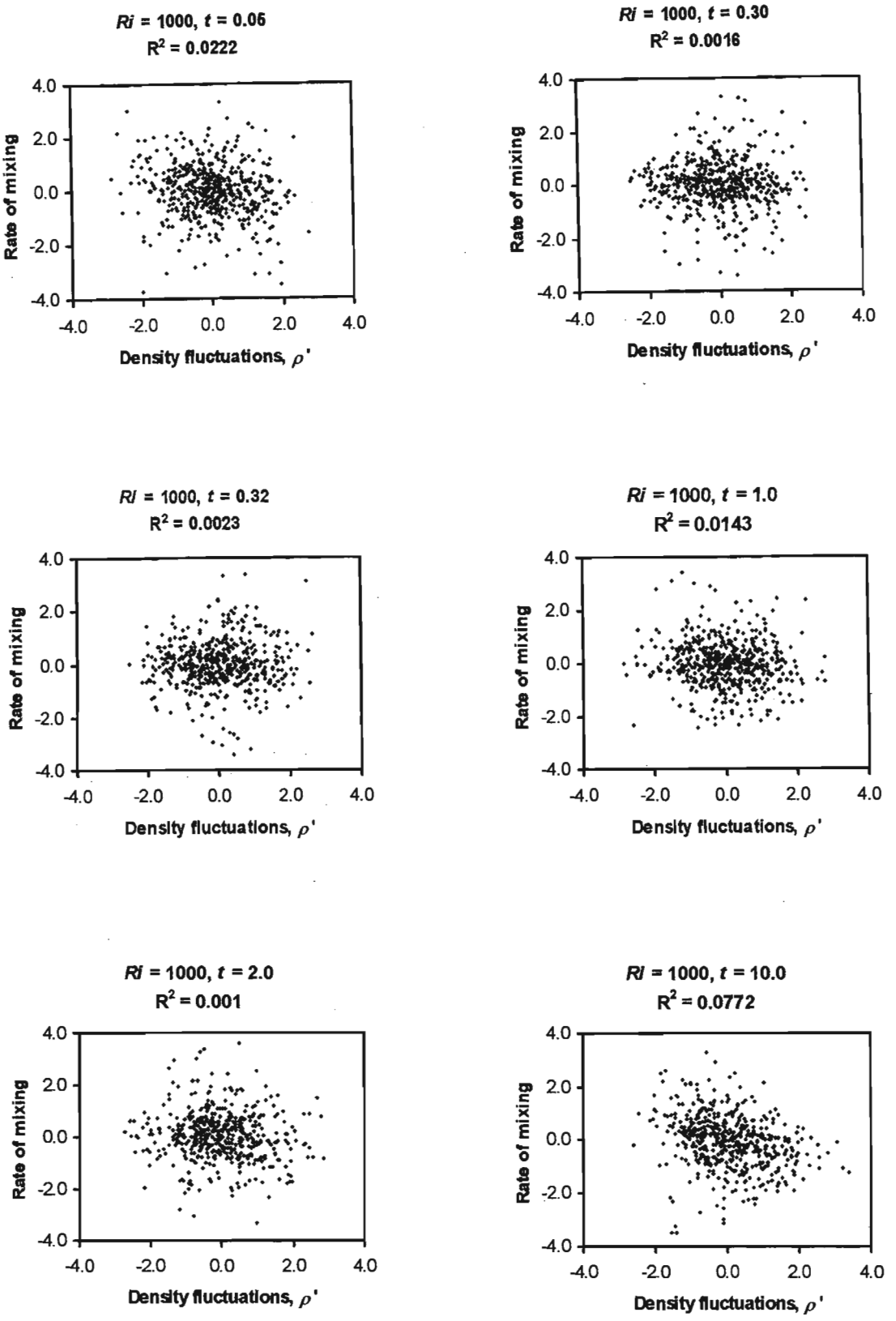

Figure 4.13e: Normalized scatter plots of the rate of mixing versus density fluctuations ρ' at t = 0.05, 0.30, 0.32, 1.0, 2.0 & 10.0 for Ri = 1000. The coefficient of determination R^2 is indicated at the top of each plot. Fluctuations are normalized by their root mean square values.

4.7.5 Correlation of Rate of Mixing with Other Flow Parameters

Correlations between the rate of mixing with the vertical velocity w and the magnitude of the acceleration, $(\dot{u}+\dot{v}+\dot{w})^{1/2}$, were investigated. Figures 4.14 shows plots of correlation coefficient versus time between the rate of mixing and the vertical velocity for the different *Ri* cases. It appears that the rate of mixing is weakly correlated with the vertical velocity, with correlation coefficients mostly in the range of 0 – 0.4. In the strongly stable case (*Ri* =1000), the correlation coefficient oscillates between positive and negative values periodically and increases in magnitude at later times as shown in figure in 4.15. Figure 4.16 shows the correlation between the rates of mixing with the magnitude of the acceleration. The correlation coefficients are relatively small averaging on zero. The oscillatory behaviour is again evident in the strongly stable flows.

4.7.6 Time Series Plots of Particle Statistics

The time series showing the evolution of the rate of mixing, density fluctuations, vertical velocity and the magnitude of the acceleration were plotted for the particles with the highest rate of mixing magnitudes. These series are shown in figures 4.17a to 4.17c. The temporal intermittency of these high amplitude events is evident in these plots. At *Ri* >>1, oscillations are evident indicating wave related phenomenon in these flows.

It is clear that the density fluctuations are at their peak values when the rate of mixing is at its highest value. It is evident from these plots that the rate of change in the density fluctuations at these high amplitude events is mainly from the molecular mixing. However, there are no overall consistencies in the trends, this indicates poor correlations even for these high mixing events. The magnitude of the acceleration also peaks at the high mixing values. Further investigation of the relationship between mixing rate and other flow parameters was beyond the scope of this study.

Figures 4.18a and 4.18b show the absolute values of the rate of mixing versus time for particles with the high mixing events. The total change in density as a percentage is superimposed on the plots. It can be noticed that the contributions of these high intensity, short duration mixing events constitute a significant proportion of the total change in density in the particle's history (at least 70% in most cases). This suggests that these high intensity, short duration mixing events constitute the bulk of the mixing

that occurs in these flows. Since this is a very limited (and biased) sample, further statistical analysis would be required to be conclusive of this observation.

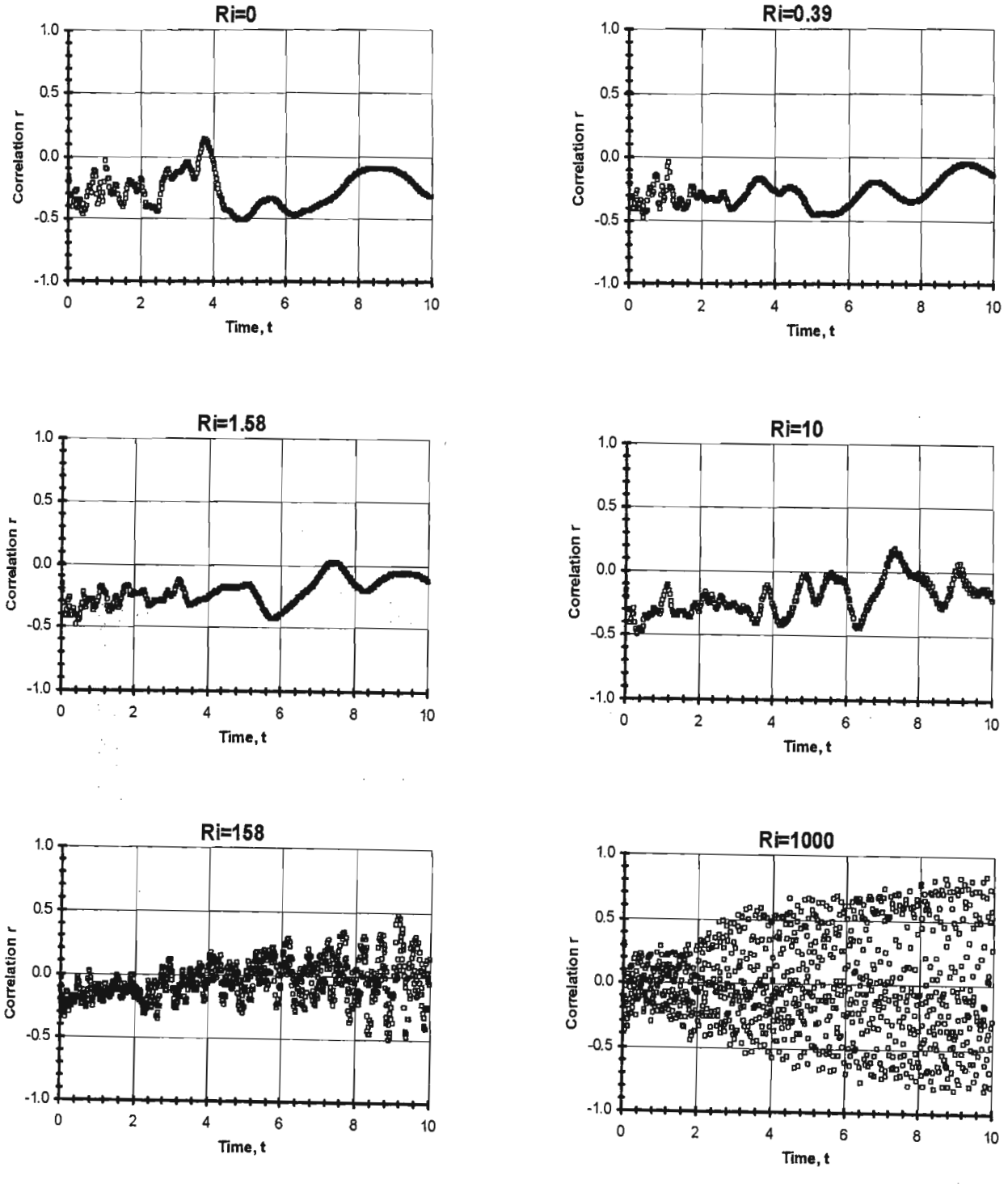

Figure 4.14: The correlation coefficient between the rate of mixing $\kappa\nabla^2\rho'(t)$ and vertical velocity w(t) versus time for Ri = 0, 0.39, 1.58, 10, 158 & 1000.

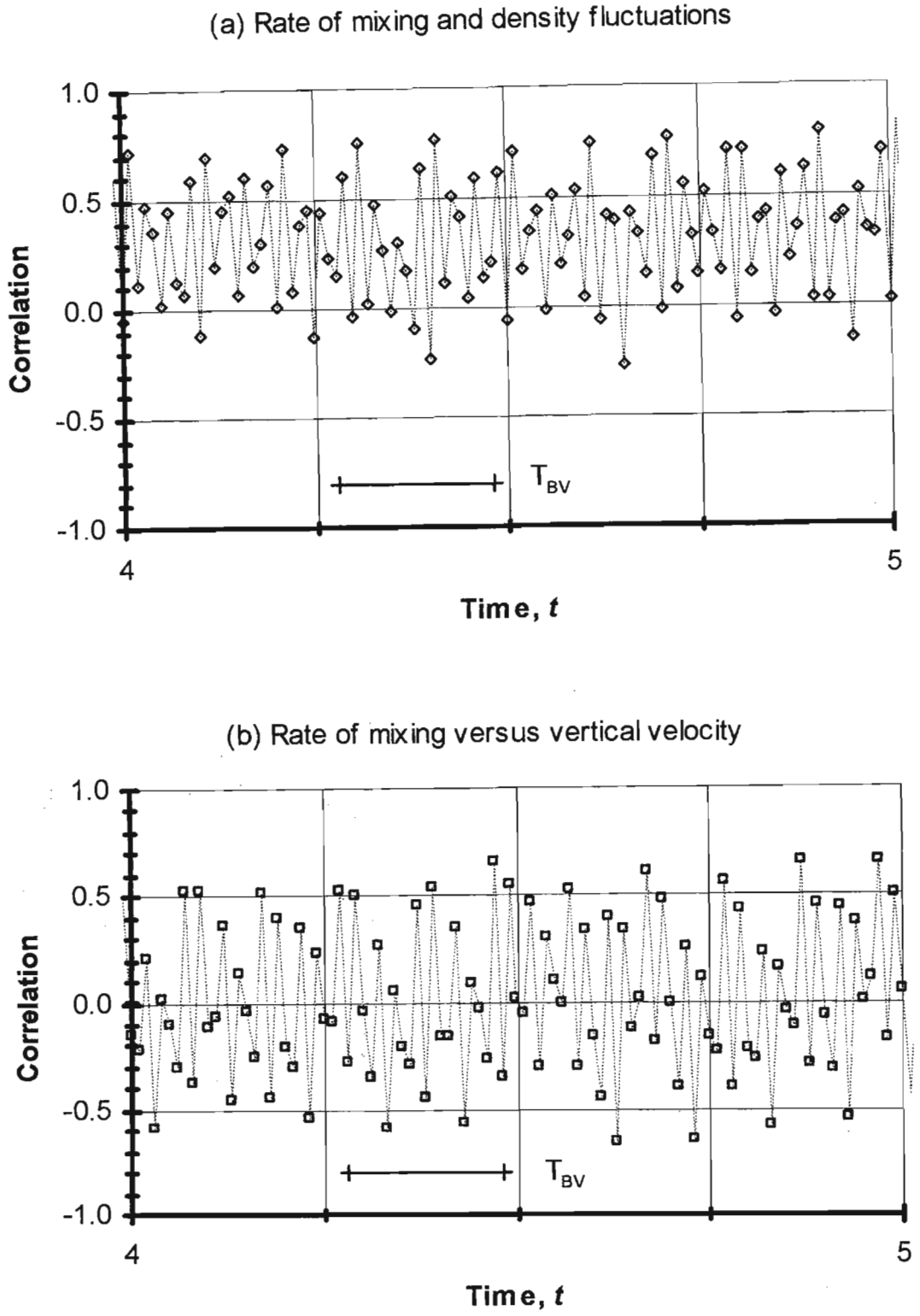

Figure 4.15: The correlation coefficient between the rate of mixing $\kappa\nabla^2\rho'(t)$ and (a) $\rho'(t)$ and (b) vertical velocity w(t) versus time for Ri = 1000. Note how the correlation coefficient oscillates between successive points in time. The magnitude of the buoyancy period is indicated on the plots.

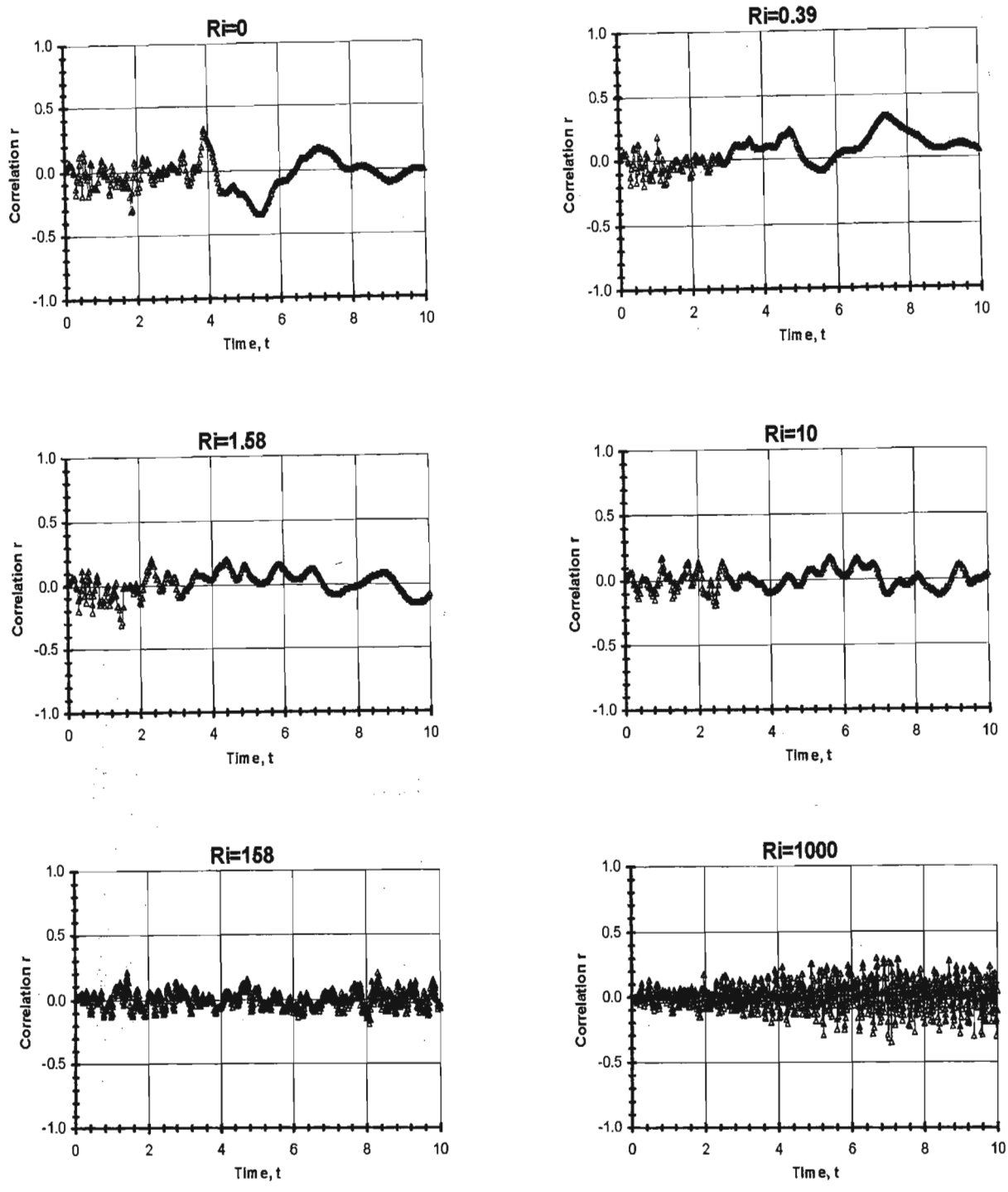

Figure 4.16: The correlation coefficient between the rate of mixing $\kappa\nabla^2\rho'(t)$ and magnitude of acceleration, versus time for Ri = 0, 0.39, 1.58, 10, 158 & 1000.

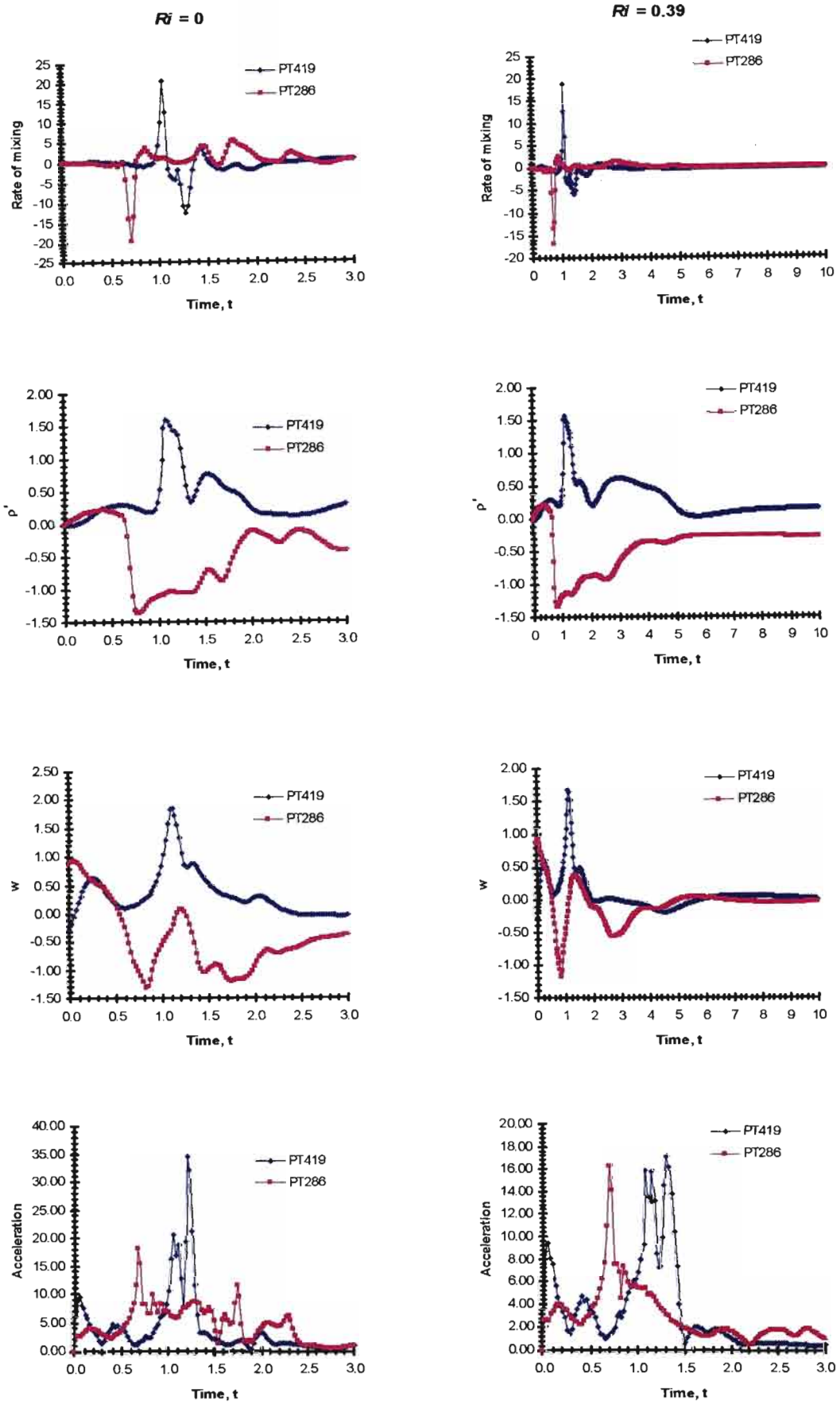

Figure 4.17a: Times series of rate of mixing, density fluctuation ρ', vertical velocity w and magnitude of acceleration for particles with highest rate of mixing at Ri = 0 & 0.39.

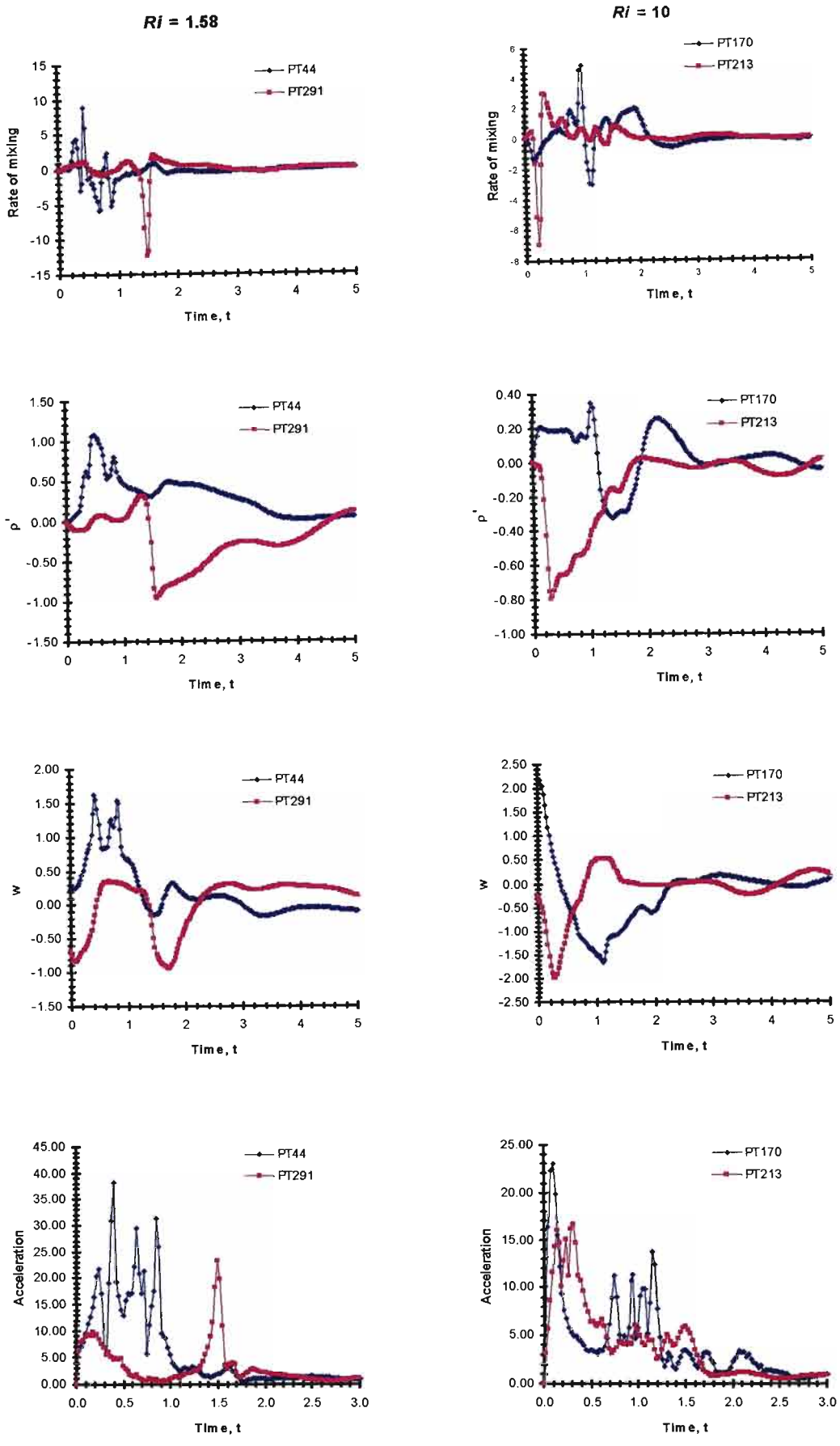

Figure 4.17b: Times series of rate of mixing, density fluctuation ρ', vertical velocity w and magnitude of acceleration for particles with highest rate of mixing at Ri = 1.58 & 10.

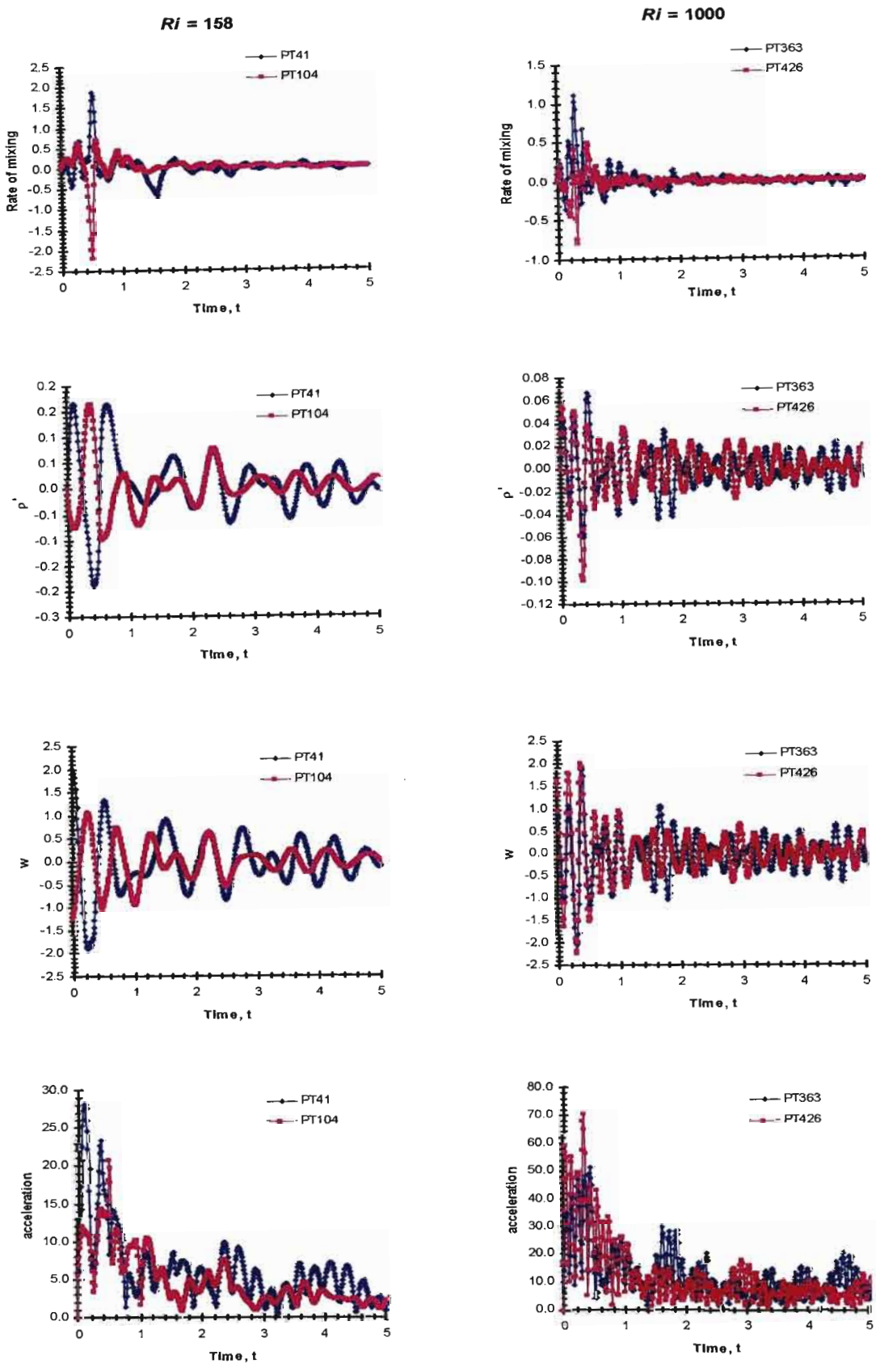

Figure 4.17c: Times series of rate of mixing, density fluctuation ρ', vertical velocity w and magnitude of acceleration for particles with highest rate of mixing at Ri = 158 & 1000.

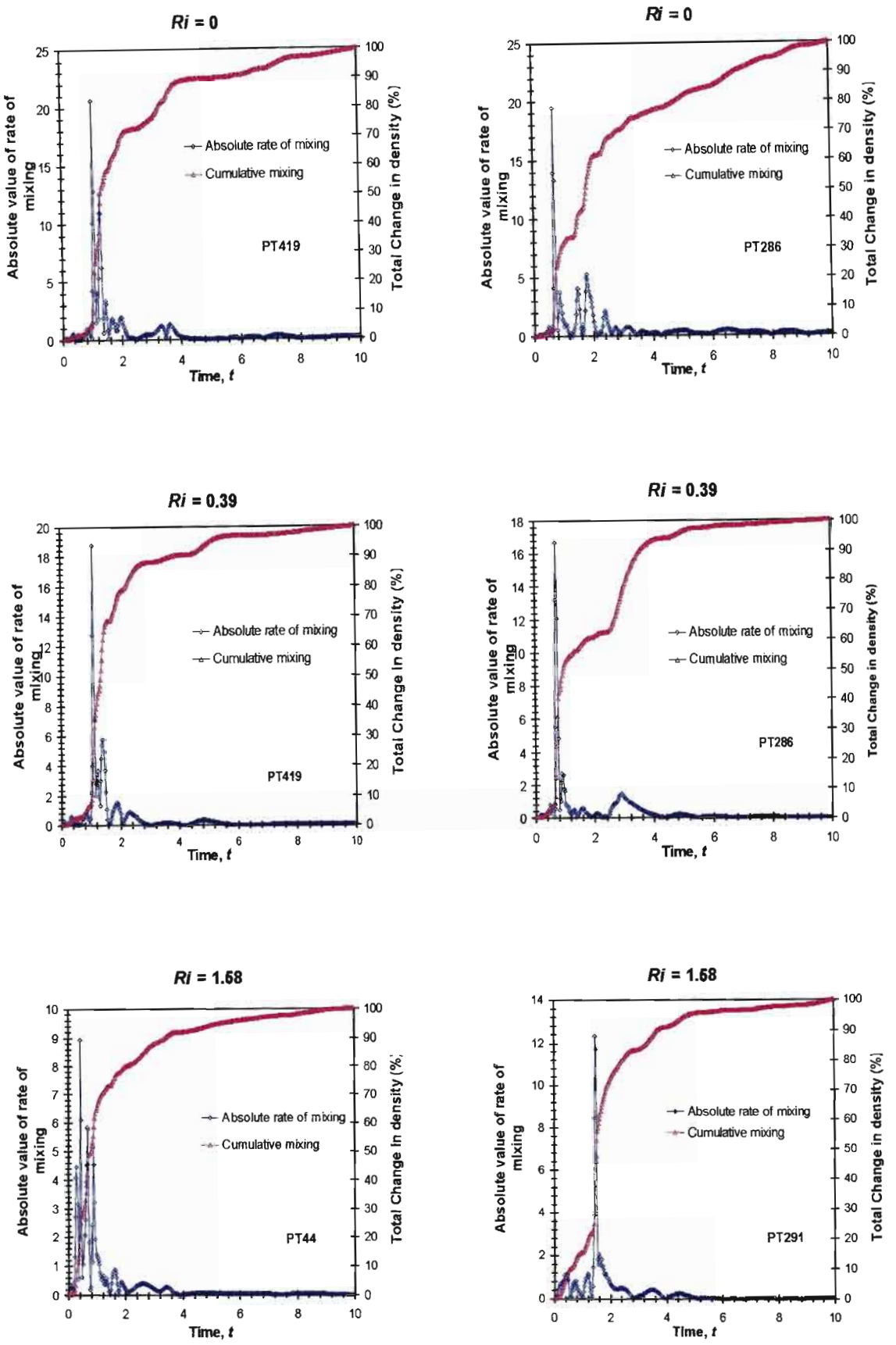

Figure 4.18a: Absolute values of rate of mixing versus time for Ri = 0, 0.39 & 1.58. Note the total change in density is superimposed on the plots.

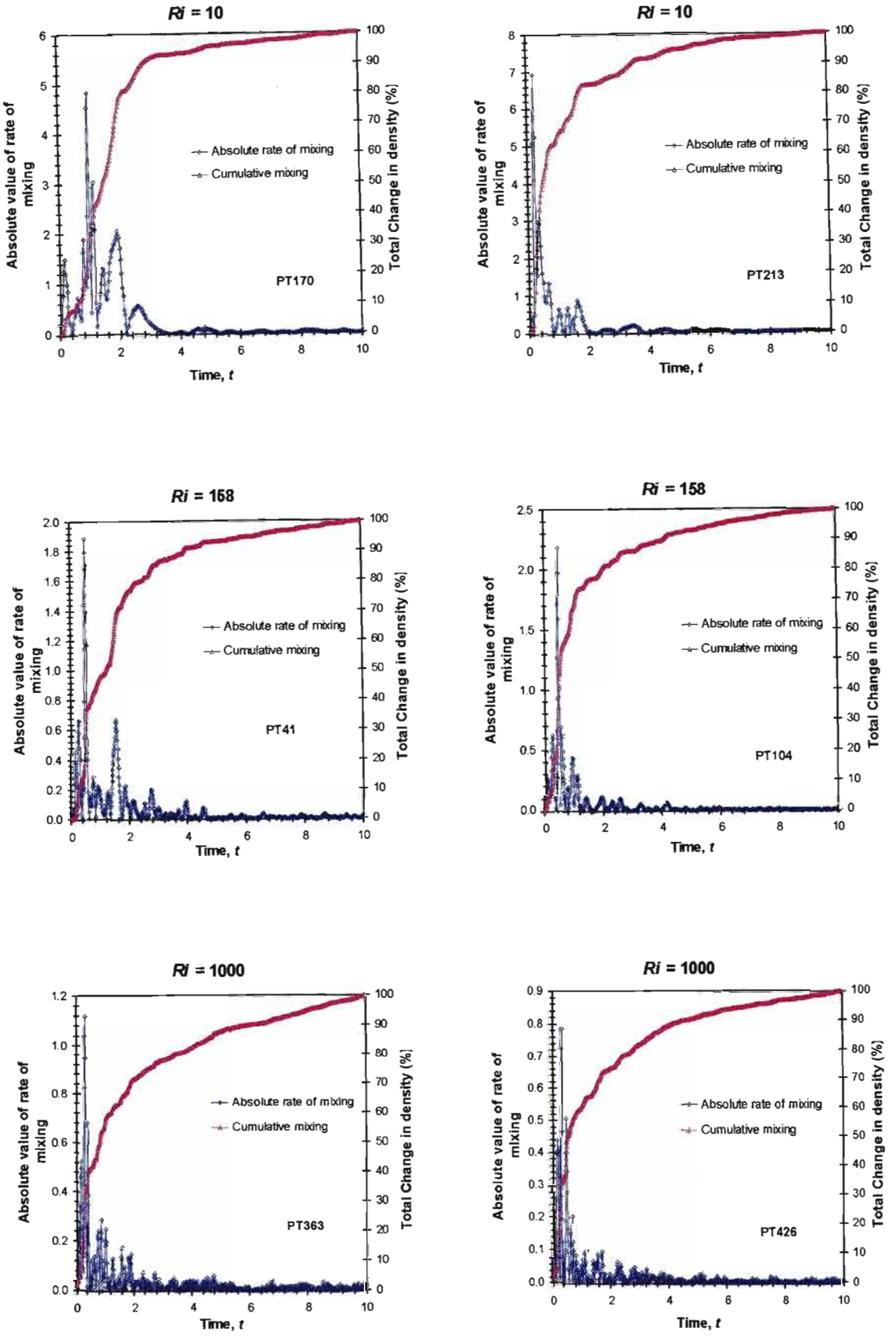

Figure 4.18b: Absolute values of rate of mixing versus time for Ri = 10, 158 & 1000. Note the total change in density is superimposed on the plots.

4.8 Summary

This chapter has presented the study of mixing in stably stratified decaying turbulence within a Lagrangian framework using particle tracking. Two important insights have emerged from this study. Firstly we have made the important link that the asymptotic value of the mean square vertical displacement gives a measure of the total irreversible mixing that has taken place in the flow. Hence the mixing efficiency could be calculated from the displacement statistics. Secondly, we find that the PPH model for describing small scale mixing is inadequate. The development of new models or modifications to the PPH model for mixing is beyond the scope of this study and might be addressed as part of further work on mixing in stably stratified turbulence.

The next chapter discusses the flow structures associated with stably stratified turbulent flows. Flow visualization software is used to study the flow fields and gain insights into possible relationships that might exist between the properties of mixing and diffusion with the structure of the flow.

CHAPTER 5

FLOW STRUCTURES IN STABLY STRATIFIED TURBULENCE

5.1 Introduction

The question of whether there are coherent structures in turbulent flows in general has been and is a very important question. DNS provides a convenient avenue to capture the statistics of the flow fields, which can then be visualized. Kimura and Herring (1996) have shown that strongly stratified turbulence comprises patches of vertical vorticity with regions of intense horizontal vorticity, which accounts for most of the dissipation. Data from DNS studies on decaying isotropic turbulence e.g. Ooi, Martin, Soria & Chong (1999) have revealed tube-like vortex structures ("worms"). In this chapter, flow fields are visualized using volumetric data visualization software ("Slicer Dicer" by Visualogic). This chapter comprises a three-fold investigation. Firstly the Eulerian fields at different times for varying stratifications are analysed to understand the flow structures associated with them from a general perspective. Secondly, the flow fields of the very high mixing events discussed in sections 4.7.3 & 4.7.6 are visualized to identify key features in the structure to explain these high mixing events. Finally, flow structures of very strongly stable flow fields obtained from RDT simulations are compared with their respective counterparts from DNS.

5.2 Flow Structures from DNS Fields

The following fields were written and saved from simulations for Ri = 0, 0.39, 1.58, 10, 158 and 1000 for visualization purposes:

- Enstrophy (mean squared vorticity)
- Horizontal vorticity (magnitudes of the horizontal components)
- Vertical vorticity
- Density
- Vertical density gradient
- u component of velocity
- v component of velocity
- w component of velocity

Only a few snap shots in time of these fields were archived due to memory restrictions. Basically fields at whole numbers of time non-dimensionalized by the L_0/u_0 timescale were saved.

The statistics as obtained from the results' files for the DNS are given in tables 5.1 to 5.6. Information presented in these tables include:

- Mean square velocities $\overline{u^2}, \overline{v^2}, \overline{w^2}$ respectively
- Standard deviation of velocity fluctuations $\sigma_{\bar{u}} = \sqrt{\overline{u^2}}$, $\sigma_{\bar{v}} = \sqrt{\overline{v^2}}$, $\sigma_{\bar{w}} = \sqrt{\overline{w^2}}$
- Mean square density fluctuations $\overline{\rho^2}$
- Standard deviation of the density fluctuations $\sigma_{\bar{\rho}} = \sqrt{\overline{\rho^2}}$
- Normalized mean square vorticity $\left| \overline{\omega^2} \right|$
- Enstrophy (average of the square of vorticity) $\overline{\omega^2}$
- Magnitude of horizontal vorticity $\left| \overline{\omega_H} \right|$
- Mean square vertical vorticity $\overline{\omega_z^2}$
- Standard deviation of vertical vorticity $\sigma_{\bar{\omega}} = \sqrt{\overline{\omega_z^2}}$

The normalized mean square vorticity is based on the vorticity at time t = 0 where $\overline{\omega^2} = 83.82$. These statistics are used as a basis for determining the threshold values used in generating the 3-D plots.

Table 5.1: Statistics for flow fields for Ri = 0

t	$\overline{u^2}$	$\overline{v^2}$	$\overline{w^2}$	$\sigma_{\bar{u}}$	$\sigma_{\bar{v}}$	$\sigma_{\bar{w}}$	$\overline{\rho^2}$	$\sigma_{\bar{\rho}}$	$\lvert\overline{\omega^2}\rvert$	$\overline{\omega^2}$	$\lvert\overline{\omega_H}\rvert$	$\overline{\omega_z^2}$	$\sigma_{\bar{\omega}}$
0	0.99	1.15	1.02	0.99	1.07	1.01	0.00	0.00	1.00	83.82	7.42	28.71	5.36
1	0.59	0.50	0.60	0.77	0.71	0.77	0.29	0.54	1.70	142.8	9.67	49.24	7.02
2	0.26	0.23	0.28	0.51	0.48	0.52	0.42	0.65	0.68	56.59	6.18	18.36	4.28
3	0.12	0.12	0.14	0.35	0.35	0.37	0.42	0.65	0.29	24.62	4.10	7.81	2.79
4	0.06	0.07	0.08	0.25	0.26	0.28	0.39	0.63	0.13	11.27	2.76	3.67	1.91

Table 5.2: Statistics for flow fields for Ri = 0.39

t	$\overline{u^2}$	$\overline{v^2}$	$\overline{w^2}$	$\sigma_{\bar{u}}$	$\sigma_{\bar{v}}$	$\sigma_{\bar{w}}$	$\overline{\rho^2}$	$\sigma_{\bar{\rho}}$	$\lvert\overline{\omega^2}\rvert$	$\overline{\omega^2}$	$\lvert\overline{\omega_H}\rvert$	$\overline{\omega_z^2}$	$\sigma_{\bar{\omega}}$
0	0.99	1.15	1.02	0.99	1.07	1.01	0.00	0.00	1.00	83.82	7.42	28.71	5.36
1	0.57	0.48	0.51	0.75	0.70	0.71	0.26	0.51	1.59	133.17	9.34	46.02	6.78
2	0.24	0.20	0.16	0.49	0.44	0.41	0.31	0.55	0.53	44.76	5.47	14.80	3.85
3	0.11	0.10	0.06	0.34	0.31	0.24	0.22	0.46	0.19	16.33	3.24	5.80	2.41
4	0.06	0.05	0.04	0.24	0.23	0.20	0.12	0.35	0.08	7.00	2.15	2.39	1.55

Table 5.3: Statistics for flow fields for Ri = 1.58

t	$\overline{u^2}$	$\overline{v^2}$	$\overline{w^2}$	$\sigma_{\bar{u}}$	$\sigma_{\bar{v}}$	$\sigma_{\bar{w}}$	$\overline{\rho^2}$	$\sigma_{\bar{\rho}}$	$\lvert\overline{\omega^2}\rvert$	$\overline{\omega^2}$	$\lvert\overline{\omega_H}\rvert$	$\overline{\omega_z^2}$	$\sigma_{\bar{\omega}}$
0	0.99	1.15	1.02	0.99	1.07	1.01	0.00	0.00	1.00	83.82	7.42	28.71	5.36
1	0.53	0.44	0.33	0.73	0.66	0.57	0.20	0.45	1.34	112.07	8.58	38.52	6.21
2	0.22	0.16	0.12	0.47	0.40	0.34	0.10	0.32	0.39	33.09	4.72	10.83	3.29
3	0.11	0.10	0.08	0.33	0.31	0.28	0.04	0.21	0.14	11.96	2.85	3.82	1.95
4	0.07	0.07	0.03	0.27	0.26	0.17	0.04	0.21	0.06	5.18	1.88	1.64	1.28

Table 5.4: Statistics for flow fields for Ri = 10

t	$\overline{u^2}$	$\overline{v^2}$	$\overline{w^2}$	$\sigma_{\bar{u}}$	$\sigma_{\bar{v}}$	$\sigma_{\bar{w}}$	$\overline{\rho^2}$	$\sigma_{\bar{\rho}}$	$\lvert\overline{\omega^2}\rvert$	$\overline{\omega^2}$	$\lvert\overline{\omega_H}\rvert$	$\overline{\omega_z^2}$	$\sigma_{\bar{\omega}}$
0	0.99	1.15	1.02	0.99	1.07	1.01	0.00	0.00	1.00	83.82	7.42	28.71	5.36
1	0.50	0.38	0.33	0.71	0.61	0.58	0.03	0.18	1.08	90.52	8.27	22.34	4.73
2	0.24	0.17	0.09	0.49	0.41	0.30	0.02	0.13	0.33	28.07	4.67	6.27	2.50
3	0.16	0.11	0.04	0.39	0.32	0.20	0.01	0.09	0.12	10.30	2.87	2.06	1.44
4	0.12	0.07	0.02	0.34	0.26	0.15	0.006	0.08	0.06	4.85	1.98	0.91	0.96

Table 5.5: Statistics for flow fields for Ri = 158

t	$\overline{u^2}$	$\overline{v^2}$	$\overline{w^2}$	$\sigma_{\bar{u}}$	$\sigma_{\bar{v}}$	$\sigma_{\bar{w}}$	$\overline{\rho^2}$	$\sigma_{\bar{\rho}}$	$\lvert\overline{\omega^2}\rvert$	$\overline{\omega^2}$	$\lvert\overline{\omega_H}\rvert$	$\overline{\omega_z^2}$	$\sigma_{\bar{\omega}}$
0	0.99	1.15	1.02	0.99	1.07	1.01	0.00	0.00	1.00	83.82	7.42	28.71	5.36
1	0.60	0.63	0.26	0.77	0.79	0.51	0.002	0.04	0.77	64.52	7.24	12.08	3.48
2	0.38	0.39	0.12	0.62	0.63	0.34	0.001	0.04	0.35	29.46	5.01	4.35	2.09
3	0.26	0.30	0.08	0.51	0.54	0.28	0.0009	0.03	0.20	16.83	3.83	2.16	1.47
4	0.19	0.24	0.06	0.44	0.49	0.25	0.0005	0.02	0.13	11.17	3.15	1.24	1.11

Table 5.6: Statistics for flow fields for Ri = 1000

t	$\overline{u^2}$	$\overline{v^2}$	$\overline{w^2}$	$\sigma_{\bar{u}}$	$\sigma_{\bar{v}}$	$\sigma_{\bar{w}}$	$\overline{\rho^2}$	$\sigma_{\bar{\rho}}$	$\lvert\overline{\omega^2}\rvert$	$\overline{\omega^2}$	$\lvert\overline{\omega_H}\rvert$	$\overline{\omega_z^2}$	$\sigma_{\bar{\omega}}$
0	0.99	1.15	1.02	0.99	1.07	1.01	0.00	0.00	1.00	83.82	7.42	28.71	5.36
1	0.63	0.72	0.29	0.80	0.85	0.54	0.0003	0.02	0.78	65.34	7.22	13.18	3.63
2	0.41	0.51	0.14	0.64	0.71	0.38	0.0002	0.01	0.39	32.38	5.19	5.41	2.33
3	0.31	0.34	0.07	0.55	0.58	0.82	0.0002	0.01	0.22	18.86	3.99	2.94	1.71
4	0.23	0.27	0.04	0.48	0.52	0.21	0.0002	0.01	0.16	13.40	3.41	1.77	1.33

5.2.1 Plots of Enstrophy

Figures 5.1, 5.2, 5.3 and 5.4 show three-dimensional plots of the isosurfaces of enstrophy (average of the square of the vorticity) for Ri = 0, 0.39, 1.58, 10, 158 and 1000 at times t = 1, 2, 3 and 4 respectively. The surface levels are three times the mean square values. At t = 1 in figure 5.1, the enstrophy "structures" for the small stratification (low Ri) are almost identical to the structures for the unstratified case (Ri = 0). These structures are very random tube-like focal structures similar in nature to those observed by Ooi et al (1999) (see figures 5.1(a), (b), (c)). However, the picture is significantly different in the strongly stratified cases (see figures 5.1 (d), (e)) where at time t = 1, stratification effects have become significant (as time on the Nt scale is greater than 1) and the structures are randomly distributed mostly in the horizontal plane. As the flow evolves, the enstrophy structures for low Ri cases are still mainly randomly distributed isotropic patches. For the high Ri cases, there is clear emergence of randomly distributed pancake-shaped structures oriented almost in the horizontal plane (see figures 5.4 (e), (f)). It appears that these structures can be related to the de-correlation of the vertical dynamics of the flow from the horizontal dynamics. The enstrophy in these patches is dominated by horizontal vorticity (see section 5.3.2). Kimura and Herring (1996) have also previously noted the presence of pancake-shaped vortex patches dominated by horizontal vorticity in their decaying turbulence simulations. They argue that this observation makes a strong case against the notion that stratified turbulence is two-dimensional.

The changes in the turbulence structure as the stratification increases are consistent with a strong suppression of the vertical displacements of fluid elements as noted in section 4.5. However, as can be seen in figure 3.6 (section 3.6), the mixing efficiency is largest for these strongly stratified cases. This implies the reduced vertical dispersion is compensated for by increased density differences as the stratification increases so that the potential energy changes are higher compared to the weakly stratified cases. For $Ri \geq 10$, these effects balance each other giving approximately constant mixing efficiency.

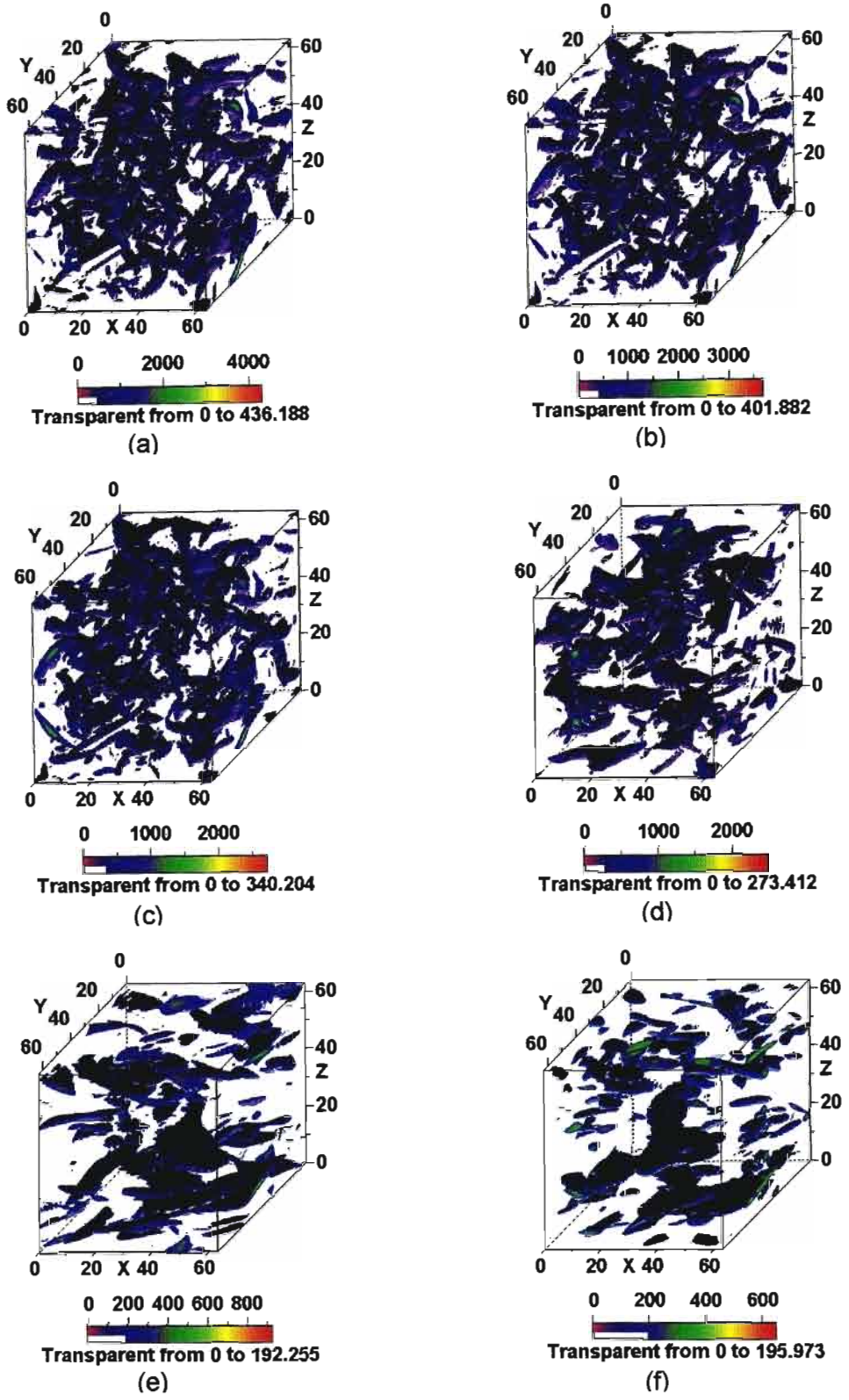

Figure 5.1: Isosurfaces of enstrophy at t = 1. (a) Ri = 0, (b) Ri = 0.39, Nt = 0.6, (c) Ri = 1.58, Nt = 1.3, (d) Ri = 10, Nt = 3.2, (e) Ri = 158, Nt = 12.6, (f) Ri = 1000, Nt = 31.6. The surface level is three times the mean-square enstrophy. Note enstrophy surfaces above the threshold value of three times the mean square enstrophy are hidden inside surfaces at the threshold value.

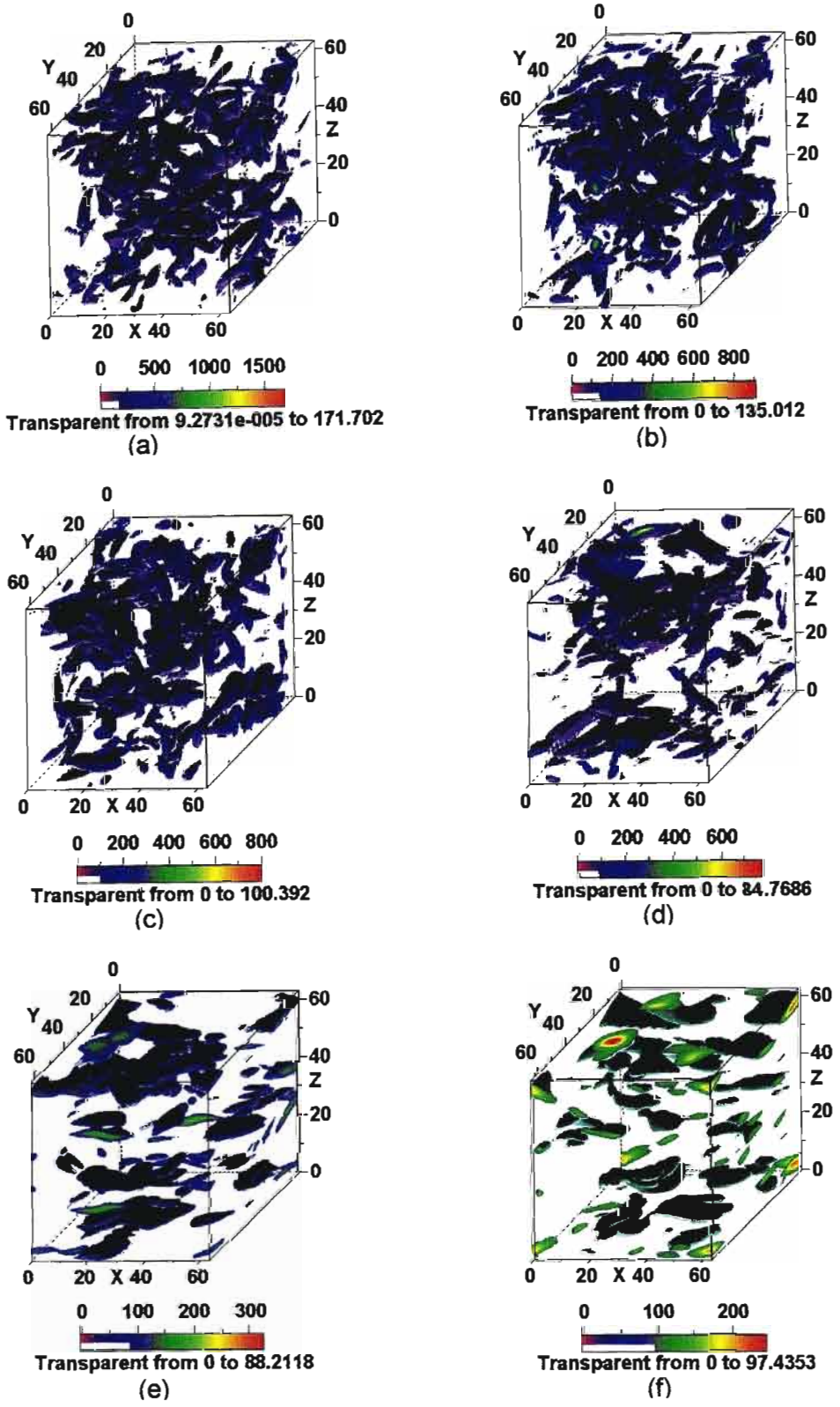

Figure 5.2: Isosurfaces of enstrophy at t = 2. (a) Ri = 0, (b) Ri = 0.39, Nt = 1.2, (c) Ri = 1.58, Nt = 2.5, (d) Ri = 10, Nt = 6.3, (e) Ri = 158, Nt = 25.1, (f) Ri = 1000, Nt = 63.2. The surface level is three times the mean-square enstrophy. Note enstrophy surfaces above the threshold value of three times the mean square enstrophy are hidden inside surfaces at the threshold value.

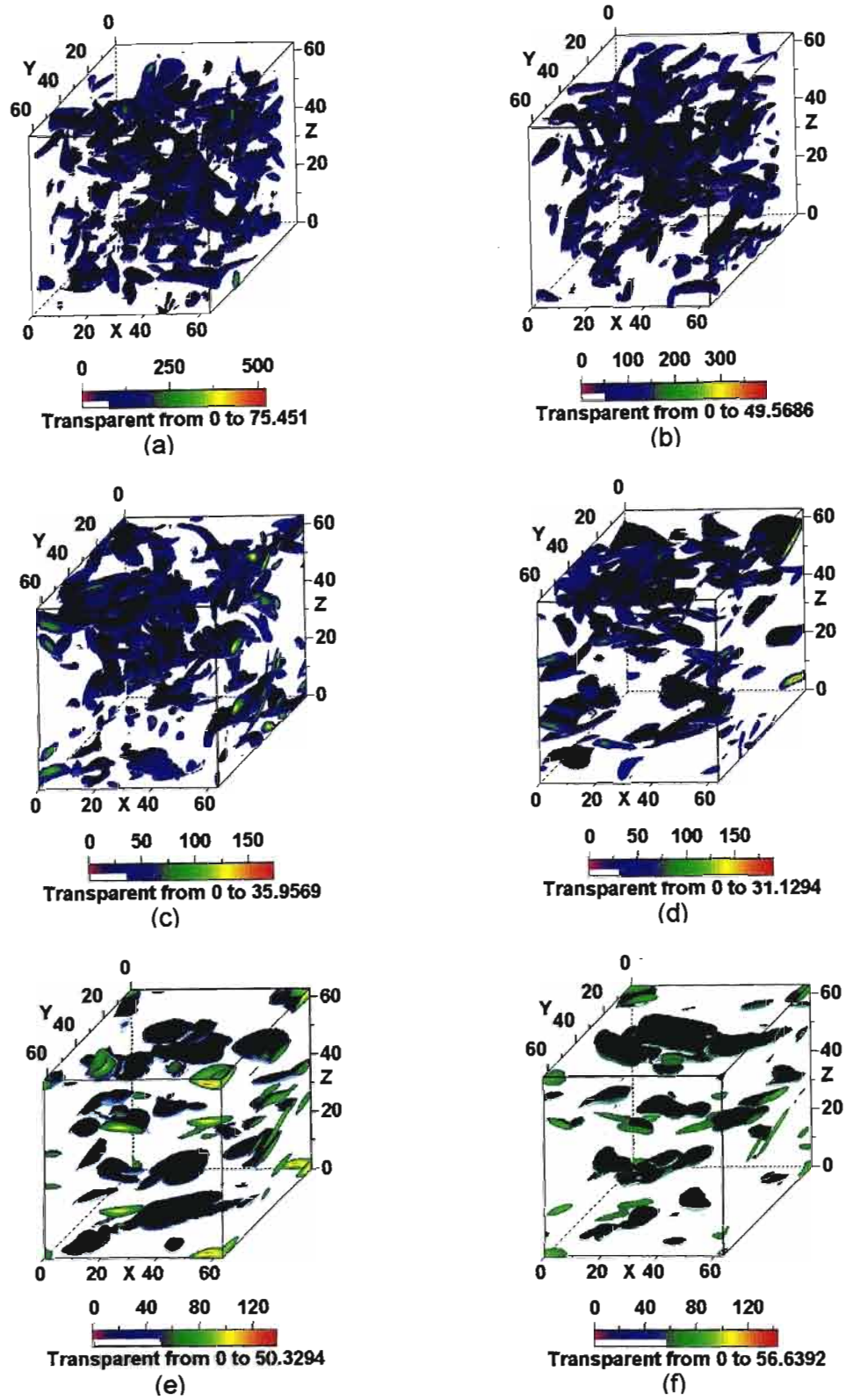

Figure 5.3: Isosurfaces of enstrophy at t = 3. (a) Ri = 0, (b) Ri = 0.39, Nt = 1.9, (c) Ri = 1.58, Nt = 3.8, (d) Ri = 10, Nt = 9.5, (e) Ri = 158, Nt = 37.7, (f) Ri = 1000, Nt = 94.9. The surface level is three times the mean-square enstrophy. Note enstrophy surfaces above the threshold value of three times the mean square enstrophy are hidden inside surfaces at the threshold value.

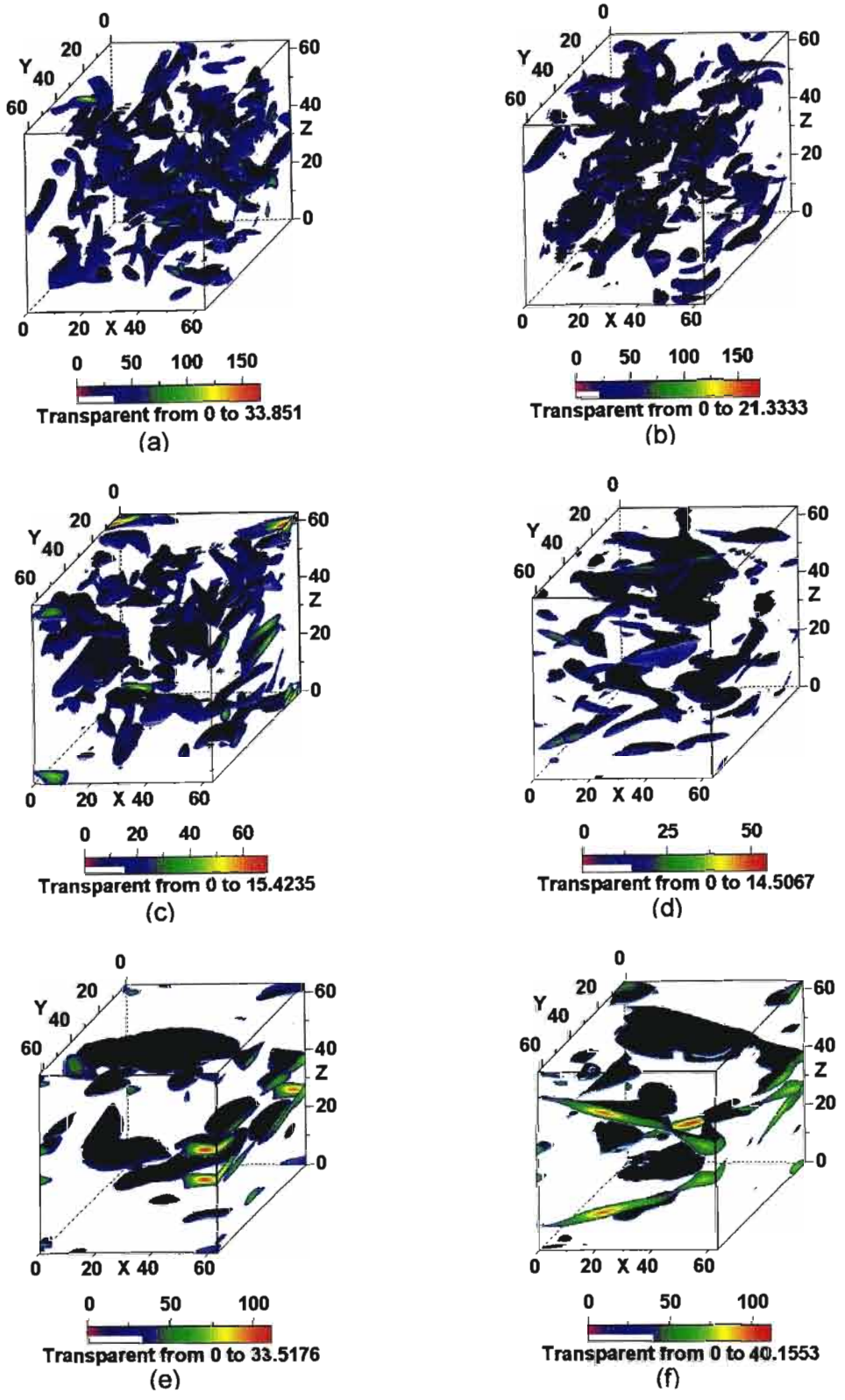

Figure 5.4: Isosurfaces of enstrophy at t = 4. (a) Ri = 0, (b) Ri = 0.39, Nt = 2.5, (c) Ri = 1.58, Nt = 5.0, (d) Ri = 10, Nt = 12.6, (e) Ri = 158, Nt = 50.3, (f) Ri = 1000, Nt = 126.5. The surface level is three times the mean-square enstrophy. Note enstrophy surfaces above the threshold value of three times the mean square enstrophy are hidden inside surfaces at the threshold value.

5.2.2 Plots of Horizontal Vorticity Fields

Figures 5.5, 5.6, 5.7 and 5.8 show three-dimensional plots of the isosurfaces of the root mean square horizontal vorticity at times t = 1, 2, 3, 4 for Ri = 0, 0.39, 1.58, 10, 158 & 1000. The surface levels are twice the root mean square values respectively. The qualitative patterns of the isosurface structures are very similar to those observed for the enstrophy. This is not surprising as it is clear from the statistics that the main contribution to the enstrophy comes from the horizontal vorticity. At late times, the flow is characterized by large horizontal vorticity compared to the vertical vorticity (Riley & Lelong, 2000).

Vertical planes were examined through the flow for high Ri flows to identify if any form of layering or striations were evident in the flow. Figures 5.9 (a), (b), (c), (d), show the vertical slices taken in the YZ-plane at X = 0, 22, 43, 63. It is clear from the plots, that the horizontal structures evident at X = 0 carry through to the slices at X = 22 and 43. The slice at X = 63 is identical to that at X = 0 due to periodicity. Animations of the flow in the YZ-plane from X = 0 to X = 63 indicate qualitatively the presence of horizontal layering in the flow structure of the horizontal vorticity. This seems to suggest the presence of quasi-horizontal structures stacked one above the other, with the motion in each somewhat decoupled from that above and below as suggested by Riley et al (1981).

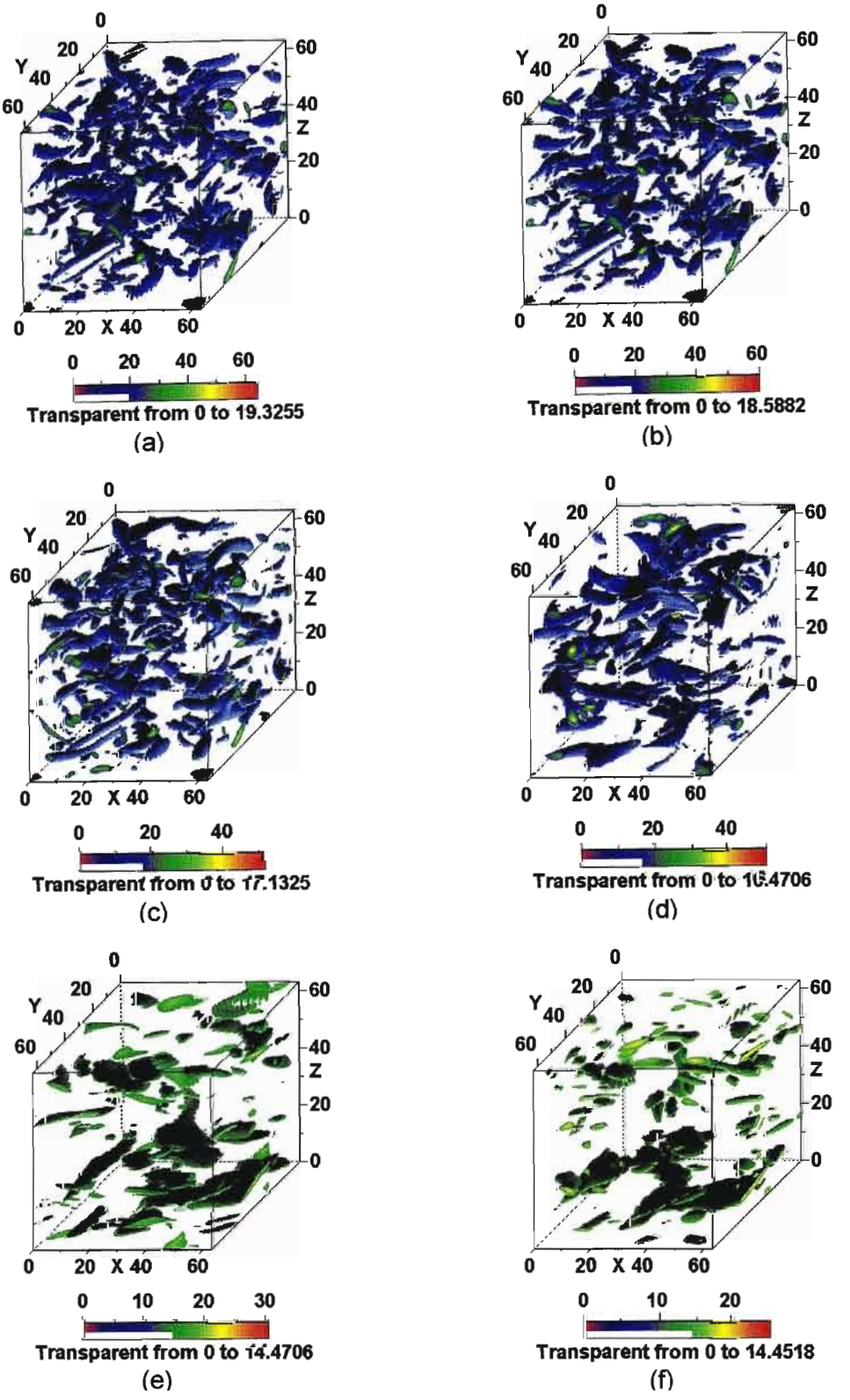

Figure 5.5: Isosurfaces of horizontal vorticity at t = 1. (a) Ri = 0, (b) Ri = 0.39, Nt = 0.6, (c) Ri = 1.58, Nt = 1.3, (d) Ri = 10, Nt = 3.2, (e) Ri = 158, Nt = 12.6, (f) Ri = 1000, Nt = 31.6. The surface level is two times the root mean square horizontal vorticity. Note surfaces above the threshold value of two times the root mean square horizontal vorticity are hidden inside surfaces at the threshold value.

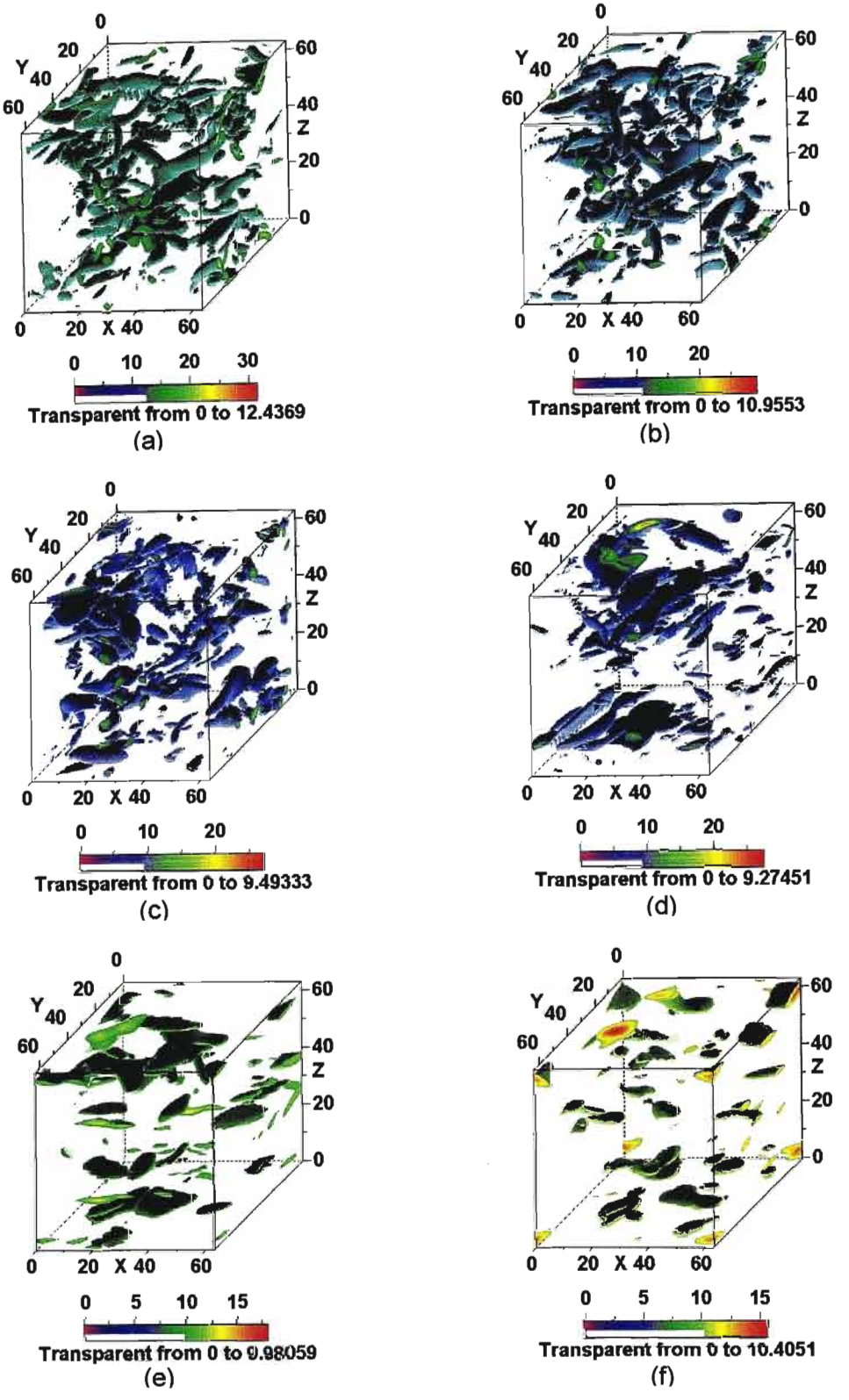

Figure 5.6: Isosurfaces of horizontal vorticity at t = 2. (a) Ri = 0, (b) Ri = 0.39, Nt = 1.2, (c) Ri = 1.58, Nt = 2.5, (d) Ri = 10, Nt = 6.3, (e) Ri = 158, Nt = 25.1, (f) Ri = 1000, Nt = 63.2. The surface level is two times the root mean square horizontal vorticity. Note surfaces above the threshold value of two times the root mean square horizontal vorticity are hidden inside surfaces at the threshold value.

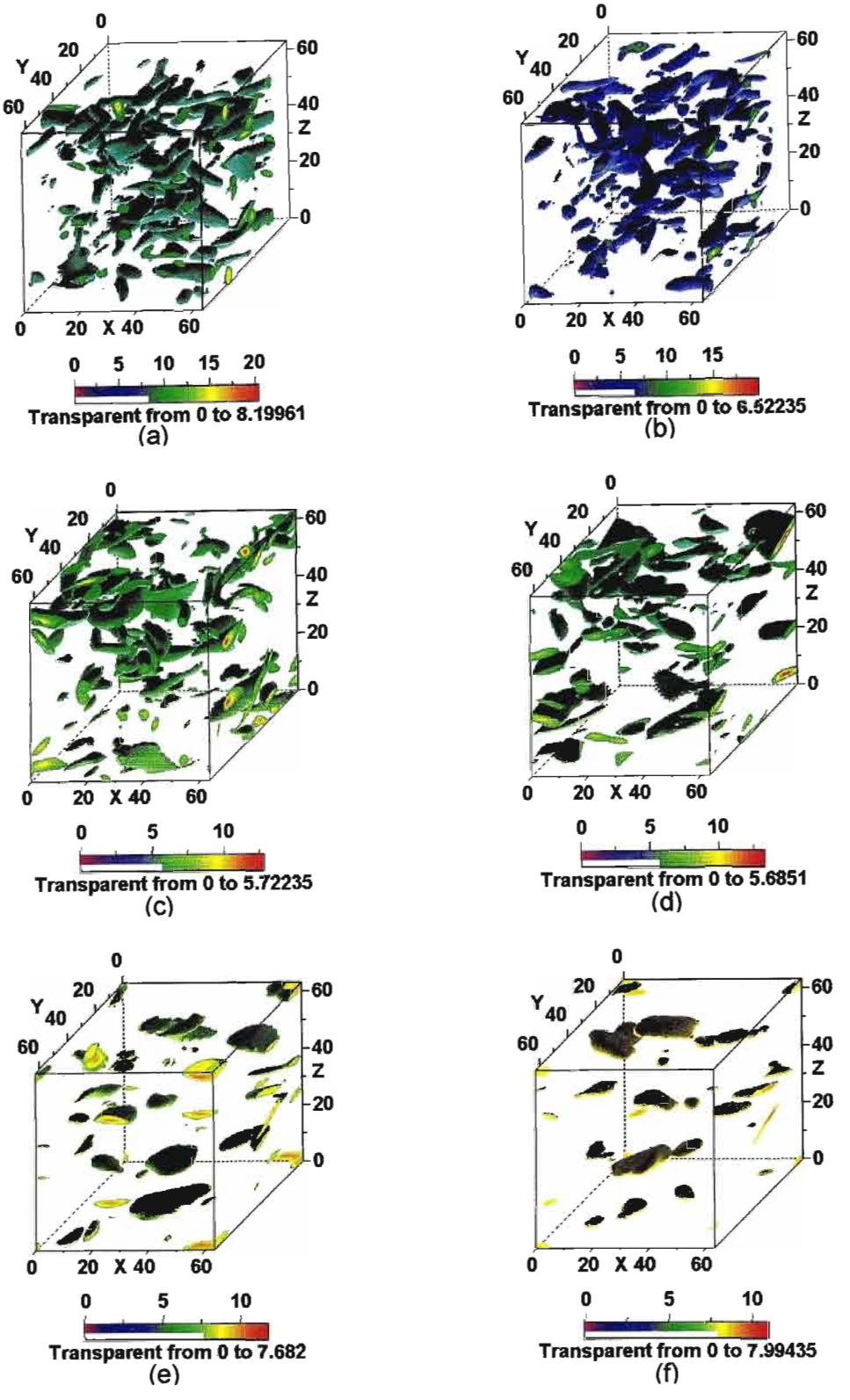

Figure 5.7: Isosurfaces of horizontal vorticity at t = 3. (a) Ri = 0, (b) Ri = 0.39, Nt = 1.9, (c) Ri = 1.58, Nt = 3.8, (d) Ri = 10, Nt = 9.5, (e) Ri = 158, Nt = 37.7, (f) Ri = 1000, Nt = 94.9. The surface level is two times the root mean square horizontal vorticity. Note surfaces above the threshold value of two times the root mean square horizontal vorticity are hidden inside surfaces at the threshold value.

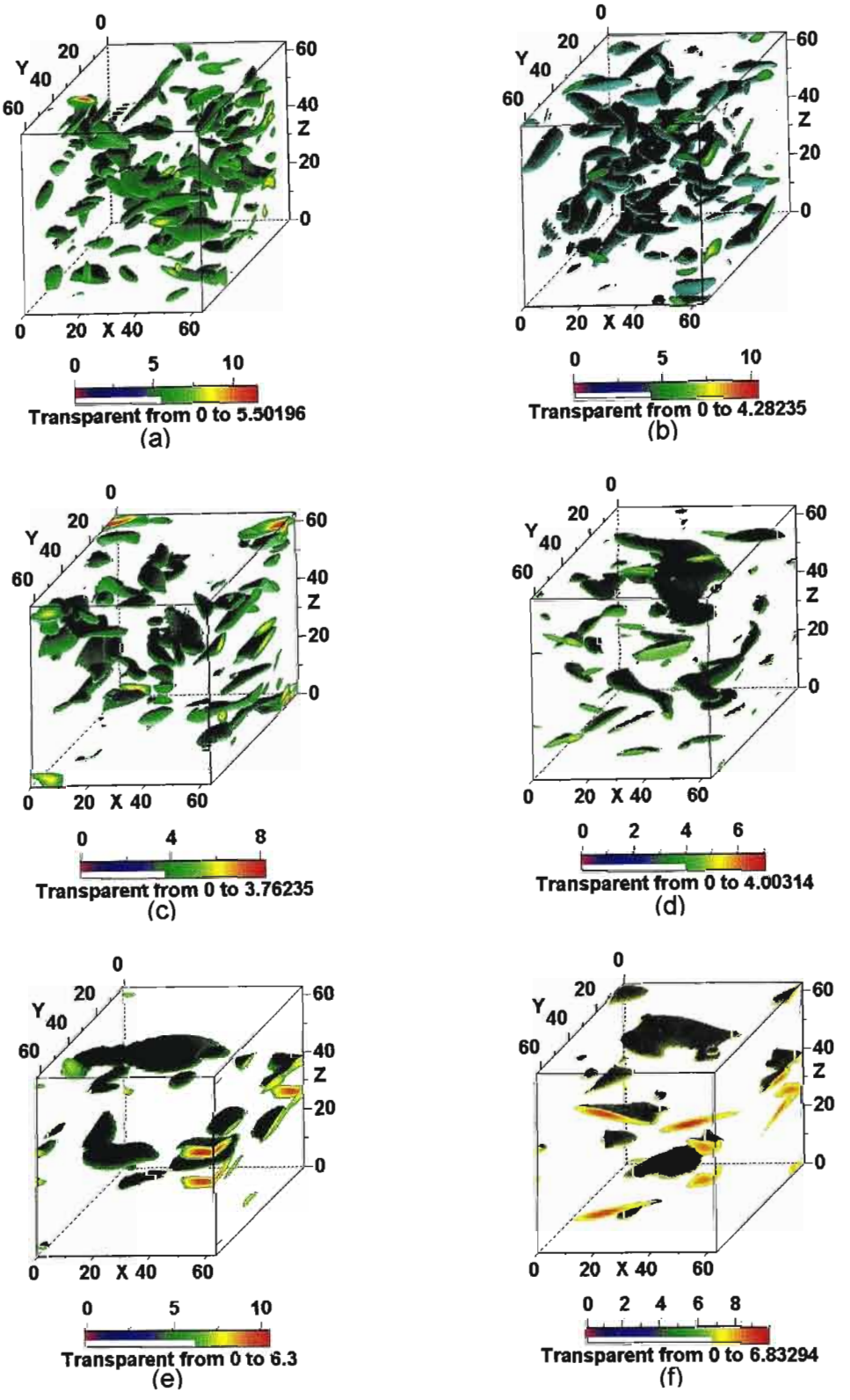

Figure 5.8: Isosurfaces of horizontal vorticity at t = 4. (a) Ri = 0, (b) Ri = 0.39, Nt = 2.5, (c) Ri = 1.58, Nt = 5.0, (d) Ri = 10, Nt = 12.6, (e) Ri = 158, Nt = 50.3, (f) Ri = 1000, Nt = 126.5. The surface level is two times the root mean square horizontal vorticity. Note surfaces above the threshold value of two times the root mean square horizontal vorticity are hidden inside surfaces at the threshold value.

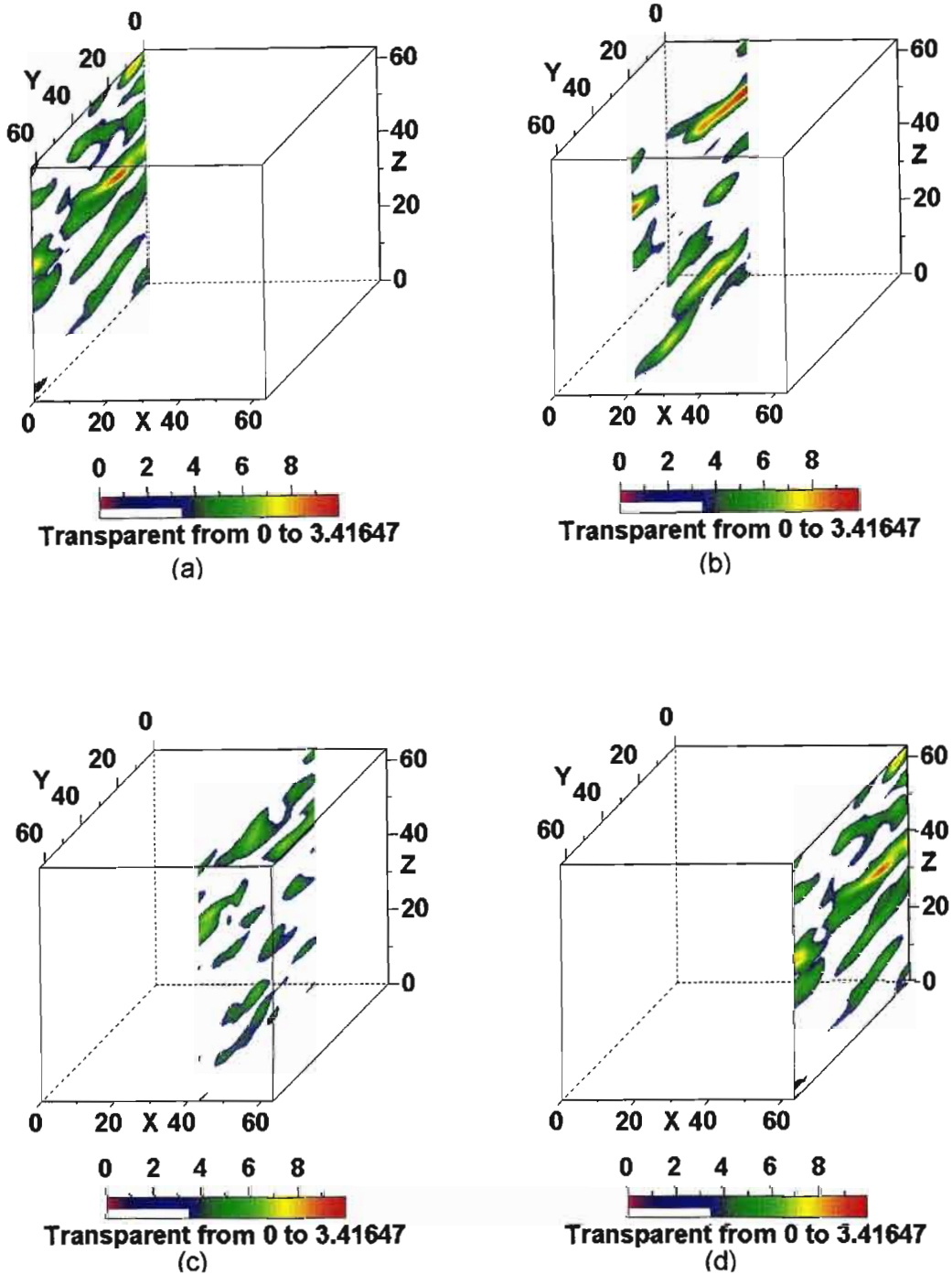

Figure 5.9: Vertical slices of the root mean square horizontal vorticity through the YZ-plane for Ri = 1000 at t = 4 for (a) X = 0, (b) X = 22, (c) X = 43 and (d) X = 63. The magnitudes shown are at the root mean square values.

5.2.3 Plots of Vertical Vorticity Fields

Figures 5.10, 5.11, 5.12 and 5.13 show three-dimensional plots of the isosurfaces of the vertical vorticity at times t = 1, 2, 3, 4 for Ri = 0, 0.39, 1.58, 10, 158 & 1000. The surface levels are at ± 2 times the standard deviation of the vertical vorticity. The structures are random in all cases for the times shown, but with fewer small scales at the strongly stratified cases (Ri = 158 & 1000).

5.2.4 Plots of Density Fields

Figures 5.14, 5.15, 5.16 and 5.17 show three-dimensional plots of the isosurfaces of the density fluctuations at times t = 1, 2, 3, 4 for Ri = 0, 0.39, 1.58, 10, 158 & 1000. The surface levels are at ± 2 times the standard deviation of the density fluctuations. The flow structures appear to be random. Note that the magnitudes of the density fluctuations are suppressed in the strongly stable cases.

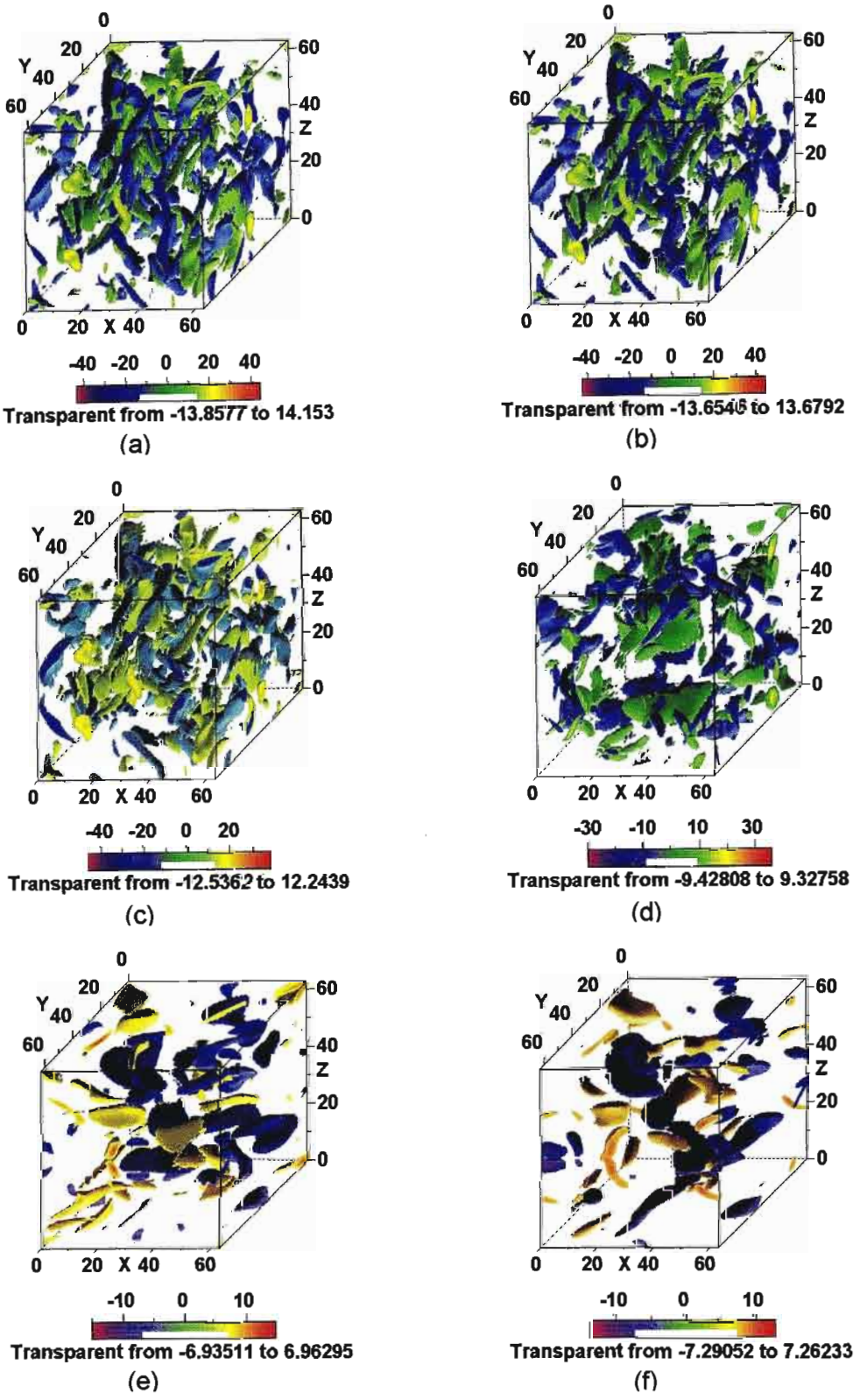

Figure 5.10: Isosurfaces of vertical vorticity at t = 1. (a) Ri = 0, (b) Ri = 0.39, Nt = 0.6, (c) Ri = 1.58, Nt = 1.3, (d) Ri = 10, Nt = 3.2, (e) Ri = 158, Nt = 12.6, (f) Ri = 1000, Nt = 31.6. The surface levels are ± 2 times the standard deviation of the vertical vorticity. Note surfaces above the threshold value are hidden inside surfaces at the threshold value.

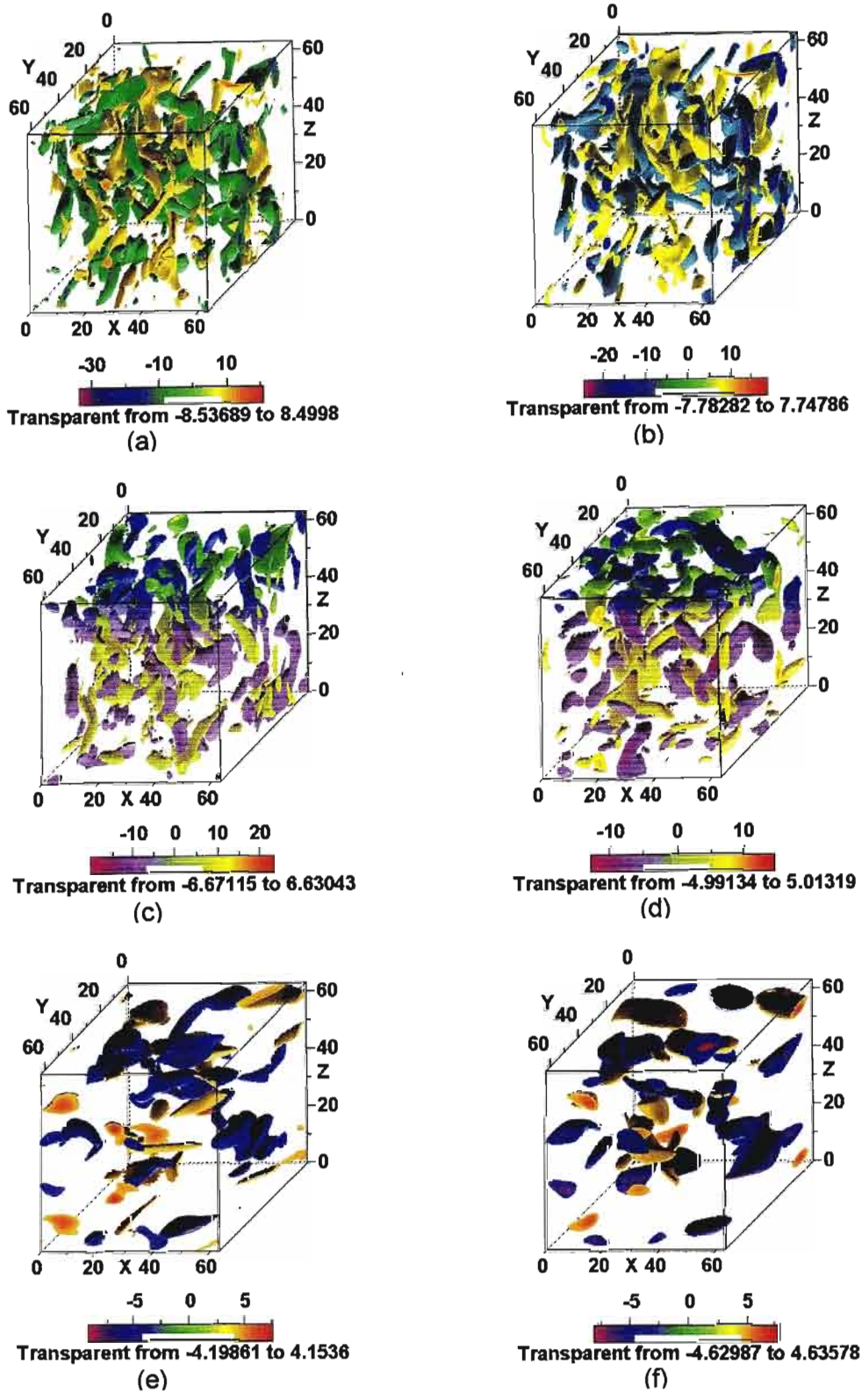

Figure 5.11: Isosurfaces of vertical vorticity at t = 2. (a) Ri = 0, (b) Ri = 0.39, Nt = 1.2, (c) Ri = 1.58, Nt = 2.5, (d) Ri = 10, Nt = 6.3, (e) Ri = 158, Nt = 25.1, (f) Ri = 1000, Nt = 63.2. The surface levels are ± 2 times the standard deviation of the vertical vorticity. Note surfaces above the threshold value are hidden inside surfaces at the threshold value.

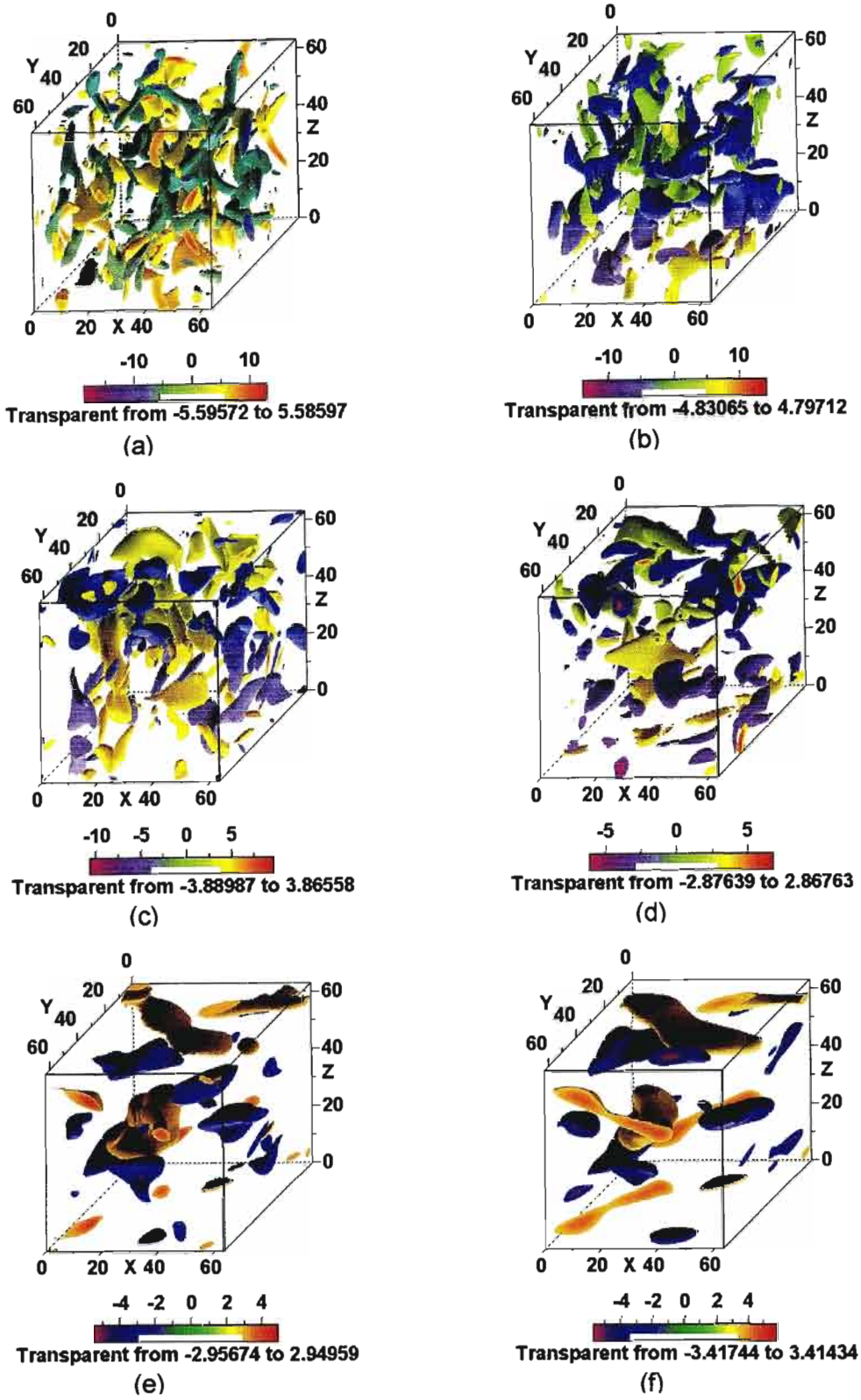

Figure 5.12: Isosurfaces of vertical vorticity at t = 3. (a) Ri = 0, (b) Ri = 0.39, Nt = 1.9, (c) Ri = 1.58, Nt = 3.8, (d) Ri = 10, Nt = 9.5, (e) Ri = 158, Nt = 37.7, (f) Ri = 1000, Nt = 94.9. The surface levels are ± 2 times the standard deviation of the vertical vorticity. Note surfaces above the threshold value are hidden inside surfaces at the threshold value.

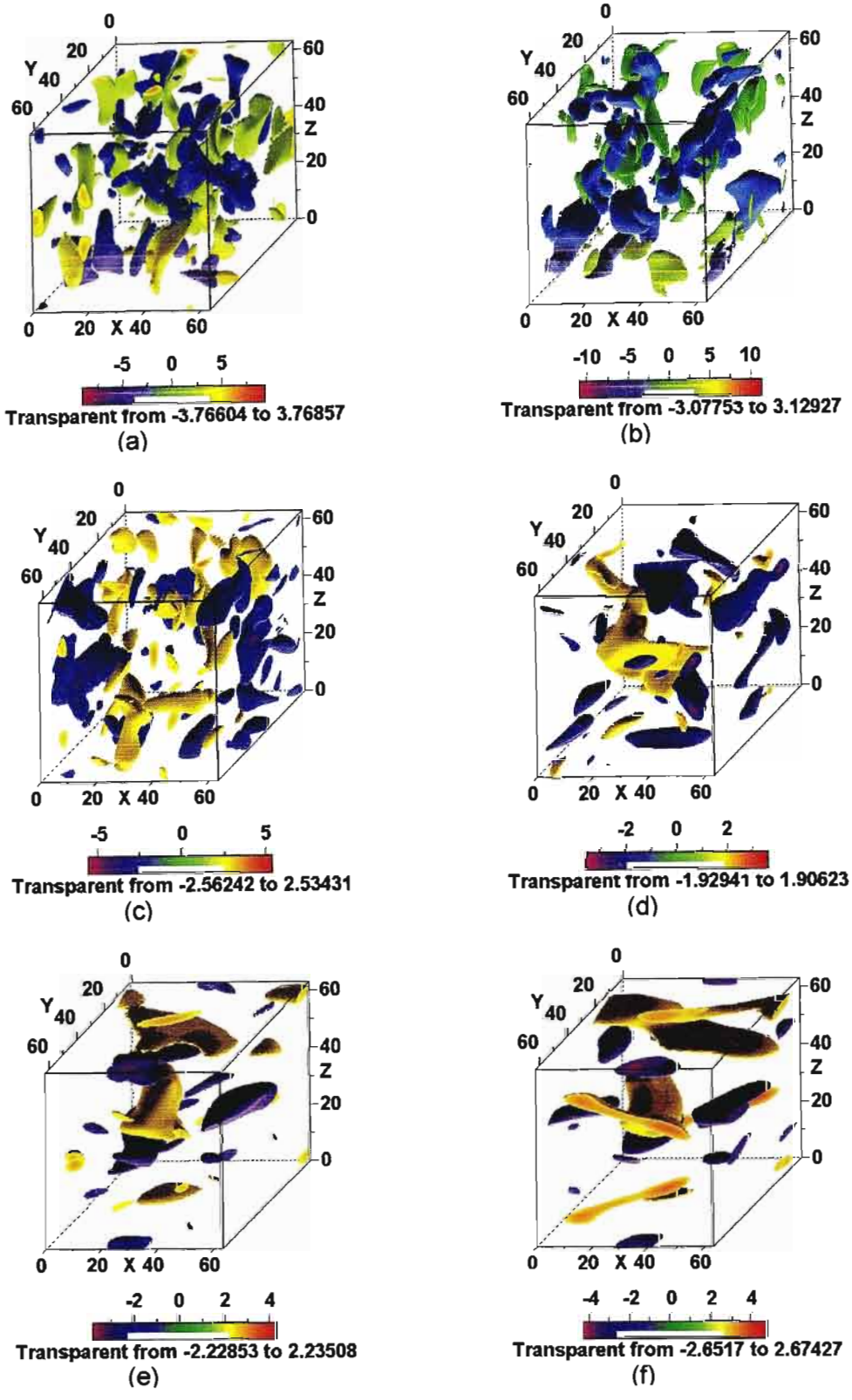

Figure 5.13: Isosurfaces of vertical vorticity at t = 4. (a) Ri = 0, (b) Ri = 0.39, Nt = 2.5, (c) Ri = 1.58, Nt = 5.0, (d) Ri = 10, Nt = 12.6, (e) Ri = 158, Nt = 50.3, (f) Ri = 1000, Nt = 126.5. The surface levels are ± 2 times the standard deviation of the vertical vorticity. Note surfaces above the threshold value are hidden inside surfaces at the threshold value.

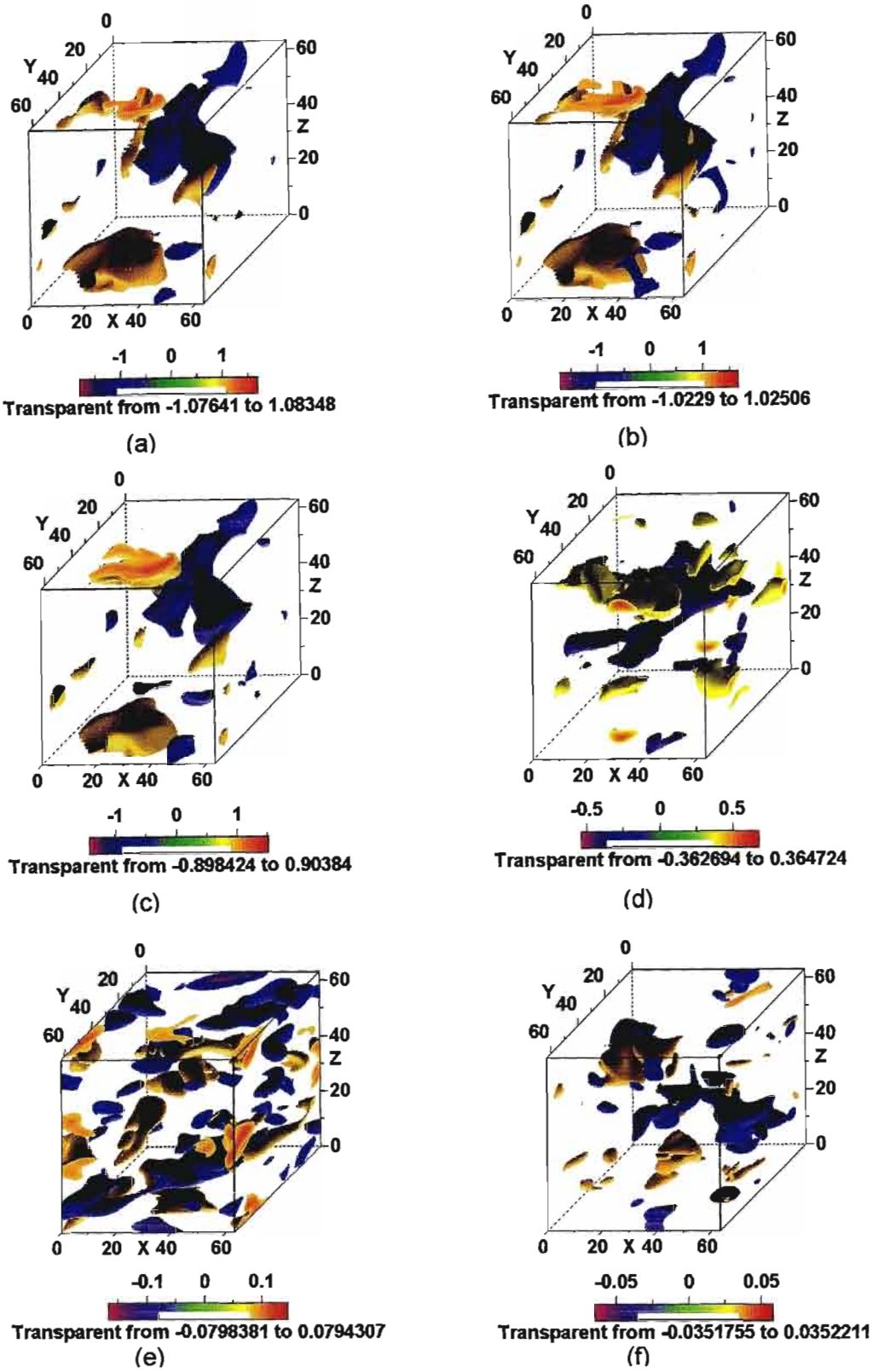

Figure 5.14: Isosurfaces of density fluctuations at t = 1. (a) Ri = 0, (b) Ri = 0.39, Nt = 0.6, (c) Ri = 1.58, Nt = 1.3, (d) Ri = 10, Nt = 3.2, (e) Ri = 158, Nt = 12.6, (f) Ri = 1000, Nt = 31.6. The surface levels are ± 2 times the standard deviation of the density fluctuations. Note surfaces above the threshold value are hidden inside surfaces at the threshold value.

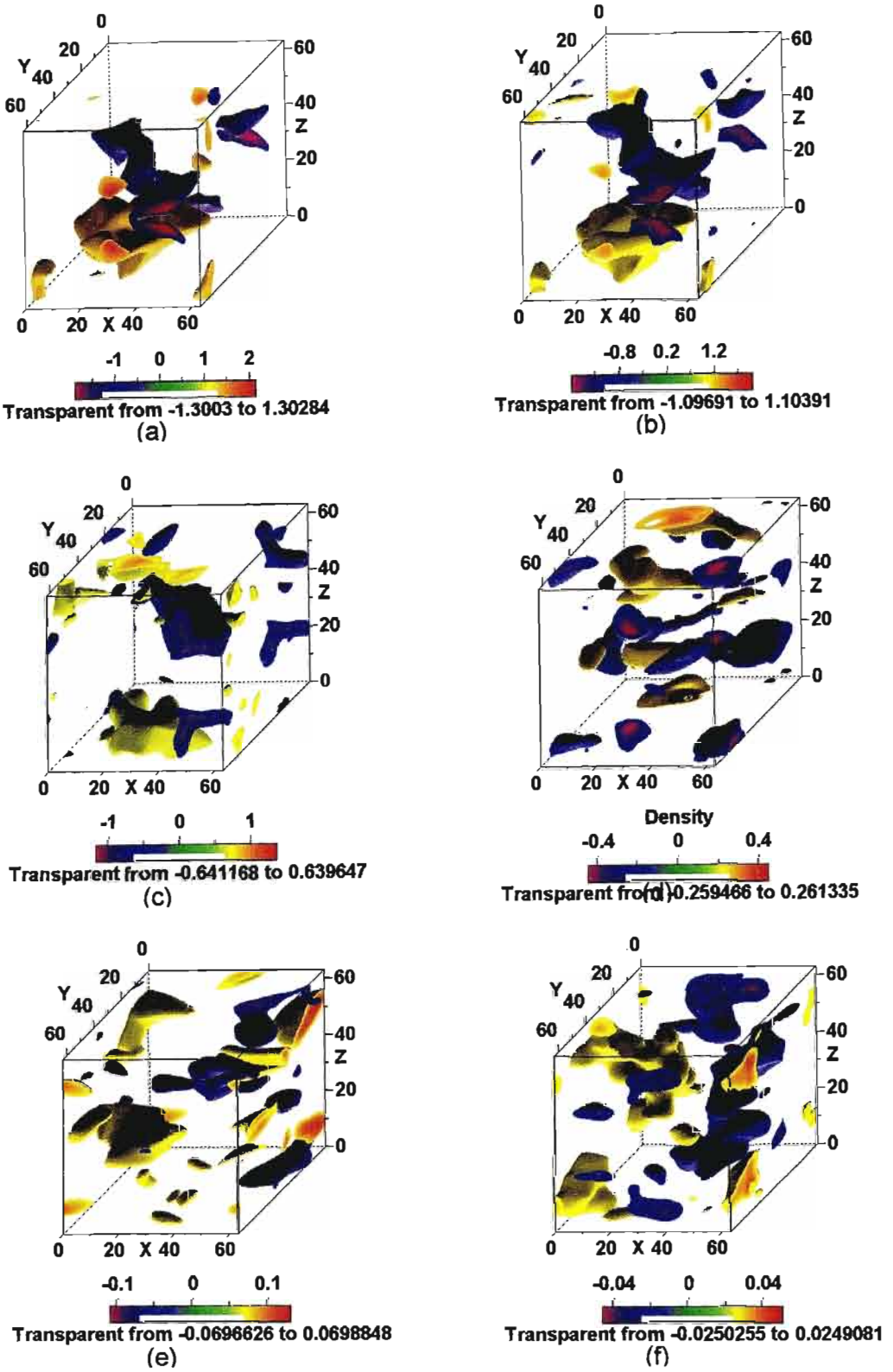

Figure 5.15: Isosurfaces of density fluctuations at t = 2. (a) Ri = 0, (b) Ri = 0.39, Nt = 1.2, (c) Ri = 1.58, Nt = 2.5, (d) Ri = 10, Nt = 6.3, (e) Ri = 158, Nt = 25.1, (f) Ri = 1000, Nt = 63.2. The surface levels are ± 2 times the standard deviation of the density fluctuations. Note surfaces above the threshold value are hidden inside surfaces at the threshold value.

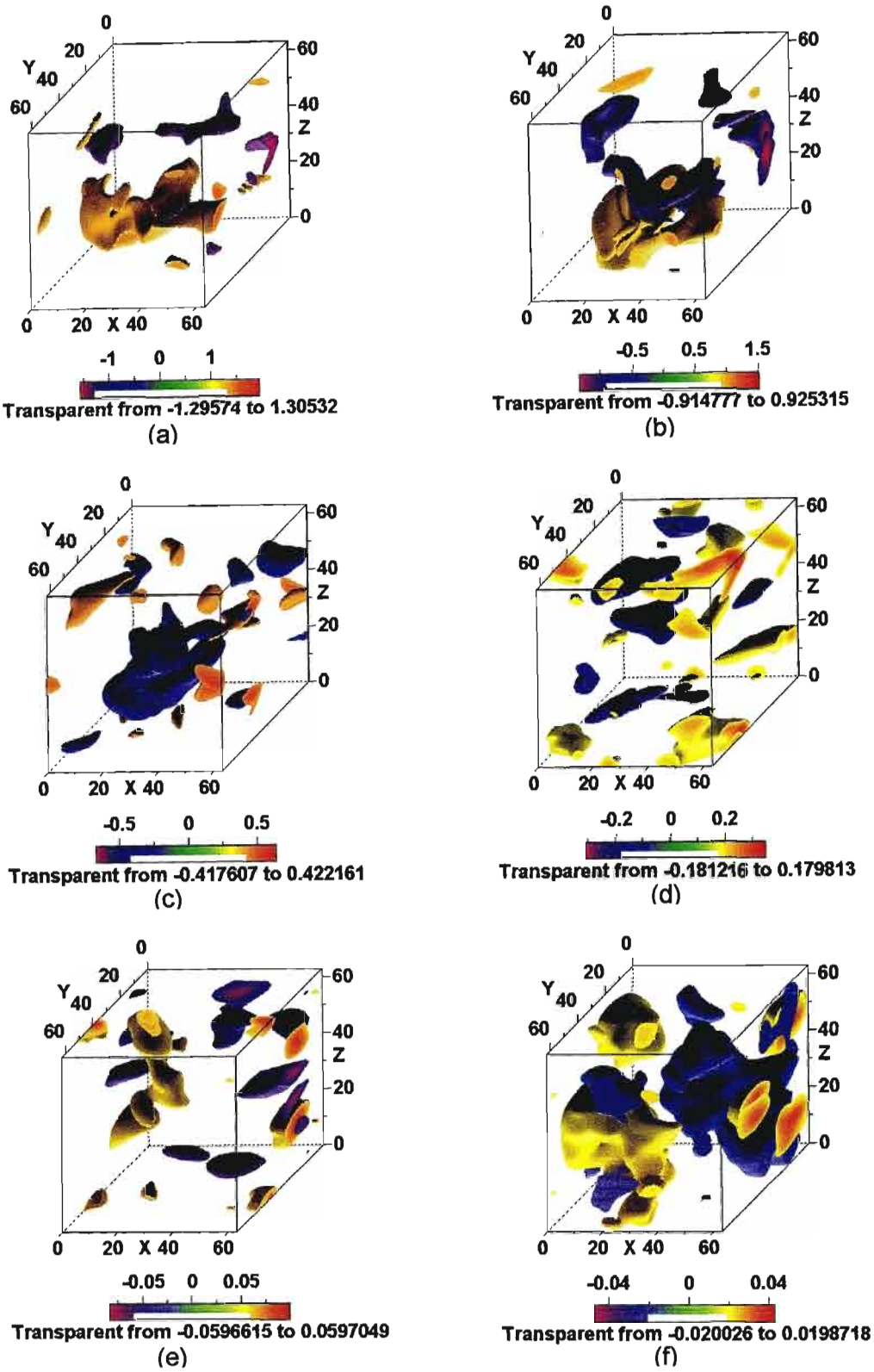

Figure 5.16: Isosurfaces of density fluctuations at t = 3. (a) Ri = 0, (b) Ri = 0.39, Nt = 1.9, (c) Ri = 1.58, Nt = 3.8, (d) Ri = 10, Nt = 9.5, (e) Ri = 158, Nt = 37.7, (f) Ri = 1000, Nt = 94.9. The surface levels are ± 2 times the standard deviation of the density fluctuations. Note surfaces above the threshold value are hidden inside surfaces at the threshold value.

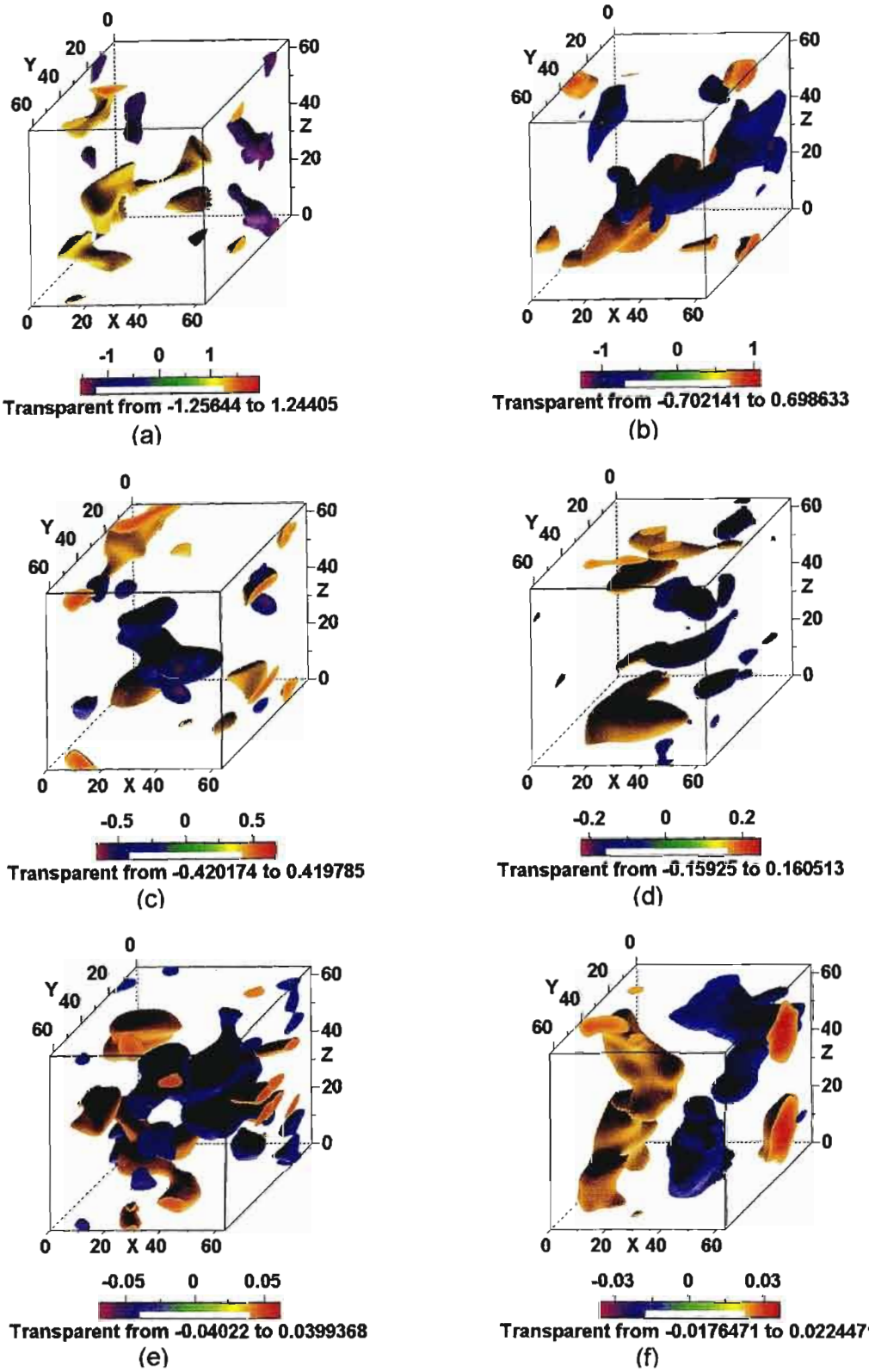

Figure 5.17: Isosurfaces of density fluctuations at t = 4. (a) Ri = 0, (b) Ri = 0.39, Nt = 2.5, (c) Ri = 1.58, Nt = 5.0, (d) Ri = 10, Nt = 12.6, (e) Ri = 158, Nt = 50.3, (f) Ri = 1000, Nt = 126.5. The surface levels are ± 2 times the standard deviation of the density fluctuations. Note surfaces above the threshold value are hidden inside surfaces at the threshold value.

Plots of Vertical Density Gradient Fields

Visualization of the vertical density gradient can indicate the presence or absence of overturning motions in the flow. These overturning motions generate unstable density gradients and can be a mechanism through which mixing takes place. The vertical density gradients can be calculated from the density fluctuations as follows:

The density of a fluid element is given by equation (5.1)

$$\rho = \rho_0 + \overline{\rho} + \rho' \tag{5.1}$$

where ρ_0 is the constant reference density, $\overline{\rho}$ is the mean density at a level z and ρ' is the density fluctuation from the mean at the point (x,y,z).

Differentiating equation (5.1) with respect to z yields

$$\frac{\partial \rho}{\partial z} = \frac{\partial \overline{\rho}}{\partial z} + \frac{\partial \rho'}{\partial z} \tag{5.2}$$

Dividing equation (5.2) by $\left|\frac{\partial \overline{\rho}}{\partial x}\right|$, (with negative gradient), an expression for the vertical density gradient normalized by the background mean vertical density gradient can be obtained as

$$\left.\partial\rho/\partial z\right/\left|\overline{\partial\rho}/\partial z\right| = \left.\partial\rho'/\partial z\right/\left|\overline{\partial\rho}/\partial z\right| \quad - \quad 1 \tag{5.3}$$

The vertical density fluctuation gradient was calculated by a central difference approximation. A zero value for the vertical density gradient implies the limiting scenario where the fluid is on the verge of instability. Values greater than zero indicate unstable density gradients and hence overturning motions in the flow.

Three dimensional plots of the vertical density gradient fields calculated as per equation (5.3) are shown in figures 5.18, 5.19, 5.20, and 5.21 at times t = 1, 2, 3, 4 for Ri = 0, 0.39, 1.58, 10, 158 & 1000. The surface levels shown mark the outer edges of overturning regions while the non-overturning regions are transparent. It is evident that there are high positive gradients in the unstratified case as well as the low Ri cases. On the other hand, there are no positive gradients at the strongly stable cases of Ri = 158 and Ri = 1000 even at early times (see figures 5.18 (e) and (f)). The overturning regions become smaller with time for the all the case e.g. for Ri = 10 where they disappear for $t \geq 3$ (see figure 5.21(d)). These regions disappear at times Nt = 6 to 9 for all the cases i.e. after about one buoyancy period.

This corresponds well with the root mean square mixing statistics presented in section 4.7.1 where it was shown how Lagrangian mixing rates decrease rapidly for $Nt \geq 2\pi$. Therefore these observations are consistent with the conclusion that the overturning motions provide the main mechanism by which mixing takes place in these flows.

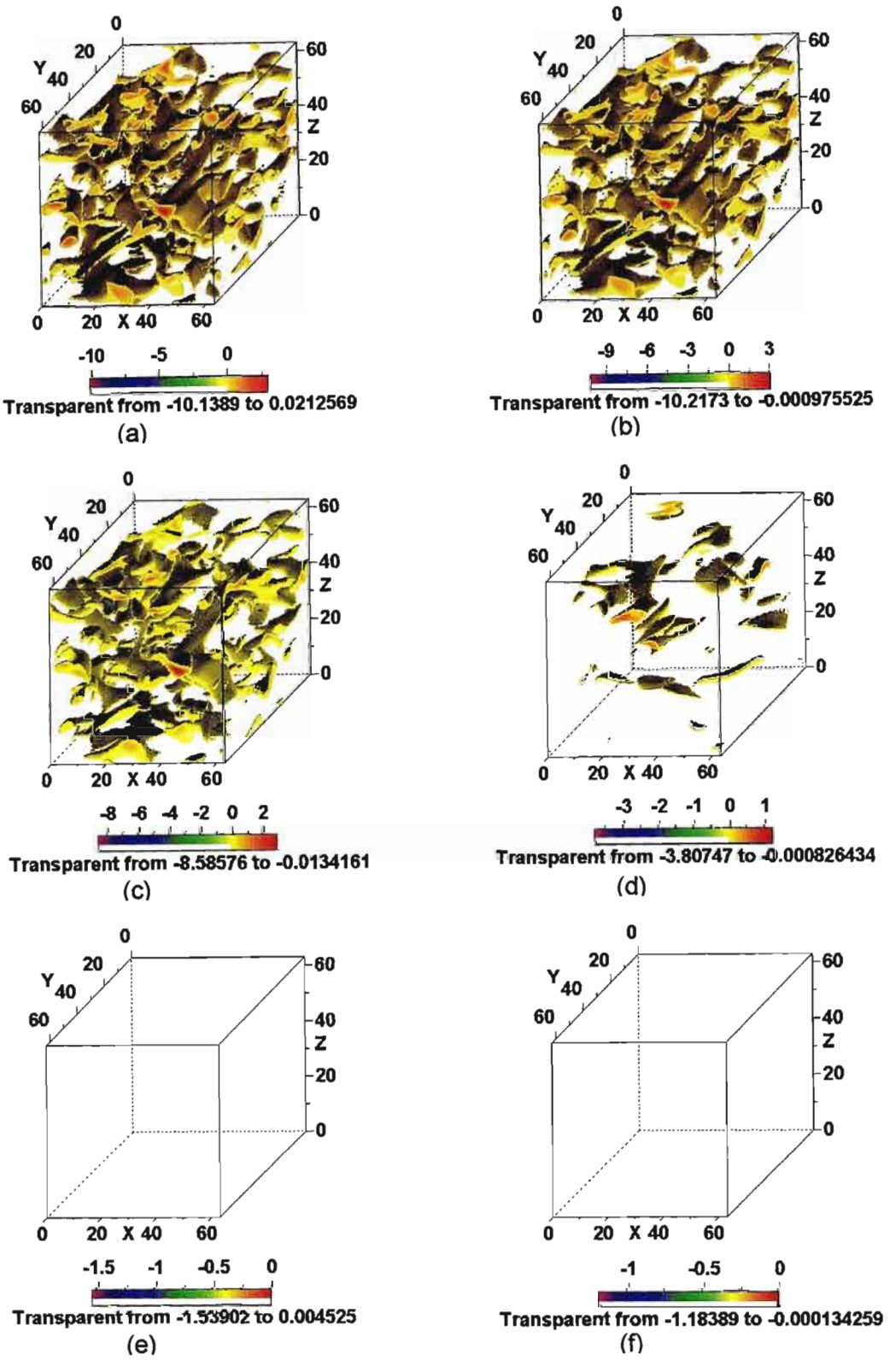

Figure 5.18: Isosurfaces of vertical density gradient at t = 1. (a) Ri = 0, (b) Ri = 0.39, Nt = 0.6, (c) Ri = 1.58, Nt = 1.3, (d) Ri = 10, Nt = 3.2, (e) Ri = 158, Nt = 12.6, (f) Ri = 1000, Nt = 31.6. The surface levels are at the limiting value of zero, values greater than zero imply unstable density gradients. Note surfaces above the threshold value are hidden inside surfaces at the threshold value.

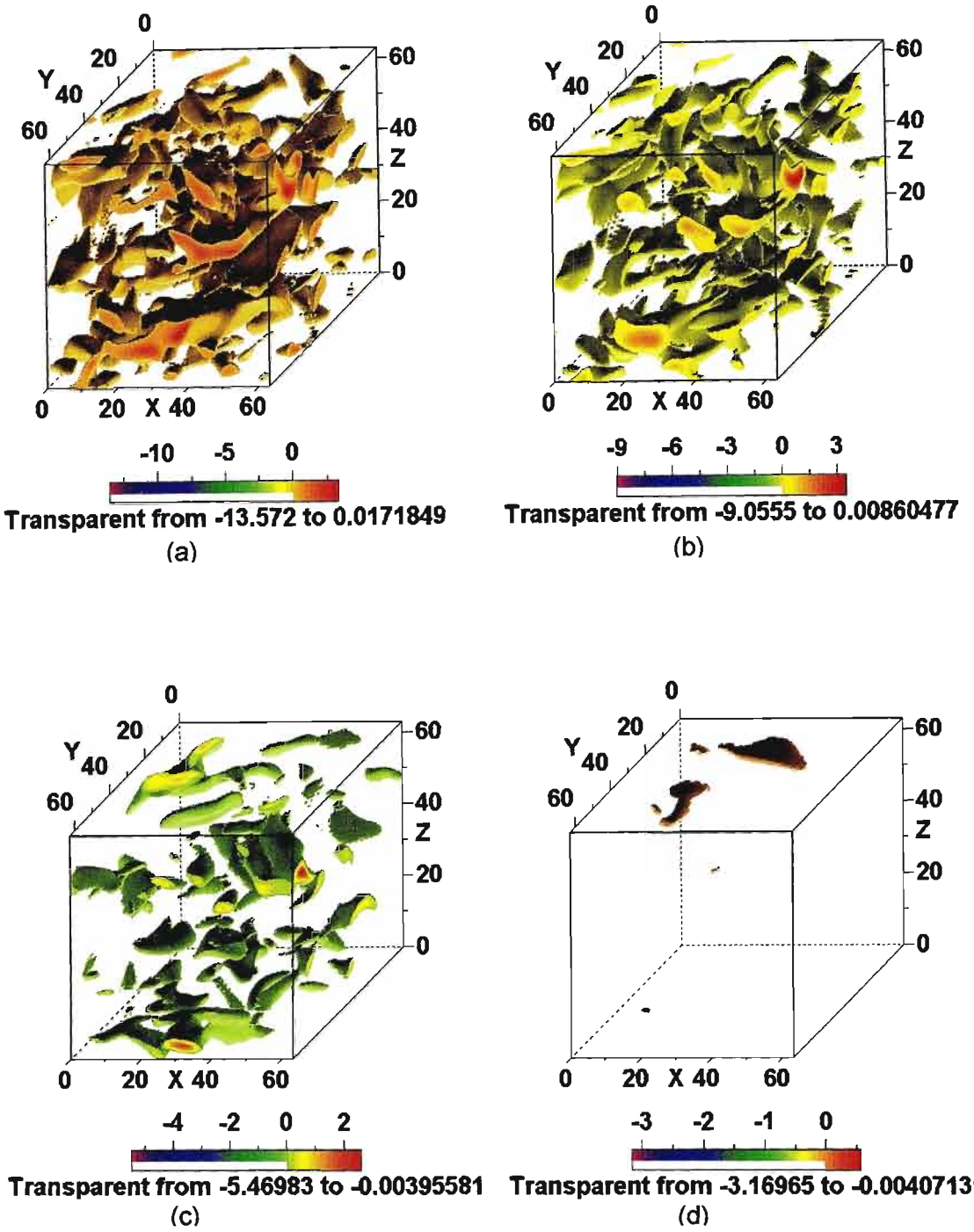

Figure 5.19: Isosurfaces of vertical density gradient at t = 2. (a) Ri = 0, (b) Ri = 0.39, Nt = 1.2, (c) Ri = 1.58, Nt = 2.5, (d) Ri = 10, Nt = 6.3. The surface levels are at the limiting value of zero, values greater than zero imply unstable density gradients. Note surfaces above the threshold value are hidden inside surfaces at the threshold value.

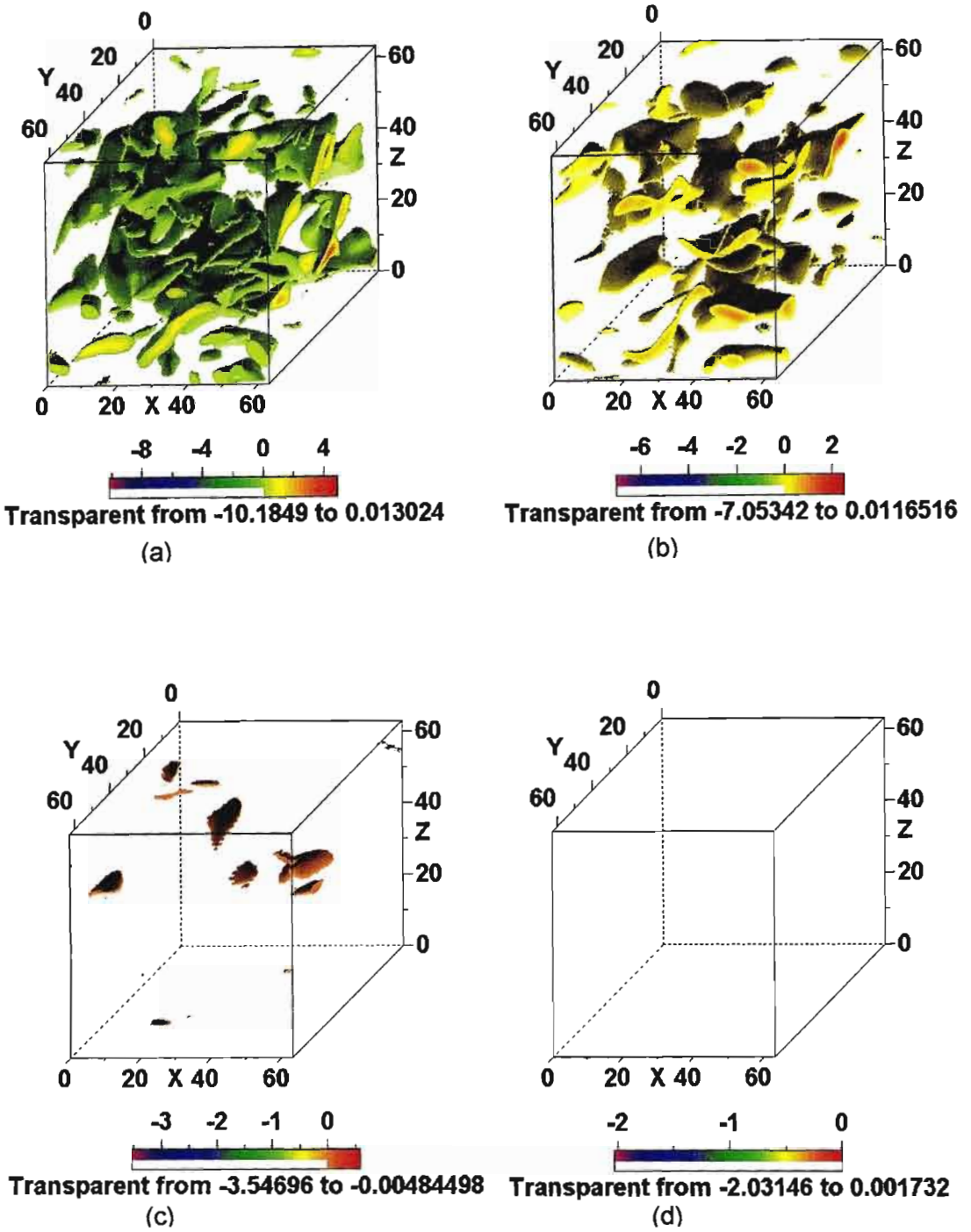

Figure 5.20: Isosurfaces of vertical density gradient at t = 3. (a) Ri = 0, (b) Ri = 0.39, Nt = 1.9, (c) Ri = 1.58, Nt = 3.8, (d) Ri = 10, Nt = 9.5. The surface levels are at the limiting value of zero, values greater than zero imply unstable density gradients. Note surfaces above the threshold value are hidden inside surfaces at the threshold value.

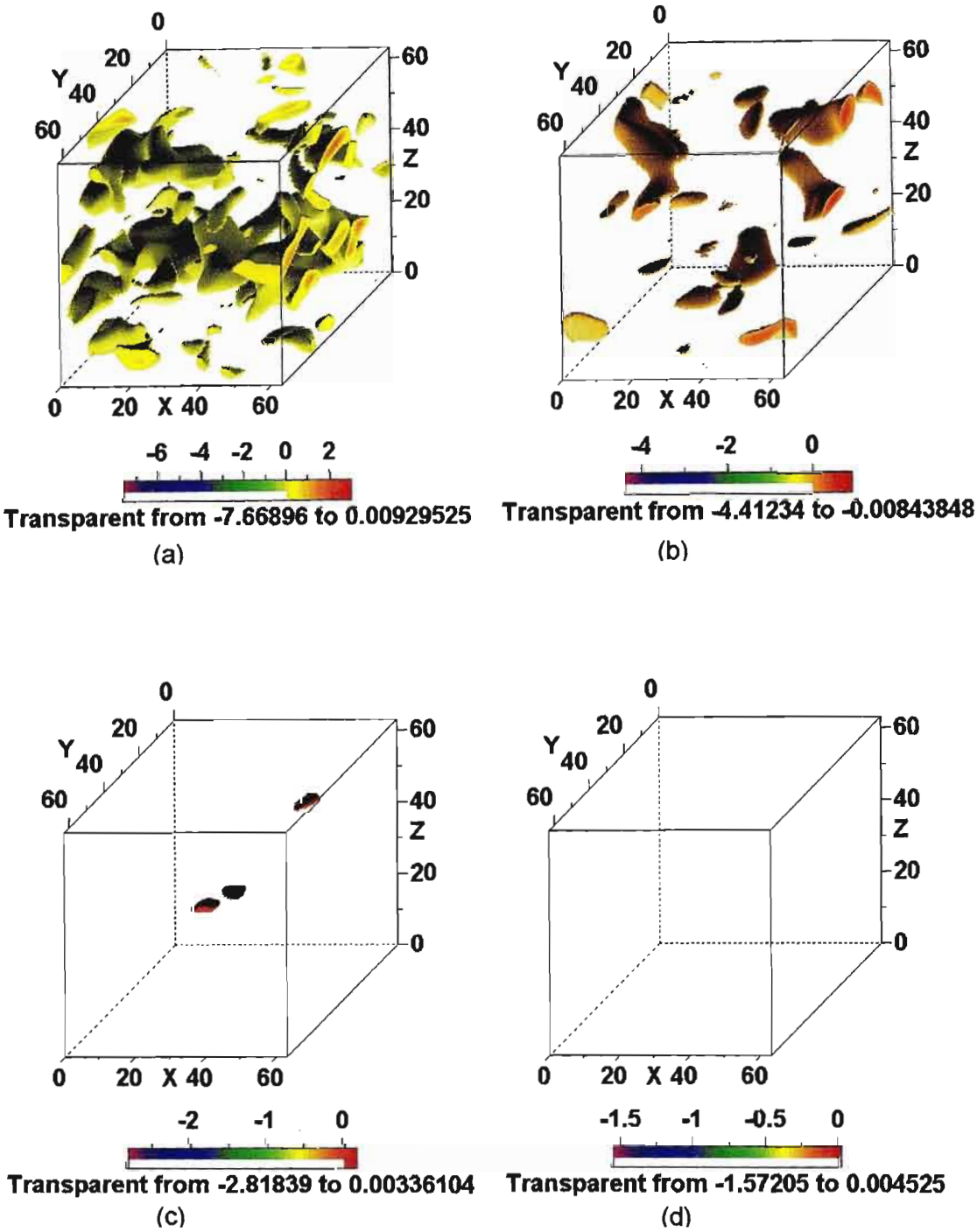

Figure 5.21: Isosurfaces of vertical density gradient at t = 4. (a) Ri = 0, (b) Ri = 0.39, Nt = 2.5, (c) Ri = 1.58, Nt = 5.0, (d) Ri = 10, Nt = 12.6. The surface levels are at the limiting value of zero, values greater than zero imply unstable density gradients. Note surfaces above the threshold value are hidden inside surfaces at the threshold value.

5.2 Flow Structures of Fields Exhibiting High Mixing Events

The flow fields associated with the high mixing events discussed in section 4.7.3 (see table 5.7) were archived and visualized to identify key structures that might explain these events. It must however be noted that this sample is biased since it represents only the events with highest rates of mixing out of an ensemble of 512 events at any given time.

Table 5.7: High mixing events obtained from DNS using particle tracking.

Ri	Time @ which event occurred	Rate of Mixing $\kappa\nabla^2\rho'$	*X* Coordinate of particle position	*Y* Coordinate of particle position	*Z* Coordinate of particle position
0	0.700	-19.5	44.2	23.4	36.7
0	1.050	+20.6	34.9	41.4	53.7
0.39	0.725	-16.7	44.4	23.3	36.7
0.39	1.100	+18.7	35.2	41.5	54.0
1.58	0.425	+9.0	20.2	41.1	4.5
1.58	1.475	-12.3	37.7	26.8	33.3

The vertical density gradient fields provided some insights on the relationship of these mixing events to the overturning motions. Figure 5.22 shows vertical slices taken through the *XZ*-plane at the relevant *Y*-coordinate for each of these events. It appears that these high mixing events occur near the boundaries of the overturning regions, but not within. This suggests that these high mixing events are linked with overturning in the flow. These tentative results agree with the findings of Diamessis & Nomura (2001) concerning the dynamics of overturns in stably stratified turbulence in a shear flow.

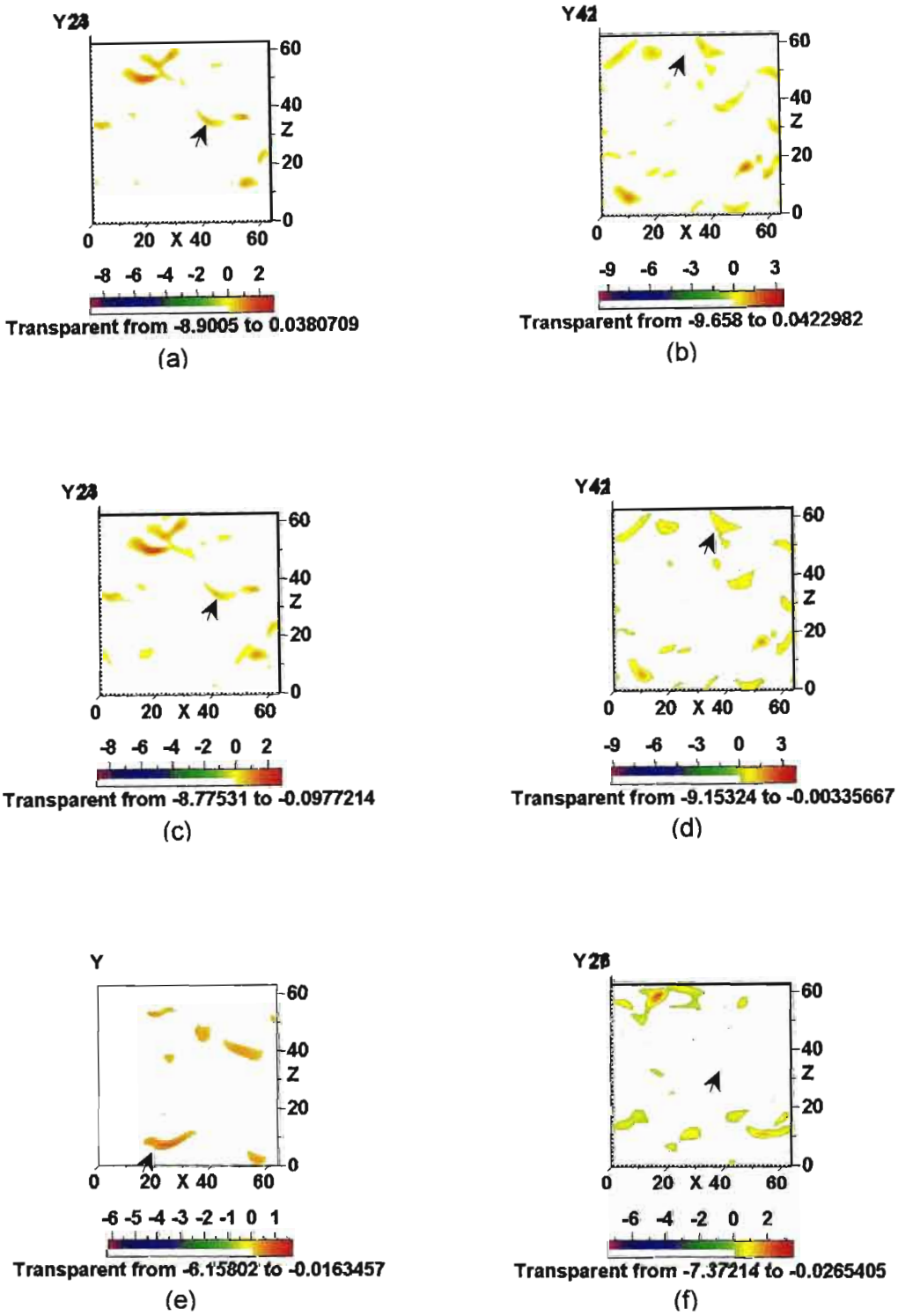

Figure 5.22: Contour plots of the vertical density gradient in the XZ-plane for high mixing events. (a) Ri = 0, t = 0.700, (b) Ri = 0, t = 1.050, (c) Ri = 0.39, t = 0.725, (d) Ri = 0.39, t = 1.100, (e) Ri = 1.58, t = 0.425, (f) Ri = 1.58, t = 1.475. The arrows indicate the approximate position of the particle in the XZ-plane at the high mixing event.

5.3 Flow Structures from RDT Simulation Fields

The structures of velocity and enstrophy fields obtained from identical initializations of DNS and RDT simulations at Ri = 1000 were visualized.

Figures 5.23 and 5.24 show three-dimensional plots of the isosurfaces of vertical velocity fields at times t = 1, 2, 3, 4 from DNS and RDT simulations. There are some general similarities in the velocity structures. The magnitudes of the vertical velocities from the RDT simulations are higher than those from the DNS, which is caused by the slightly lower dissipation rate in the linear RDT simulations. Similar plots of the horizontal velocity fields show no correlations in the structures.

Figures 5.25 show three-dimensional plots of the isosurfaces of the enstrophy at times t = 1, 4 from DNS and RDT simulations. The flattened pancakes structures are not evident in the RDT plots. It appears that these pancake structures are related to the non-linear effects which are excluded from the linear theory.

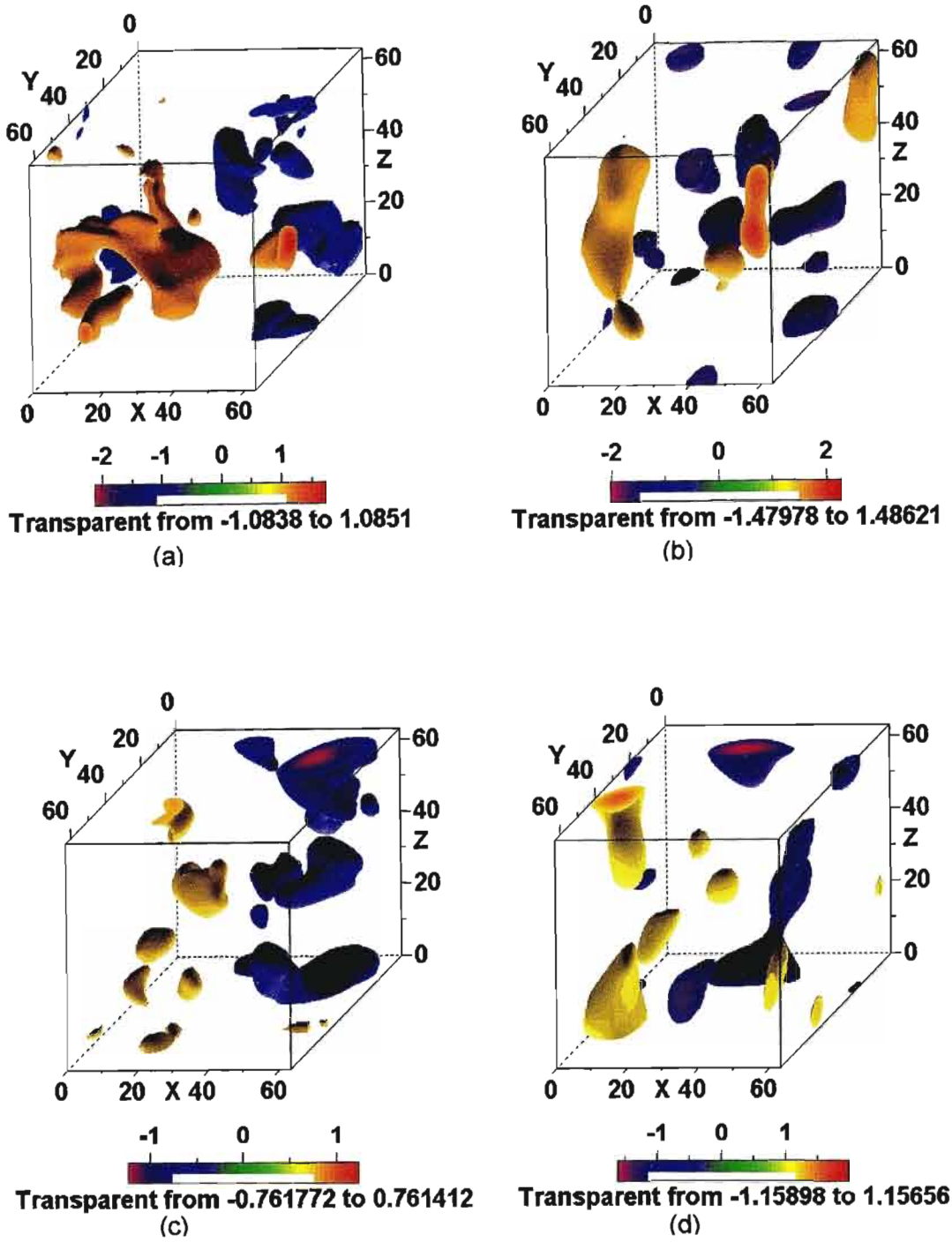

Figure 5.23: Isosurfaces of vertical velocity at Ri = 1000, (a) DNS, t=1, (b) RDT, t =1, (c) DNS, t =2, (d) RDT, t= 2. The surface levels are ± 2 times the standard deviation of the vertical velocity. Note surfaces above the threshold value are hidden inside surfaces at the threshold value.

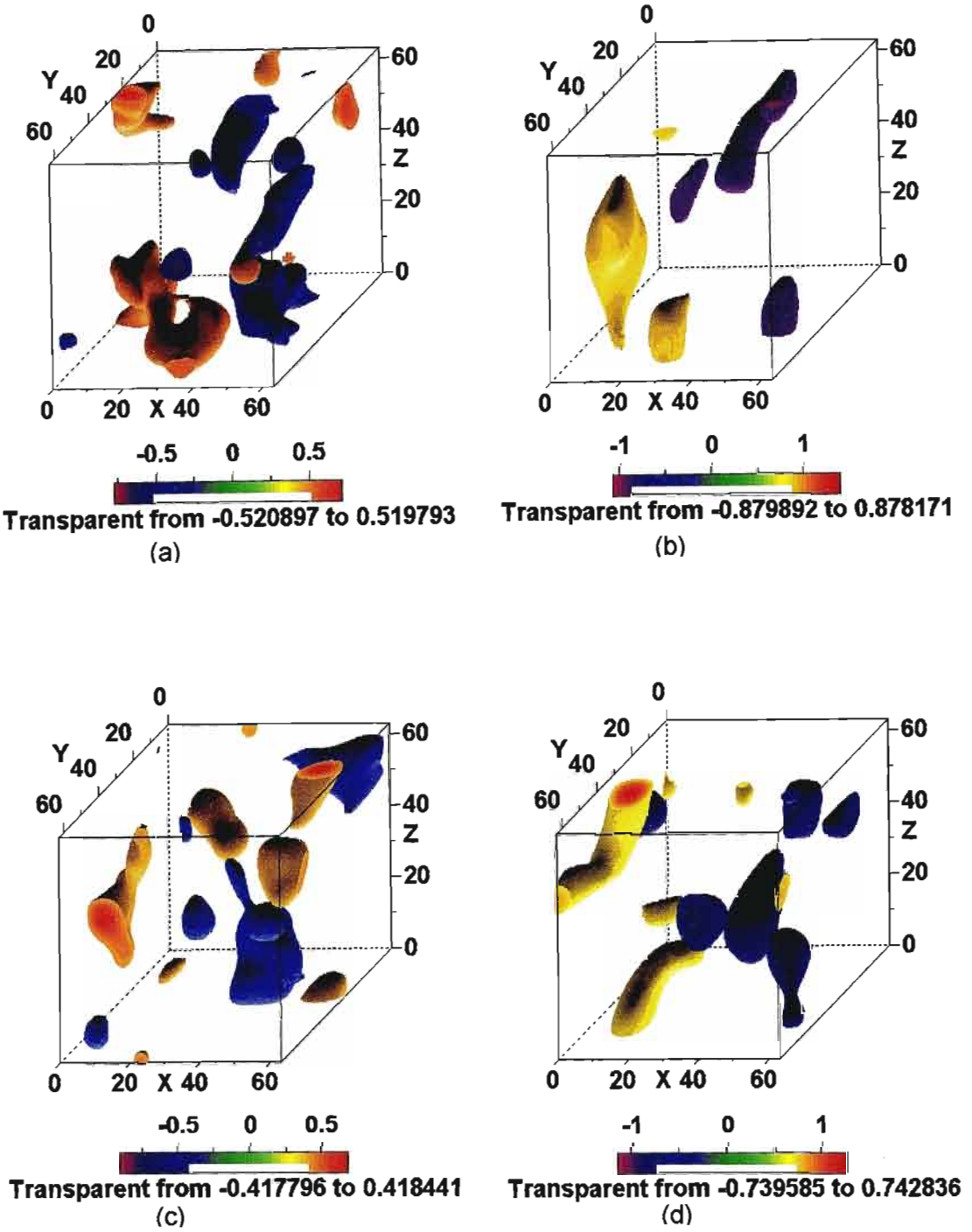

Figure 5.24: Isosurfaces of vertical velocity at Ri = 1000, (a) DNS, t=3, (b) RDT, t =3, (c) DNS, t =4, (d) RDT, t= 4. The surface levels are ± 2 times the standard deviation of the vertical velocity. Note surfaces above the threshold value are hidden inside surfaces at the threshold value.

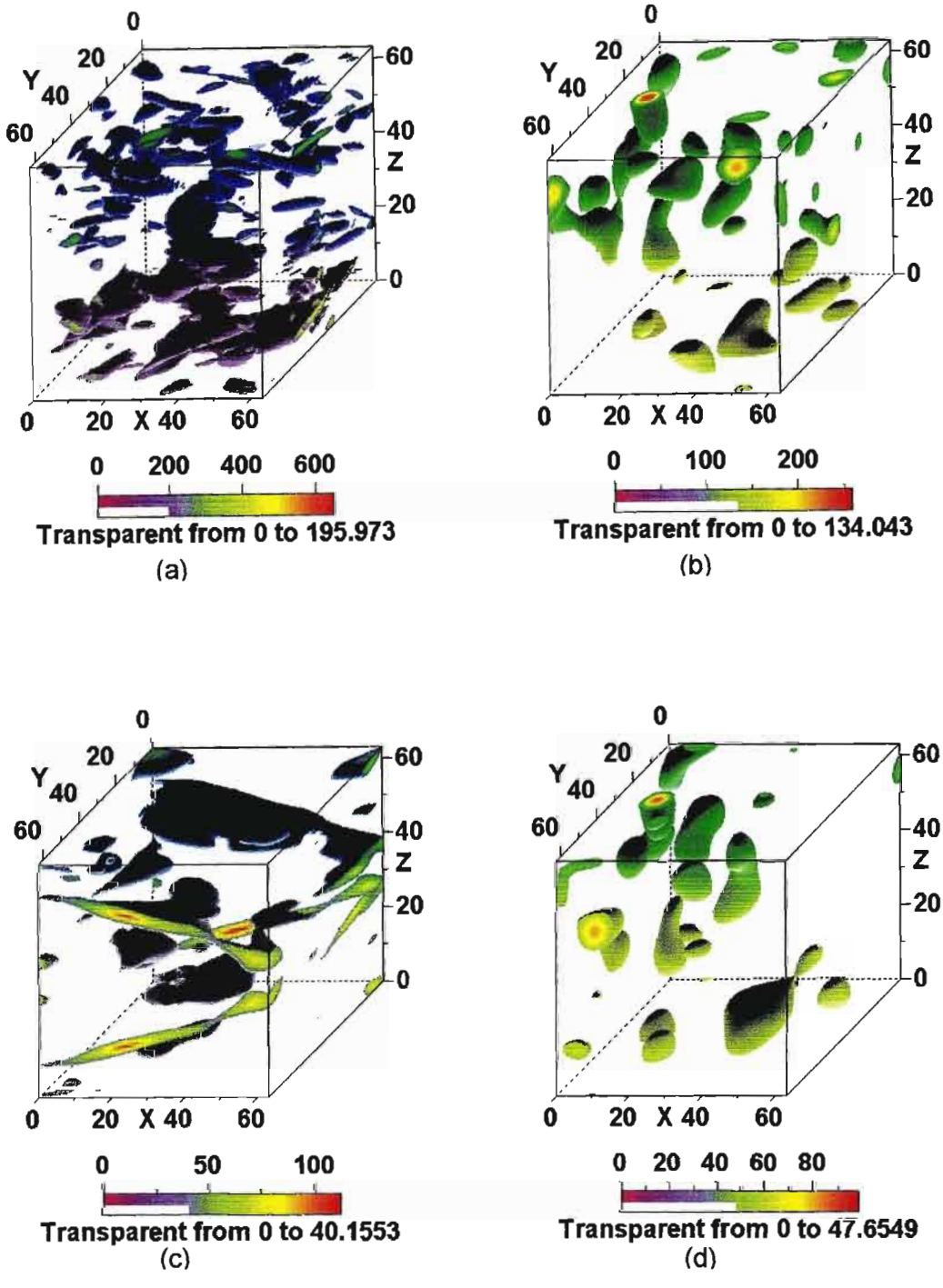

Figure 5.25: Isosurfaces of enstrophy at Ri = 1000, (a) DNS, t=1, (b) RDT, t =1, (c) DNS, t =4, (d) RDT, t= 4. The surface level is three times the mean-square enstrophy. Note enstrophy surfaces above the threshold value of three times the mean square enstrophy are hidden inside surfaces at the threshold value.

5.5 Summary

This chapter has presented a qualitative study on the flow structures in stably stratified turbulence. The visualizations indicate significant changes as the stratification increases. It appears that the turbulence structure for strong stratification resembles randomly scattered pancakes that are flattened in the horizontal plane as suggested by Kimura and Herring (1996). The vertical density gradient plots gives rise to an important question on whether the mixing in these flows is governed by overturning motions. At least qualitatively, the answer to this question is yes, however a more detailed study is required to be conclusive of this speculation. The structures at very stable stratifications from RDT simulations have general similarities with the DNS flow structures as far as the vertical velocity fields are concerned. However the enstrophy structures are very different. Precise interpretations of these flow structures would require further analysis.

CHAPTER 6

SUMMARY AND CONCLUSIONS

6.1 Summary of Investigation

In this dissertation, stably stratified decaying turbulence has been studied using direct numerical simulations (DNS) of the full Navier-Stokes equations. The main results of the research have been presented in chapters 3, 4 and 5 respectively.

Firstly, in Chapter 3, the mixing efficiency and energetics of stably stratified flows were studied for varying strengths of stratification. Limited investigation of molecular effects was carried out. The discussion on energetics and mixing efficiency were focused on six main simulations (i.e. Ri = 0, 0.39, 1.58, 10, 158 & 1000) representing flows that are unstratified to those that are very strongly stratified.

Secondly, in Chapter 4, a Lagrangian approach was used to study small scale mixing and dispersion in stably stratified turbulence. Particle tracking in DNS was used to calculate the displacements and instantaneous rates of mixing of fluid particles. Ensemble averaged results of mean square displacements and rate of mixing were presented. The dependence of the rate of mixing on the density fluctuations as modelled by PPH was investigated.

Finally, flow visualizations were used to study the structural features of stably stratified turbulence. Several diagnostics were used to gain understanding of the flow structure and their relationship to mixing.

6.2 Main Conclusions

The following is a brief description of the important results obtained from this study:

The mixing efficiency in stably stratified flows increases with increasing stratification and then approaches a constant value of about 30% at Richardson numbers greater than 10. The energetics in these flows is characterized by the exchange between kinetic and potential energies and associated oscillations in the buoyancy fluxes. It appears from this study that the discrepancy between the values of mixing efficiency

predicted by grid turbulence experiments and DNS cannot be attributed to molecular effects. However, it may be related to inaccurate accounting of the initial energy budget in the laboratory experiments. RDT simulations indicate that linear theory can be used to predict well the mixing efficiency of very strongly stable flows, as it appears the vertical dynamics of these flows are essentially linear.

The Lagrangian analysis has revealed three new important insights. Firstly, it is seen that the asymptotic value of the mean square vertical displacement gives a measure of the total irreversible mixing that has occurred in the flow. Secondly, the analysis indicates that the model used by Pearson, Puttock & Hunt (1983) for density exchanges between fluid elements is inadequate because the assumption that mixing rate is linearly proportional to density fluctuations clearly does not hold. Thirdly, mixing rates and overturns are strongly suppressed by stratification at times $Nt \geq 2\pi$.

Visualizations of the turbulence structure indicate significant changes as the stratification increases although detailed interpretation of these changes requires further analyses. It appears that the turbulence structure for strong stratification resembles randomly scattered pancakes that are flattened in the horizontal plane. The vertical density gradient plots suggest that overturning motions are the main mechanism by which mixing occurs in these flows.

6.3 Suggestions for Further Research

This dissertation has only focused on decaying stably stratified flows, which allowed an understanding of stratified flows at a relatively simple level. Some suggestions for further research are:

- The study should be extended to include shear in the DNS since most real stably stratified flows are shear flows. This would be a step towards developing a working model for describing mixing in real stably stratified flows.

- Laboratory experiments should be carried out with modifications to eradicate the sloshing motions noticed in earlier grid turbulence experiment. The mixing efficiency in such experiments should be closer to values predicted by DNS. This would clarify the quantitative discrepancy that exists between grid experiments and DNS.

- The tests of the PPH model should ideally be done in stationary homogenous turbulence. It would be worthwhile extending the results of this investigation to stationary turbulence to overcome some of the subtleties associated with comparing results between decaying and stationary turbulence.

- A lot of work still remains to be done in understanding the structure of turbulence associated with stratified flows. So far, in almost all the numerical results, little attempt has been made to simulate the visualization results from the laboratory (Riley & Lelong, 2000). DNS studies should focus closely in simulating laboratory visualization results to help determine how closely the numerical results replicate the laboratory experiments.

- Finally, it is noted that DNS alone may not provide answers to all the questions; it is of utmost importance to link DNS studies (which can be described as "exploratory computation") with laboratory experiments and theoretical concepts. This should pave the way to better understanding and improved models for mixing and dispersion in stably stratified flows.

The remainder of this dissertation consists of appendices and references referred to in the previous chapters.

" Man, irrespective of whether he is a theologian or scientist, has a strong tendency to see what he hopes to see" (Eiseley, L. 1979).

APPENDIX A

A.1 Introduction

This appendix contains the numerical and experimental data on mixing efficiency discussed in Chapter Three of this dissertation. It also provides a listing of the main DNS code and other program files mentioned in Chapter Three.

A.2: Experimental Results on Mixing Efficiency

Table A.1: Experimental data of mixing efficiency, (a) Rehmann & Koseff (2000), (b) Rottman & Britter (1986), (c) Britter (1985). Note S = salt stratified experiments, H = heat-stratified experiments, SH = salt & heat stratified experiments

(a)

Ri #	R_f	
0.08	0.0184	S
0.84	0.0464	S
0.41	0.0405	S
0.01	0.0058	S
0.03	0.0111	S
0.19	0.0328	S
3.26	0.0554	S
1.07	0.0501	S
0.1	0.0304	H
0.01	0.0067	H
0	0.0051	H
0.26	0.0468	H
0	0.0017	H
0.02	0.0089	H
0.04	0.0118	H
0	0.0022	H
0	0.0032	H
0.06	0.0193	SH

(b)

Ri #	R_f
0.01	0.008
0.02	0.01
0.073	0.02
0.181	0.03
0.41	0.04
1.3	0.05

(c)

Ri #	R_f
0.05	0.0172
0.05	0.01
0.14	0.03
0.85	0.05
0.85	0.06
3.39	0.0599
3.39	0.0561

A.3: DNS Results on Mixing Efficiency

Table A.2: Mixing efficiency results from DNS, (a) 32^3 runs (b) 64^3 runs, (c) 128^3 (runs). Note Pr = 0.5 for all runs

(a) 32^3 Runs

Sim. #	*Fr #*	*Ri #*	Buoyancy flux, *B*	Initial KE	Final KE	Final PE	Mixing efficiency $R_f = B/\Delta KE$	Mixing efficiency $R_f' = \Delta PE/\Delta KE$	Change in R_f	Remarks
1	Infinity	0	0.000	1.600	0.000	0.000	0.000	0.000	0	ΔT = 0.01, No. of time step = 1000
2	100.00	0.004	0.004	1.600	0.023	0.004	0.003	0.002	0.002	ΔT = 0.01, No. of time step = 1000
3	70.00	0.008	0.009	1.600	0.022	0.007	0.005	0.005	0.002	ΔT = 0.01, No. of time step = 1000
4	50.00	0.016	0.016	1.600	0.021	0.014	0.010	0.009	0.004	ΔT = 0.01, No. of time step = 1000
5	40.00	0.025	0.024	1.600	0.020	0.021	0.015	0.013	0.005	ΔT = 0.01, No. of time step = 1000
6	30.00	0.04	0.039	1.600	0.018	0.035	0.024	0.022	0.009	ΔT = 0.01, No. of time step = 1000
7	22.50	0.08	0.059	1.600	0.018	0.056	0.037	0.035	0.013	ΔT = 0.01, No. of time step = 1000
8	17.50	0.13	0.082	1.600	0.019	0.080	0.052	0.051	0.015	ΔT = 0.01, No. of time step = 1000
9	15.00	0.18	0.100	1.600	0.019	0.099	0.063	0.062	0.012	ΔT = 0.01, No. of time step = 1000
10	12.00	0.27	0.134	1.600	0.018	0.132	0.085	0.083	0.021	ΔT = 0.01, No. of time step = 1000
11	10.00	0.39	0.168	1.600	0.017	0.166	0.106	0.105	0.021	ΔT = 0.01, No. of time step = 1000
12	8.75	0.52	0.195	1.600	0.017	0.194	0.123	0.123	0.018	ΔT = 0.01, No. of time step = 1000
13	7.50	0.70	0.231	1.600	0.018	0.230	0.146	0.145	0.023	ΔT = 0.01, No. of time step = 1000
14	6.75	0.87	0.258	1.600	0.020	0.257	0.163	0.163	0.017	ΔT = 0.01, No. of time step = 1000
15	6.25	1.01	0.278	1.600	0.021	0.277	0.176	0.175	0.013	ΔT = 0.01, No. of time step = 1000
16	5.00	1.58	0.335	1.600	0.025	0.335	0.213	0.213	0.037	ΔT = 0.01, No. of time step = 1000
17	3.25	3.74	0.443	1.600	0.028	0.444	0.282	0.282	0.070	ΔT = 0.01, No. of time step = 1000
18	2.50	6.32	0.504	1.600	0.033	0.505	0.322	0.322	0.040	ΔT = 0.01, No. of time step = 1000
19	2.00	9.87	0.550	1.600	0.034	0.552	0.351	0.353	0.030	ΔT = 0.01, No. of time step = 1000
20	1.30	23.36	0.584	1.600	0.036	0.587	0.373	0.375	0.023	ΔT = 0.01, No. of time step = 1000
21	1.00	39.48	0.569	1.600	0.041	0.578	0.365	0.371	-0.004	ΔT = 0.01, No. of time step = 1000
22	0.75	70.18	0.545	1.600	0.044	0.560	0.350	0.360	-0.011	ΔT = 0.01, No. of time step = 1000
23	0.50	157.91	0.535	1.600	0.047	0.535	0.344	0.344	-0.015	ΔT = 0.002, No. of time step = 5000
24	0.35	322.27	0.517	1.600	0.047	0.515	0.333	0.332	-0.013	ΔT = 0.001, No. of time step = 10000
25	0.2	986.96	0.497	1.600	0.049	0.495	0.320	0.319	-0.012	ΔT = 0.0005, No. of time step = 20000

Table A.2-continued

(b) 64^3 Runs

Sim. #	*Fr #*	*Ri #*	Buoyancy flux, *B*	Initial KE	Final KE	Final PE	Mixing efficiency $R_f = B/\Delta KE$	Mixing efficiency $R_f' = \Delta PE/\Delta KE$	Change in R_f	Remarks
1	100.00	0.004	0.004	1.380	0.019	0.003	0.003	0.002	0	ΔT = 0.005, No. of time steps = 2000
2	10.00	0.395	0.172	1.460	0.011	0.170	0.119	0.117	0.115	ΔT = 0.005, No. of time steps = 2000
3	5.00	1.579	0.304	1.260	0.022	0.302	0.246	0.244	0.127	ΔT = 0.005, No. of time steps = 2000
6	1.99	10	0.500	1.280	0.031	0.498	0.400	0.399	0.155	ΔT = 0.005, No. of time steps = 2000
5	1.00	39.478	0.538	1.350	0.052	0.537	0.414	0.414	0.170	ΔT = 0.005, No. of time steps = 2000
4	0.50	157.914	0.561	1.600	0.075	0.556	0.368	0.365	-0.049	ΔT = 0.002, No. of time steps = 5000
7	0.20	1000	0.508	1.530	0.077	0.514	0.350	0.354	-0.011	ΔT = 0.002, No. of time steps = 2000

(c) 128^3 Runs

Sim. #	*Fr #*	*Ri #*	Buoyancy flux, *B*	Initial KE	Final KE	Final PE	Mixing efficiency $R_f = B/\Delta KE$	Mixing efficiency $R_f' = \Delta PE/\Delta KE$	Change in R_f	Remarks
1	100.00	0.004	0.004	1.400	0.000	0.004	0.003	0.003	0	ΔT = 0.002, No of time steps = 5000
2	10.00	0.395	0.181	1.460	0.013	0.178	0.125	0.123	0.120	ΔT = 0.002, No of time steps = 5000
3	5.00	1.579	0.370	1.520	0.027	0.365	0.248	0.244	0.121	ΔT = 0.002, No of time steps = 5000
5	1.00	39.478	0.544	1.420	0.074	0.540	0.404	0.401	0.157	ΔT = 0.002, No of time steps = 5000
4	0.50	157.914	0.600	1.610	0.049	0.596	0.384	0.382	-0.019	ΔT = 0.002, No of time steps = 5000

Table A.3: Mixing efficiency results from DNS at 64^3 grid with density field initialized at t =1.

Sim. #	F #	Ri #	PEo/Eo	R_f = B/Eo for t >= 1	R_f = B/Eo for t >= 0	Comments
1	100.00	0.004	0	0.003	0.003	ΔT = 0.005, with N = 2000
2	10.00	0.39	0	0.110	0.119	ΔT = 0.005, with N = 2000
3	5.00	1.58	0	0.206	0.246	ΔT = 0.005, with N = 2000
4	1.00	39.50	0	0.379	0.414	ΔT = 0.005, with N = 2000
5	0.50	158.00	0	0.362	0.368	ΔT = 0.005, with N = 2000

Table A.4: Mixing efficiency results for Pr = 0.1, 0.5, 1.0 & 2.0 from DNS at 64^3.

				Pr=0.1	*Pr*=0.5	*Pr*=1.0	*Pr*=2.0	
Sim. #	Fr #	Rl #	PEo/Eo	R_f = B/ΔKE	R_f = B/ΔKE	R_f = B/ΔKE	R_f = B/ΔKE	Comments
1	100.00	0.004	0	0.003	0.003	0.004	0.003	ΔT = 0.005, No. of time steps = 2000
2	10.00	0.39	0	0.104	0.119	0.114	0.089	ΔT = 0.005, No. of time steps = 2000
3	5.00	1.58	0	0.258	0.246	0.242	0.213	ΔT = 0.005, No. of time steps = 2000
6	1.9869	10.00	0	0.467	0.400	0.306	0.278	ΔT = 0.005, No. of time steps = 2000
5	1.00	39.48	0	0.591	0.414	0.318	0.252	ΔT = 0.005, No. of time steps = 2000
4	0.50	157.91	0	0.562	0.368	0.313	0.210	ΔT = 0.002, No. of time steps = 5000
7	0.1987	1000.0	0	0.503	0.350	0.238	0.172	ΔT = 0.002, No. of time steps = 5000

Table A.5: Mixing efficiency results from RDT simulations at 32^3 grid resolution

				Pr=0.1	*Pr*=0.5	*Pr*=1.0	*Pr*=2.0	
Sim. #	**Fr #**	**Ri #**	**PEo/Eo**	**R_f = B/ΔKE**	**R_f = B/ΔKE**	**R_f = B/ΔKE**	**R_f = B/ΔKE**	**Comments**
1	100.00	0.004	0	0.006	0.017	0.021	0.024	ΔT = 0.01, No. of time step = 1000
2	10.00	0.39	0	0.187	0.214	0.190	0.155	ΔT = 0.01, No. of time step = 1000
3	5.00	1.58	0	0.279	0.264	0.211	0.152	ΔT = 0.01, No. of time step = 1000
6	1.9869	10.00	0	0.373	0.298	0.225	0.153	ΔT = 0.01, No. of time step = 1000
5	1.00	39.48	0	0.407	0.305	0.228	0.155	ΔT = 0.01, No. of time step = 1000
4	0.50	157.91	0	0.426	0.314	0.240	0.170	ΔT = 0.002, No. of time step = 5000
7	0.1987	1000.0	0	0.427	0.311	0.233	0.160	ΔT = 0.002, No. of time step = 5000

A.4 Fortran Code Listing for DNS

A.4.1 Main Program listing for DNS at 64^3 grid resolution

```
      program main
C     MAIN PROGRAM TO SIMULTANEOUSLY SOLVE THE NAVIER STOKES EQUATIONS
C     WITH THE BOUSSINESQ APPROXIMATION USING FOURIER ANALYSIS
C     IN ALL THREE SPATIAL DIRECTIONS AT 64^3 GRID RESOLUTION.
      use numerical_libraries
      COMMON /UCOEF/ UF(2,62855,4)
      COMMON /PHYS/  AKMAX,AKMIN,XNU,DIF,DT,DT2,RI,ROT
      COMMON /INTEG/ IX,NDIM,NMID,NMODE,NFOR,NBAC,ISTEP,NSMTH,ISTAT,IDN
      COMMON /CALC/  TF(66,64,64,7),DELT(3,3)
      COMMON /INITL/ USQTO,EPSO,ISTART
      COMMON /ISOTR/ ANON(3),ISEED(1)
      COMMON /OUTP/  IOUT,JOUT,IPIC
      CHARACTER*64   FILE1,FILE2,FILE3
      COMPLEX        UF
      real delt !not there before
C     THE CONSTANTS ARE DEFINED IN THE FILE INIT.F
      INCLUDE 'INIT.F'
C     OPEN FILE TO WHICH TO WRITE OUTPUT STATISTICS
      OPEN (UNIT=IOUT,FILE=FILE1,STATUS='new')!'NEW'
      DO 1 I = 1,3
      DO 1 J = 1,3
      DELT(I,J) = 0.0
      IF ( I .EQ. J ) DELT(I,J) = 1.0
    1 CONTINUE
C     IF ISAVE EQUALS (DOES NOT EQUAL) ZERO, THIS IS NOT (IS) A RESTART
      IF (ISAVE .EQ. 0) GO TO 20
      OPEN(UNIT=JOUT,FILE=FILE2,STATUS='OLD',FORM='UNFORMATTED')
      READ (UNIT=JOUT) ISTEP,USQTO,EPSO,((UF(NBAC,I,J),I=1,NMODE),J=1,4)
      CLOSE (UNIT=JOUT)
C     IF IADJST EQUALS (DOES NOT EQUAL) ZERO, THIS IS NOT (IS) A RESTART
C     AFTER ALLOWING THE SKEWNESS TO ADJUST.
      IF (IADJST .EQ. 0) GO TO 21
C     SET THE PERTURBATION DENSITY FIELD TO ZERO.
      DO 50 I = 1,NMODE
      UF(NBAC,I,4) = (0.,0.)
   50 CONTINUE
      GO TO 21
   20 CONTINUE
C     COMPUTE THE INITIAL ENERGY SPECTRA
      CALL SPECTRA
C     INITIALIZE THE VELOCITY AND DENSITY FIELDS
      CALL START
   21 CONTINUE
C     PERFORM THE TIME STEPPING.
      TYPE *,'TIME STEPS :'
    3 CONTINUE
      TYPE *,' ',ISTEP
C     PREPARE TO TRANSFORM THE FOURIER VELOCITY, VORTICITY, AND DENSITY FIELDS.
      CALL PACK
C     PERFORM TRANSFORM OF THE FOURIER VELOCITY, VORTICITY, AND DENSITY FIELDS.
      ISWTCH = -1
      CALL THRDETR (TF(1,1,1,1),NXB2P1,NY,NZ,ISWTCH)
      CALL THRDETR (TF(1,1,1,2),NXB2P1,NY,NZ,ISWTCH)
      CALL THRDETR (TF(1,1,1,3),NXB2P1,NY,NZ,ISWTCH)
      CALL THRDETR (TF(1,1,1,4),NXB2P1,NY,NZ,ISWTCH)
      CALL THRDETR (TF(1,1,1,5),NXB2P1,NY,NZ,ISWTCH)
      CALL THRDETR (TF(1,1,1,6),NXB2P1,NY,NZ,ISWTCH)
      CALL THRDETR (TF(1,1,1,7),NXB2P1,NY,NZ,ISWTCH)
      IF ( MOD(ISTEP,NSTAT) .NE. 0 ) GO TO 10
C     COMPUTE THE PHYSICAL SPACE STATISTICS FOR STEP ISTEP.
      ISTAT = 1
      CALL STAT
      IF(IPIC .NE. 0) CALL IMAGE
   10 CONTINUE
C     TAKE THE CROSS PRODUCT OF THE PHYSICAL SPACE VELOCITY AND
C     VORTICITY, AND THE PRODUCT OF AND THE VELOCITY WITH THE DENSITY,
C     AND PREPARE THEM TO BE TRANSFORMED.
      CALL CROSS
C     TRANSFORM THE NONLINEAR TERMS BACK INTO FOURIER SPACE.
      ISWTCH = 1
      CALL THRDETR (TF(1,1,1,1),NXB2P1,NY,NZ,ISWTCH)
```

```
      CALL THRDETR (TF(1,1,1,2),NXB2P1,NY,NZ,ISWTCH)
      CALL THRDETR (TF(1,1,1,3),NXB2P1,NY,NZ,ISWTCH)
      CALL THRDETR (TF(1,1,1,4),NXB2P1,NY,NZ,ISWTCH)
      CALL THRDETR (TF(1,1,1,5),NXB2P1,NY,NZ,ISWTCH)
      CALL THRDETR (TF(1,1,1,6),NXB2P1,NY,NZ,ISWTCH)
C     COMPUTE THE TRANSFER FUNCTIONS PRIOR TO TIME STEPPING.
      CALL TRNSFR
C     COMPUTE UF AT TIME ISTEP+1.
      CALL STEP
      IF ( MOD(ISTEP,NSTAT) .NE. 0 ) GO TO 11
C     COMPUTE THE FOURIER SPACE STATISTICS FOR STEP ISTEP.
      ISTAT = 0
      CALL STAT
   11 CONTINUE
C     UPDATE VARIOUS PARAMETERS.
      ISTEP = ISTEP + 1
      ISTART = ISTART + 1
      NSTORE = NFOR
      NFOR = NBAC
      NBAC = NSTORE
C     IF ISTEP EQUALS IEND, STOP THE COMPUTATION.
      IF ( ISTEP .GE. IEND ) GO TO 4
      GO TO 3
    4 CONTINUE
C   CLOSE FILE CONTAINING OUTPUT STATISTICS.
      CLOSE (UNIT=IOUT)
C   IF NSAVE EQUALS (DOES NOT EQUAL) ZERO, THIS IS NOT (IS) A SAVE
      IF (NSAVE .EQ. 0) GO TO 30
      ISTEP = ISTEP - 1
      OPEN(UNIT=JOUT,FILE=FILE3,STATUS='NEW',FORM='UNFORMATTED')!NEW
      WRITE(UNIT=JOUT) ISTEP,USQTO,EPSO,((UF(NFOR,I,J),I=1,NMODE),J=1,4)
      CLOSE (UNIT=JOUT)
   30 CONTINUE
      TYPE *,'  END'
      STOP
      END
```

A.4.2 Initialization Program File

```
C    I/O FILENAMES
       FILE1='.\RESULTS\RUN00PT419_STATS'
       FILE2='.\RESTART\RUN02im_START'
       FILE3='.\SAVE\RUN00PT419_START'
C    IPIC CONTROLS IMAGE DUMP (0=none,1=u, 2=v, 3=w, 4=rho, 5,6,7=vorticity)
       IPIC = 1
C    I/O LOGICAL UNIT NUMBERS
       IOUT = 11
       JOUT = 21
C    DEFINE CONSTANTS
       IX = 2003
       ISEED(1)=1232
       call random_seed(put=ISEED)
       NDIM = 64
       NMID = (NDIM/2) + 1
       NX = NDIM
       NXB2P1 = (NX/2) + 1
       NY = NDIM
       NZ = NDIM
C    NMODE = NO. POINTS INSIDE MODE TRUNCATION CIRCLE
       NMODE = 62855
C    AKMIN IS THE MINIMUM AND AKMAX THE MAXIMUM WAVE NUMBERS.
       AKMIN = 2.0
       AKMAX = INT(SQRT(8./9.)*(NDIM/2)**2)+1
C    AKMAX = 966 FOR THIS CASE
       XNU = 0.005
       PRDTL = 0.5
       DIF = XNU/PRDTL
       FD = 1.9869
       PI = 4.0*ATAN(1.0)
C       RI = ((2.0*PI)/FD)**2
       RI = 0.0
       GE = 1.0
       ROT = (2.0*PI)/GE
       ROT = 0.0
C
       NBAC = 1
       NFOR = 2
       ISTEP = 0
       ISTART = 0
C    END PROGRAM AFTER IEND STEPS
       IEND = 211
C    APPLY EULER STEP FOR SMOOTHING EVERY NSMTH TIME STEPS.
       NSMTH = 25
C    SAVE RESULTS AT EVERY NSTAT TIME STEPS
       NSTAT = 210
C    IF ISAVE EQUALS ZERO, THIS IS NOT A RESTART
       ISAVE = 0
C    IF NSAVE EQUALS ZERO, THIS IS NOT A SAVE
       NSAVE = 1
C    DT IS THE TIME STEP.
       DT = 0.005
       DT2 = 2.0*DT
C    IF IDN EQUALS 0, FULL VELOCITY, DENSITY ZERO
C    IF IDN EQUALS 1, FULL VELOCITY, DENSITY NONZERO
C    IF IDN EQUALS 2, WAVE VELOCITY, DENSITY NONZERO
C    IF IDN EQUALS 3, WAVE VELOCITY, DENSITY ZERO
C    IF IDN EQUALS 4, VORTEX VELOCITY, DENSITY ZERO
       IDN = 0
C    IF IADJST DOES NOT EQUAL ZERO, THIS IS A RESTART
C    AFTER ALLOWING THE SKEWNESS TO ADJUST.
       IADJST = 1
       ANON(1) = 1.0
       ANON(2) = 1.0
       ANON(3) = ANON(2)
```

A.4.3 Program for computation of integrals

```
C     PROGRAM FOR FORMATTING AND COMPUTING INTEGRALS OF BUOYANCY FLUX,
C     POTENTIAL AND KINETIC ENERGY DISSIPATIONS.
      program formatting
!
      DIMENSION U(1001),V(1001),W(1001),R(1001),B(1001),KE(1001),
     $          PE(1001),E(1001),D(1001),DD(1001),T(1001),HKE(1001),
     $          VKE(1001),SB(1001),SD(1001),SDD(1001)
      DIMENSION PLOT1(1001,5),PLOT2(1001,4),PLOT3(1001,4)
      REAL      U,V,W,R,B,KE,PE,E,D,DD,T,HKE,VKE,SB,SD,SDD
      CHARACTER*20 FILENAME
      CHARACTER*12 DUMMY(10)
C
      TYPE *,'Enter data filename (in apostrophes)'
      ACCEPT *, FILENAME
      OPEN (UNIT=1,STATUS='OLD',FILE=FILENAME,READONLY)
      OPEN (UNIT=2,STATUS='NEW',FILE='PLOT.DAT')
C Read relevant parameters
      TYPE *, 'Enter Froude no, DT & NSTATS'
      ACCEPT *, F,DT,NSTATS
      PI=4.0*ATAN(1.0)
      RI=(2.0*PI/F)**2
C     RI=0.0
C Skip data from initialization-14 lines
      READ(1,100)
100   FORMAT(//////////////)
C Start loop to read data for all times
      DO 10 I=1,NSTATS
C*************************************************************
C The following is a test to check the file-reading
C       READ(1,210) (DUMMY(K),K=1,10)
C210    FORMAT(////40X,3A12//76X,2A12//64X,3A12
C     $        ////////////////9X,A12/////////////////////
C     $        9X,A12///////)
C       WRITE(6,211) DUMMY
C211  FORMAT(5A12)
C*************************************************************
      READ(1,200) U(I),V(I),W(I),R(I),B(I),KE(I),PE(I),
     $              E(I),D(I),DD(I)
200   FORMAT(////40X,3E12.3//76X,2E12.3//64X,3E12.3
     $        /////////////////9X,E13.6////////////////////////////
     $        9X,E13.6/////////////)
        T(I)=FLOAT(I-1)*DT
        B(I)=B(I)*RI
          DD(I)=DD(I)*RI
        HKE(I)=0.5*(U(I)+V(I))
        VKE(I)=0.5*W(I)
10    CONTINUE
      CLOSE (UNIT=1)
C Start time integrations of buoyancy prod, KE & PE  dissip
      SB(1)=0.0
      SD(1)=0.0
      SDD(1)=0.0
      DO 20 K=2,NSTATS
        SB(K)=SB(K-1)+0.5*(B(K-1)+B(K))*DT
        SD(K)=SD(K-1)+0.5*(D(K-1)+D(K))*DT
        SDD(K)=SDD(K-1)+0.5*(DD(K-1)+DD(K))*DT
20    CONTINUE
C Write out the data
      DO 30 K=1,NSTATS
      WRITE(2,300) T(K),U(K),V(K),W(K),R(K),B(K),KE(K),PE(K),
     $             E(K),D(K),DD(K),SB(K),SD(K),SDD(K)
300   FORMAT(1X,1P14E9.2)
30    CONTINUE
      end program
```

A.4.4 Image file for flow visualization

```
      SUBROUTINE IMAGE

      COMMON /CALC/  TF(66,64,64,7),DELT(3,3)
      COMMON /INTEG/ IX,NDIM,NMID,NMODE,NFOR,NBAC,ISTEP,NSMTH,ISTAT,IDN
      COMMON /OUTP/  IOUT,JOUT,IPIC
      DIMENSION      RPLOT1(64,64,64),RPLOT2(64,64,64),RPLOT3(64,64,64),
     1               RPLOT4(64,64,64),RPLOT5(64,64,64),RPLOT6(64,64,64),
     1               RPLOT7(64,64,64),RPLOT8(64,64,64)
      CHARACTER*64   NAME
      CHARACTER*1   NUM(10),N0,N1,N2,N3
        DATA  NUM /'0','1','2','3','4','5','6','7','8','9'/
      PI = 4.0*ATAN(1.0)
        AFAC=-1
      DO 5 K=1,NDIM
        AFAC=-AFAC
      DO 5 I=1,NDIM
        AFAC=-AFAC
      DO 5 J=1,NDIM
        AFAC=-AFAC
      RPLOT1(I,J,K)=TF(I,J,K,1)*AFAC
      RPLOT2(I,J,K)=TF(I,J,K,2)*AFAC
      RPLOT3(I,J,K)=TF(I,J,K,3)*AFAC
      RPLOT4(I,J,K)=TF(I,J,K,4)*AFAC
     ORPLOT5(I,J,K)=(TF(I,J,K,5)**2+TF(I,J,K,6)**2
     1               +TF(I,J,K,7)**2)
      KM1=K-1
      KP1=K+1
      IF(K.EQ.1)KM1=NDIM
      IF(K.EQ.NDIM)KP1=1
      RPLOT6(I,J,K)=-AFAC*(TF(I,J,KP1,4)-TF(I,J,KM1,4))*
     1               NDIM/(4*PI)-1.
      RPLOT7(I,J,K)=SQRT(TF(I,J,K,5)**2+TF(I,J,K,6)**2)
      RPLOT8(I,J,K)=TF(I,J,K,7)*AFAC
5     CONTINUE
        N3=NUM(ISTEP/1000+1)
        N2=NUM(MOD(ISTEP,1000)/100+1)
        N1=NUM(MOD(ISTEP,100)/10+1)
        N0=NUM(MOD(ISTEP,10)+1)
      NAME='.\IMAGES\PIC_1'//N3//N2//N1//N0//'(64x64x64)'
      OPEN(51,FILE=NAME,STATUS='NEW',FORM='UNFORMATTED')
      WRITE(51) RPLOT1
      CLOSE(51)
      NAME='.\IMAGES\PIC_2'//N3//N2//N1//N0//'(64x64x64)'
      OPEN(51,FILE=NAME,STATUS='NEW',FORM='UNFORMATTED')
      WRITE(51) RPLOT2
      CLOSE(51)
      NAME='.\IMAGES\PIC_3'//N3//N2//N1//N0//'(64x64x64)'
      OPEN(51,FILE=NAME,STATUS='NEW',FORM='UNFORMATTED')
      WRITE(51) RPLOT3
      CLOSE(51)
      NAME='.\IMAGES\PIC_4'//N3//N2//N1//N0//'(64x64x64)'
      OPEN(51,FILE=NAME,STATUS='NEW',FORM='UNFORMATTED')
      WRITE(51) RPLOT4
      CLOSE(51)
      NAME='.\IMAGES\PIC_5'//N3//N2//N1//N0//'(64x64x64)'
      OPEN(51,FILE=NAME,STATUS='NEW',FORM='UNFORMATTED')
      WRITE(51) RPLOT5
      CLOSE(51)
      NAME='.\IMAGES\PIC_6'//N3//N2//N1//N0//'(64x64x64)'
      OPEN(51,FILE=NAME,STATUS='NEW',FORM='UNFORMATTED')
      WRITE(51) RPLOT6
      CLOSE(51)
      NAME='.\IMAGES\PIC_7'//N3//N2//N1//N0//'(64x64x64)'
      OPEN(51,FILE=NAME,STATUS='NEW',FORM='UNFORMATTED')
      WRITE(51) RPLOT7
      CLOSE(51)
      NAME='.\IMAGES\PIC_8'//N3//N2//N1//N0//'(64x64x64)'
      OPEN(51,FILE=NAME,STATUS='NEW',FORM='UNFORMATTED')
      WRITE(51) RPLOT8
      CLOSE(51)
      RETURN
      END
```

APPENDIX B

B.1 Introduction

This appendix provides information related to Chapter Four of this dissertation. The basis functions for the cubic spline interpolation are given together with particle tracking code developed in Fortran.

B.2 Cubic Spline Basis Functions

The one-dimensional expressions for the basis functions used in the particle-tracking algorithm are (Yeung & Pope, 1988):

Numbering the nodal points from x_1 *to* x_N, and defining $x_0 = x_1 - \Delta x$, $x_{N+1} = x_N + \Delta x$, $x_{N+2} = x_N + 2\Delta x$. Further defining $\xi = (x - x_i)/\Delta x$, for i = 0, 1,..., N+1, N+2, the ith basis function at any given position x is given by

$$b_i(x) = \begin{cases} \frac{1}{6}(2+\xi)^3 & -2 < \xi < -1 \\ \frac{1}{6}(-3\xi^3 - 6\xi^2 + 4) & -1 < \xi < 0 \\ \frac{1}{6}(3\xi^3 - 6\xi^2 + 4) & 0 < \xi < 1 \\ \frac{1}{6}(2-\xi)^3 & 1 < \xi < 2 \\ 0 & otherwise \end{cases}$$

B.3 Particle Tracking Code in DNS

The main program code together with subroutines developed for the particle tracking are listed in this section.

B.3.1 Main DNS code with particle tracking

```
      program main
      use numerical_libraries
C     MAIN PROGRAM TO SIMULTANEOUSLY SOLVE THE NAVIER STOKES EQUATIONS
C     WITH THE BOUSSINESQ APPROXIMATION USING FOURIER ANALYSIS
C     IN ALL THREE SPATIAL DIRECTIONS AND TRACK FLUID PARTICLES..
C*********************************************************************
C    THE PARAMETER VALUES MUST BE INITIALIZED AT THE START
C    NP IS THE NUMBER OF PARTICLES RELEASED IN THE FLOW
      PARAMETER N=64,IEND=2002,NP=512,NB=N+2
      DIMENSION Eu(0:NB,0:NB,0:NB),Ev(0:NB,0:NB,0:NB),Ew(0:NB,0:NB,0:NB)
      DIMENSION Er(0:NB,0:NB,0:NB),D(N,N,N)
      DIMENSION x(0:IEND,NP),y(0:IEND,NP),z(0:IEND,NP),rho(0:IEND,NP)
      DIMENSION rmix(0:IEND,NP),TI(0:NB,0:NB),Acc(0:IEND,NP)
      DIMENSION U(0:IEND,NP),V(0:IEND,NP),W(0:IEND,NP),Drho(0:IEND,NP)
      DIMENSION Xdisp(0:IEND,NP),Ydisp(0:IEND,NP),Zdisp(0:IEND,NP)
      COMMON /UCOEF/ UF(2,62855,4)
      COMMON /PHYS/  AKMAX,AKMIN,XNU,DIF,DT,DT2,RI,ROT
      COMMON /INTEG/ IX,NDIM,NMID,NMODE,NFOR,NBAC,ISTEP,NSMTH,ISTAT,IDN
      COMMON /CALC/  TF(66,64,64,7),DELT(3,3)
      COMMON /INITL/ USQTO,EPSO,ISTART
      COMMON /ISOTR/ ANON(3),ISEED(1)
      COMMON /OUTP/  IOUT,JOUT,IPIC
      CHARACTER*64   FILE1,FILE2,FILE3
      COMPLEX        UF
      real delt !not there before
C*********************************************************************
C    INITIALIZATION SEGMENT TO SETUP SIMULATION
C    I/O FILENAMES
      FILE1='.\RESULTS\RUN02ptn_STATS'
      FILE2='.\RESTART\RUN02ptn_START'
      FILE3='.\SAVE\RUN02ptn_START'
C    I/O LOGICAL UNIT NUMBERS
      IOUT = 11
      JOUT = 21
C    DEFINE CONSTANTS
      IX = 2003
      ISEED(1)=1232
      call random_seed(put=ISEED)
      NDIM=64
      NMID = (NDIM/2) + 1
      NX = NDIM
      NXB2P1 = (NX/2) + 1
      NY = NDIM
      NZ = NDIM
C    NMODE = NO. POINTS INSIDE MODE TRUNCATION CIRCLE
      NMODE=62855
C    AKMIN IS THE MINIMUM AND AKMAX THE MAXIMUM WAVE NUMBERS.
      AKMIN = 2.0
      AKMAX = INT(SQRT(8./9.)*(NDIM/2)**2)+1
C    AKMAX = 966 FOR THIS CASE
      XNU = 0.005
      PRDTL = 0.5
      DIF = XNU/PRDTL
      FD = 10.0
      PI = 4.0*ATAN(1.0)
      RI = ((2.0*PI)/FD)**2
c     RI = 0.0
      GE = 1.0
      ROT = (2.0*PI)/GE
      ROT = 0.0
C
      NBAC = 1
      NFOR = 2
      ISTEP = 0
      ISTART = 0
C    APPLY EULER STEP FOR SMOOTHING EVERY NSMTH TIME STEPS.
      NSMTH = 25
C    SAVE RESULTS AT EVERY NSTAT TIME STEPS
      NSTAT =5
      NPARTICLE =5
C    IF ISAVE EQUALS ZERO, THIS IS NOT A RESTART
```

```
      ISAVE = 0
C     IF NSAVE EQUALS ZERO, THIS IS NOT A SAVE
      NSAVE = 1
C     DT IS THE TIME STEP.
      DT = 0.005
      DT2 = 2.0*DT
C     IF IDN EQUALS 0, FULL VELOCITY, DENSITY ZERO
C     IF IDN EQUALS 1, FULL VELOCITY, DENSITY NONZERO
C     IF IDN EQUALS 2, WAVE VELOCITY, DENSITY NONZERO
C     IF IDN EQUALS 3, WAVE VELOCITY, DENSITY ZERO
C     IF IDN EQUALS 4, VORTEX VELOCITY, DENSITY ZERO
      IDN = 0
C     IF IADJST DOES NOT EQUAL ZERO, THIS IS A RESTART
C     AFTER ALLOWING THE SKEWNESS TO ADJUST.
      IADJST = 0
      ANON(1) = 1.0
      ANON(2) = 1.0
      ANON(3) = ANON(2)
C*****************************************************************************
C     OPEN FILES FOR OUTPUT STATISTICS AND PARTICLE POSITIONS
      OPEN (UNIT=IOUT,FILE=FILE1,STATUS='NEW')
C*****************************************************************************
      DO 1 I = 1,3
      DO 1 J = 1,3
      DELT(I,J) = 0.0
      IF ( I .EQ. J ) DELT(I,J) = 1.0
    1 CONTINUE
C     IF ISAVE EQUALS (DOES NOT EQUAL) ZERO, THIS IS NOT (IS) A RESTART
      IF (ISAVE .EQ. 0) GO TO 20
      OPEN(UNIT=JOUT,FILE=FILE2,STATUS='old',FORM='UNFORMATTED')
      READ (UNIT=JOUT) ISTEP,USQTO,EPSO,((UF(NBAC,I,J),I=1,NMODE),J=1,4)
      CLOSE (UNIT=JOUT)
C     IF IADJST EQUALS (DOES NOT EQUAL) ZERO, THIS IS NOT (IS) A RESTART
C     AFTER ALLOWING THE SKEWNESS TO ADJUST.
      IF (IADJST .EQ. 0) GO TO 21
C     SET THE PERTURBATION DENSITY FIELD TO ZERO.
      DO 50 I = 1,NMODE
      UF(NBAC,I,4) = (0.,0.)
   50 CONTINUE
      GO TO 21
   20 CONTINUE
C     COMPUTE THE INITIAL ENERGY SPECTRA
      CALL SPECTRA
C     INITIALIZE THE VELOCITY AND DENSITY FIELDS
      CALL START
   21 CONTINUE
C*****************************************************************************
C     INITIALIZE PARTICLE POSITIONS
      kk=0.
      do 2 k=2,58,8
      do 2 j=2,58,8
      do 2 i=2,58,8
      kk=kk+1
      z(0,kk)=k
      y(0,kk)=j
      x(0,kk)=i
      rmix(0,kk)=0.
      Drho(0,kk)=0.
      Acc(0,kk)=0.
      Xdisp(0,kk)=0.
      Ydisp(0,kk)=0.
      Zdisp(0,kk)=0.
2     continue
C*****************************************************************************
C     INITIALIZE SPLINE INTERPOLATION
      CALL SPLINE_INIT(NB,TI)
C     PERFORM THE TIME STEPPING.
      TYPE *,'TIME STEPS :'
    3 CONTINUE
      TYPE *,' ',ISTEP
C     PREPARE TO TRANSFORM THE FOURIER VELOCITY, VORTICITY, AND DENSITY FIELDS.
```

```
      CALL PACK
C     PERFORM TRANSFORM OF THE FOURIER VELOCITY, VORTICITY, AND DENSITY FIELDS.
      ISWTCH = -1
      CALL THRDETR (TF(1,1,1,1),NXB2P1,NY,NZ,ISWTCH)
      CALL THRDETR (TF(1,1,1,2),NXB2P1,NY,NZ,ISWTCH)
      CALL THRDETR (TF(1,1,1,3),NXB2P1,NY,NZ,ISWTCH)
      CALL THRDETR (TF(1,1,1,4),NXB2P1,NY,NZ,ISWTCH)
      CALL THRDETR (TF(1,1,1,5),NXB2P1,NY,NZ,ISWTCH)
      CALL THRDETR (TF(1,1,1,6),NXB2P1,NY,NZ,ISWTCH)
      CALL THRDETR (TF(1,1,1,7),NXB2P1,NY,NZ,ISWTCH)
      IF ( MOD(ISTEP,NSTAT) .NE. 0 ) GO TO 10
C     COMPUTE THE PHYSICAL SPACE STATISTICS FOR STEP ISTEP.
      ISTAT = 1
      CALL STAT
   10 CONTINUE

C*********************************************************************************
C     PARTICLE INTERPOLATION
      DDT=DT*NDIM/(2.*PI)
      xmm=float(NDIM)
      ymm=float(NDIM)
      zmm=float(NDIM)
C     CALL IMAGE GENERATES THE REQUIRED FIELDS AT THE CURRENT TIME STEP
C     THE NUMBERS 1,2,3,4 ARE EQUAL TO U,V,W AND RHO FIELDS RESPECTIVELY
C     CALL SPLINE SUBROUTINE TO EVALUATE BASIS FUNCTION COEFFICIENTS
      call image(NDIM,1,D)
      call spline(NDIM,NB,D,TI,Eu)
      call image(NDIM,2,D)
      call spline(NDIM,NB,D,TI,Ev)
      call image(NDIM,3,D)
      call spline(NDIM,NB,D,TI,Ew)
      call image(NDIM,4,D)
      call spline(NDIM,NB,D,TI,Er)
C     CALL INTERPOLATE SUBROUTINE TO GET PARTICLE VELOCITIES
C     GET INITIAL DENSITY FLUCTUATIONS AT T=0 AND DO INITIAL EULER TIME STEPPING
      DO 11 kk=1,NP
      if (istep .eq. 0) then
          call interpolate(x(0,kk),y(0,kk),z(0,kk),xmm,ymm,zmm,NB,Er,rp)
          rho(0,kk)=rp
          call interpolate(x(0,kk),y(0,kk),z(0,kk),
     1         xmm,ymm,zmm,NB,Eu,up)
          call interpolate(x(0,kk),y(0,kk),z(0,kk),
     1         xmm,ymm,zmm,NB,Ev,vp)
          call interpolate(x(0,kk),y(0,kk),z(0,kk),
     1         xmm,ymm,zmm,NB,Ew,wp)
          U(0,kk)=up
          V(0,kk)=vp
          W(0,kk)=wp
       x(1,kk)=x(0,kk)+DDT*(up)
       y(1,kk)=y(0,kk)+DDT*(vp)
       z(1,kk)=z(0,kk)+DDT*(wp)
       else
       call interpolate(x(istep,kk),y(istep,kk),z(istep,kk),
     1         xmm,ymm,zmm,NB,Eu,up)
       call interpolate(x(istep,kk),y(istep,kk),z(istep,kk),
     1         xmm,ymm,zmm,NB,Ev,vp)
       call interpolate(x(istep,kk),y(istep,kk),z(istep,kk),
     1         xmm,ymm,zmm,NB,Ew,wp)
C     ADVANCE PARTICLE POSITIONS USING ADAMS_BASHFORTH TIME STEPPING
       x(istep+1,kk)=x(istep,kk)+DDT*(3./2.*up-1./2.*U(istep-1,kk))
       y(istep+1,kk)=y(istep,kk)+DDT*(3./2.*vp-1./2.*V(istep-1,kk))
       z(istep+1,kk)=z(istep,kk)+DDT*(3./2.*wp-1./2.*W(istep-1,kk))
C     CALCULATE DENSITY FLUCTUATIONS AT TIMES GREATER THAN 0
       call interpolate(x(istep,kk),y(istep,kk),z(istep,kk),
     1     xmm,ymm,zmm,NB,Er,rp)
       rho(istep,kk)=rp
       U(istep,kk)=up
       V(istep,kk)=vp
       W(istep,kk)=wp
C     CALCULATE MIXING RATE
       rmix(istep,kk)=(rho(istep,kk)-rho(istep-1,kk))/DT-wp
```

```
C   CALCULATE CHANGE IN VELOCITY, DENSITY FLUCTUATIONS AND DISPLACEMENTS
      Acc(istep,kk)=sqrt((U(istep,kk)-U(istep-1,kk))**2+
     1     (V(istep,kk)-V(istep-1,kk))**2+
     1     (W(istep,kk)-W(istep-1,kk))**2)
      Drho(istep,kk)=(rho(istep,kk)-rho(istep-1,kk))/DT
      Xdisp(istep,kk)=x(istep,kk)-x(0,kk)
      Ydisp(istep,kk)=y(istep,kk)-y(0,kk)
      Zdisp(istep,kk)=z(istep,kk)-z(0,kk)
      endif
11    continue
C*******************************************************************************
C   TAKE THE CROSS PRODUCT OF THE PHYSICAL SPACE VELOCITY AND
C   VORTICITY, AND THE PRODUCT OF AND THE VELOCITY WITH THE DENSITY,
C   AND PREPARE THEM TO BE TRANSFORMED.
      CALL CROSS
C   TRANSFORM THE NONLINEAR TERMS BACK INTO FOURIER SPACE.
      ISWTCH = 1
      CALL THRDETR (TF(1,1,1,1),NXB2P1,NY,NZ,ISWTCH)
      CALL THRDETR (TF(1,1,1,2),NXB2P1,NY,NZ,ISWTCH)
      CALL THRDETR (TF(1,1,1,3),NXB2P1,NY,NZ,ISWTCH)
      CALL THRDETR (TF(1,1,1,4),NXB2P1,NY,NZ,ISWTCH)
      CALL THRDETR (TF(1,1,1,5),NXB2P1,NY,NZ,ISWTCH)
      CALL THRDETR (TF(1,1,1,6),NXB2P1,NY,NZ,ISWTCH)
C   COMPUTE THE TRANSFER FUNCTIONS PRIOR TO TIME STEPPING.
      CALL TRNSFR
C   COMPUTE UF AT TIME ISTEP+1.
      CALL STEP
      IF ( MOD(ISTEP,NSTAT) .NE. 0 ) GO TO 13
C   COMPUTE THE FOURIER SPACE STATISTICS FOR STEP ISTEP.
      ISTAT = 0
      CALL STAT
   13 CONTINUE
      IF (MOD(ISTEP,NPARTICLE) .NE. 0) GO TO 14
   14 CONTINUE
C   UPDATE VARIOUS PARAMETERS.
      ISTEP = ISTEP + 1
      ISTART = ISTART + 1
      NSTORE = NFOR
      NFOR = NBAC
      NBAC = NSTORE
C   IF ISTEP EQUALS IEND, STOP THE COMPUTATION.
      IF ( ISTEP .LT. IEND ) GO TO 3
    4 CONTINUE

C   CLOSE FILE CONTAINING OUTPUT STATISTICS.
      CLOSE (UNIT=IOUT)
C   IF NSAVE EQUALS (DOES NOT EQUAL) ZERO, THIS IS NOT (IS) A SAVE
      IF (NSAVE .EQ. 0) GO TO 30
      ISTEP = ISTEP - 1
      OPEN(UNIT=JOUT,FILE=FILE3,STATUS='NEW',FORM='UNFORMATTED') !new
      WRITE(UNIT=JOUT) ISTEP,USQTO,EPSO,((UF(NFOR,I,J),I=1,NMODE),J=1,4)
      CLOSE (UNIT=JOUT)
   30 CONTINUE
      OPEN(UNIT=JOUT,FILE='.\TRACKS\RUN02PTN_TRACKS',STATUS='NEW',
     1     FORM='FORMATTED')
      WRITE(UNIT=JOUT,FMT=100)((x(k,kk),y(k,kk),z(k,kk),U(k,kk),
     1     V(k,kk),W(k,kk),Acc(k,kk),rho(k,kk),rmix(k,kk),Drho(k,kk),
     1     Xdisp(k,kk),Ydisp(k,kk),Zdisp(k,kk), kk=1,NP),k=0,251,5)
100   FORMAT(1x,13F10.5)
      CLOSE (UNIT=JOUT)

      TYPE *,'  END'
      STOP
      END
```

B.3.2 Spline Initialization

This subroutine sets up the coefficient matrix T_{ij}

```
      SUBROUTINE spline_init(NB,TI)
C   SUBROUTINE TO INITIALIZE THE COEFFICIENT MATRIX
      DIMENSION   T(0:NB,0:NB),TI(0:NB,0:NB)
C   CREATE TRIADIAGONAL MATRIX Tij
      NB1=NB+1
      do 5 i =0,NB
      do 5 j=0,NB
      T(i,j)=0.
      if(i .eq. j) T(i,j)=2./3.
      if(iabs(i-j) .eq. 1) T(i,j)=1./6.
5     continue
      T(0,NB)=1./6.
      T(NB,0)=1./6.
C   USE IMSL LIBRARY TO INVERT Tij MATRIX
      CALL LINRG(NB1,T,NB1,TI,NB1)
      return
      end
```

B.3.3 Input of Fields

This subroutine outputs the instantaneous velocity and density fluctuation field to the main program to be used for the interpolation

```
      SUBROUTINE IMAGE(NDIM,IPIC,D)
      DIMENSION D(NDIM,NDIM,NDIM)
      COMMON /CALC/  TF(66,64,64,7)
        AFAC=-1
      DO 5 K=1,NDIM
        AFAC=-AFAC
      DO 5 I=1,NDIM
        AFAC=-AFAC
      DO 5 J=1,NDIM
        AFAC=-AFAC
      D(I,J,NDIM+1-K)=TF(I,J,K,IPIC)*AFAC
5     CONTINUE
      RETURN
      END
```

B.3.4 Spline Subroutine

This subroutine calculates the cubic spline coefficients required for the interpolation

```
      SUBROUTINE spline (N,NB,D1,TI,E)
C     SUBROUTINE TO COMPUTE CUBIC SPLINE COEFFICIENTS
C     PASSES THE SPLINE COEFFICIENTS INTO THE INTERPOLATE SUBROUTINE
      DIMENSION E(0:NB,0:NB,0:NB), TI(0:NB,0:NB),D1(N,N,N)
      DIMENSION F(0:NB,0:NB,0:NB),A1(0:NB,0:NB,0:NB),F1(0:NB,0:NB,0:NB)
C     ASSIGN 3D INPUT FIELDS FROM IMAGE SUBROUTINE INTO A NEW ARRAY F
      DO 1 k=1,N
      DO 1 j=1,N
      DO 1 i=1,N
      F(i,j,k)=D1(i,j,k)
1     CONTINUE
C     PERIODICALLY EXTEND 3D FIELD TO NB1 DIMENSIONS
      do 2 k= 1,N
      do 2 j= 1,N
      F(0,j,k)=F(N,j,k)
      do 2 i= N+1,NB
      F(i,j,k)=F(i-N,j,k)
2     continue
      do 3 k= 1,N
      do 3 i= 0,NB
      F(i,0,k)=F(i,N,k)
      do 3 j= N+1,NB
      F(i,j,k)=F(i,j-N,k)
3     continue
      do 4 j= 0,NB
      do 4 i= 0,NB
      F(i,j,0)=F(i,j,N)
      do 4 k= N+1,NB
      F(i,j,k)=F(i,j,k-N)
4     continue
C     GENERATE CUBIC SPLINE
      DO 10 k=0,NB
      DO 10 j=0,NB
      DO 10 i=0,NB
          A1(i,j,k)=0.
          DO 10 M=0,NB
           A1(i,j,k)=A1(i,j,k)+TI(i,M)*F(M,j,k)
10    CONTINUE
      DO 11 k=0,NB
      DO 11 j=0,NB
      DO 11 i=0,NB
          F1(i,j,k)=0.
          DO 11 M=0,NB
           F1(i,j,k)=F1(i,j,k)+TI(j,M)*A1(i,M,k)
11    CONTINUE
      DO 12 k=0,NB
      DO 12 j=0,NB
      DO 12 i=0,NB

          E(i,j,k)=0.
          DO 12 M=0,NB
           E(i,j,k)=E(i,j,k)+TI(k,M)*F1(i,j,M)
12    CONTINUE
      RETURN
      END
```

B.3.5 Interpolation Subroutine

The interpolation using the cubic coefficients and basis functions is computed using a tensor product in this subroutine.

```
      SUBROUTINE interpolate(xi,yi,zi,xmm,ymm,zmm,NB,E,up)
C     USES THE CUBIC SPLINE COEFFICIENTS GENERATED IN SPLINE SUBROUTINE TO
C     INTERPOLATE FOR THE VELOCITIES AND OTHER SCALARS USING A 3D TENSOR PRODUCT
C     REPRESENTATION
      DIMENSION E(0:NB,0:NB,0:NB)
      DIMENSION B(0:NB),C(0:NB),D(0:NB)
C     SETTING OF PERIODIC BOUNDARY CONDITIONS TO WRAP-AROUND PARTICLES
      xx=xi
      yy=yi
      zz=zi
      IF(xx .lt. 1.) xx=MOD(xx,xmm)+xmm
      IF(xx .gt. xmm+1) xx=MOD(xx,xmm)
      IF(yy .lt. 1.) yy=MOD(yy,ymm)+ymm
      IF(yy .gt. ymm+1) yy=MOD(yy,ymm)
      IF(zz .lt. 1.) zz=MOD(zz,zmm)+zmm
      IF(zz .gt. zmm+1) zz=MOD(zz,zmm)
C     GENERATE THE BASIS FUNCTIONS
      DO 20 L=0,NB
      etax=(xx-L)
      etay=(yy-L)
      etaz=(zz-L)
      B(L)=0.
      C(L)=0.
      D(L)=0.
      IF(etax .ge. -2. .and. etax .le. -1.) B(L)=(2.+ etax)**3/6.
      IF(etay .ge. -2. .and. etay .le. -1.) C(L)=(2.+ etay)**3/6.
      IF(etaz .ge. -2. .and. etaz .le. -1.) D(L)=(2.+ etaz)**3/6.
      IF(etax .ge. -1. .and. etax .le. 0.)
     1B(L)=(-3.*etax**3- 6.*etax**2+4.)/6.
      IF(etay .ge. -1. .and. etay .le. 0.)
     1C(L)=(-3.*etay**3- 6.*etay**2+4.)/6.
      IF(etaz .ge. -1. .and. etaz .le. 0.)
     1D(L)=(-3.*etaz**3- 6.*etaz**2+4.)/6.
      IF(etax .ge. 0. .and. etax .le. 1.)
     1B(L)=(3.*etax**3- 6.*etax**2+4.)/6.
      IF(etay .ge. 0. .and. etay .le. 1.)
     1C(L)=(3.*etay**3- 6.*etay**2+4.)/6.
      IF(etaz .ge. 0. .and. etaz .le. 1.)
     1D(L)=(3.*etaz**3- 6.*etaz**2+4.)/6.
      IF(etax .ge. 1. .and. etax .le. 2.) B(L)=(2.- etax)**3/6.
      IF(etay .ge. 1. .and. etay .le. 2.) C(L)=(2.- etay)**3/6.
      IF(etaz .ge. 1. .and. etaz .le. 2.) D(L)=(2.- etaz)**3/6.
20    CONTINUE
C     INITIALIZE VARIABLE BEING INTERPOLATED AND CALCULATES THE TENSOR PRODUCT
      up=0.
      DO 30 kk=0,NB
      DO 30 jj=0,NB
      DO 30 ii=0,NB
      up=up+B(ii)*C(jj)*D(kk)*E(ii,jj,kk)
30    CONTINUE
      RETURN
      END
```

REFERENCES

Ahlberg, J.H., Wilson, E.N.& Walsh, J.L. (1967), *The Theory of Splines and Their Applications*, Academic Press, New York

Barry, M.E., Ivey, G.N., Winters, K.B. & Imberger, J. (2001), Measurements of diapycnal diffusivities in stratified fluid, *J. Fluid Mech.*, **442**, 267-291.

Batchelor, G.K. (1967), *An Introduction to Fluid Dynamics*, Cambridge University Press

Briggs, D.A., Ferziger, J.H., Koseff, J.R. & Monismith, S.G. (1998), Turbulent mixing in a shear-free stably stratified two-layer fluid, *J. Fluid Mech.*, **354**, 175-208.

Britter, R.E., Hunt, J.C.R., Marsh, G.L. & Synder, W.H. (1983), The effects of stratification on turbulent diffusion and the decay of grid turbulence, *J. Fluid Mech.*, **127**, 27-44.

Carruthers, D.J., Holroyd, R.J., Hunt, J.C.R., Weng, W.S., Robin, A.G., Apsley, D.D., Smith, F.B., Thomson, D.J. & Hudson, B. (1991), UK atmospheric dispersion modeling system, *Proc. of 19th NATO/CCMS International Technical Meeting on Air Pollution Modelling and its Application*, H. van Dop and G. Kallos (ed.) Plenum.

Csanady, G.T. (1964), Turbulent diffusion in a stratified fluid, *J. Atmos. Sci.* **21**, 439-447

De Boor, C. (1978), *A Practical Guide to Splines*, Springer-Verlag, New York.

Derbyshire, S.H. & Hunt, J.C.R. (1985), Structure of turbulence in stably stratified atmospheric boundary layers; Comparison of large eddy simulations and theoretical results. In *Waves and Turbulence in Stably Stratified Flows* (ed. S.D. Mobbs & J.C.King), pp. 23-59. Clarendon.

Diamessis, P.J. & Nomura, K.K. (2001), The structure and dynamics of overturns in stably stratified homogenous turbulence, Submitted to *J.Fluid Mech.*.

Dickey, T.D. & Mellor, G.L. (1980), Decaying turbulence in neutral and stratified fluids, *J. Fluid Mech.*, **99**, 13.

Eiseley, L. (1979), Darwin and the mysterious mr. X: *New light on the evolutionists*, Dutton, E.P., New York.

Eswaran, V. & Pope, S.B. (!988), An examination of forcing in direct numerical simulations of turbulence, *Comput. Fluids* **16**, 257-278

Fernando, H.J.S. (1991), Turbulent mixing in stratified fluids, *Annu. Rev. Fluid Mech.*, **23**: 455-493.

Hanazaki, H. & Hunt, J.C.R. (1996), Linear processes in unsteady stably stratified turbulence, *J. Fluid Mech.*, **318**, 303-337.

Holt, S.E., Koseff, J.R. & Ferziger, J.H. (1992), A numerical study of the evolution and structure of homogenous stably stratified sheared turbulence, *J.Fluid Mech.*, **237**, 499-539.

Hunt, J.C.R. (1982), Diffusion in the stable boundary layer, *In Atmospheric Turbulence and Air Pollution Modelling* (ed. F.T.M. Nieuwstadt & H. van Dop), pp. 231-274, Reidel.

Hunt, J.C.R. (1985), Diffusion in the stably stratified atmopheric boundary layer, *Journal of climate and applied metereology*, **24**, 1187-1195

Hunt, J.C.R & Carruthers, D.J. (1990), Rapid distortion theory and the 'problems' of turbulence, *J. Fluid Mech.*, **212**, 497-532.

Hunt, J.C.R., Stretch, D.D. & Britter, R.E. (1988), Length scales in stably stratified turbulent flows and their use in turbulence models. In *Stably Stratified Flow and Dense Gas Dispersion,* Proc. IMA conf., Chester, UK, 9-10 April 1986.

Itsweire, E.C., Helland, K.N. & Van Atta, C.W. (1986), The evolution of grid-generated turbulence in a stably stratified fluid, *J. Fluid Mech.*, **207**, 419-452.

Kaneda, Y. & Ishida, T. (2000), Suppression of vertical diffusion in strongly stratified turbulence, *J. Fluid Mech.*, **402**, 311-327.

Keller, K.H. & Van Atta, C.W. (2000), On the evolution of turbulent kinetic and potential energies in homogenous stratified shear turbulence, Submitted to *J.Fluid Mech.*.

Kimura, Y. & Herring, J.R. (1996), Diffusion in stably stratified turbulence, *J.Fluid Mech.*, **328**, 253-269.

Kolmogorov, A.N. (1942), On degeneration of isotropic turbulence in an incompressible viscous liquid, *Dokl. Akad. Nauk.* SSSR **31**, 538-541

Lin, J.T. & Pao, Y.H. (1979), Wakes in stratified fluids, *Annu. Rev. Fluid Mech.*, **11**:317-338

Linden, P.F. (1979), Mixing in stratified fluids, *Geophys. Astrophys. Fluid Dynamics*, **13**, 3-23.

Linden, P.F. (1980), Mixing across a density interface produced by grid turbulence, *J. Fluid Mech.*, **100**, 691-703.

Metais, O. & Herring, J.R. (1989), Numerical simulations of freely evolving turbulence in stably stratified fluids, *J. Fluid Mech.*, **202**, 117-148.

Moin, P. & Kim, J. (1997), Tackling turbulence with supercomputers, *Scientific American*, January 1997, 1-10.

Monin, A.S. & Yaglom, A.M. (1971), *Statistical Fluid Mechanics: Mechanics of Turbulence*, MIT

Nicolleau, F. & Vassilicos, J.C. (2000), Turbulent diffusion in stably stratified non-decaying turbulence, *J. Fluid Mech.*, **410**, 123-146.

Oduyemi, K. (1993), Mixing efficiency of a stably stratified fluid, *Boundary-Layer Meteorology*, **62**, 107-115

Ooi, A., Martin, J., Soria, J. & Chong, M. (1999), A study of the evolution and characteristics of the invariants of the velocity gradient tensor in isotropic turbulence, *J. Fluid Mech.*, **381**, 141-174.

Osborn, T.R. (1980), Estimates of the local rate of vertical diffusion from dissipation measurements, *J. Phys. Oceanogr.*, **10**, 83-89

Park, Y.G., Whitehead, J.A. & Gnanadeskian, A. (1994), Turbulent mixing in stratified fluids, layer formation and energetics, *J. Fluid Mech.*, **279**, 279-311.

Pearson, H.J., Puttock, J.S. & Hunt, J.C.R. (1983), A statistical model of fluid element motions and vertical diffusion in a homogenous stratified turbulent flow, *J. Fluid Mech.*, **129**, 219-249.

Rehmann, C.R. & Koseff, J.R. (2000), Mean potential energy change in weakly and strongly stratified grid turbulence, Submitted to *J.Fluid Mech.*.

Riley, J.J. & Lelong, M.P. (2000), Fluid motions in the presence of strong stable stratification, *Annu. Rev. Fluid Mech.*, **32**: 613-657.

Riley, J.J., Metcalfe, R.W. & Weissman, M.A. (1981), Direct numerical simulations of homogenous turbulence in density-stratified fluids, In Non-linear properties of internal waves, *Proc. AIP Conference, La Jolla Institute,* (ed. By B.J.West).

Riley, J.J. & Patterson, G.S. (1974), Diffusion experiments with numerically integrated isotropic turbulence, *Phys. Fluids*, **17**, 292-297.

Rogallo, R.S. & Moin, P. (1984), Numerical simulation of turbulent flows, *Annu. Rev. Fluid Mech.*, **16**: 99-137.

Rohr, J.J., Itsweire, C. & Van Atta, C.W. (1984), Mixing efficiency in stably-stratified decaying turbulence, *Geophys. Astrophys. Fluid Dynamics*, **29**, 221-236

Rottman, J.W. & Britter, R.E. (1986), The mixing efficiency and decay of grid-generated turbulence in stably stratified fluids, *Proc. of the 9th Australasian Fluid Mechanics Conference*, Univ. of Auckland, Auckland. New Zealand, 8-12 December, 1986.

Rottman, J.W., Seshadri, K., Nomura, K.K. & Stretch, D.D. (2001), On potential energy changes and the Boussinesq approximation in stratified flows, *Bulletin of the American Physical Society*, Vol. 46, No. 10, November 2001

Sato, Y. & Yamamoto, K. (1987), Lagrangian measurement of fluid –particle motion in an isotropic turbulent field, *J. Fluid Mech.*, **175**, 183-199

Sawford, B. (2001), Turbulent Relative Dispersion, *Annu. Rev. Fluid Mech.*, **33**: 289-317.

Squires, K.D. & Eaton, J.K. (1991), Lagrangian and Eulerian statistics obtained from direct numerical simulations of homogenous turbulence, *Phys. Fluids*, A 3, 130-143

Streeter, V.L., Wylie, E.B. & Bedford, K.W. (1998), *Fluid Mechanics*, WCB/McGraw-Hill.

Stretch, D.D., Nomura, K.K. & Rottman, J.W. (2000), Mixing efficiency in decaying stably stratified turbulence, presented at the *5th international symposium on stratified flows*, Vancouver, Canada, July 10-13, 2000.

Stretch, D.D., Rottman, J.W., Nomura, K.K. & Venayagamoorthy, S.K. (2001), Transient mixing events in stably stratified turbulence, *Proc. of the 14th Australasian Fluid Mechanics Conference*, Adelaide University, Adelaide, Australia, 10-14 December 2001.

Snyder, W.H. & Lumley, J. (1971), Some measurements of particle velocity autocorrelation functions in a turbulent flow, *J. Fluid Mech.*, **48**, 41-71.

Taylor, G.I. (1921), Diffusion by continuous movements, *Proc.Lond.Math.Soc. (Ser.2)* **20**, 196-212.

Tennekes, H. & Lumley, J. L. (1973), *A first course in turbulence*, Cambridge, The Massachusetts Institute of Technology Press.

Townsend, A.A. (1976), The structure of turbulent shear flow, *Cambridge University Press*.

Truesdall, G.C. (1993), *The interaction between decaying isotropic turbulence and dispersed solid particles*, Ph.D dissertation, University of California, Irvine.

Turner, J.S. (1973), *Buoyancy Efects in Fuids*, New York/London, Cambridge University Press.

Venayagamoorthy, S.K. (2000), *Mixing efficiency in environmental flows using direct numerical simulations*, BScEng dissertation in civil engineering, University of Natal, Durban.

Venayagamoorthy, S.K., Stretch, D.D., Rottman, J.W. & Nomura, K.K. (2002), Mixing efficiency of turbulence in environmental flows, accepted for presentation at the *1st International Conference on Heat Transfer, Fluid Mechanics, and Thermodynamics,* Kruger Park, South Africa, 8-10 April 2002.

Weinstock, J. (1978), Vertical turbulent diffusion in a stably stratified fluid, *J. Atmos.Sci.,* **35**, 1022-1027.

Winters, B.G., Lombard, P.N., Riley, J.J. & D'Asaro, E.A. (1995), Available potential energy and mixing in density-stratified fluids, *J. Fluid Mech.,* **289**, 115-128.

Yeung, P.K. & Pope, S.B. (1988), An algorithm for tracking fluid particles in numerical simulations of homogenous turbulence, *J.Comp. Phys.*, **79**, 373-416

Yeung, P.K. & Pope, S.B. (1989), Lagrangian statistics from direct numerical simulations of isotropic turbulence, *J. Fluid Mech.*, **207**, 531.586.